53 Wissenschaftliche Berichte des Instituts für Meteorologie und Klimaforschung
des Karlsruher Instituts für Technologie

KRISTINA LUNDGREN

Direct Radiative Effects of Sea Salt on the Regional Scale

KIT Scientific Publishing

Kristina Lundgren

Direct Radiative Effects of Sea Salt on the Regional Scale

Wissenschaftliche Berichte des Instituts für Meteorologie und
Klimaforschung des Karlsruher Instituts für Technologie
Band 53

Herausgeber: Prof. Dr. Ch. Kottmeier
Institut für Meteorologie und Klimaforschung
am Karlsruher Institut für Technologie
Kaiserstr. 12, 76128 Karlsruhe

Eine Übersicht über alle bisher in dieser Schriftenreihe erschienenen Bände
finden Sie am Ende des Buchs.

Direct Radiative Effects of Sea Salt on the Regional Scale

by
Kristina Lundgren

KIT Scientific Publishing

Dissertation, Karlsruher Institut für Technologie
Fakultät für Physik
Tag der mündlichen Prüfung: 28.05.2010
Referenten: Prof. Dr. Christoph Kottmeier, Prof. Dr. Thomas Leisner

Impressum

Karlsruher Institut für Technologie (KIT)
KIT Scientific Publishing
Straße am Forum 2
D-76131 Karlsruhe
www.ksp.kit.edu

KIT – Universität des Landes Baden-Württemberg und nationales
Forschungszentrum in der Helmholtz-Gemeinschaft

KIT Scientific Publishing 2012
Print on Demand

ISSN 0179-5619
ISBN 978-3-86644-773-8

Abstract

This thesis aims to quantify the direct radiative effects (DRE) of sea salt aerosol in the atmosphere. The online coupled regional scale model system COSMO-ART (Vogel et al., 2009) is extended for this objective with respect to the sea salt aerosol. A method for treating sea salt containing internal mixtures of sodium chloride, water, and sodium sulphate is introduced to the model. To consider the aerosol sulphate of both anthropogenic and natural origin, the emission of oceanic dimethyl sulphide (DMS) is implemented in COSMO-ART within this thesis.

A case study is performed for the Mediterranean, North East Atlantic Ocean and South and Central Europe with the extended model system. In this study, DMS oxidation is the dominant source for sea salt aerosol sulphate over the Atlantic Ocean and locally contributes up to 40% of the sea salt aerosol sulphate over the Mediterranean. The sea salt chemical composition is dominated by water and the water uptake significantly influences the aerosol size distribution.

The simulated sea salt aerosol optical depth is found to show strong dependence on the 10 m wind speed under cloud free conditions. This relation is best described by a power law fit and compares well with satellite observations. To the author's knowledge, this is the first time such an investigation has been performed with both AOD and wind speed information achieved from model calculations.

A new sea salt optical parameterisation is developed for both the shortwave and longwave spectrum. The total extinction in the solar range is dominated by scattering. In the longwave range, the relative contribution of absorption becomes increasingly important due to the absorption of water and sulphate. The extinction of radiation due to sea salt modifies the atmospheric properties, which in turn alter the wind and aerosol size distributions. The wind speed is modified at ±0.2 m s^{-1}, and the mass and number densities up to 50% and 20%, respectively, with respect to the undisturbed reference fields. For cloud free conditions, the impact on the shortwave and longwave radiative budgets are approximately in the same order of magnitudes. This is found both over the cloud free continent and the cloud free ocean and causes the net radiative effect to be approximately zero. Thus, the perturbations of the radiative fluxes are too small to cause any distinct temperature change (< 0.01 K). The mean effect over the ocean exceeds that of over land, suggesting a more meaningful effect above surfaces with lower albedo. Although the aerosol effect is found to be small in the present study, a comparison with the DRE of anthropogenic aerosol implies the relative importance of sea salt DRE for the Mediterranean and North East Atlantic Ocean, including during polluted conditions.

Table of Contents

Abstract i

1. Introduction 1

2. Sea Salt – the Primary Marine Aerosol 11
- 2.1. Generation and Removal Processes 11
- 2.2. Distribution 16
- 2.3. Aerosol Characteristics 20
- 2.4. Direct Radiative Effects 24
- 2.5. Basics Regarding the Modelling of Sea Salt Aerosol 27

3. The Model System COSMO-ART 33
- 3.1. General Overview of the Model System 33
- 3.2. Treatment of Sea Salt Aerosol in COSMO-ART 36
  - 3.2.1. Aerosol Dynamics for Pure Sea Salt 41
  - 3.2.2. Parameterisation of the Sea Salt Aerosol Production . 45
- 3.3. Treatment of Radiative Fluxes 48

4. Introduction of Wet Internally Mixed Sea Salt Aerosol to COSMO-ART 53
- 4.1. Formation of Internally Mixed NaCl-Sulphate Aerosol 53
  - 4.1.1. Production of Sulphuric Acid in Clean Marine Air . . 54
  - 4.1.2. Condensation of Sulphuric Acid on Aerosols 59

4.2. Sea Salt Aerosol Liquid Water Content 62
  4.2.1. Electrolyte Formation 64
  4.2.2. Aqueous Electrolyte Binary Molality 66
4.3. The Conservation Equations for the Internally Mixed Aerosol 67

5. A New Optical Parameterisation for Sea Salt Aerosol 71
5.1. The Effective Refraction Index of the Multi-component Aerosol 72
  5.1.1. The Real Part of Multicomponent Aerosol Refractive Index 77
  5.1.2. The Imaginary Part of the Multicomponent Aerosol Refractive Index 81
5.2. Mie Calculations for the Sea Salt Aerosol 82
  5.2.1. The Extinction Coefficient 87
  5.2.2. The Single Scattering Albedo 90
  5.2.3. The Asymmetry Parameter 94

6. 3-D Simulation with the Extended Model System COSMO-ART 99
6.1. Simulation Setup 100
6.2. Synoptic Situation During 24th-26th July 2007 102
6.3. Gaseous and Anthropogenic Particulate Emissions 106
  6.3.1. Emissions of Dimethyl Sulphide (DMS) 106
  6.3.2. Anthropogenic Gaseous and Particulate Emissions . . 108
6.4. 3-D Simulation Results 110
  6.4.1. Distribution of Gaseous Species 111
  6.4.2. Impact of Water Uptake on the Aerosol Size Distribution 116
  6.4.3. Simulated Sea Salt Aerosol Composition 124
  6.4.4. Horizontal and Vertical Distributions 129
  6.4.5. Simulated Aerosol Optical Depth (AOD) 132
  6.4.6. Influence on Atmospheric Radiative Fluxes and Temperature 142

6.4.7. Feedback on the Sea Salt Density Fields 153
6.5. Comparison with Simulated Anthropogenic DRE 155
6.5.1. Simulated Fields of Anthropogenic Aerosol 156
6.5.2. Simulated AOD and Impact on Atmospheric Variables 158

7. Summary and Conclusions 167

A. Results from Mie Calculations 175
A.1. Extinction Coefficients 175
A.2. Single Scattering Albedo 184
A.3. Asymmetry Parameters 193

List of Symbols 202

List of Figures 215

List of Tables 222

Bibliography 224

Chapter 1

Introduction

Aerosols, i.e. suspensions of liquid and solid particles in the air, influence the state of the atmosphere with potentially as large climate effects as those caused by greenhouse gases, however with larger uncertainties (Intergovernmental Panel on Climate Change; IPCC, 2007). The aerosol impact is for this reason to this date still in need of further investigation. The state of knowledge regarding the aerosol impact on various atmospheric processes on the regional scale is even worse than on the global scale (e.g., Vogel et al., 2009, and references therein). The radiative impact caused by aerosol particles is seasonal, shows large spatial variations and can become dominant on the regional scale (Tzanis and Varotsos, 2008).

Aerosol particles are either produced primarily by ejection into the atmosphere, or secondarily by gas-to-particle conversion processes within the atmosphere. Aerosols are generally classified as anthropogenic or natural, with respect to their origin. Anthropogenic aerosols result from human activities with major contributions from bio mass burning and fossil fuel consumption, for example. Natural aerosols, for example, are black carbon from natural fires (Jacobson, 2001b), mineral dust, sea salt, biogenic aerosol from land and oceans, sulphate aerosol and dust aerosol produced by volcanic eruptions (IPCC, 2007). As the emission processes of the natural aerosols are not directly affected by human activities they will remain regardless of changes in anthropogenic emissions and cannot be controlled, which might be one of their most important qualities.

Currently there is a wide interest in increasing the state of knowledge concerning the impacts of human activities on climate change. To establish a better understanding of the anthropogenic impacts it is indeed of central importance to separate the anthropogenic contribution from the natural one. It is for this purpose essential to minimise the uncertainties regarding the aerosol effects caused by the naturally emitted aerosols, which still are large (Satheesh and Krishna Moorthy, 2005).

When considering the natural aerosol impact on the atmosphere, that of the sea salt is one of the most substantial. Considering that the earth's surface is covered by oceans by 70%, it is understandable that the sea salt aerosol is the key aerosol constituent over much of it. The total production of natural aerosols on the global scale is dominated by that of sea salt, which accounts for about 1,000-10,000 Tg yr^{-1} or 30-75% of the total natural aerosol production (Blanchard and Woodcock, 1980; Winter and Chýlek, 1997). The sea salt aerosol is a primary aerosol introduced to the lowest atmosphere through emissions from the ocean as a result of the wind effect on the water surface. One important quality of sea salt is its wide size range between tenths of nano-meters to tenths of micro-meters (e.g., Gong et al., 1997; Clarke et al., 2006). The sea salt concentration shows large spatial variations with relatively lower concentrations above land compared to over oceans (Foltescu et al., 2005).

Numerous studies indicate the importance of the sea salt aerosol within a broad range of atmospheric processes. The emission of the sea salt from the sea surface has already been suggested to impact on the exchange of heat and moisture in the interface between the ocean and atmosphere (Foltescu et al., 2005, and references therein). Within this matter, the largest sea salt aerosol, the so-called spume mode aerosol, is propbably the most important aerosol (Andreas, 1998). Further aspects include air quality, visibility, and atmospheric heterogeneous chemistry (e.g., O'Dowd et al., 1999; Li-Jones et al., 2001; Myhre and Grini, 2006; Athanasopoulou et al., 2008). Due to the participation in chemical reactions, the sea salt affects the atmospheric cycle of the other reactants. Sea salt has been shown to react with nitric acid and thereby influence the burden of particulate nitrate (e.g., Myhre and Grini, 2006; Athanasopoulou et al., 2008). Such reactions lead to less available nitric acid and can in turn cause a reduction of the global burden of ammonium nitrate particles by 25 % when sea salt is present (Myhre and Grini, 2006). The sea salt may also impact the tropospheric ozone chemistry due to the NaCl and NaBr sea salt components, which are precursors to highly reactive chlorine and bromine atoms. These in turn play a significant role for the ozone chemistry (Finlayson-Pitts and Hemminger, 2000). The peak in number of submicron aerosol together with its hygroscopic nature makes the sea salt important for cloud formation as it is an important cloud condensation nuclei. Especially in the clean marine boundary layer at high wind speed conditions, the sea salt aerosol comprises the primary source for cloud nuclei (e.g., O'Dowd and Smith, 1993; Foltescu et al., 2005). It is not only submicron sea salt aerosol that influence the features and evolution of cloud formation and subsequent rain formation. Jensen and Lee (2008) drew the conclusion that both small and giant aerosol are of equal importance for warm rain formation and that giant sea salt aerosol determine the rainfall rate of marine stratocumulus clouds for wind speeds exceeding 4-5 m s^{-1}. Not least the sea salt aerosol is responsible for the majority of aerosol scattered light in clean background air (e.g., Murphy et al., 1998; Quinn et al., 1998; Quinn and Bates, 2005). Through the scattering of light and the contribution to cloud formation, sea salt modifies the atmospheric radiation budget and consequently affects the atmospheric state and climate, directly and indirectly, respectively. Under the direct radiative effect, or direct aerosol effect, extinction, i.e. scattering and absorption of radiation, by the aerosol is understood. The sea salt aerosol has a direct cooling effect as the extinction is dominated by the scattering of sunlight, which leads to a decreased surface temperature (e.g., Lewis and Schwartz, 2004). With the indirect radiative effect, or indirect aerosol effect, the extinction that occurs when the aerosol acts as seed particles for cloud drops is meant. In this way, the sea salt aerosol helps to increase the marine boundary layer albedo via cloud formation. In which proportion the clouds in turn affect the atmospheric radiative fluxes depends on the cloud properties. The sea salt radiative effect is the most important above ocean areas and coastal regions, as a result of the large gradients towards lower concentrations over land.

A combination of measurements and model studies is required for investigations regarding the impact caused by sea salt on atmospheric processes. The available observations often show site specific characteristics and are mainly taken during fair wind conditions (Heintzenberg et al., 2000; Satheesh and Krishna Moorthy, 2005). Due to the lack of an adequate database the validation of the model results is subsequently restricted.

The intention of this thesis is to contribute to the better understanding of the interaction between the sea salt aerosol and the state of the atmosphere via the sea salt aerosol direct radiative effect. The tool for this investigation is the regional scale non-hydrostatic numerical atmospheric model COSMO-ART (Vogel et al., 2009). Simulating the sea salt influence on the state of the atmosphere in an accurate way is a complex task. The state of the particle is variable due to ageing and exchange processes with ambient aerosols. In some models the concentrations of sea salt are determined in rather simplified manners. For example, Wilson et al. (2001) and Ma et al. (2008) determined the sea salt concentration as a function of the wind speed, without calculating the emission flux, whereas the most common way is to determine the emission flux of sea salt as a function of wind speed. Regarding the chemical composition, sea salt is often found as internal mixtures with other chemical compounds and aerosols (e.g., Andreae et al., 1986; Sievering et al., 1992; O'Dowd et al., 1997; Clegg et al., 1998; Katoshevski et al., 1999). Internal mixtures of the sea salt aerosol with non sea salt sulphate, as a result of the condensation of sulphuric acid or aqueous phase oxidation, has been found in several studies (e.g., Sievering et al., 1992; O'Dowd et al., 1997; Clegg et al., 1998; Katoshevski et al., 1999). The sea salt is very hygroscopic and effectively grows due to the uptake of water. This process depends on the chemical composition of the aerosol (e.g., Tang, 1997) and leads to additional mass on the aerosol, which consequently modifies the aerosol life cycle. Due to the water content the optical properties are modified, for example, making this an important process to consider for describing the sea salt atmospheric cycle and impact correctly. A simplified way of treating the water uptake in numerical models is to parameterise the wet sea salt size dependent on the ambient relative humidity and dry aerosol size, assuming a constant chemical composition (e.g., Grini et al., 2002; Li et al., 2008; Ma et al., 2008; Yu and Luo, 2009). E.g. Stier et al. (2005) and Jacobson (1997) applied another common, more accurate method for calculating the water content, which is referred to as the Zdanovskii-Stokes-Robinson (ZSR) relation (Stokes and Robinson, 1966). The ZSR-relation empirically expresses the aerosol liquid water content of a multicomponent mixture as a function of electrolyte molality and ambient relative humidity. The most accurate and time consuming way of determining the liquid aerosol water content is to consider the thermodynamic equilibrium between the components in the gas phase and aerosol phase and thereafter calculate the water absorption as a function of the aerosol phase chemical composition. However in model studies, the composition of sea salt is often assumed to remain constant during transport, thus any exchange with ambient gaseous and aerosol species is neglected (e.g., Foltescu et al., 2005; Grini et al., 2002; Ma et al., 2008). As variations of the chemical composition are most often neglected, the water uptake calculations also become simplified. The feedback between the sea salt aerosol and the atmosphere is, furthermore, seldom investigated. No application with one of the few existing non-hydrostatic online coupled models WRF/Chem (Grell et al., 2005) addressed to the sea salt feedback with the atmosphere is available in the literature.

There exist several atmospheric models taking the direct sea salt radiative effect into consideration. These models are, however, mainly applied to the global scale (e.g., Grini et al., 2002; Ma et al., 2008) while studies on regional scales are rare. Although there exist some model studies addressed to the sea salt direct radiative effect on climate, the magnitude of this effect is still connected to large uncertainties and needs further investigation (e.g., Lewis and Schwartz, 2004; Satheesh and Krishna Moorthy, 2005). Lewis and Schwartz (2004) summarised the global annually averaged direct effect from different studies to range from -0.08 W m^{-2} to -6.2 W m^{-2}. For comparison, the direct radiative effect is estimated to be -0.4 ±0.2 W m^{-2} for sulphate, 0.03 ±0.12 W m^{-2} for biomass burning aerosol, -0.05 ±0.05 W m^{-2} for fossil fuel organic carbon, +0.2 ±0.15 W m^{-2} for fossil fuel black carbon aerosol, +0.1 ±0.1 W m^{-2} for nitrate, and -0.1 ±0.2 W m^{-2} for mineral dust (IPCC, 2007). Studies concerning the sea salt direct effect on climate are most often focused on the annually averaged effect, and the underlying physics related to the effect are seldom investigated (Li et al., 2008). If not the only, then one of few, 3-D studies where the physics associated to the sea salt direct radiative effect on climate is the one by Ma et al. (2008). In their study, Ma et al. (2008) applied the parameterisation of Li et al. (2008) for describing the sea salt optical properties. The parameterisation of Li et al. (2008) is the only parameterisation describing both the longwave and shortwave sea salt optical properties. The optical properties are expressed as a function of the wet sea salt aerosol size by assuming a pure sodium chloride aerosol and applying the parameterisation of Lewis and Schwartz (2006) for determining the corresponding wet radius as a function of ambient relative humidity. By applying the parameterisation of Li et al. (2008), Ma et al. (2008) assumed that the sea salt aerosol optical properties were determined by the amount of water that a pure sodium chloride aerosol would absorb together with the optical properties of the dry sea salt aerosol. The internal mixing with e.g., sulphate, which also can affect the optical properties, was neglected. The optical parameterisation of Li et al. (2008) was based on the volume mixing rule. The volume mixing rule is however not valid for aerosols such as sea salt, which dissolve to liquid droplets at high relative humidity (Liu and Daum, 2008; Irshad et al., 2009). Furthermore, Ma et al. (2008) calculated the sea salt mean concentration directly as a function of wind speed, without considering the sea salt emission flux specifically.

The lack of studies regarding the processes resulting in the direct radiative effect is one of the great motivations behind this present work. As most studies are applied for the global scale, such detailed investigations are not possible due to the simplifications that are required in such studies. Compared to global scale applications, higher resolutions are possible in regional scale studies. Thus, on the regional scale, more detailed investigations can be performed. The main objective of this thesis is to examine the feedback between the sea salt concentrations and the state of the atmosphere on the regional scale, induced by the sea salt direct radiative effect. The feedback mechanism arises as sea salt emissions depend on meteorological variables such as wind speed and water temperature and at the same time the state of the atmosphere is modified by the radiative impact caused by the emitted aerosol. Simulations are performed with the regional scale online coupled non-hydrostatic model system COSMO-ART (Vogel et al., 2009). COSMO-ART is an enhanced model system that has been designed to simulate the spatial and temporal distribution of reactive gaseous and particulate matter on the regional scale. The meteorological module COSMO is online coupled with a chemistry and transport module treating gaseous chemistry and aerosol dynamics. COSMO-ART is, within this work, extended with respect to the treatment of sea salt. Internally mixed wet aerosol composed by sea salt, non-sea salt sulphate and water formed through the condensation of sulphuric acid onto the aerosol is introduced to the model. The production of sulphate via wet phase chemistry is neglected in this study. The formation of sulphuric acid via the oxidation processes of dimethyl sulphide released from the ocean surface and of sulphur dioxide emitted from ship tracks and additional anthropogenic sources are considered and introduced to the model within this thesis. Any exchange or release of semi-volatile species such as HNO_3, HCl, and NH_3 are neglected in this work. The water content of the internally mixed aerosol is calculated as a function of its composition and ambient relative humidity following the ZSR-mixing rule. A new parameterisation describing the internally mixed sea salt aerosol optical properties is developed within this thesis, as a function of the wet mixed aerosol composition, by using detailed Mie-calculations.

The extended version of COSMO-ART is applied to an area including the Mediterranean, North East Atlantic Ocean and a large part of the continent of Europe. The considered region is influenced by natural as well as anthropogenic aerosol, whereas it is unknown in which order of magnitude the role of the respective aerosol species play. To be able to separate the impact of sea salt from the anthropogenic and that of other natural aerosols, such as mineral dust, the effect of sea salt must firstly be investigated. The interaction of sea salt with other aerosols and continental anthropogenic emissions is not considered and, moreover, it is assumed that sea salt does not take part in cloud formation. The focus here is put on COSMO-ART simulations with respect to sea salt. Additional simulations are performed where anthropogenic direct radiative effects are also considered. Thus, the aim of this work is to answer the following questions when assuming that no loss of sea salt by cloud formation takes place:

- Which role do emissions of sulphur precursors from DMS and anthropogenic emissions, respectively, play on the sulphate content on the sea salt aerosol?

- In which order of magnitude does water uptake modify the sea salt aerosol size distributions?

- How do atmospheric variables respond to the disturbances caused by the sea salt aerosol direct effect?

- To what extent do the modifications of the state of the atmosphere, caused by the direct radiative effect, show feedback on the sea salt concentrations?

- In which proportion do the sea salt DRE stand compared to the DRE of anthropogenic aerosols?

In the following, the outline of this thesis is presented. The sea salt aerosol will be further described in chapter 2. The tool of this study, the model system COSMO-ART, is presented in chapter 3. To consider the formation of internally mixed sea salt aerosol with sulphate and the corresponding water uptake, COSMO-ART has been extended with new routines. The equations on which these routines are based are presented in chapter 4. The optical properties of the dissolved internally mixed sea salt aerosol are calculated with detailed Mie-calculations as a function of a pre-calculated sea salt aerosol field and the refractive index of the respective aerosol components. Based on these calculations a new optical parameterisation is developed and presented in chapter 5. The new optical parameterisation is applied within COSMO-ART for a period in July 2007. The 3-D study together with the results are described in chapter 6. Finally, the present study and the conclusions drawn from it are summarised in chapter 7.

Chapter 2

Sea Salt – the Primary Marine Aerosol

Two distinguishable aerosol types, primary and secondary, comprise the marine aerosol. The primary marine aerosol is composed of sea salt aerosol particles that are produced by direct ejection into the atmosphere. The secondary marine aerosol mainly constitutes non-sea salt sulphate and organic species produced via atmospheric gas-to-particle conversion processes (O'Dowd et al., 1997, and references therein). In this chapter the properties of sea salt aerosol are described within the framework of their atmospheric life cycle, distribution and aerosol characteristics. Furthermore, the direct radiative effects (DRE) due to sea salt are discussed, as well as the assumptions necessary to describe the sea salt aerosol distribution and composition in atmospheric numerical models.

2.1 Generation and Removal Processes

One very important quality of the sea salt aerosol is that it will be continuously emitted into the atmosphere regardless of anthropogenic activities. Considering the mass production rate of all natural aerosols, the sea salt aerosol contributes to the largest proportion with an estimated global annual production of 1,000-10,000 Tg yr^{-1}, which corresponds to approx. 30-75%

of all natural aerosols (Blanchard and Woodcock, 1980; Winter and Chýlek, 1997). It is not only when considering natural aerosols that the sea salt source is the dominant. In the study by Textor et al. (2006) sea salt was observed to dominate the global annual aerosol production rate compared to those of dust, sulphate, particulate organic carbon, and black carbon.

The formation of sea salt aerosol is influenced by several meteorological and environmental factors such as wind speed, sea surface temperature, precipitation and surface-active materials in the near surface ocean (Lewis and Schwartz, 2004). The most important process by which sea salt aerosol is introduced into the atmosphere from the ocean is the wind stress on the sea surface. Two mechanisms are believed to be the major sources for sea salt aerosol formation. The first mechanism is the bursting of air bubbles when air is mixed into the water by breaking waves. The second mechanism is the mechanical tearing by the wind directly off the wave crests. These two mechanisms are often denoted as the indirect effect (bubble bursting) and the direct effect (mechanical tearing) with respect to the action of the wind. The formation mechanism, which causes the so-called sea spray, is illustrated in Figure 2.1. Breaking waves may occur for wind speeds at 10 m exceeding 3 m s^{-1} (Blanchard, 1963). In breaking waves, air is mixed into the water and air bubbles are formed. Whitecaps are formed when the air bubbles through transport gather at the sea surface. At a 10 m wind speed of 8 m s^{-1} approx. 1% of the sea is covered by whitecaps (Monahan, 1971). When the bubbles burst, two kinds of droplets, film drops, and jet drops, are injected into the atmosphere (e.g., Blanchard and Woodcock, 1980). The processes by which the bubbles burst and produce droplets are shown in Figure 2.1(i). The film drops are the remainder of the film of the water that separates the air in the bubble from the atmosphere. The surface free energy of the bubble is thereafter converted into kinetic energy in the form of a jet, i.e. a vertical column of water, from the bottom of the collapsing bubble into the air. 1-10 jet droplets are produced when the jet becomes unstable and breaks apart

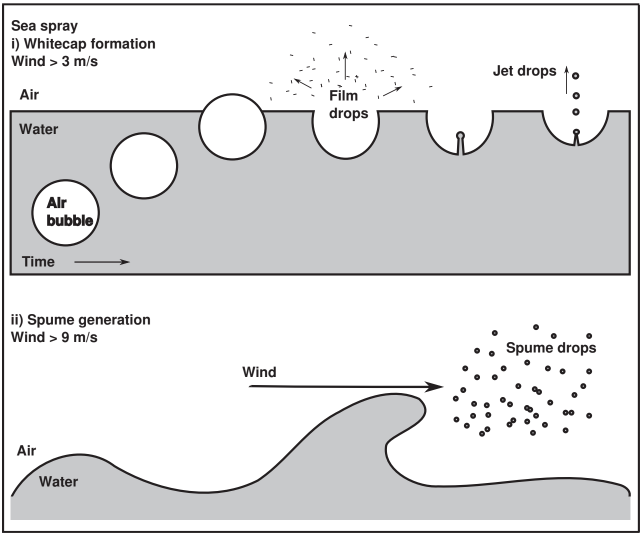

Figure 2.1.: Sketch of the sea salt aerosol formation, i.e. sea spray, mechanism.

(Blanchard and Woodcock, 1980). This bubble bursting process represents the indirect wind effect on the emission of sea salt. The direct wind effect occurs for wind speeds higher than approx. 9 m s^{-1} and is shown in Figure 2.1(ii). Via this process, so-called spume droplets are torn directly off the wave crests by the action of the wind. Film drops are typically found with radii ranging from of 0.5 to 5 μm and jet droplets with radii ranging between 3 and 5 μm, whereas the spume drops have radii in the order of magnitude of 20 μm minimum (Andreas, 1998). Thus, sea salt droplets are introduced to the atmosphere through direct transport off the waves at sufficient wind speed and, after the wave breaking through, whitecap formation.

The sea salt aerosol is produced when the droplets evaporate. Over seawater, the relative humidity (RH) is approximately 98% (e.g., Blanchard and Woodcock, 1980; Lewis and Schwartz, 2006). This means that at the point of leaving the surface, the sea salt droplet has an ambient RH of 98%. Due to the evaporation of the droplet the particle size at a RH of 80% is approximately half the size (Lewis and Schwartz, 2006). Because of the frequently rather high air humidity prevailing in the vicinity of the sea salt aerosol and the hygroscopic nature of the sea salt, the droplets will however never evaporate completely. In the atmosphere, sea salt aerosol is found as solution droplets rather than dry aerosol particles.

The marine aerosol is usually characterised by three modes, the Aitken mode ($D_p < 0.1$ μm), the accumulation mode ($0.1 < D_p < 0.6$ μm) and the coarse mode ($D_p > 0.6$ μm) (Fitzgerald, 1991), where D_p is the aerosol diameter. Typically, sea salt has been thought to be composed of the coarse mode, which represents 95% of the aerosol mass but only about 5-10% of the aerosol number (e.g., Seinfeld and Pandis, 1998; Fitzgerald, 1991; O'Dowd et al., 1997). Moreover, it has recently been shown that sea salt is not only found in the super-micrometer size range, but also as small as only some tenths of nano-meters in the atmosphere (e.g., Gong et al., 1997; Clarke et al., 2006). Thus, sea salt aerosol may be found in all the marine aerosol modes.

During its time in the atmosphere, the sea salt aerosol undergoes several processes. These impact the sea salt chemical composition and size distributions. Such processes are for instance hygroscopic growth or evaporation as a function of the aerosol composition and ambient conditions, interactions with other aerosols via coagulation or in-cloud processes, and heterogeneous reactions. The sea salt chemical composition will be discussed further in section 2.3. For the smallest aerosol, the residence time in the atmosphere is determined most effectively by the coagulation process due to Brownian diffusion. Coagulation results in mass transfer from smaller to larger aerosols. As the aerosol grows, sedimentation generally becomes the dominant atmospheric removal process. A minimum of aerosol deposition rates is found for aerosol in the size-range 0.1-1 μm. As a consequence, the aerosol will agglomerate in this size range. Therefore, this range is referred to as the accumulation regime or accumulation mode. For the aerosol in the accumulation mode, the wet deposition is thought to be more of importance. Thus, for sea salt aerosol, dry and wet depositions are the most important sink-processes. The wet deposition process refers to the removal of any species from the atmosphere by precipitation, either by in-cloud or below-cloud scavenging. The in-cloud process is thought to be most important for small sea salt aerosol, which effectively form cloud condensation nuclei, whereas larger aerosol are removed by falling raindrops (below-cloud scavenging) (Lewis and Schwartz, 2004, and references therein). Dry deposition refers to removal mechanisms that do not involve precipitation. For dry deposition of aerosol processes such as gravitational sedimentation, turbulent transfer, Brownian diffusion, and impaction are considered. In the viscous sublayer, which is the lowest layer of the troposphere with a thickness of typically 0.1-1 mm, Brownian diffusion, impaction and gravitational sedimentation are important contributions to the aerosol transfer. In the surface layer, which extends from the surface to a height of about 30-50 m, depending on the state of the atmosphere, the dry deposition is primarily determined by turbulent diffusion and gravitational sedimentation. As the fluxes act in parallel, the total aerosol transfer flux is given by their sum for the respective layer.

The mean transfer of sea salt back to the surface has been shown to be most efficient by dry deposition compared to wet deposition on the global scale (e.g., Grini et al., 2002; Textor et al., 2006). In their study on Europe with its surrounding waters, Foltescu et al. (2005) found the dry deposition fluxes to be most efficient in regions with high production, while the wet deposition was more scattered over the continent (Figure 2.2). On the global scale the largest atmospheric dry deposition of sea salt is also found in areas with high production such as in the high latitude regions of both the northern and southern hemisphere, whereas in areas associated with the Intertropical Convergence Zone, the sea salt aerosol is removed efficiently by wet as well as dry deposition (Erickson and Duce, 1988).

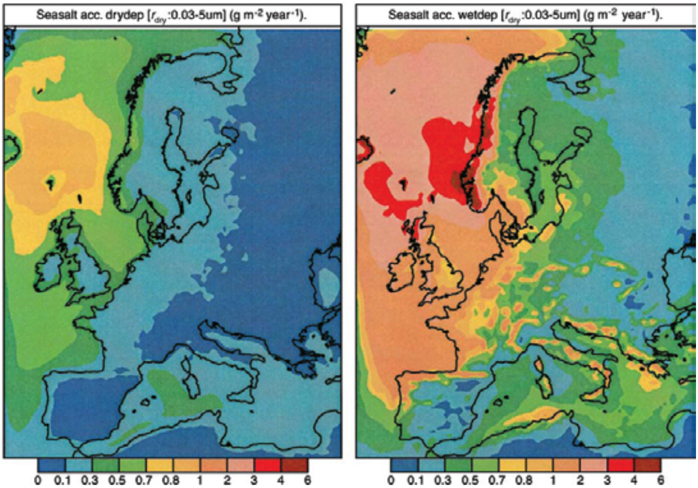

Figure 2.2.: Averaged dry (left) and wet (right) deposition rates in g m^{-2} yr^{-1} of sea salt aerosol with dry radius of up to 5 μm for January 1999 to December 2001. Figure reproduced from Foltescu et al. (2005).

2.2 Distribution

The temporal and spatial distribution of all atmospheric aerosols is highly dependent on their atmospheric residence times. The residence time of an aerosol is the average time, of the aerosol, in the atmosphere, after it leaves a source and before it encounters a sink. The shorter the residence time is for an aerosol, the faster it will be removed from the atmosphere and any significant transport away from its source is unlikely. The difference in atmospheric residence time causes differences in the distribution patterns; aerosols with longer residence times will show more homogeneous concentrations fields compared to those with shorter residence times.

As aforementioned, the largest sea salt is effectively removed from the atmosphere to the earth's surface due to large deposition velocities. This causes a short residence time of aerosol in this size range. As a result of the short residence time, no long-range transport is likely for the large sea salt aerosol. Due to the efficient diffusivity of the smallest sea salt aerosol, aerosol in this size range are likely to be deposited on pre-existing marine aerosol surfaces (Clarke et al., 2003). Any long range transport for aerosol of this size is thus also unlikely.

For the lowest atmospheric layer (0-200 m), Gong et al. (1997) found the mean residence time to range from up to 60 hours for aerosol with a dry diameter ranging from 0.26 to 0.50 μm, down to 30 minutes for those with dry diameters of 8 to 16 μm. Gong et al. (2002) estimated the mean residence time in the marine boundary layer to range from 0.3 to 10 hours for aerosol with a 7.7 μm dry diameter and between 80 to 360 hours for aerosol with a 0.4 μm dry diameter. On the global scale, sea salt has an average residence time of about half a day (Textor et al., 2006; Kerkweg et al., 2008; Croft et al., 2009). The global averaged residence time for sea salt can be compared to that of dust and sulphate aerosols of about 4 days and about six and seven days for particulate organic matter and black carbon, respectively (Textor et al., 2006). Due to the short atmospheric residence time of the sea salt aerosol, its burden shows a large gradient horizontally and vertically.

Regions with a high sea salt concentrations generally coincide with regions with high sea salt aerosol production rate. The maximum production of sea salt is from the global point of view mainly found in the mid-latitude regions where the wind speed and the fraction of ocean are high (Figure 2.3).

Heintzenberg et al. (2000) reviewed some 30 years of marine aerosol data and saw that the global and annual average meridional distribution of the measured sea salt mass concentration shows two maxima, one on the southern hemisphere at about 45-60°S and one on the northern hemisphere between 45-75°N. Results from model studies on a global scale show a more distinct maxima on the southern hemisphere, than that in the marine aerosol

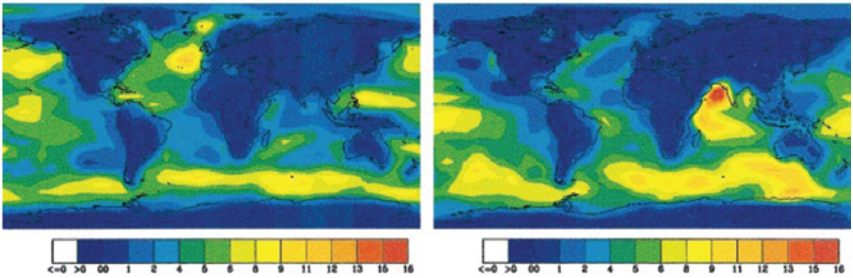

Figure 2.3.: Global sea salt surface near mass density in μg(Na) m^{-3} for January (left) and July (right). Reproduced from Grini et al. (2002).

data. Heintzenberg et al. (2000) suspected this difference between the measurement data and model results to partly be due to the lack of data and because aerosol samples in this latitudinal belt often have been taken during fair weather conditions. The open ocean surface number flux shows strong regional and temporal differences (Clarke et al., 2006) and in coastal regions large concentration gradients are observed towards low concentrations over land (Foltescu et al., 2005). The typical order of magnitude of sea salt concentrations are 10-20 μg m^{-3} with respect to mass and 100-300 cm^{-3} with respect to the amount of aerosol (Song and Carmichael, 1999). The average sea salt mass concentration near the surface from the study of Foltescu et al. (2005) is shown in Figure 2.4 for January 1999-December 2001 for sea salt with a dry radius of up to 5 μm. It is noteworthy that the large spatial variation in the sea salt aerosol distribution, which is seen in Figure 2.4, is almost completely invisible from the global point of view (Figure 2.3). When considering the whole globe especially the gradients of the sea salt aerosol distribution in the Mediterranean Basin is underestimated. This shows the importance of the investigations on the regional scale, as studies on the global scale are applied with too coarse resolutions to capture such features of aerosol fields. The mean concentrations of shorter time periods in the order of magnitude of hours to days the gradients will be even larger. The spatial and temporal distribution of sea salt during such a time period will be investigated and presented within this study.

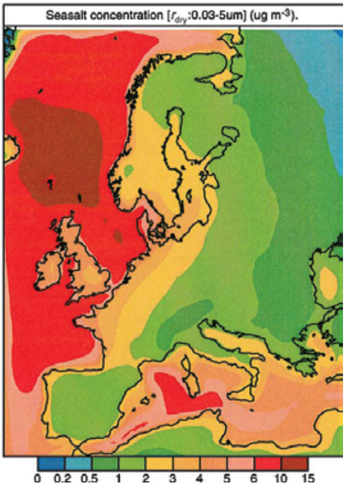

Figure 2.4.: Average sea salt mass concentration in μg m^{-3} in the surface layer for January 1999-December 2001 for sea salt with a dry radius of up to 5 μm from Foltescu et al. (2005).

The emission flux of sea salt not only shows meridional variation, but also seasonal. The sea salt production rate is for both hemispheres larger in the winter compared to the summer months. In January, a maximum in the sea salt aerosol production is observed over the Atlantic Ocean and in July the highest production rate occurs for the mid-latitudes in the southern hemisphere (e.g., Grini et al., 2002; Gong et al., 2002). The strongest seasonal variation is however observed for the northern hemisphere (e.g., Wilson et al., 2001), where the contribution to the total global sea salt flux is about 45% in the winter and approximately 24% in the summer (Gong et al., 2002). The mean annual global emission flux shows a maximum in the southern hemisphere over the South Pacific (e.g., Wilson et al., 2001; Grini et al., 2002; Textor et al., 2006). The contribution from the northern hemisphere is on annual average about 32% (Gong et al., 2002). From areas with the largest production rates the sea salt concentration decreases towards regions with less efficient production where e.g. wind speeds are lower. The aerosol mass fraction of sea salt, which is found at the poles, is according to the study by Textor et al. (2006) about 3.3% ± 90%.

The largest fraction of sea salt mass is found in the lowest troposphere. Textor et al. (2006) estimated about 90% of the sea salt aerosol mass to remain within the lowest 2.5 km, and Grini et al. (2002) found no significant mass of sea salt above 750 hPa. The global sea salt mass mean dry diameter over the ocean has been estimated as 2.8 μm at the surface and 1.9 μm in the mid-troposphere (Gong et al., 2002).

2.3 Aerosol Characteristics

There are major uncertainties regarding the initial chemical composition and the state of the sea salt aerosol in the source regions. The chemical composition of the sea salt aerosol, based on the composition of seawater and ignoring atmospheric transformations, is 55.0% Cl^-, 30.6% Na^+, 7.7% ${SO_4}^{2-}$, 3.7% Mg^{2+}, 1.2% Ca^{2+}, 1.1% K^+, 0.19% Br^- and, some per cent of other inorganic compounds, with respect to weight (Seinfeld and Pandis, 1998). It has also been suggested that freshly emitted sea salt aerosol incorporates organics (Middlebrook et al., 1998; Modini et al., 2010) and iodine (Middlebrook et al., 1998), originating from the surface layer of the ocean, by way of the bubble bursting process. Middlebrook et al. (1998) estimated the organic mass fraction to contribute to about 10% of the sea salt mass at Cape Grim.

The sea salt aerosol composition is not only determined by the ocean water chemical composition. The change in composition for this reason varies during transport by exposure to secondary precursors (SO_2, H_2SO_4, NH_3 and HNO_3) and combustion driven pollutants (SO_2, NO_x, etc.), e.g. due to mixing between different air masses. Song and Carmichael (1999) explored the ageing of sea salt in a box model equipped with a detailed thermodynamic module and found that the deposition of SO_2 and H_2SO_4 on sea salt is favoured by the fine sea salt aerosol, due to the higher available surface area. As the fine mode becomes sulphate rich, during neutralisation it begins to capture ammonia from the gas phase. At the time the ammonia is depleted from the gas phase, the fine mode starts to neutralise itself, i.e. sulphuric acid is dissociated to bisulphate and hydrogen ions. On the fine mode aerosol, particulate nitrate is quickly replaced by the deposited sulphate, whereas the slow deposition rate of sulphate onto the coarse mode leads to that the nitric acid being associated with the coarse mode in order to neutralise the cation species. As the amount of sulphate on the aerosol increases, the chloride levels decrease resulting in a so-called *chlorine deficiency*. This is a well-known phenomenon and has been observed in several studies (see e.g. Murphy et al., 1997; von Glasgow and Sander, 2001). When examining the chemical composition of single particles in the MBL outside Cape grim, Tasmania, Murphy et al. (1997) observed that chlorine, bromine and iodine were anti-correlated with sodium sulphate, suggesting that all three halogens were lost during aerosol ageing. In addition, measurements by Lee et al. (2009) showed heavy depletions of bromine and chloride compared to fresh sea salt aerosol, indicating intense halogen activation.

Several studies have shown that the scavenging of SO_2 and H_2SO_4 by the sea salt aerosol leads to a considerable fraction of the non-sea salt sulphate and sea salt aerosol is not a distinct population (e.g., Katoshevski et al., 1999). The enrichment of excess non-sea salt sulphate on sea salt aerosol is due to the condensation of sulphuric acid or processes in cloud drops, i.e. wet phase chemistry (e.g., Katoshevski et al., 1999; Sievering et al., 1992). Several studies have suggested that cloud processing is the dominant non-sea salt SO_4^{2-} formation (Sievering et al., 1992; Clegg et al., 1998; O'Dowd et al., 1999). Sea salt has also been observed to form internally mixtures with other aerosols, such as mineral dust particles (Levin et al., 2005). The internal mixing with mineral dust is the result of processes within clouds, including droplet coalescence (Andreae et al., 1986).

The sea salt aerosol is one of the most hygroscopic atmospheric aerosols. The sea salt aerosol size is known to show hysteresis behaviour with changes in ambient RH, which means that the change in the amount of ions and water in the aerosol depends on the former state of the droplet. The aerosol transformation, growth and evaporation with respect to a sea salt aerosol generated from Atlantic Ocean seawater compared to a pure sodium chloride particle as a function of the ambient RH was illustrated and discussed in Tang et al. (1997) (Figure 2.5a). In Figure 2.5b, the corresponding behaviour of a mixed salt containing equal amounts of sodium chloride and sodium sulphate is compared to the features of the single salts of each of the compounds. The uptake of water is the result of several sequential processes. The first process that takes place is the adsorption of water onto the surface of the particle. At a certain point a salt can become a solution due to the absorption of moisture from the ambient air. This process is called deliquescence and the critical point, at which this process happens, is referred to as the deliquescence relative humidity (DRH). When the DRH is reached and exceeded, deliquescence occurs due to the lower Gibbs free energy of the solution versus the solid. The absorption of water into the particle then takes place dependent on the Gibbs free energy, which is dependent on the ambient conditions, and the chemical composition of the solution. Throughout this study, this sequence of processes will simply be referred to as water uptake. The water uptake of mixed salt is more complex than that of a single salt, due to the dependence on the chemical composition (e.g., Tang, 1997). A pure NaCl particle exists as a solid particle at low RH and will deliquesce to form a solution droplet at a RH of 75.3%. For the sea salt aerosol, which contains more complex mixtures of inorganic species and organics, the uptake of water is more complicated. The deliquescence point, at which the aerosol becomes a solution droplet, depends on the composition of the aerosol. For instance, the growth

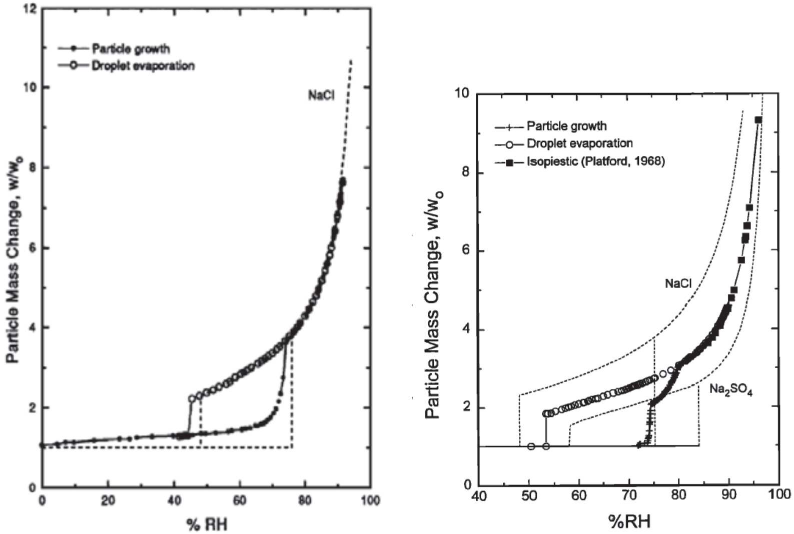

(a)

(b)

Figure 2.5.: (a): Water uptake of sea salt aerosol (circles) compared to pure NaCl particle (dotted line) as a function of RH. Reproduced from Tang et al. (1997).
(b): Water uptake of mixed NaCl-Na$_2$SO$_4$ particle (circles) compared to the single salt behaviour of NaCl and Na$_2$SO$_4$ (dotted line). Reproduced from Tang (1997).

of sea salt can be reduced through organic species in sea salt aerosol (e.g., Ming and Russell, 2001; Randles et al., 2004). A sea salt aerosol may begin to deliquesce at low RH due to the presence of compounds with low deliquescence points, such as calcium and magnesium (Tang et al., 1997). As the RH increase the other salts present in the aerosol will dissolve and when the deliquescence point of the NaCl is finally reached the aerosol becomes a homogeneous droplet. After becoming a solution droplet, the aerosol will remain so and grow as a result of water absorption with increasing RH, and lose water through evaporation with decreasing RH. When the efflorescence point of NaCl is reached, which occurs at about 45%, the sea salt follows the behaviour of NaCl and loses water rapidly. The difference between the pure NaCl particle and the mixed sea salt aerosol is that the NaCl particle will become a solid particle, whereas the sea salt aerosol will contain some residual water, even at a very low RH in the atmosphere. As seen in Figure 2.5b, the behaviour of a mixed salt as a function of ambient conditions is determined by the characteristics of each of its compounds. The differences in NaCl and Na_2SO_4 makes a mixed aerosol containing both compounds more effective in the uptake of water, than a pure Na_2SO_4 but less effective than a pure NaCl particle. Thus, the modification of the sea salt aerosol chemical composition through ageing will influence the water uptake.

2.4 Direct Radiative Effects

Atmospheric aerosols may influence the atmospheric radiative budget directly through the absorption and scattering of radiation, which is referred to as the direct radiative effect (DRE). By taking part in cloud formation, and thereby increasing the tropospheric albedo, aerosols have a so-called indirect radiative effect. As aerosols absorb shortwave radiation, the warming of the troposphere occurs and thermodynamic properties such as relative humidity and the stability of the troposphere are modified. These changes in turn influence the formation and life time of clouds. The mechanism by which the radiation fluxes are disturbed by these changes in cloud properties is referred to as the semi-direct radiative effect (Forster et al., 2007). As cloud formation is neglected in this study, this section will focus on the direct and semi-direct radiative effects.

The optical properties of the sea salt aerosol depend on the composition and aerosol size. The effective real and imaginary refractive index of the aerosol is determined by the refractive index of each of its chemical components. The refractive index in turn settles the single scattering albedo, which is the ratio of scattering to extinction. The sea salt aerosol is non-absorbing in the visible region with a single scattering albedo close to unity and partly absorbing in the long wave region (e.g., Satheesh and Krishna Moorthy, 2005). Li et al. (2008) found in their sensitivity study that the sea salt DRE in the shortwave range is an order of magnitude larger and of the opposite sign than that in the longwave range.

Several studies indicate that sea salt dominates the light extinction in remote marine environments (e.g., Murphy et al., 1998; Quinn et al., 1998; Quinn and Bates, 2005). The contribution of sea salt to light extinction in continental air masses that have been transported into the marine atmosphere is variable but still almost always significant for all size ranges (Quinn and Bates, 2005). Both submicron and super micron sea salt aerosol have been observed to affect the scattering of radiation. Marshall et al. (2007) performed air craft measurements in the marine environment surrounding Nova Scotia and concluded that roughly half the total scattering and most of the backscattering was due to the contribution from super micron particles to an altitude of approximately 1000 m. Above 1000 m the scattering and backscattering coefficients were significantly lower and were primarily due to scattering by submicron particles. When considering all the radiative effects, including the indirect effect, intermediate-size aerosol with a diameter between 0.08 and 1 μm have been proposed to be most the important for radiative impacts due to the efficient scattering of sunlight and the partitioning in cloud formation (Murphy et al., 1998).

Besides the aerosol properties and the aerosol distribution, the aerosol influence on the atmospheric radiative budget is determined by the ambient atmospheric conditions such as clear or cloud free skies (Figure 2.6). In the case of a cloudy atmosphere, the type and altitude of adjacent clouds may play a major role on the DRE. The effects of aerosols are reduced when most of the aerosol is present below an elevated cloud layer. Most of the incident solar radiation is reflected by the cloud layer and only a fraction

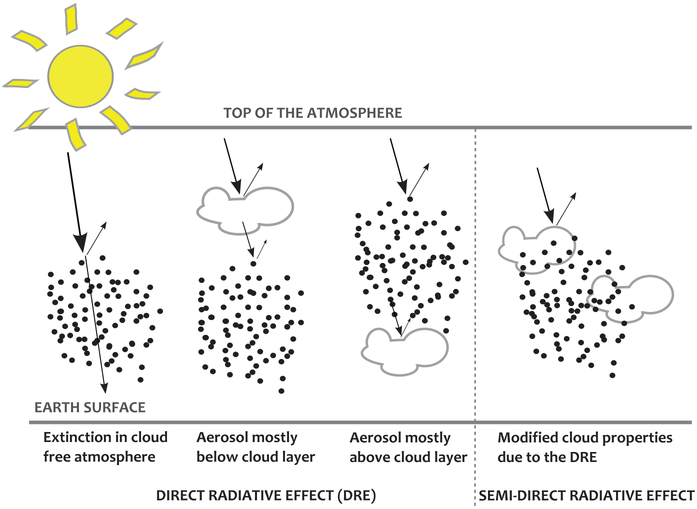

Figure 2.6.: Simplified sketch of the direct and semi-direct interaction between the aerosol and incoming solar radiation for cloud free and cloudy conditions.

of the radiation can interact with the aerosol. However, when the aerosol is mostly present above the cloud layer an enhanced effect occurs. In this case the aerosol interacts with the incoming solar radiation and the radiation reflected by the underlying cloud layer. When a cloud layer is present both the absorption and scattering of the aerosol is moreover amplified as multiple interactions take place due to the reflection of the radiation between the aerosol and cloud layer or clouds and surface (Heintzenberg, 1997; Freese and Kottmeier, 1998). Studies on the global scale show that the DRE due to sea salt in cloud free and cloudy conditions leads to cooling, whereas the magnitude of the effect varies between the studies (e.g., Jacobson, 2001a; Ma et al., 2008). This effect has been proposed to partly offset the warming by soot aerosols (Satheesh, 2002). For low solar zenith angles, $<30°$, the sea salt can however cause warming at the top of the atmosphere (Li et al., 2008). Furthermore, the surface albedo significantly affects the sea salt shortwave

DRE, with diminishing effects as the surface albedo approaches unity (Li et al., 2008).

The aerosol in the Mediterranean region comprises maritime aerosol, continental aerosol and desert dust (e.g., Barnaba and Gobbi, 2004). To investigate the order of magnitude of the DRE of a single type of aerosol in such an area comprised by external and internal mixtures is complex, as the effects of the different aerosols are difficult to separate. Clean maritime conditions are for example rare at Lampedusa, central Mediterranean (Di Ioro et al., 2003; Pace et al., 2006). For example, Tzanis and Varotsos (2008) evaluated retrievals from satellite data and investigated the total aerosol direct effect in Athens, Greece, at noon for cloud free atmospheres during winter and summer 2000-2001. The incoming shortwave radiation reaching the surface was observed to be reduced with as much as 11-20 W m^{-2}, due to both anthropogenic and natural aerosols. The outgoing longwave radiation was reduced by 0.02 to 0.04 W m^{-2} in the winter and from 0.04 to 0.05 W m^{-2} in the summer at the top of the atmosphere. The monthly averaged DRE at the surface has been estimated to vary between -7±1 W m^{-2} to -4±1 W m^{-2} during spring-summer at polluted and less polluted sites in the Mediterranean region (Bergamo et al., 2008). From the same study, the corresponding values during autumn-winter was -4±3 W m^{-2} for polluted and -1±1 W m^{-2} for less polluted sites. In which proportion the sea salt DRE stand to the effect of the other types of aerosols in this region has not been addressed. This is investigated within the framework of the present thesis.

2.5 Basics Regarding the Modelling of Sea Salt Aerosol

Modelling the distribution and chemical transformation of aerosol particles requires a coupling between the aerosol and gas phase and the meteorological processes. Simulating such processes in 3-D models is computationally very expensive and can only be treated in a simplified way. This problem is often referred to as the trade off between resolution and computational time. Particularly time consuming is the determination of the mass partitioning between the aerosol phase and gas phase, where the mass transfer has to be calculated explicitly through iterations. The trade off problem leads to more simplifications needing to be made the larger the considered scale becomes. For instance, for a certain spatial resolution, the amount of grid points rapidly increases the larger the model domain that is chosen. Thus, the resolution has to be decreased to lower the computational costs when a larger domain is considered. For this reason, models built for local to regional scales can perform with much higher spatial and temporal resolution than those that operate on the global scale.

The size distribution of the aerosols in numerical models must be described by analytical functions, which for 3-D models has to be solved without significant computational costs. The most common are the sectional and modal techniques (Whitby et al., 1991). An example of the two techniques for an aerosol distribution is shown in Figure 2.7.

The sectional technique approximates the size distribution of the aerosol with several small size intervals, so-called *bins*, and within each bin a constant distribution function is assumed. As the amount of bins increase, the quality and at the same time the computational cost increase. According to Gong et al. (2002) a minimum of 12 bins are required when describing the number density of aerosol, whereas the number of bins regarding mass is less critical. The modal technique is based on the findings by Whitby (1978), that the aerosol populations observed in the atmosphere show a modal structure. The aerosol distribution is thus represented by several overlapping *modes*, each approximated by an analytical function. As the functions are only dependent on a few parameters, the number of differential equations that needs to be solved for determining the temporal and spatial change in the aerosol size distribution is rather few. The modal approach will be used within the

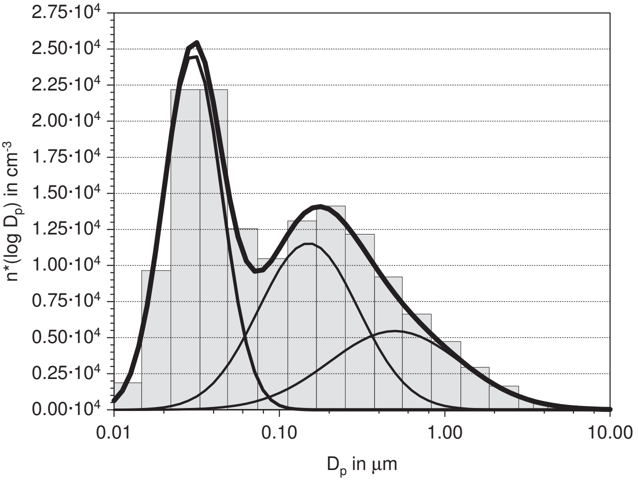

Figure 2.7.: The modal and sectional approximation to the aerosol size distribution. Reproduced from Riemer (2002).

simulations in this thesis. The approach in this work is further described in chapter 3.

The change of sea salt size with the changes in the RH can be treated with different accuracies. The water uptake on sea salt aerosol can be calculated by different methods in a 3-D model. One method is the use of parameterisations determining the wet size as function of the dry size, assuming a constant composition of the dry aerosol. Parameterisations determining the wet radius are for example Fitzgerald (1975) (e.g., Grini et al., 2002), Gerber (1985) (e.g., Yu and Luo, 2009), Zhang et al. (2005), Lewis and Schwartz (2006) (e.g., Li et al., 2008). Another method is the use of the simple empirical relationship, which is known as the Zdanovskii-Stokes-Robinson (ZSR) relation (Stokes and Robinson, 1966), which expresses the aerosol liquid water content as a function of electrolyte molality and sub-saturated conditions. The ZSR method has been shown to be adequate over the entire concentration range from a dilute solution to high super saturation droplets (Tang, 1997). The ZSR relation will be used in this work to calculate the sea salt aerosol liquid water content and was already applied in several other atmospheric models (e.g., Stier et al., 2005; Jacobson, 1997).

The sea salt emission cannot be resolved into each detail in 3-D atmospheric models. One solution for this is to apply parameterisations to calculate the emission flux. Most parameterisations describe the emission flux of sea salt as a function of the, in measurements commonly reported, 10 m level horizontal wind speed. A recent parameterisation was developed by Mårtensson et al. (2003), where the flux of sub-micrometer aerosol was determined as a function of the sea water temperature and the wind speed. The parameterisations of Mårtensson et al. (2003) and that of Clarke et al. (2006) are the only parameterisations available in the literature that describe the emission flux of aerosol in the sub-micrometer size range. For an overview of the available source functions cf. Andreas (1998) and Clarke et al. (2006). In some models, the sea salt concentrations are directly determined as a function of the wind speed without calculating the emission flux (e.g., Wilson et al., 2001; Ma et al., 2008).

Most 3-D simulation studies regarding the sea salt aerosol are applied on the global scale (e.g., Wilson et al., 2001; Grini et al., 2002; Myhre and Grini, 2006; Pierce and Adams, 2006; Kerkweg et al., 2008; Ma et al., 2008; Croft et al., 2009; Yu and Luo, 2009). For the global scale applications such as the indirect radiative forcing (e.g., Ma et al., 2008), the direct radiative forcing (e.g., Grini et al., 2002; Ma et al., 2008), impact of sea salt on the marine boundary layer (MBL) chemistry (e.g., Myhre and Grini, 2006; Kerkweg et al., 2008), and the influence of sea salt on cloud formation and vice versa (e.g., Pierce and Adams, 2006; Croft et al., 2009; Yu and Luo, 2009) are available in the literature.

The high temporal and spatial variation in the sea salt loading and consequently the variation in its corresponding effect on the atmospheric state cannot be discussed when using global scale models, which commonly give results as annual averages for the globe. 3-D studies on the sea salt aerosol at regional scales are available, but rare (e.g., Foltescu et al., 2005; Athanasopoulou et al., 2008). These studies are more focused on examining the spatial distribution and the contribution of sea salt to the total aerosol mass concentrations and no interactions with the state of the atmosphere was integrated.

To simulate the feedback between aerosols and the atmosphere, online coupled model systems are required. This implies that all the calculations are carried through for each time step and grid point, without interpolations in space and time. All the variables are available at every time step enabling the study of feedback processes between meteorological parameters, emissions, and chemical composition. An online coupled model system is more time consuming than an offline system and, therefore, the feedbacks between aerosols and the state of the atmosphere are most often neglected. For models with horizontal resolutions up to a few kilometres, a non-hydrostatic approximation is required as phenomena such as land-sea breeze and mountain and valley winds occur (Wippermann, 1980). One of few available online coupled non-hydrostatic model system, is the WRF/Chem model (Grell et al., 2005). Another one is the model system COSMO-ART (Vogel et al., 2009), which is applied in this thesis. It is described in chapter 3.

Chapter 3

The Model System COSMO-ART

In this thesis, simulations of sea salt aerosol are performed with the comprehensive regional scale model system COSMO-ART (Vogel et al., 2009). This chapter gives an overview of the model system, with a special focus on the sea salt treatment.

3.1 General Overview of the Model System

An overview of the model sysyem COSMO-ART is given in Figure 3.1. COSMO stands for **CO**nsortium for **S**mall-scale **MO**delling, and ART stands for **A**erosols and **R**eactive **T**race gases. COSMO (Steppeler et al., 2003) is the meteorological driver of the model system and was developed by the German Weather Service (*Deutscher Wetterdienst, DWD*). COSMO is a non-hydrostatic limited-area atmospheric prediction model and is used on an international basis for weather forecasting and atmospheric research. In COSMO-ART a chemistry and transport model (CTM) has been implemented in COSMO. COSMO-ART has been developed for the purpose of studying the influence of aerosols and gases and the state of the atmosphere, and vice versa, on the regional to continental scale. With COSMO-ART, the feedbacks between aerosol particles and the state of the atmosphere via direct radiative effects can be investigated. The feedback processes that are currently accounted for in COSMO-ART are depicted with black lines in Figure 3.2. The dotted lines imply processes that are currently neglected but will be considered in the model as well. During a simulation with COSMO-ART all variables (gaseous and aerosol species, and meteorological variables) are treated at every time step. At each time step, the gaseous and aerosol species alter radiative fluxes through extinction, which leads to modifications of the atmospheric state. Through the modified radiative fluxes, a feedback loop is initialised, starting with changes in temperature. As a a consequence of the temperature changes, the humidity, cloud cover pattern, wind field, and turbulence are in turn also modified. These changes modify the chemical composition of the gaseous and aerosol components. Furthermore, the precipitation is also modified, in turn leading to another feedback mechanism as the efficiency of the washout of aerosols is altered. At the same time step, the properties and distribution of gaseous and aerosol components are determined as a function of the meteorological variables. This approach in COSMO-ART, where the all variables are coupled to each other and are treated at the same time step, is called online coupling. Being online coupled

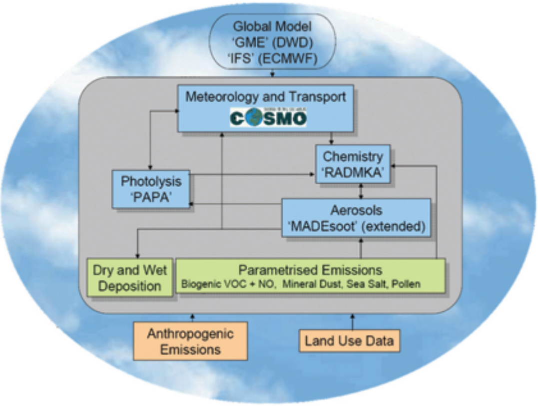

Figure 3.1.: The model system COSMO-ART.

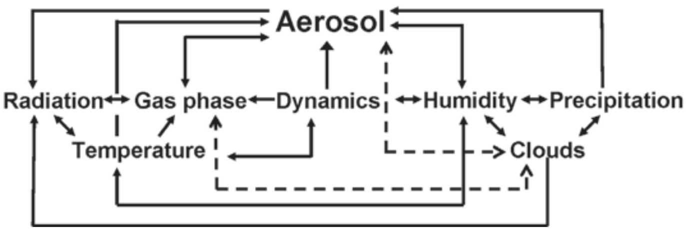

Figure 3.2.: The feedback loop accounted for in COSMO-ART.

is a crucial feature for the investigation of interactions and feedbacks between the state of the atmosphere and gaseous and aerosol species.

For simulations with COSMO-ART, meteorological initial and boundary data are required. These are either obtained from the global model GME of the German Weather Service or from the the global model IFS from the European Centre for Medium-Range Weather Forecasts (ECMWF). It is also possible to nest COSMO-ART into COSMO-ART at different resolutions and domains.

In COSMO-ART, the primary emissions of pollen (Vogel et al., 2006b), sea salt (Lundgren, 2006), mineral dust (Hoose, 2004; Vogel et al., 2006a) and biogenic VOC's (volatile organic compounds) (Vogel et al., 1995) are calculated at each time step as a function of the current state of the atmosphere. The anthropogenic emissions of gases and particles are available from Pregger et al. (2007). In addition to the primary emitted aerosols, secondary aerosols are formed from the gas phase. The aerosol dynamics is calculated in the extended version of the module $MADE_{soot}$ (extended version of the Modal Aerosol Dynamics Model for Europe (Riemer, 2002)). In $MADE_{soot}$ the aerosol population is described by overlapping modes that are approximated by log-normal distributions. In the extended version of $MADE_{soot}$ 12 modes describe the aerosol population:

- Two modes: internally mixed aerosol containing sulphate, nitrate, ammonium, water and SOA.

- Two modes: internally mixed aerosol containing sulphate, nitrate, ammonium, water, SOA and soot.
- One mode: pure soot aerosol.
- One mode: aerosol particles from PM_{10} emissions.
- Three modes: mineral dust aerosol.
- Three modes: sea salt aerosol.

SOA stands for secondary organic aerosols. The pollen species are however assumed to be monodisperse, i.e. all having the same size, and are not represented by modes.

In COSMO-ART, the removal of aerosol through below cloud scavenging is a parameterised as a function of the aerosol size distribution and of the size distribution of rain droplets (Rinke, 2008). The removal through deposition to the surface is based on the parameterisation by Slinn and Slinn (1980) and Kramm et al. (1992).

The transformation of the most important tropospheric gaseous species is treated in the gas phase mechanism RADMKA (Regional Acid Deposition Model version KArlsruhe). RADMKA is based on the RADM2-mechanism by Stockwell et al. (1990). For more information about the modifications made to RADM2, cf. Vogel et al. (2009) and references therein. The photolysis frequencies are calculated fully coupled to the radiation scheme GRAALS (Ritter and Geleyn, 1992) in COSMO-ART as described in Bangert (2006).

3.2 Treatment of Sea Salt Aerosol in COSMO-ART

The mathematical concept for describing the aerosol population in COSMO-ART is based on the findings by Whitby (1978), that the aerosol populations observed in the atmosphere show a modal structure. Thus, the aerosol population is represented by several overlapping distributions, approximated by log-normal functions. The sea salt aerosol is represented by three overlapping size intervals, or modes. The method to describe the sea salt aerosol distribution by a tri modal lognormal distribution is based on the measurement by O'Dowd et al. (1997). The sea salt modes are usually referred to as the film mode, jet mode and spume mode, respectively. The median mode diameter $D_{gi,ini}$ and geometric standard deviation σ_{gi} which O'Dowd et al. (1997) found in their measurements are used as reference values for freshly emitted sea salt aerosol in COSMO-ART with respect to the number of particles. For each of the three sea salt modes, these reference values are presented in Table 3.1. The geometric standard deviation can be calculated as the ratio of the particle diameter, which is larger than approx. 84% of all particles, to the geometric median diameter (Seinfeld and Pandis, 1998). Through this definition, the geometric standard deviation is non-dimensional and always dependent on the geometric median diameter of the distribution. Except for the spume mode geometric standard deviation σ_{g3}, were all the parameter values taken from the measurements by O'Dowd et al. (1997). The geometric standard deviation of the spume mode has been modified from $\sigma_{g3} = 3.0$ to $\sigma_{g3} = 1.7$ with the assumption that the largest particles have a very short residence time in the atmosphere. The distribution of the largest particles is, therefore, described by a narrower distribution than that presented by O'Dowd et al. (1997).

Table 3.1.: Initial median diameter $D_{gi,ini}$ and corresponding standard deviation with respect to the number density of freshly emitted aerosol in the sea salt film mode, jet mode, and spume mode.

Size mode	Mode diameter $D_{gi,ini}$ in m	Geometric standard deviation σ_{gi}
$i = 1$, *film*	$0.2 \cdot 10^{-6}$	1.9
$i = 2$, *jet*	$2.0 \cdot 10^{-6}$	2.0
$i = 3$, *spume*	$12.0 \cdot 10^{-6}$	1.7

Being polydisperse, the total particle number density N_i for each of the three sea salt modes i is given by the integral

$$N_i = \int_0^\infty n_i(D_p)\, dD_p \tag{3.1}$$

where $n_i(D_p)$ dD_p describes the number density of mode i given in particles with diameter D_p per m^{-3} air within the size range D_p and $(D_p + dD_p)$. The total number density N of sea salt aerosol population is achieved by taking the sum of the integrals for all modes

$$N = \sum_i N_i. \tag{3.2}$$

Thus, to calculate the total number density, the number density distribution is needed, which for each mode i is defined as

$$n_i\,(D_p) = \frac{N_i}{(2\pi)^{1/2}\, D_p \ln \sigma_{gi}} \exp\left(-\frac{(\ln D_p - \ln D_{g0,i})^2}{2 \ln \sigma_{gi}}\right) \tag{3.3}$$

where σ_{gi} is the non-dimensional geometric standard deviation of the distribution and is assumed to be constant for each mode. When considering the logarithm, a dimensionles quantity must be considered. Thus, the relationship $\ln D_p$ should be interpreted as the logarithm of a normalised diameter: $\ln(D_p/1)$, where 1 referres to a reference diameter of 1 m when the particle diameter is given in m. Throughout the text, this is not explicitly indicated. $D_{g0,i}$ denotes the geometric median diameter in m with respect to the number of particles. Since the diameter D_p, given in m, may vary within size ranges over several order of magnitudes it is however preferable to use the logarithm of the diameter, which gives the following expression for the number density distribution

$$n_i^*\,(\ln D_p) = \frac{N_i}{(2\pi)^{1/2} \ln \sigma_{gi}} \exp\left(-\frac{(\ln D_p - \ln D_{g0,i})^2}{2 \ln^2 \sigma_{gi}}\right). \tag{3.4}$$

The corresponding mass density distribution is given by

$$\begin{aligned} m_i^*(\ln D_p) &= \frac{m_i}{(2\pi)^{1/2}\ln\sigma_{gi}}\exp\left(-\frac{(\ln D_p - \ln D_{g3,i})^2}{2\ln^2\sigma_{gi}}\right) \\ &= \frac{m_i}{(2\pi)^{1/2}\ln\sigma_{gi}}\exp\left(-\frac{\left(\ln D_p - \left(\ln D_{g0,i} + 3\ln^2\sigma_{gi}\right)\right)^2}{2\ln^2\sigma_{gi}}\right) \end{aligned} \tag{3.5}$$

where m$_i$ is the total mass of each mode i and D$_{g0,i}$ and D$_{g3,i}$ are the median diameters with respect to the number and mass density, respectively, related as

$$D_{g3,i} = D_{g0,i}\ \exp(\ln^2\sigma_{gi}).$$

The median diameter of the respective mode i is variable with space and time and determined as a function of the current mass and number density of aerosol in each mode

$$D_{g0,i} = \left(\frac{m_i}{\frac{\pi}{6}\rho_p \exp\left(4.5\ln^2\sigma_{gi}\right) N_i}\right)^{\frac{3}{2}}. \tag{3.6}$$

Considering a log-normal distribution, the kth moment M$_k$ of the distribution is defined as

$$M_{k,i} = \int_{-\infty}^{\infty} D_p^k\, n_i^*(\ln D_p)\, d(\ln D_p) \tag{3.7}$$

for mode i, with the solution

$$M_{k,i} = N_i D_{g0,i}^k \exp\left(\frac{k^2}{2}\ln^2\sigma_{gi}\right). \tag{3.8}$$

Under this definition the zeroth moment M_0 is identical to the total number of aerosol particles within the mode per unit volume air

$$N_i = M_{0,i}. \tag{3.9}$$

By assuming spherical aerosol particles, the total particulate surface area S_i and the total particulate volume V_i and in turn the particle mass m_i can be expressed as moments for each mode. The surface area per unit volume air is proportional to the second moment

$$S_i = \int_0^\infty \pi \, D_p^2 \, n_i^*(\ln D_p) \, d(\ln D_p) \; = \; \pi \, M_{2,i} \tag{3.10}$$

whereas the volume V per unit volume air and mass m_i in kg per unit volume of air are proportional to the third moment

$$V_i = \int_0^\infty \frac{\pi}{6} \, D_p^3 \, n_i^*(\ln D_p) \, d(\ln D_p) = \frac{\pi}{6} \, M_{3,i} \tag{3.11}$$

$$m_i = \rho_p \, V_i = \frac{\pi}{6} \, \rho_p M_{3,i} \tag{3.12}$$

with ρ_p denoting the particle bulk density.

For a mode consisting of several substances, the total third moment for each mode i is the sum of the moments for each substance l

$$M_{3,i} = \sum_{l=1}^{l_{subs}} M_{3,i_l} = \sum_{l=1}^{l_{subs}} 6 \, \frac{m_{i,l}}{\pi \rho_{p_l}} \tag{3.13}$$

where $m_{i,l}$ is the mass density in mode i for substance l, and l_{subs} denotes the number of different substances within the mode. ρ_{p_l} is the density of each of the substances l.

3.2.1. Aerosol Dynamics for Pure Sea Salt

For the description of aerosol dynamics of the three sea salt modes i, the normalised mass density $\Psi_{m,i}$ and the normalised zeroth moment, i.e. the normalised number density, $\Psi_{N,i}$ are considered

$$\begin{aligned} \Psi_{N_i} &= \frac{M_{0,i}}{N_a} && (3.14) \\ \Psi_{m_i} &= \frac{m_i}{\rho_a} && (3.15) \\ & && (3.16) \end{aligned}$$

N$_a$ denotes the total number density of air including air molecules and ρ_a is the total density of humid air. The conservation law of the aerosol is described by using the density weighted Reynolds average, which for the arbitrary variable ψ take the form

$$\hat{\psi} = \frac{\overline{\rho_a \psi}}{\overline{\rho}_a} \qquad (3.17)$$

where $\overline{\rho}_a$ is the mean density of air. The Reynolds averaged conservation equation for the normalised zeroth moment and the normalised mass density of each sea salt mode are given by

$$\begin{aligned} \frac{\partial \hat{\Psi}_{N_i}}{\partial t} &= -\hat{\mathbf{v}} \cdot \nabla \hat{\Psi}_{N_i} - \overline{v}_{sed,N_i} \frac{\partial \hat{\Psi}_{N_i}}{\partial z} + \frac{1}{\overline{\rho}_a} \nabla \cdot F^{\Psi_{N_i}} - \overline{W}_{N_i} && (3.18) \\ \frac{\partial \hat{\Psi}_{m_i}}{\partial t} &= -\hat{\mathbf{v}} \cdot \nabla \hat{\Psi}_{m_i} - \overline{v}_{sed,m_i} \frac{\partial \hat{\Psi}_{m_i}}{\partial z} + \frac{1}{\overline{\rho}_a} \nabla \cdot F^{\Psi_{m_i}} - \overline{W}_{m_i}. && (3.19) \end{aligned}$$

$\hat{\mathbf{v}}$ represents the density weighted average of the horizontal wind vector. $\overline{v}_{sed,N_i}$ and $\overline{v}_{sed,m_i}$ are the mean sedimentation velocities of the number and mass density, respectively, and will be described hereunder. $F^{\Psi_{N,i}}$ and $F^{\Psi_{m,i}}$

denote the turbulent fluxes of the number density and mass density, respectively

$$F^{\Psi_{N_i}} = -\overline{\rho_a v'' \Psi''_{N_i}} \tag{3.20}$$

$$F^{\Psi_{m_i}} = -\overline{\rho_a v'' \Psi''_{m_i}}. \tag{3.21}$$

where v'', Ψ''_{N_i} and Ψ''_{m_i} are the sub-grid scale values. These cannot be resolved in the model and are parameterised with the same technique as is applied for the humidity parameters in COSMO (cf. Steppeler et al., 2003). $\overline{W}_{N_i}$ and $\overline{W}_{m_i}$ describe the removal through below cloud scavenging with respect to the aerosol number density and mass density. The parameterisation of the washout process is described in detail in Rinke (2008). Thus, the time rate of change of the normalised averaged mass and number density of the sea salt aerosol is given by horizontal and vertical advection and vertical diffusion. Coagulation between sea salt and other aerosols is not accounted for in this study. Dry deposition to the surface is treated as a lower boundary condition for the vertical diffusion. In addition, emissions enter the equations via the lower boundary conditions. The emission parameterisation is described in section 3.2.2.

Sedimentation and Deposition

For a monodisperse aerosol population, i.e. particles all having the same size, the sedimentation velocity is

$$v_{sed} = \frac{gC_c}{18\nu}\left(\frac{\rho_p}{\rho_a} D_p^2\right) \tag{3.22}$$

where ρ_p and ρ_a are densities of the aerosol particle and air, respectively. g is the gravity acceleration, ν denotes the kinematic viscosity coefficient of air, and λ_a the mean free path of air. C$_c$ is the Cunningham slip correction factor

$$C_c = 1.0 \, + \, 1.246 \frac{2\lambda_a}{D_p} = 1.0 \, + \, 1.246 \, \mathrm{Kn}_g \tag{3.23}$$

with Kn$_g$ denoting the Knudsen number. Considering a polydisperse aerosol and the k:th moment of the distribution, the corresponding expression for the sedimentation velocity takes the form (Kramm et al., 1992)

$$\overline{v}_{sed,k} = \frac{1}{M_k} \int_{-\infty}^{\infty} v_{sed} D_p^k \, n^*(\ln D_p) \, d(\ln D_p) \tag{3.24}$$

As the distributions are approximated by log-normal functions the sedimentation velocity for the k:th moment of the polydisperse aerosol is

$$\begin{aligned} \overline{v}_{sed,k} = \frac{g}{18\nu} \left(\frac{\rho_p}{\rho_a} D_g^2 \right) \left(\exp \left(\frac{4k+k}{2} \ln^2 \sigma_g \right) + \right. \\ \left. +1.246 \cdot \mathrm{Kn}_g \exp \left(\frac{2k+1}{2} \ln^2 \sigma_g \right) \right) . \end{aligned} \tag{3.25}$$

The sedimentation of the sea salt mass and number densities for the sea salt modes consequently are expressed as

$$\overline{v}_{sed,N_i} = \frac{g\rho_p}{18\nu\rho_a} D_{g0,i}^2 \left(\exp\left(2 \ln^2 \sigma_{gi}\right) + \right.$$
$$\left. +1.246 \frac{2\lambda_a}{D_{g0,i}} \exp \left(\frac{1}{2} \ln^2 \sigma_{gi} \right) \right)$$

$$\overline{v}_{sed,m_i} = \frac{g\rho_p}{18\nu\rho_a} D_{g0,i}^2 \left(\exp\left(8 \ln^2 \sigma_{gi}\right) + \right.$$
$$\left. +1.246 \frac{2\lambda_a}{D_{g0,i}} \exp \left(\frac{7}{2} \ln^2 \sigma_{gi} \right) \right)$$

where D$_{g0,i}$ is determined as a function of the total mass and total number density of the respective mode i from Equation (3.6).

The calculations of the mean deposition velocity of the polydisperse aerosol are based on Slinn and Slinn (1980)

$$\overline{v}_{dep,k} = \overline{v}_{sed,k} + \left(r_a + \overline{r}_{d,k} + r_a\, \overline{r}_{d,k}\, \overline{v}_{sed,k}\right)^{-1}. \tag{3.26}$$

r_a describes the aerodynamic resistance and is determined by meteorological variables such as wind velocity and the atmospheric stability, which are obtained from COSMO. $\overline{r}_{d,k}$ is the surface layer resistance

$$\overline{r}_{d,k} = \left(\left(Sc_k^{-2/3} \;+\; 10^{-3/St_k}\right)\left(1 + 0.24\frac{w_*^2}{u_*^2}\right)u_*\right)^{-1} \tag{3.27}$$

where Sc_k is the Schmidt number $\mathrm{Sc}_k = \frac{\nu}{\hat{D}_k}$ and St_k is the Stokes number $\mathrm{St}_k = \frac{u_*^2}{g\nu}\overline{v}_{sed,k}$. u_* is the friction velocity and w_* is the convective velocity scale, both given in m s^{-1}. $\hat{D}_k$ is the diffusion coefficient in m^2 s^{-1} for polydisperse aerosol, which is described by

$$\begin{aligned}\hat{D}_k = \frac{k_B T}{3\pi\mu D_{g0}}&\left(\exp\left(\frac{-2k+1}{2}\ln^2\sigma_g\right) + \right.\\ &\left. +1.246\frac{2\lambda_a}{D_{g0,i}}\,\exp\left(\frac{-4k+4}{2}\ln^2\sigma_g\right)\right).\end{aligned} \tag{3.28}$$

The deposition of sea salt aerosol to the surface is calculated for the lowest model layer. For the other vertical layers, only the sedimentation velocity is calculated. In Figure 3.3, the deposition velocity is shown for the mass density and the zeroth moment (number density) for a geometric standard deviation of 2 and $r_a = 50$ s m^{-1} as a function of the geometric median diameter. For the smallest particles, the Brownian diffusion process is the dominant, whereas the sedimentation becomes more effective with larger median diameters and conversely the Brownian diffusion becomes less effective. The deposition is the least effective for aerosol with sizes close to 1 μm in median diameter. As a result of this fact, aerosol distributions with a median

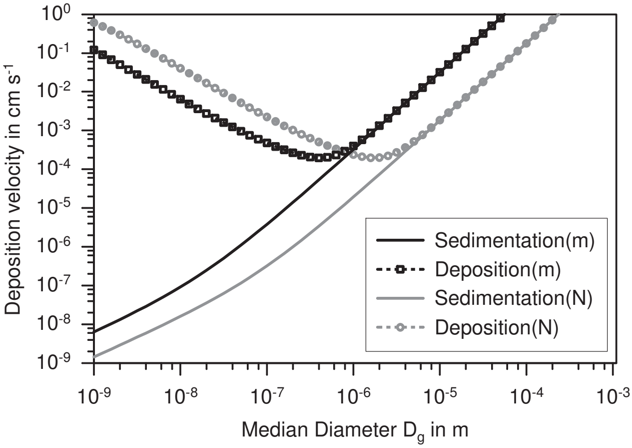

Figure 3.3.: Deposition of number (N) and mass density (m) for distributions with $\sigma_g = 2$ m and $r_a = 50$ s m^{-1} as a function of the geometric median diameter D_g.

diameter as close as possible to this minimum show a longer residence time in the atmosphere. This explains the existence of the so-called accumulation mode, which was aforementioned in chapter 2.

3.2.2. Parameterisation of the Sea Salt Aerosol Production

The sea salt emission module was developed and introduced to COSMO-ART by Lundgren (2006). Here, a brief overview of the chosen sea salt source functions is given.

For simplification, the freshly emitted sea salt aerosol is assumed to consist of pure NaCl. The flux of sea salt aerosol particles from the sea surface to the lowest atmosphere is described as a function of the water surface temperature and horizontal wind speed at 10 metres above the surface. A combination of three parameterisations describes the emission of particles within the size range of 0.02-28 μm.

In COSMO-ART, the parameterisation of Mårtensson et al. (2003) is utilised for sub-micrometer particles with dry diameters between 0.02-1 μm. The flux according to Mårtensson et al. (2003) is calculated as a function of the wind speed at 10 m level U_{10} (in m s^{-1}) and as a function of the sea surface temperature T_w.

$$\frac{dF_0}{d\log D_p} = \Phi(T_w, D_p)\, 3.84 \cdot 10^{-6}\, U_{10}^{3.41} \tag{3.29}$$

The flux is given in m^{-2} s^{-1}. F_0 is the aerosol number flux $\Phi(\mathrm{T}_w,\mathrm{D}_p)$ that describes the particle flux per whitecap area and is dependent on the water temperature and particle diameter D_p given in metres

$$\Phi(T_w, D_p) \;=\; A_q(D_p) \cdot T_w + B_q(D_p) \qquad\qquad q \;=\; 1, 2, 3. \tag{3.30}$$

The coefficients $A_q(D_p)$ and $B_q(D_p)$ are given in Mårtensson et al. (2003) and Lundgren (2006). Probably the most common source function for sea salt aerosol production in atmospheric models of Monahan et al. (1986), is within COSMO-ART adapted for the production of super micrometer aerosol in the size range 1-9 μm D_p

$$\frac{dF_0}{dr_{80}} = 1.373\, U_{10}^{3.41}\, r_{80}^{-3}\, \left(1 + 0.057 r_{80}^{1.05}\right) 10^{1.19 e^{-B^2}} \tag{3.31}$$

$$\text{where } B = \frac{0.380 - \log r_{80}}{0.650}.$$

The flux is given in m^{-2} s^{-1} $\mu\mathrm{m}^{-1}$ for U_{10} in m s^{-1} and in r_{80} in μm. r_{80} referres to the wet radius size of the aerosol an the ambient relative humidity of 80%. Emission of aerosol in the size range 9-28 μm is described by Smith et al. (1993) in the form of two log-normal distributions

$$\frac{dF_0}{dr_{80}} = \sum_{x=1,2} C_x \exp\left(-f_x\left(\ln\frac{r_{80}}{r_x}\right)\right) \tag{3.32}$$

where $\begin{cases} f_1 = 3.1\,\mu m, & r_1 = 2.1\,\mu m, & \log C_1 = 0.676\,U_{10} + 2.43 \\ f_2 = 3.3\,\mu m, & r_2 = 9.2\,\mu m, & \log C_2 = 0.959\,U_{10}^{0.5} - 1.475. \end{cases}$

The emission flux is given in m^{-2} s^{-1} μm^{-1} for U$_{10}$ in m s^{-1} and in r$_{80}$ in μm. The parameterisations (3.29), (3.31), and (3.32) are brought to the same form by applying the parameterisation of Lewis and Schwartz (2006), which describes the wet aerosol size as a function of the dry size. The number density flux F$_{N,i}$ in each mode i is achieved through numerical integration over the respective size interval

$$F_{N,i} = \int_{D_a}^{D_b} \frac{dF_0}{d\log D_p}\, d\log D_p = \lim_{n\to\infty} \sum_{i=1}^{n} \frac{dF_0}{d\log D_p}\,\Delta\log D_p \tag{3.33}$$

with the constant step $\Delta\log D_p$=0.1. The mass density flux F$_m$ is calculated from the number density flux for each of the three sea salt modes by using the following relation

$$F_{m,i} = \frac{\pi\rho_p D_{gi,ini}^3}{6} \exp\left(4.5\ \ln^2\sigma_{g,i}\right) \cdot F_{N,i}. \tag{3.34}$$

The initial mode diameter D$_{gi,ini}$ and the distribution standard deviation for fresh emitted sea salt aerosol in each mode are given in Table 3.1. The emissions of sea salt, E$_{N,i}$ and E$_{m,i}$, enter the conservation equations (3.18) and (3.19) for each mode i via the lower boundary conditions

$$E_{N,i} = \frac{F_{N,i}}{\Delta z_s} \tag{3.35}$$

$$E_{m,i} = \frac{F_{m,i}}{\Delta z_s} \tag{3.36}$$

where Δz_s represents the height of the lowest model layer.

3.3 Treatment of Radiative Fluxes

The calculations of vertical profiles of the solar and thermal radiative fluxes within the COSMO model are performed with the radiation scheme GRAALS (General Radiative Algorithm Adapted to Linear-type Solutions, Ritter and Geleyn (1992)). This radiation scheme treats radiative transfer by the so-called two-steam method, which is a commonly used method in e.g., weather forecast and climate models. The two-stream method is based on the assumption that the angle dependency of the radiation intensity is constant in each hemisphere and only upward and downward fluxes are considered. The radiative transfer equation and its solution for the two-stream method has been described by Stanelle (2008). In the GRAALS radiation scheme eight spectral bands k_b are considered, three in the solar and five in the thermal range (Table 3.2).

Table 3.2.: List of the spectral bands considered in COSMO-ART based on the GRAALS radiation scheme (Ritter and Geleyn, 1992).

Spectral range	Spectral band k_b	Wavelength λ in μm
Solar	1	1.53-4.64
	2	0.7-1.53
	3	0.25-0.7
Thermal	4	20.0-104.5
	5	12.5-20.0
	6	8.33-9.01 and 10.31-12.5
	7	9.01-10.31
	8	4.64-8.33

In GRAALS, the aerosol optical depth has been treated with constant fields for different aerosol categories. The aerosol optical depth (AOD) is the non-dimensional vertical integral of the extinction coefficient. Between -19 to

54°E and 26 to 54°N the horizontal maritime aerosol AOD in GRAALS is shown in Figure 3.3.

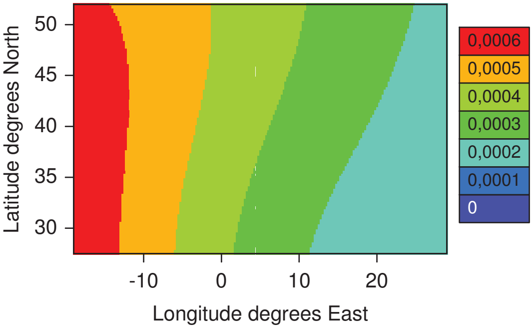

Figure 3.4.: Maritime aerosol optical depth in GRAALS.

The maritime aerosol optical depth in GRAALS was until now max. 0.0007 and treated constant in time. Thus, for the calculations of the radiative fluxes in the current version of COSMO-ART, the maritime AOD is treated very simplified, by neglecting all temporal variations that are caused by e.g. changes in wind speed. The comparison with measurements imply that the current approach underestimates the sea salt AOD. The clean marine air mass AOD for the northeast Atlantic region has been estimated to have an average value of 0.4 ± 0.29 for the period 2002-2004 (Mulcahy et al., 2009). Within this study, the maritime AOD in GRAALS is therefore replaced by the simulated sea salt aerosol optical depth. The radiative fluxes are calculated fully coupled to the current sea salt distribution in COSMO-ART, as shown in Figure 3.3. To perform these fully coupled simulations, the aerosol optical properties of each of the spectral bands are required at every grid cell and time step. For determining these optical properties, all of the aerosols are assumed to be spherical and Mie calculations are necessary as a function of the aerosol size distribution, the chemical composition and the complex refractive index of each aerosol component. Due to the enormous amount of computational time required for the Mie calculations, these cannot be per-

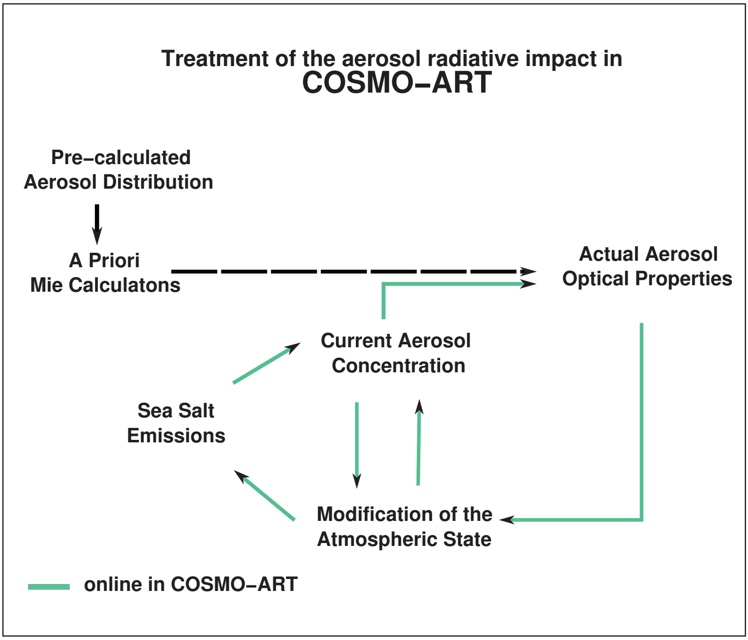

Figure 3.5.: Overview of the treatment of the aerosol radiative impact on the atmosphere and the resulting modification of the sea salt concentration and subsequent impact on the aerosol optical properties.

formed online in atmospheric models. For this reason, Mie calculations are performed as a priori for pre-simulated aerosol distributions with COSMO-ART. The well proven code of Bohren and Huffman (1983) is used for the detailed Mie calculations with the simulated aerosol size distribution, the corresponding aerosol composition and the complex index of refraction of each chemical component provided as input parameters. The calculations give the optical properties for each aerosol mode, grid cell, and for every considered wavelength. The required optical properties are the extinction coefficient b_{k_b}, the single scattering albedo ω_{k_b} and the asymmetry parameter g_{k_b} for each spectral band k$_b$, respectively. The coefficients for each band are achieved by weighting the value at each considered wavelength with the available energy to the total available energy within the spectral band. For shortwave wavelengths, the optical constants are weighted to the available energy from the solar spectra and averaged band-wise over the three respective shortwave spectral bands. For the longwave spectra, the optical coefficients are weighted with the Planck function at 275 K at each individual wavelength and averaged band-wise over the five longwave spectral bands. The coefficients b_{k_b}, ω_{k_b}, and g_{k_b} are determined from a new optical parameterisation provided with a look up table with the necessary information for each spectral band, cf. chapter 5. The new optical parameterisation is implemented in COSMO-ART within a new routine. Based on the optical constants and the online simulated sea salt concentration, the actual aerosol optical depth τ, the scattering optical depth τ_s and the absorption optical depth τ_a are calculated for each gridcell (x,y,z) and spectral band by

$$\tau(x,y,z,k_b) = b_{x,y,z,k_b} \cdot \Delta z(x,y,z) \tag{3.37}$$

$$\tag{3.38}$$

$$\tau_s(x,y,z,k_b) = \omega_{k_b} \cdot \tau(x,y,z,k_b)$$

$$\tag{3.39}$$

$$\tau_a(x,y,z,k_b) = \tau(x,y,z,k_b) - \tau_s(x,y,z,k_b)$$

where $\Delta z(x,y,z)$ denotes the height of each model layer. The asymmetry parameter g_{k_b}, together with the scattering optical depth τ_s, and the absorption optical depth τ_a enters the calculations of the radiative fluxes in the COSMO model. The aerosol initialised modifications of the radiative fluxes leads to the feedback loop in Figure 3.2. Altered aerosol emissions are one of the consequences of the modified state of the atmosphere. In turn, the aerosol concentrations are changed. The current aerosol concentration is utilisied every hour to calculate τ, τ_s, and τ_a within the new routine in COSMO-ART.

Chapter 4

Introduction of Wet Internally Mixed Sea Salt Aerosol to COSMO-ART

Within the framework of the present thesis, the treatment of the sea salt aerosol in COSMO-ART is extended from a pure sodium chloride (NaCl) aerosol to an internally mixed aerosol containing NaCl, sodium sulphate (Na_2SO_4), and water. This extension includes two main parts that will be described in this chapter:

- condensation of sulphuric acid onto the existing sea salt particles
- calculations of the aerosol liquid water content with respect to the internally mixed aerosol.

4.1 Formation of Internally Mixed NaCl-Sulphate Aerosol

Aerosol containing mixtures of sea salt and sulphate is for instance a result of the condensation of sulphuric acid onto sea salt aerosol. Sulphuric acid is formed in the atmosphere through oxidation processes. In marine air, the sources of sulphur species are mainly emissions of oceanic dimethyl sulphide (DMS), which contribute to the most important natural source (Pham et al., 1995), ship emissions and transport from anthropogenic emission over the continent and along the coast. In the following section (4.1.1) the production of sulphuric acid from oceanic DMS in COSMO-ART is described. Thereafter, section 4.1.2 describes the treatment of the aerosol growth rate due to the condensation of sulphuric acid.

4.1.1. Production of Sulphuric Acid in Clean Marine Air

Air-Sea Gas Exchange of DMS

The oceanic dimethyl sulfide (DMS), CH_3SCH_3, accounts for the largest natural source of atmospheric sulphur (Pham et al., 1995). The source for oceanic DMS is the decomposition of dimethyl sulfoniopropionate (DMSP), that is produced by phytoplankton. The mean concentration of DMS in sea water is dependent on the depth and location and shows diurnal and seasonal variations (Seinfeld and Pandis, 1998). The highest ocean water DMS concentrations occur in the Southern Hemisphere in January, especially in Antarctic waters, and in the Northern Hemisphere in July. Seawater concentrations of DMS are much higher than the atmospheric concentrations that result in a lack of equilibrium, and in turn a flux of DMS from the ocean to the atmosphere occurs.

Gas transfer at the air-sea interface is thought to be regulated by factors such as turbulence at the interface, boundary layer stability, surfactants and bubbles (Wanninkhof, 1992, and references therein). As several experiments have shown that wind speed has a major influence on the gas exchange and only limited data on other parameters that may influence or be linked to the surface turbulence is available, the wind speed is commonly used to describe the gas transfer rate. Empirical relationships have been developed to determine the gas transfer F_g from the air-water concentration difference ΔC_g and wind speed U above the ocean as

$$F_g = -K_w(U)\ \Delta C_g.$$

K_w, which is known as the gas transfer velocity, incorporates the physical factors that control the gas transport through the air-sea interface (Miller et al., 2009). As the atmospheric DMS concentration usually is negligible compared to the saturated concentration in the ocean, C_w, the concentration difference Δ C_g can be approximated by Δ $C_g \approx$ -C_w. With this assumption, the flux of DMS F_{DMS} is determined by

$$F_{DMS} = K_w(U)\ C_w. \tag{4.1}$$

For DMS, the transfer velocity K_w can be described as a function of the horizontal wind speed U (e.g., Liss and Merlivat, 1986; Wanninkhof, 1992; Nightingale et al., 2000). In this study the relationship of Nightingale et al. (2000) is applied

$$K_w = 0.222 \cdot U_{10}^2 + 0.333 \cdot U_{10}. \tag{4.2}$$

The transfer velocity is calculated in cm hour^{-1} as a function of the wind speed at 10 m above the ocean given in m s^{-1}. Besides for the transfer velocity, the seawater DMS concentration C_w has to be determined. As oceanic DMS is produced from the biological activity of phytoplankton (Tarrasón et al., 1995) the concentration varies with geographical location and season. As a function of biogeochemical properties, Longhurst et al. (1995) proposed a scheme where they divided the earth's ocean into 57 provinces for the global primary production in the ocean. Four of these provinces; the North Atlantic Drift (NADR), the Northeast Atlantic Continental Shelf (NECS), the eastern part of the North Atlantic Subtropical Gyre (NASTE) and the Mediterranean

Sea (MEDI) are considered in this study (Figure 4.1). Concentrations for the month of July were taken from Kettle and Andreae (2000) and from the *Global Surface Seawater DMS Database* (http://saga.pmel.noaa.gov/dms/) for each province. With this data, a new DMS seawater climatology was implemented in COSMO-ART as shown in Table 4.1. Finally, the transfer rate of DMS is determined in the flux of mass per square metre water and second on the form

$$F_{DMS} = \frac{C_w \cdot M_{w,DMS}}{3.6 \cdot 10^2} \left(0.222 \cdot U_{10}^2 + 0.333 \cdot U_{10}\right) \tag{4.3}$$

where $M_{w,DMS}$ denotes the molecular weight of DMS. The temporal change of the DMS concentration due to emissions in the lowest model layer is thus calculated as

$$E_{DMS} = \frac{F_{DMS}}{\Delta z_s} \tag{4.4}$$

where Δ z_s is the height of the lowest model layer.

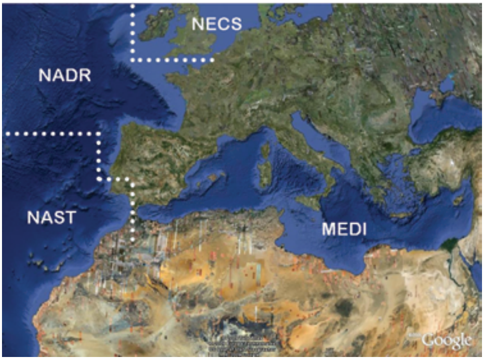

Figure 4.1.: The considered DMS sea water provinces.

Table 4.1.: DMS sea water concentration in COSMO-ART.

Province	C_w in mol L^{-1}
NADR	$8.0{\cdot}10^{-9}$
NAST	$5.0{\cdot}10^{-9}$
NECS	$6.0{\cdot}10^{-9}$
MEDI	$5.0{\cdot}10^{-9}$

Production of Sulphate through DMS Oxidation

In the atmosphere, the destruction of DMS is dominated by reactions with the hydroxyl radical (OH) and the nitrate radical (NO_3). The removal of DMS by OH occurs mainly at low latitudes and only during the daytime because of the photochemical source of OH. The rate constant of the reaction with OH is approximately a factor of 4 times greater than that of the DMS-NO_3 reaction. For this reason, the oxidation by the nitrate radical will occur where OH is not present, i.e. at nighttime and in colder and darker regions compared to the DMS-OH reaction. The lifetime of DMS in the atmosphere ranges between one to several days in the atmosphere. In the following, the gas phase reactions related to the destruction of DMS, which were included in the model, are presented. The nitrate radical NO_3 is formed from the reaction of NO_2 and ozone O_3 as

$$\mathrm{O_3} + \mathrm{NO_2} \longrightarrow \mathrm{NO_3} \tag{4.5}$$

and the hydroxyl radical (OH) results from the reaction between water and the oxygen atom $O(^1D)$, which is formed from the photolysis of ozone as

$$\mathrm{O_3} \xrightarrow{hv} \mathrm{O(^1D)} + \mathrm{O_2} \tag{4.6}$$

$$\mathrm{O(^1D)} + \mathrm{H_2O} \longrightarrow 2\,\mathrm{OH}. \tag{4.7}$$

Sulphur dioxide is produced through the oxidation of DMS by NO_3

$$NO_3 \ + \ DMS \longrightarrow SO_2 \ + ... \tag{4.8}$$

When DMS is oxidised by OH, dimethyl sulphoxide (DMSO) and sulphur dioxide are generated

$$OH \quad + \quad DMS \longrightarrow SO_2 \ + ... \tag{4.9}$$

$$OH \quad + \quad DMS \longrightarrow \ 0.6\,SO_2 \ + \ 0.4\,DMSO \ + ... \tag{4.10}$$

DMSO is in turn oxidised to sulphur dioxide and methanesulphonic acid (MSA) by its reaction with OH

$$OH \ + \ DMSO \longrightarrow 0.6\,SO_2 \ + \ 0.4\,MSA \ + ... \tag{4.11}$$

The MSA production during the oxidation of DMS of nitrogen oxides is however not well understood and for this reason it is not taken into account in COSMO-ART. Sulphuric acid is subsequently formed when SO_2, which was formed by the above-mentioned reactions, is oxidised by OH in a three body reaction

$$OH \ + SO_2 \xrightarrow{M} H_2SO_4 \ + \ HO_2. \tag{4.12}$$

The rate constants of the implemented reactions (4.8)-(4.11) in this work are obtained from Pham et al. (1995). The other reactions are already accounted for in the chemistry module RADMKA in COSMO-ART.

In COSMO-ART, the dry deposition velocity of DMS is set to zero (Huneeus and Chevallier, 2009) and the dry deposition velocity of DMSO is set to 1 cm s^{-1} over the ocean and zero over the continent based on Pham et al. (1995), and Huneeus and Chevallier (2009). The dry deposition of SO_2 is parameterised according to Bär and Nester (1992).

4.1.2. Condensation of Sulphuric Acid on Aerosols

The sulphuric acid, which was formed through reaction (4.12) may condense on the sea salt aerosol and anthropogenic aerosols. Any condensation on other aerosols is not yet accounted for in COSMO-ART. Condensation onto anthropogenic aerosols was introduced to COSMO-ART by Riemer (2002), whereas the condensation onto sea salt is introduced within this thesis.

Condensation leads to additional mass on the aerosol, which causes a temporal change of the third moment, whereas the number of aerosol remains uninfluenced. The calculation of the aerosol growth rate due to condensation is based on the method presented by Whitby et al. (1991). When assuming spherical particles and neglecting the Kelvin effect, the temporal change of the third moment of the distribution is represented by the product of a size-independent contribution and a size-dependent contribution. The size-dependent contribution has two asymptotic forms for the near continuum and free molecular regimes. The free molecular regime is applied for particles with Knudsen numbers (Kn_g=$2\lambda_{air}/\mathrm{D}_p$) >10 and the near continuum regime is for particles with $0.1 < \mathrm{Kn}_g \leq 1$. Consequently, the temporal change of the third moment due to condensation takes different forms for the two size regimes

$$\begin{aligned}
\overline{G}_{3,i}^{nc} &= \frac{6}{\pi}\,\Psi_T \int_0^\infty 2\pi D_v\, D_p n_i\left(D_p\right)\mathrm{d}D_p = \frac{6}{\pi}\Psi_T\,\underbrace{2\pi D_v M_1}_{I_{3,i}^{nc}} \\
\overline{G}_{3,i}^{fm} &= \frac{6}{\pi}\,\Psi_T \int_0^\infty \frac{\pi\alpha\bar{c}}{4}\,D_p^2 n_i\left(D_p\right)\mathrm{d}D_p = \frac{6}{\pi}\Psi_T\,\underbrace{\frac{\pi\alpha\bar{c}}{4}M_2}_{I_{3,i}^{fm}}
\end{aligned} \tag{4.13}$$

$\overline{G}_{3,i}^{nc}$ and $\overline{G}_{3,i}^{fm}$ denote the mean condensational growth rates in the near continuum regime and the free molecular regime for each sea salt mode i, respectively. The size independent contribution Ψ_T is $\Psi_T = \dfrac{M_w \, p_s \, (S_v - 1)}{\rho_l \, R \, T}$, where M_w is the molecular weight, R is the ideal gas constant, p_s and S_v are the saturation vapour pressure and the saturation ratio of condensing species, in this case sulphuric acid. D_v is the vapour diffusivity, α is the accommodation coefficient, and $\overline{c}$ is the kinetic velocity of vapour molecules $(=\sqrt{\frac{8\,R\,T}{\pi\,M_w}})$.

To achieve the mean growth rate over the total size range $\overline{G}_{3,i}$, the harmonic mean of $I^{nc}_{3,i}$ and $I^{fm}_{3,i}$ are formed.

$$\overline{G}_{3,i} = \frac{6}{\pi} \Psi_T \, I_{3,i} = \frac{6}{\pi} \Psi_T \, \frac{I^{nc}_{3,i} \cdot I^{fm}_{3,i}}{I^{nc}_{3,i} + I^{fm}_{3,i}}. \tag{4.14}$$

$I^{nc}_{3,i}$ and $I^{fm}_{3,i}$ represent the solutions of the size-dependent integrals in Equation (4.13). The total temporal change of the third moment that is caused by condensation on the aerosols is given by the sum over the three sea salt modes and the five anthropogenic aerosol modes

$$\overline{G}_3 = \sum_{i=1}^{8} \overline{G}_{3,i} \tag{4.15}$$

The condensation processes are assumed to be quick compared to the generation of condensable material from the gas phase. As a result, a steady state develops between the third moment aerosol growth rate $\overline{G}_3$ and the production rate of the third moment of the sulphuric acid $\dot{M}_{3,sulph}$. The production rate of the third moment of the sulphuric acid is determined by the production rate of condensational vapour $\dot{C}_{sulph}$, obtained from the chemistry module RADMKA, and its density ρ_{sulph}

$$\dot{M}_{3,sulph} = \frac{6}{\pi} \frac{\dot{C}_{sulph}}{\rho_{sulph}}. \tag{4.16}$$

Because the produced sulphuric acid is assumed to directly enter condensational processes, the rate of production of the third moment from the condensable vapour must be equal to the total growth rate of the aerosol third moment

$$\overline{G}_3 = \dot{M}_{3,sulph}. \tag{4.17}$$

The fraction of sulphuric acid that enters each mode is given by the dimensionless coefficient Ω_i

$$\Omega_i = \frac{\overline{G}_{3,i}}{\overline{G}_3} = \frac{\frac{6}{\pi}\Psi_T \, I_{3,i}}{\frac{6}{\pi}\Psi_T \, \sum_{i=1}^{8} I_{3,i}} = \frac{I_{3,i}}{\sum_{i=1}^{8} I_{3,i}} \tag{4.18}$$

Combining Equations (4.17) and (4.18), the third moment growth rate for each mode can be expressed as a function of the fraction of the injected material and the production rate of the condensable material itself

$$\overline{G}_{3,i} = \Omega_i \, \dot{M}_{3,sulph} = \Omega_i \frac{6}{\pi} \frac{\dot{C}_{sulph}}{\rho_{sulph}} \tag{4.19}$$

Hence, the size-independent contribution Ψ_T, which is a function of rather complex variables, is no longer required for the determination of the aerosol growth rate.

By recalling that m=ρV=$\frac{\pi}{6}\rho$M$_3$ the mass growth rate $\overline{G}_{m,i}$ is finally obtained as a function of the production rate of sulphuric acid and the size-dependent integrals $\mathrm{I}_{3,i}^{nc}$ and $\mathrm{I}_{3,i}^{fm}$ in Equation (4.13)

$$\overline{G}_{m,i} = \Omega_i \, \dot{C}_{sulph} \tag{4.20}$$

Sulphuric acid, which does not take part in the condensation processes, will participate in binary homogeneous nucleation with water. The nucleation rate is calculated as a function of the production rate of sulphuric acid and the loss rate through condensation. These calculations are based on Kerminen and Wexler (1994) and are described in Riemer (2002).

4.2 Sea Salt Aerosol Liquid Water Content

The uptake of liquid water by an aerosol particle is determined by factors such as ambient relative humidity (RH) and the chemical composition of the aerosol. The chemical composition is represented by the molality, describing the amount of a component per kg solvent (water). The aerosol liquid water content (LWC) increases as the molality or RH increase. For very high humidity, approaching 100%, the amount of liquid water on the aerosol increases super linearly. As the RH decrease, the aerosol liquid water content evaporates. When the RH drops bellow the so-called efflorescence point, the aerosol crystallises and the water uptake stops. At which RH the water uptake discontinues depends on the aerosol compounds and their respective efflorescence points. As different compounds have different efflorescence points, it is much more difficult to determine at which RH a mixed aerosol might crystallise, compared to a pure particle.

As no semi-volatile compounds are taken into account in this study, a simplified approach can be used without taking the mass transfer between the gas phase and aerosol phase into account. For the mass partitioning between the two phases, the equilibrium partial pressure over an aerosol surface is required, for which the recently developed PD-FiTE (Topping et al., 2005) is ideal. As a function of the equilibrium pressure, the mass has however to be partitioned between the two phases that for example, can be solved via iterations. Thus, these calculations become extremely time-consuming. For this reason the composition of sea salt is assumed to consist of compounds that will stay in the aerosol phase only, and no semi-volatile components are treated. Hence, mass transfer calculations will not be needed with the method that is used in this study.

After the condensation of sulphuric acid on the sea salt aerosol, the aerosol will contain a mixture of H^+-Na^+-Cl^--SO_4^{2-}-HSO_4^- ions dissolved in water

$$\mathrm{NaCl}(s) \;\rightarrow\; \mathrm{Na}^+(aq) \;+\; \mathrm{Cl}^-(aq) \tag{4.21}$$

$$\mathrm{H_2SO_4}(g) \;\rightarrow\; \mathrm{H}^+(aq) \;+\; \mathrm{HSO}_4^-(aq) \tag{4.22}$$

$$\mathrm{HSO}_4^-(aq) \;\rightarrow\; \mathrm{H}^+(aq) \;+\; \mathrm{SO}_4^{2-}(aq). \tag{4.23}$$

The determination of the aerosol liquid water content in an aerosol containing H^+-Na^+-Cl^--SO_4^{2-}-HSO_4^- is introduced to COSMO-ART within this work. The total water concentration m_w is calculated with the use of the Zdanovskii-Stokes-Robinson (ZSR) relation (Stokes and Robinson, 1966)

$$m_w = \sum_E \frac{n_E}{m_E^0\left(a_w\right)}, \tag{4.24}$$

where m_w is given in kg of aerosol liquid water per cubic metre air, n_E is the concentration of electrolyte E in mol/m^3_{air} and $m_E^0\left(a_w\right)$ is the binary electrolyte molality of electrolyte E as a function of the water activity a_w(=RH) given in mol of solution per kg of solvent (water). The binary molality is the molality of an electrolyte that is alone in solution. To calculate the electrolyte concentration n_E a technique is needed to determine the partitioning of the present ions into electrolytes. For this purpose the method presented by Zaveri et al. (2005) is applied and described in section 4.2.1. The binary electrolyte molality is determined as a function of the ambient RH by polynomials, for which the parameters are obtained from Tang (1997). These calculations are summarised in section 4.2.2.

4.2.1. Electrolyte Formation

Within the composition space H^+-Na^+-Cl^--SO_4^{2-}-HSO_4^- two electrolyte formation domains are possible, the "sulphate-rich" and "sulphate-poor" domain. Zaveri et al. (2005) separated these domains by using the sulphate ratio X_s

$$X_s \;=\; \frac{n_{Na^+}}{n_{SO(VI)}} \;=\; \frac{n_{Na^+}}{n_{SO_4^{2-}} + n_{HSO_4^-}} \quad \begin{cases} X_s \leq 2 & \text{sulphate-poor domain} \\ X_s > 2 & \text{sulphate-rich domain} \end{cases}$$

where n_{Na^+},$n_{SO_4^{2-}}$ and $n_{HSO_4^-}$ denote the number of moles of each ion, respectively. In the sulphate-poor domain, S(VI) is completely neutralised by Na^+, which means that S(VI) exists in the form of SO_4^{2-}. In the sulphate-rich domain, S(VI) is, on the other hand, not completely neutralised and may exist in the form of SO_4^{2-} or HSO_4^-. In this study it is assumed that n_{Na^+} » $n_{S(VI)}$. Thus, the liquid water calculations are restricted to the sulphate-poor domain. Hence, the sulphuric acid is assumed to be completely dissociated to SO_4^{2-} as in Reaction (4.23). The water uptake of aerosol in the sulphate-rich domain is neglected.

In the sulphate-poor domain, only strong electrolytes, which dissociates completely into ions in aqueous solution, are formed. To determine the aerosol liquid water content, the number of moles of each present electrolyte has to be calculated. The number of moles of the respective ions is most often known, rather than that of the electrolytes.

Here, the mixing scheme of Zaveri et al. (2005) is applied for determining the number of moles of strong electrolytes n_E. For these calculations, equivalent ion fractions ϕ_a and ϕ_c for anions and cations, respectively, are used. The equivalent ion fraction of each ion j is a function of the number of moles n_j and the corresponding magnitude of the charge γ_j as

$$\phi_a = \frac{\gamma_a n_a}{\sum_a \gamma_a n_a} \qquad \text{for anions} \tag{4.25}$$

$$\phi_c = \frac{\gamma_c n_c}{\sum_c \gamma_c n_c} \qquad \text{for cations.} \tag{4.26}$$

The equivalent ion fractions for the present ions in the solution of interest are consequently given by

$$\phi_{Na^+} = \frac{n_{Na^+}}{n_{H^+} + n_{Na^+}} \tag{4.27}$$

$$\phi_{H^+} = \frac{n_{H^+}}{n_{H^+} + n_{Na^+}} \tag{4.28}$$

$$\phi_{Cl^-} = \frac{n_{Cl^-}}{n_{Cl^-} + 2n_{SO_4^{2-}}} \tag{4.29}$$

$$\phi_{SO_4^{2-}} = \frac{n_{SO_4^{2-}}}{n_{Cl^-} + 2n_{SO_4^{2-}}} \tag{4.30}$$

The number of moles of each ion per cubic metre air is calculated by $n_j = \frac{m_j}{M_{w,j}}$ where $M_{w,j}$ is the molecular weight of ion j and m_j is the mass density from MADE$_{soot}$.

The concentration of the electrolytes are subsequently calculated by using the equivalent ion fractions

$$n_E = \frac{\phi_c\, n_a\, M_{w,a} + \phi_a\, n_c\, M_{w,c}}{\nu_a\, M_{w,a} + \nu_c\, M_{w,c}} \tag{4.31}$$

where ν_a and ν_c denote the number of moles of anion a and cation c in electrolyte E. Within the considered, sulphate-poor, domain the possible aqueous electrolytes are NaCl and Na_2SO_4. Na_2SO_4 is formed when sodium chloride reacts with sulphuric acid

$$H_2SO_4(g) + 2NaCl \rightarrow Na_2SO_4 + 2HCl(g). \tag{4.32}$$

The number of moles of NaCl and Na_2SO_4 are finally calculated as

$$n_{NaCl} = \frac{\phi_{Na^+}\, n_{Cl^-}\, M_{w,Cl^-} + \phi_{Cl^-}\, n_{Na^+}\, M_{w,Na^+}}{M_{w,Na^+} + M_{w,Cl^-}} \tag{4.33}$$

$$n_{Na_2SO_4} = \frac{\phi_{Na^+}\, n_{SO_4^{2-}}\, M_{w,SO_4^{2-}} + \phi_{SO_4^{2-}}\, n_{Na^+}\, M_{w,Na^+}}{2\, M_{w,Na^+} + M_{w,SO_4^{2-}}}. \tag{4.34}$$

4.2.2. Aqueous Electrolyte Binary Molality

The binary molality m_E^0 is in addition to the electrolyte concentration required for calculating the liquid water content from Equation (4.24). The binary electrolyte molalities are determined by polynomial fits as a function of the water activity. The water activity is commonly assumed to be equal to the ambient RH in fractional form, i.e. the Kelvin effect is neglected, for atmospheric conditions

$$a_w = \frac{RH}{100}. \tag{4.35}$$

Based on experimental data for water activity as a function of the binary electrolyte molality, polynomial fits for the electrolyte molality as a function of the water activity are obtained (e.g. Tang and Munkelwitz, 1994; Tang et al., 1997). These polynomial expressions, by which the binary molalities are determined, take the form

$$m_E^0 = Y_{E,0} \, + \, Y_{E,1}\, a_w \, + \, Y_{E,2}\, a_w^2 \, + \, Y_{E,3}\, a_w^3 \, + \, Y_{E,4}\, a_w^4. \tag{4.36}$$

For E=NaCl, Na_2SO_4 the coefficients $Y_{E,0}$-$Y_{E,4}$ were achieved from Tang (1997). The coefficient values that were used in this work are shown in Table 4.2. For NaCl, the coefficients are valid for conditions where RH $>$ 47% and for Na_2SO_4 they are valid for RH $>$ 58%. This means that when the relative humidity drops under 58% Na_2SO_4 is not hydrating in the model. For conditions where the relative humidity drops under 47% the sea salt aerosol LWC is neglected. For RH $>$ 99% the LWC remains constant in the model.

Table 4.2.: Coefficients of polynomial fits of m_E^0 Eq.(4.36) obtained from Tang (1997) for NaCl and Na_2SO_4 in the sulphate-poor domain assuming a_w = RH .

Coefficients	NaCl	Na_2SO_4
Y_0	$5.875248 \cdot 10^1$	$5.5983158 \cdot 10^2$
Y_1	$-1.8781997 \cdot 10^2$	$-2.56942664 \cdot 10^3$
Y_2	$2.7211377 \cdot 10^2$	$4.47450201 \cdot 10^3$
Y_3	$-1.8458287 \cdot 10^2$	$-3.45021842 \cdot 10^3$
Y_4	$4.153689 \cdot 10^1$	$9.8527913 \cdot 10^1$

4.3 The Conservation Equations for the Internally Mixed Aerosol

For the internally mixed aerosol, the total mass density $m_{i,mix}$ of each mode is

$$m_{i,mix} = m_{i,ssa} + m_{i,sulph} + m_{i,w} \tag{4.37}$$

where $m_{i,ssa}$ is the mass density of dry sea salt aerosol (sodium chloride), $m_{i,sulph}$ is the mass density of the sulphate component and $m_{i,w}$ is the mass density of water on the mixed sea salt aerosol. The density $\rho_{i,mix}$ of the internally mixed aerosol is calculated from the third moment $M_{3,i,mix}$ of the mixed aerosol and the mass density $m_{i,mix}$ according to Equation (3.12).

The third moment of the internally mixed aerosol is achieved by applying Equation (3.13) for the sea salt, sulphate and water substances

$$M_{3,i,mix} = \frac{6}{\pi}\left(\frac{m_{i,ssa}}{\rho_{NaCl}} + \frac{m_{i,sulph}}{\rho_{sulph}} + \frac{m_{i,w}}{\rho_w}\right). \tag{4.38}$$

The density of the internally mixed aerosol in each mode is now given by

$$\rho_{i,mix} = \frac{6}{\pi}\frac{m_{i,mix}}{M_{3,i,mix}}. \tag{4.39}$$

The geometric median diameters of the internally mixed sea salt aerosol distributions are determined, following Equation (3.6), which for mixed aerosol distributions take the form

$$D_{g0,i,mix} = \left(\frac{m_{i,mix}}{\frac{\pi}{6}\rho_{i,mix}\exp\left(4.5\ln^2\sigma_{gi}\right)N_{i,mix}}\right)^{\frac{3}{2}}. \tag{4.40}$$

The number density $\mathrm{N}_{i,mix}$ of internally mixed sea salt aerosol is, as already mentioned, not directly influenced by the condensation of sulphuric acid or by the water uptake. A difference in the number density of pure sea salt aerosol and internally mixed sea salt aerosol occurs, however, through the modification of the processes such as sedimentation, deposition, and washout via the change of size of the aerosol.

The water content on the aerosol is not transported but locally equilibrated. The conservation equations of the internally mixed sea salt aerosol are solved for the sulphate content, the content of sea salt, and the number density. The conservation equations for the number density of the internally mixed sea salt aerosol take the form

$$\frac{\partial\hat{\Psi}_{N_{i,mix}}}{\partial t} = -\hat{\mathbf{v}}\cdot\nabla\hat{\Psi}_{N_{i,mix}} - \overline{v}_{sed,N_{i,mix}}\frac{\partial\hat{\Psi}_{N_{i,mix}}}{\partial z} + \frac{1}{\overline{\rho}_a}\nabla\cdot F^{\Psi_{N_{i,mix}}} - \overline{W}_{N_{i,mix}}. \tag{4.41}$$

For the mass densities, the following equations are solved

$$\begin{aligned}\frac{\partial \hat{\Psi}_{m_{i,ssa}}}{\partial t} &= -\hat{\mathbf{v}} \cdot \nabla \hat{\Psi}_{m_{i,ssa}} - \overline{v}_{sed,m_{i,ssa}} \frac{\partial \hat{\Psi}_{m_{i,ssa}}}{\partial z} + \frac{1}{\overline{\rho}_a} \nabla \cdot F^{\Psi_{m_{i,ssa}}} \\ &- \overline{W}_{m_{i,ssa}} \end{aligned} \tag{4.42}$$

$$\begin{aligned}\frac{\partial \hat{\Psi}_{m_{i,sulph}}}{\partial t} &= -\hat{\mathbf{v}} \cdot \nabla \hat{\Psi}_{m_{i,sulph}} - \overline{v}_{sed,m_{i,sulph}} \frac{\partial \hat{\Psi}_{m_{i,sulph}}}{\partial z} + \frac{1}{\overline{\rho}_a} \nabla \cdot F^{\Psi_{m_{i,sulph}}} \\ &- \overline{W}_{m_{i,sulph}} + \overline{G}_{m,i} \end{aligned} \tag{4.43}$$

where $\overline{G}_{m,i}$ is the mean condensational loss or gain of mass in each mode. $\Psi_{m_{i,ssa}}$ and $\Psi_{m_{i,sulph}}$ are the normalised mass densities

$$\Psi_{m_{i,ssa}} = \frac{m_{i,ssa}}{\rho_a} \tag{4.44}$$

$$\Psi_{m_{i,sulph}} = \frac{m_{i,sulph}}{\rho_a} \tag{4.45}$$

and $\hat{\Psi}_{m_{i,ssa}}$ and $\hat{\Psi}_{m_{i,sulph}}$ the corresponding density weighted Reynolds averages (cf. Equation (3.17)). For the internally mixed aerosol, the sedimentation and deposition velocities are now determined as a function of the geometric median diameter of the mixed aerosol distributions and the corresponding density in each mode. The settling velocity of each compound in mode i is equal to that of mode i

$$\begin{aligned}\overline{v}_{sed,N_i,mix} = \frac{g\rho_{i,mix}}{18\nu\rho_a}\, D^2_{g0,i,mix} \Big(\exp\left(2\ln^2\sigma_{gi}\right) + \\ +1.246\frac{2\lambda_a}{D_{g0,i,mix}}\exp\left(\frac{1}{2}\ln^2\sigma_{gi}\right)\Big)\end{aligned} \tag{4.46}$$

$$\begin{aligned}\overline{v}_{sed,m_i,mix} = \frac{g\rho_{i,mix}}{18\nu\rho_a}\, D^2_{g0,i,mix} \Big(\exp\left(8\ln^2\sigma_{gi}\right) + \\ +1.246\frac{2\lambda_a}{D_{g0,i,mix}}\exp\left(\frac{7}{2}\ln^2\sigma_{gi}\right)\Big)\end{aligned}$$

$$\begin{aligned}\overline{v}_{sed,m_i,ssa} &= \overline{v}_{sed,m_i,mix} \\ \overline{v}_{sed,m_i,sulph} &= \overline{v}_{sed,m_i,mix}.\end{aligned} \tag{4.47}$$

The deposition velocities for each mode and respective compound are determined as in Equation (3.26) with the sedimentation velocities of the internally mixed aerosol distributions (Equation (4.46)) and the median diameter of the internally mixed modes i $\mathrm{D}_{g0,i,mix}$.

Chapter 5

A New Optical Parameterisation for Sea Salt Aerosol

Atmospheric radiative fluxes are modified through extinction, i.e. absorption and scattering, by gaseous molecules and aerosols. The sea salt optical properties are for this reason required. In this work, the sea salt aerosol optical properties of both shortwave and longwave radiation due to the wet internally mixed sea salt aerosol, as described in chapter 4, are parameterised. These optical properties are the single scattering albedo, the asymmetry factor and the extinction coefficient. For a known aerosol size distribution and its corresponding aerosol refractive index, the optical properties can be calculated using the Mie theory. As already mentioned in chapter 3 are Mie calculations too time consuming for atmospheric 3-D models and cannot be performed online. Thus, accurate optical parameterisations based on the Mie theory are needed. Existing parameterisations for sea salt aerosol optical properties are rare and mainly not applicable for the longwave and shortwave ranges (Li et al., 2008). For this reason, Li et al. (2008) developed an optical parameterisation for both ranges for wet sea salt aerosol. This parameterisation was based on the mean volume mixing rule for determining the effective refractive index of the multicomponent aerosol. This method is however only valid for quasi-homogeneous mixtures or for mixtures with components with very similar refractive indices (Liu and Daum, 2008) and has been stressed to be valid for solid particles, but may not hold for solutions of salts that dissolve in water (Irshad et al., 2009). As the sea salt aerosol dissolves at ambient relative humidities exceeding the deliquescence point and remains dissolved at RH higher than the efflorescence conditions, the volume mixing rule is invalid for most atmospheric conditions. Hence, it may be questioned as to how well optical parameterisations based on such mixing rules represent the reality of sea salt aerosol optical features. In this study, a new sea salt aerosol optical parameterisation is developed based on Mie calculations and the so-called partial molar refraction approach for determining the effective refractive index (Stelson, 1990; Tang, 1997). The Mie calculations are performed with the code that originally was developed by Bohren and Huffman (1983). Input variables for the Mie calculations are the effective refractive index and pre-simulated sea salt size distributions. Calculations are performed for each grid point of a chosen area in the Mediterranean Region, for which the sea salt aerosol size distribution was pre-simulated. The necessary calculations for determining the effective refractive index of a multi component aerosol is described in the following section. Thereafter, the new optical parameterisation is presented. Three dimensional applications with the new optical parameterisation introduced to COSMO-ART are treated in chapter 6.

5.1 The Effective Refraction Index of the Multi-component Aerosol

The complex refractive index $\widetilde{m}_\lambda$ is for the light of wavelength λ

$$\widetilde{m}_\lambda = \eta_\lambda + i\kappa_\lambda. \tag{5.1}$$

The real part η_λ of the refractive index describes the change of the phase speed of an electromagnetic wave as it passes from one medium to another

$$\eta_\lambda = \frac{c}{c'} \tag{5.2}$$

where c is the reference phase velocity, i.e. the speed of light in vacuum with wavelength λ, and c' is the corresponding speed in the considered medium. $\eta_\lambda > 1$ implies a reduced speed of light in the media relative to that in vacuum, which is the case in most physical media (Petty, 2006). The imaginary part κ_λ of the refractive index describes to which extent the intensity of light with wavelength λ is reduced as it passes through the material. It is, for the bulk case, related to the absorption coefficient b_a via the relation

$$\kappa_\lambda = \frac{b_a \lambda}{4\pi}. \tag{5.3}$$

For a multicomponent aerosol, the refractive index of each compound needs to be combined with the use of a mixing rule to achieve the effective refractive index of the aerosol. Before the methods to describe the real and imaginary parts of the refractive index for the internally mixed sea salt aerosol in this study are described, some general properties that are needed for these calculations are presented.

To avoid confusion between the number density, which in the other chapters has been denoted by n, and the real part of the refractive index η, the notation $\mathrm{c}_{n,s}$ will be used for the number density of solution s in this chapter. For consistency, the mass density is denoted as $\mathrm{c}_{m,s}$. The volume density of a solution is given in m^3 aerosol per m^3 air by the fraction of the mass density in kg m^{-3} and the solution density ρ_s given in kg m^{-3}

$$V_s = \frac{c_{m,s}}{\rho_s}. \tag{5.4}$$

The total mass density $c_{m,s}$ is the sum of the mass density $c_{m,l}$ of each component l

$$c_{m,s} = \sum_{l=1}^{N_s} c_{m,l}. \tag{5.5}$$

The mass density of each component can be expressed as a function of the mole concentration $c_{n,l}$ of each component l in mol m^{-3} and the corresponding molar mass $M_{w,l}$ in kg mol^{-1}

$$c_{m,l} = c_{n,l} \cdot M_{w,l}. \tag{5.6}$$

The molar volume $\tilde{V}_s$ in m^3 mol^{-1} of a solution aerosol is

$$\tilde{V}_s = \frac{\sum_{l=1}^{N_s} x_l \, M_{w,l}}{\rho_s} \tag{5.7}$$

where x_l is the dimensionless mole fraction of each component l. l denotes all the components in the solution, including water and ions or aqueous electrolytes. N_s is the total number of solution components. The mole fraction is given by

$$x_l = \frac{c_{n,l}}{c_{n,s}} \tag{5.8}$$

where $c_{n,l}$ denotes the number density of moles of component l and $c_{n,s}$ is the total solution number density of moles, both per m^3 air. Thus, the molar volume can be expressed as

$$\tilde{V}_s = \frac{\frac{1}{c_{n,s}} \sum_{l=1}^{N_s} c_{n,l} M_{w,l}}{\rho_s} = \frac{1}{c_{n,s}} V_s \tag{5.9}$$

where V_s denotes the volume concentration of the solution in m^3 aerosol per m^3 air given in Equation (5.4). The density of the aerosol is given in kg m^{-3} by (Tang, 1997)

$$\rho_s = \left(\sum_{q=1}^{N_E} \frac{y_q}{\rho_q^0} \right)^{-1} \tag{5.10}$$

where y_q is the solute mass fraction of component q

$$y_q = \frac{c_{m,q}}{\sum_{q=1}^{N_E} c_{m,q}} \tag{5.11}$$

with $c_{m,q}$ as the mass of electrolyte q in kg m^{-3}. N_E is the total number of aqueous electrolytes in the solution. The density of a binary solution ρ_q^0 of electrolyte q is expressed by the polynomial (Tang, 1997)

$$\rho_q^0 = \left(0.9971 + \sum A_i w^i \right) \cdot 10^3 \tag{5.12}$$

where the factor 10^3 converts the binary density from g cm^{-3} into kg m^{-3} and w is the total solute weight in per cent

$$w = \frac{\sum_{q=1}^{N_E} c_{m,q}}{\sum_{l=1}^{N_s} c_{m,l}} \cdot 100. \tag{5.13}$$

A_i is the coefficient of the ith term, which is specific for different electrolytes q.

When considering the dissolved interally mixed aerosol containing aqueous NaCl and Na_2SO_4, the solution volume is given by

$$V_{mix} = \frac{1}{\rho_{mix}} \left(c_{n,H_2O} \cdot M_{w,H_2O} + c_{n,NaCl} \cdot M_{w,NaCl} + c_{n,Na_2SO_4} \cdot M_{w,Na_2SO_4} \right). \tag{5.14}$$

The corresponding density for the wet internally mixed sea salt aerosol is calculated by

$$\rho_{mix} = \left(\frac{1}{c_{m,NaCl} + c_{m,Na_2SO_4}} \left(\frac{c_{m,NaCl}}{\rho^0_{NaCl}} + \frac{c_{m,Na_2SO_4}}{\rho^0_{Na_2SO_4}} \right) \right)^{-1} \tag{5.15}$$

with the binary densities ρ^0_{NaCl} and $\rho^0_{Na_2SO_4}$ from Equation (5.12). The coefficients A_i in Equation (5.12) are obtained from Tang (1996) for NaCl and from Tang and Munkelwitz (1994) for Na_2SO_4. Hence, the expressions for the binary densities in the sea salt aerosol take the form

$$\rho^0_{NaCl} = (0.9971 + 7.41 \cdot 10^{-3} w - 3.741 \cdot 10^{-5} w^2 + 2.252 \cdot 10^{-6} w^3 - 2.06 \cdot 10^{-8} w^4) \cdot 10^3 \tag{5.16}$$

$$\rho^0_{Na_2SO_4} = (0.9971 + 8.871 \cdot 10^{-3} w + 3.195 \cdot 10^{-5} w^2 + 2.28 \cdot 10^{-7} w^3) \cdot 10^3 \tag{5.17}$$

where the solute weight in per cent w is

$$w = \frac{c_{m,NaCl} + c_{m,Na_2SO_4}}{c_{m,NaCl} + c_{m,Na_2SO_4} + c_{m,H_20}} \cdot 100. \tag{5.18}$$

The solution volume V_{mix} of the sea salt aerosol is used to determine the effective refractive index of the multicomponent aerosol. These calculations are described in the following.

5.1.1. The Real Part of Multicomponent Aerosol Refractive Index

The Lorentz-Lorenz relation describes the dependence of the real part of the refractive index on the mass density ρ of a chemical element for a homogeneous medium

$$\frac{(\eta_\lambda^2 - 1)}{(\eta_\lambda^2 + 2)} \frac{M_w}{\rho} = \frac{N_A \alpha_p}{3} \tag{5.19}$$

where M_w denotes the molecular mass, N_A is the universal Avogadro's number and α_p is the mean molecular polarisability (Liu and Daum, 2008). The left hand side, with the effective real part of the refractive index η_λ, represents the macroscopic properties of the material. The right hand side, with the molecular polarisability α_p, represents the microscopic properties of the material. The effective molar refraction of a multi component solution can be defined as (e.g., Stelson, 1990; Tang, 1997, and references therein)

$$R_\lambda = \tilde{V}_s \frac{(\eta_\lambda^2 - 1)}{(\eta_\lambda^2 + 2)}. \tag{5.20}$$

In combining Equations (5.20) and (5.9), the effective molar refraction can be determined from

$$R_\lambda = \frac{V_s}{c_{n,s}} \frac{\left(\eta_\lambda^2 - 1\right)}{(\eta_\lambda^2 + 2)} \tag{5.21}$$

in units of $\mathrm{m}^3\ \mathrm{mol}^{-1}$. When considering each ion or aqueous electrolyte l separately the mole fraction $\frac{c_{n,l}}{c_{n,s}}$ is equal to unity and the density is represented by that of the pure substance, giving the partial molar refraction $R_{l,\lambda}$ the form

$$R_{l,\lambda} = \frac{M_{w,l}}{\rho_l} \frac{\left(\eta_{l,\lambda}^2 - 1\right)}{\left(\eta_{l,\lambda}^2 + 2\right)} \tag{5.22}$$

where η_l is the refraction index of the component l, which represents all the components in the solution including solvent and ion or aqueous electrolyte in the solution. This expression for the molar refraction corresponds to the left hand side in Equation (5.19), if considering a pure medium. Hence, the molar refraction is a macroscopic property of the considered material. From the partial molar refractions of each component (Equation 5.22), the effective solution molar refraction in $\mathrm{m}^3\ \mathrm{mol}^{-1}$ is calculated by

$$R_{s,\lambda} = \sum_{l=1}^{N_s} x_l \cdot R_{l,\lambda} \tag{5.23}$$

which can be rewritten in the form

$$R_{s,\lambda} \cdot c_{n,s} = \sum_{l=1}^{N_s} c_{n,l} \cdot R_{l,\lambda}. \tag{5.24}$$

The effective refractive index $\eta_{s,\lambda}$ for the mixed aerosol is now determined as a function of the effective molar refractive index $\mathrm{R}_{s,\lambda}$, the solution volume V_s and the total number of moles $\mathrm{c}_{n,s}$ in the solution

$$\eta_{s,\lambda} = \left(\frac{V_s + 2R_{s,\lambda} \cdot c_{n,s}}{V_s - R_{s,\lambda} \cdot c_{n,s}} \right)^{1/2}. \tag{5.25}$$

This method for determining the effective refractive index for a mixed aerosol is referred to as the partial molar refraction approach (Stelson, 1990; Tang, 1997). With this method, the effective molar refraction is achieved as the sum of the molar refraction of each component. This approximation is equal to assuming that the total molecular polarisibility of the mixture is represented by the sum of the molecular polarisibilities of each component. This method neglects any interaction between the dipoles, and only takes the sum of the molecular polarisibilities into account. There also exists mixing rules, which additionally consider interaction between the induced dipoles (Martin

Schnaiter, 2010, personal communication), such as the relation by Maxwell-Garnett and that of Bruggeman (Granqvist and Hunder, 1977, and references therein). A commonly applied method is the so-called linear volume average rule, or volume mixing rule, whereby the refractive index is the volume mean refractive index

$$\eta_{s,\lambda} = \sum f_l \cdot \eta_{l,\lambda} \tag{5.26}$$

where f_l is the volume fraction and η_l is the partial refractive index of the lth component, respectively. This method only referres to mixing of the macroscopic properties of the respective components and no microscopic characteristics are considered. This is the main difference between the molar refraction method and the volume mixing rule. The mean volume mixing rule is, as already mentioned, only applicable for mixtures with components with very similar refractive indices (Liu and Daum, 2008).

As the sea salt aerosol is assumed to be completely dissolved, the molar refractive approach is applied for the real part of the refraction index in this work. The effective refractive index is determined for the sea salt aerosol containing sodium chloride, sodium sulphate and water. To apply the molar refractive method for each wavelength the Na^+, Cl^- and SO_4^{2-} ions are combined into hypothetical electrolytes with the same method that was described in chapter 4, based on the work by Zaveri et al. (2005). To consider aqueous electrolytes instead of dissolved ions has the advantage that the refractive indices at non visible wavelengths can be estimated, where partial molar refraction data for ions are not available (Jacobson, 2001a). The partial refraction for an aqueous electrolyte has been inferred to be the same as for the corresponding solid electrolyte (Stelson, 1990; Jacobson, 2001a, 2002). Thus, the aqueous electrolyte is assumed to have the same refractive index as the solid electrolyte. This assumption has the advantage that solid electrolyte refraction index data, which most often is readily found in the literature as a function of wavelength, can be used.

When considering the ternary mixture containing water, sodium chloride and sodium sulphate, the partial molar refractions are determined based on Equation (5.22)

$$R_{H_20,\lambda} = \frac{M_{w,H_2O}}{\rho_{H_2O}} \frac{\left(\eta^2_{H_20,\lambda} - 1\right)}{\left(\eta^2_{H_20,\lambda} + 2\right)} \tag{5.27}$$

$$R_{NaCl,\lambda} = \frac{M_{w,NaCl}}{\rho_{NaCl}} \frac{\left(\eta^2_{NaCl,\lambda} - 1\right)}{\left(\eta^2_{NaCl,\lambda} + 2\right)} \tag{5.28}$$

$$R_{Na_2SO_4,\lambda} = \frac{M_{w,Na_2SO_4}}{\rho_{Na_2SO_4}} \frac{\left(\eta^2_{Na_2SO_4,\lambda} - 1\right)}{\left(\eta^2_{Na_2SO_4,\lambda} + 2\right)}. \tag{5.29}$$

$$\tag{5.30}$$

The product of the effective molar refraction and the mole concentration in the solution at the wavelength λ is given by

$$R_{mix,\lambda} \cdot c_{n,mix} = R_{H_20,\lambda} \cdot c_{n,H_2O} + R_{NaCl,\lambda} \cdot c_{n,NaCl} + R_{Na_2SO_4,\lambda} \cdot c_{n,Na_2SO_4}. \tag{5.31}$$

where c$_{n,mix}$ is the total number of moles of all the components in the sea salt aerosol

$$c_{n,mix} = c_{n,H_2O} + c_{n,NaCl} + c_{n,Na_2SO_4}. \tag{5.32}$$

The effective real part of the refraction index of the wet internally mixed sea salt aerosol is obtained as a function of wavelength from

$$\eta_{mix,\lambda} = \left(\frac{V_{mix} + 2R_{mix,\lambda} \cdot c_{n,mix}}{V_{mix} - R_{mix,\lambda} \cdot c_{n,mix}}\right)^{1/2}. \tag{5.33}$$

5.1.2. The Imaginary Part of the Multicomponent Aerosol Refractive Index

Compared to the real part of the refractive index, it is unclear as to how strong the dependence of the imaginary part is on the mass density (Liu and Daum, 2008). Various mixing rules are however also expected to hold for the complex refractive index. In this present study, the approach that was applied by Jacobson (2001a, 2002) is utilised. The effective imaginary part of the refractive index $\kappa_{s,\lambda}$ for solution s at wavelength λ is given by

$$\kappa_{s,\lambda} = \frac{A_{s,\lambda} \cdot c_{n,s}}{V_s} \tag{5.34}$$

where the product of the effective molar absorption $\mathrm{A}_{s,\lambda}$ and the mole concentration $\mathrm{c}_{n,s}$ of the solution is determined from the partial molar absorptions $\mathrm{A}_{l,\lambda}$ and the mole concentrations $\mathrm{c}_{n,l}$ of each constituent l analogous to Equation (5.23)

$$A_{s,\lambda} \cdot c_{n,s} = \sum_{l=1}^{N_s} c_{n,l} \cdot A_{l,\lambda}. \tag{5.35}$$

Both the molar absorption $\mathrm{A}_{s,\lambda}$ and the partial molar absorption $\mathrm{A}_{l,\lambda}$ are given in units of $\mathrm{m}^3\ \mathrm{mol}^{-1}$. In combining Equation (5.4) and (5.34), $\mathrm{A}_{l,\lambda}$ is given by

$$A_{l,\lambda} = \frac{M_{w,l}}{\rho_l} \kappa_{l,\lambda}. \tag{5.36}$$

In assuming that the partial molar absorptions of aqueous electrolytes are equal to those of the corresponding solid electrolytes, $\kappa_{l,\lambda}$ corresponds to the imaginary part of the refractive index of water and the electrolytes, respectively. For the sea salt and its constituents that are considered in this study, the partial molar absorptions take the form

$$A_{H_2O,\lambda} = \frac{M_{w,H_2O}}{\rho_{H_2O}} \cdot \kappa_{H_2O,\lambda} \tag{5.37}$$

$$A_{NaCl,\lambda} = \frac{M_{w,NaCl}}{\rho_{NaCl}} \cdot \kappa_{NaCl,\lambda} \tag{5.38}$$

$$A_{Na_2SO_4,\lambda} = \frac{M_{w,Na_2SO_4}}{\rho_{Na_2SO_4}} \cdot \kappa_{Na_2SO_4,\lambda}. \tag{5.39}$$

The product of the sea salt aerosol molar absorption and its total mole concentration

$$A_{mix,\lambda} \cdot c_{n,mix} = c_{n,H_20} \cdot A_{H_2O,\lambda} + c_{n,NaCl} \cdot A_{NaCl,\lambda} + c_{n,Na_2SO_4} \cdot A_{Na_2SO_4,\lambda} \tag{5.40}$$

together with the aerosol volume give the imaginary index as

$$\kappa_{mix,\lambda} = \frac{A_{mix,\lambda} \cdot c_{n,mix}}{V_{mix}}. \tag{5.41}$$

5.2 Mie Calculations for the Sea Salt Aerosol

The Mie calculations are based on a pre-simulated sea salt aerosol distribution and its corresponding chemical composition for a chosen part of the model domain. A smaller area in the Southwestern Mediterranean is chosen for the purpose of minimising the computational costs of these calculations. This area was chosen to represent the sea salt aerosol composition since the aerosol composition in this region is rather variable. The area comprises gridcells of both coastal and open sea characteristics with corresponding high and low concentrations. The area comprises Southeastern Spain, the western Mediterranean Sea and parts of the Northwestern Coast of Africa. The pre-

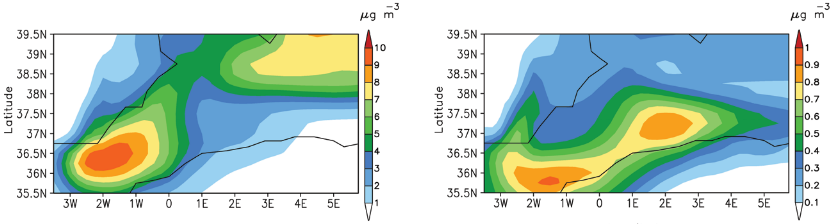

(a) NaCl. (b) SO_4^{2-}.

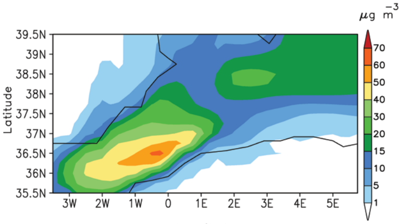

(c) H_2O.

Figure 5.1.: Pre-simulated mass densities of the respective chemical components of the film mode for the lowest approx. 40 m.

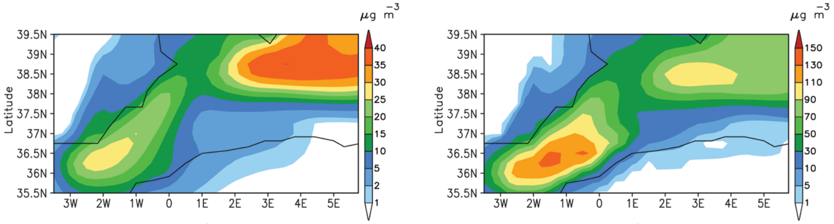

(a) NaCl. (b) H_2O.

Figure 5.2.: Pre-simulated mass densities of the jet mode for the lowest approx. 40 m.

simulated mass densities of NaCl, sulphate, and liquid water content for the film mode are shown in Figure 5.1. The NaCl and water contents for the jet and spume mode are shown in Figure 5.2 and 5.3, respectively. For these latter two modes, the maximum sulphate contents were less than $5{\cdot}10^{-2}$ and $7{\cdot}10^{-4}$ μg m^{-3}, respectively, in all grid cells and are, therefore, not shown.

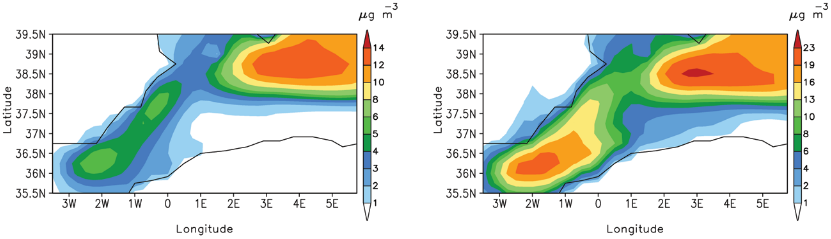

(a) NaCl.

(b) H_2O.

Figure 5.3.: Pre-simulated mass densities of the spume mode for the lowest approx. 40 m.

Hence, the aerosol sulphate is mainly found in the film mode due to the more efficient condensation onto these particles. All of the modes are composed by high fractions of liquid water, compared to the other two components. The total mass densities are about 70, 160 and 35 μg m^{-3} for the film, jet and spume mode, respectively. The simulated aerosol size distributions and chemical composition will be further discussed in chapter 6.

Mie calculations are carried through for each grid cell and 134 wavelengths between 250 nm and 30 μm. In the solar range, calculations are carried out for 101 wavelengths between 0.25 and 4 μm and in the thermal range for 33 wavelengths between 4 and 30 μm. A lack of refractive index data in the longwave range restricts the calculations to 30 μm.

In addition to the aerosol size and composition, the refractive index data is necessary. The real and imaginary parts of the refractive index are input for the Mie calculations as a function of wavelength in Figure 5.4 for the three components; sodium chloride, water and sodium sulphate. The real and imaginary parts of the refractive index of water are achieved from Segelstein (1981) as a function of wavelength. For the refractive index of NaCl, the values of bulk NaCl from Eldridge and Palik (1985) as a function of wavelength are utilised. The refractive index of sodium sulphate is however difficult to find as function of wavelength in the literature. For the solar range, the real part of the refractive index of sodium sulphate was assumed to be the same as the value at 589 nm (Mark Z. Jacobson, 2009, personal communication). In the atmosphere, solid sodium sulphate crystallises into anhydrous sodium sulphate, rather than forming the decahydrate $Na_2SO_4 \cdot 10H_20$ (Tang, 1997). The real part of the refractive index of anhydrous sodium sulphate has three components η_x=1.4669, η_y=1.4730, and η_z=1.4809 (Shannon et al., 2002). The values indicate the optical constants for different crystal axes. The mean refractive index is achieved by taking the average value of the three components. This method has been shown to be accurate for other types of crystals, such as dust particles (e.g., Mogili et al., 2007). For the thermal spectra, the wavelength dependent values of ammonium sulphate of Toon et al. (1976) are applied as a surrogate to sodium sulphate (Mark Z. Jacobson, 2009, personal communication). The absorption, i.e. the imaginary part of the refractive index of sodium sulphate, is assumed to be of minor importance in the solar range, and is set to a value of 10^{-7} and in the thermal range the data of ammonium sulphate from Toon et al. (1976) is applied (Mark Z. Jacobson, 2009, personal communication).

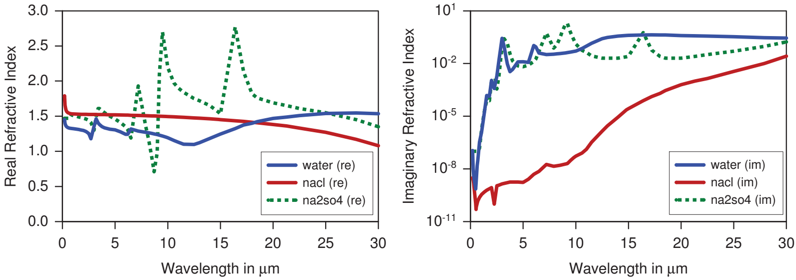

Figure 5.4.: Real (left) and imaginary (right) parts of the refractive indices as a function of wavelength.

The real part of the refractive index of NaCl remains constant around 1.5 in the solar range and decreases slowly with increasing wavelength in the thermal range to 1.1 at 30 μm. The real part of the refractive index of NaCl is the largest, compared to that of the other components, within the solar range. The real part of the refractive index of ammonium sulphate, which is applied as a surrogate for the sodium sulphate in the thermal range fluctuates between values of approx. 0.6 and 2.7 for wavelengths up to 20 μm and then decreases. The real part of the refractive index of water is the largest in the thermal range. It becomes larger than that of NaCl at 18 μm with a value of almost 1.5. For wavelengths greater than 25 μm the real part of the refractive index of water is the largest compared to the other components, with values slightly larger than 1.5.

For all three components, the imaginary part of the refractive index increases within the thermal range, indicating a more effective absorption in this range. The imaginary part of the refractive index of NaCl is very low in the whole spectral range, which is due to the ineffective absorption of NaCl. The imaginary part of the water refractive index increases within the thermal range and shows a maximum around 15 μm with a value of about 0.4. The imaginary part of the refractive index of sodium sulphate, which in the thermal range is treated by the values of ammonium sulphate as a surrogate, fluctuates up to values of 1.9 at 9.2 μm. Another local maximum is found at 16.4 μm with a value of 0.6. Except for this maximum in the ammonium sulphate imaginary part of the refractive index, the imaginary part of the water refraction index is the dominant one throughout the thermal range for wavelengths greater than 10 μm. This means that water contributes to the largest absorption of the three components within the thermal range.

5.2.1. The Extinction Coefficient

The extinction coefficient b is the sum of the absorption coefficient b_a and the scattering coefficient b_s, and describes the relative contribution of scattering and absorption to the total extinction in units of inverse length

$$b = b_a + b_s. \tag{5.42}$$

The specific extinction coefficient b$_i$ is determined for each mode and wavelength λ from the extinction efficiency Q_e, which is obtained from the Mie calculations on the form

$$b_i = \int_0^\infty \frac{\pi}{4} D_p^2 \, n_i \left(D_p\right) \; Q_e(D_p, \widetilde{m_i}, \lambda) \, dD_p \tag{5.43}$$

where $\widetilde{m}_i$ is the complex index of the refraction of the aerosol in mode i. By multiplying the extinction coefficient at each wavelength with the available solar energy and dividing the product with the total available energy within each spectral interval the extinction coefficient for each of the eight spectral bands are obtained. The volume extinction coefficients $b_{k_b,i}$ are achieved in km^{-1} from the Mie calculations. With the purpose to consider the variability in the chemical composition of the sea salt aerosol, the Mie calculations are performed with pre-simulated aerosol distribution fields over the Southwestern Mediterranean as input. The results are shown in Figures (A.1)-(A.8) for each of the 500 grid cells, for all of the eight spectral bands and for each aerosol mode, respectively. The relation between the extinction coefficient and the total wet aerosol mass of each mode shows a linear relation in the form

$$b_{k_b,i} = m_i \cdot \widetilde{b}_{k_b,i} \cdot 10^{-6} \tag{5.44}$$

where the volume extinction coefficient form is given in m^{-1}, the specific extinction coefficient $\widetilde{b}_{k_b,i}$ in m^2 g^{-1}, and the wet mass density m_i is expressed in μg m^{-3}. By applying linear fits, the specific extinction coefficients $\widetilde{b}_{k_b,i}$ are obtained as the slope of the curve. The values are summarised in Table (5.1). Thus, for any arbitrary sea salt aerosol distribution with wet mass m$_i$ the extinction coefficient is obtained for the eight spectral intervals by applying Equation (5.44) and the values of the specific extinction coefficient from the Table (5.1). The total volume extinction coefficient for the whole aerosol distribution is subsequently achieved as the sum of the extinction coefficient for each mode

$$b_{k_b} = \sum_{i=1}^{3} b_{k_b,i}. \tag{5.45}$$

Table 5.1.: Specific extinction coefficients in m^2 g^{-1} derived from Mie calculations for wet internally mixed sea salt aerosol for each mode spectral band k_b.

	k_b (Wavelength range in μm)							
	1 (1.53-4.64)	2 (0.7-1.53)	3 (0.25-0.7)	4 (20.0-104.5)	5 (12.5-20.0)	6 (8.33-9.01, 10.31-12.5)	7 (9.01-10.31)	8 (4.64-8.33)
$\widetilde{b}_{k_b,1}$	0.9813	2.1867	2.6986	0.1401	0.2489	0.1000	0.0689	0.1202
$\widetilde{b}_{k_b,2}$	0.3520	0.3232	0.3003	0.1698	0.1940	0.1655	0.1741	0.2704
$\widetilde{b}_{k_b,3}$	0.1032	0.0988	0.0969	0.1099	0.1035	0.0766	0.1241	0.1219

In the solar spectrum (k$_b$=1-3), the mass specific extinction coefficient is dominated by the film aerosol mode, and the spume mode contributes least to the extinction. Moreover, in the thermal spectrum (k$_b$=4-8) the spume mode extinction is least important, whereas the relative importance of the jet mode compared to the film and spume mode increases. Thus, with the exception of the spume mode, the extinction is the most important in the solar range. Even though the mass fraction of sea salt in the sub-micrometer range is low, compared to the other modes, these aerosols can contribute significantly to radiative extinction due to higher mass extinction coefficients.

Although some deviations from the linear curves occur, correlation coefficients exceed 0.98 for all the bands and sea salt modes. The deviations around the linear fits are explained by variations in number density, chemical composition and aerosol size. These properties determine the extinction coefficients and cause the scatter of the calculated values. The divergence towards higher values of some of the extinction coefficient values of the spume mode is explained by higher number densities compared to those points closer to the linear curve. The spreading in other ranges and for the other two modes cannot be explained by variations in the number density only. No correlation with changes in a single aerosol property is found. Thus, these deviations are rather caused by shifts in several of the aerosol properties at the same time. To which extent the extinction is determined by scattering or absorption will be discussed in connection with the single scattering albedo in the next section.

It can only be speculated as to how any participation in cloud droplet formation could influence the extinction coefficient. By forming cloud condensation nuclei (CCN), the mass and number densities of the sea salt aerosol modes would decrease. Thus, the total extinction of the sea salt aerosol itself would decrease. The linear behaviour between the extinction and mass density is however still assumed to hold for situations with lower mass densities, due to e.g., CCN formation.

5.2.2. The Single Scattering Albedo

The relative importance of scattering versus absorption is represented by the single scattering albedo

$$\omega = \frac{b_s}{b} = \frac{b_s}{b_a + b_s}. \tag{5.46}$$

For a purely absorbing medium is ω zero and approaches one as scattering becomes important. The single scattering albedo is obtained from the scattering and extinction coefficients, which are obtained from the Mie calculations.

Letting $\widetilde{\omega}_{k_b,i}$ denote the single scattering albedo of each mode i for the band k_b, the total single scattering albedo ω_{k_b} for all the aerosol modes is achieved by weighting $\widetilde{\omega}_{k_b,i}$ with the extinction coefficient

$$\omega_{k_b} = \frac{1}{b_{k_b}} \sum_{i=1}^{3} \widetilde{\omega}_{k_b,i} \cdot b_{k_b,i}. \tag{5.47}$$

$\widetilde{\omega}_{k_b,i}$ is, as already mentioned, calculated as a function of the extinction coefficient and absorption coefficient (Equation 5.46) in the Mie code.

The single scattering albedo for each aerosol mode and spectral interval is shown in Figures (A.9)-(A.16). The single scattering albedo of each mode remains approximately constant within each spectral band. Due to the generally constant values of each mode and band, the single scattering albedo is treated simplified by choosing the respective mean values. The values of the single scattering albedo for each mode and band are presented in Table 5.2.

The absorption of sea salt is negligible in the solar range. For these three bands, mass independent constants are good approximations for the single scattering albedo for each of the three modes. Standard deviations from the average values are less than 10^{-5} for all the modes in the third band, due to

Table 5.2.: Single scattering albedo derived from Mie calculations for wet internally mixed sea salt aerosol for each mode and spectral band k_b.

	k_b (Wavelength range in μm)							
	1 (1.53-4.64)	2 (0.7-1.53)	3 (0.25-0.7)	4 (20.0-104.5)	5 (12.5-20.0)	6 (8.33-9.01, 10.31-12.5)	7 (9.01-10.31)	8 (4.64-8.33)
$\widetilde{\omega}_{k_b,1}$	0.9294	0.9999	1.0000	0.0174	0.0243	0.1193	0.1672	0.4276
$\widetilde{\omega}_{k_b,2}$	0.9398	0.9996	1.0000	0.3058	0.2798	0.5479	0.7044	0.7959
$\widetilde{\omega}_{k_b,3}$	0.9111	0.9988	1.0000	0.4421	0.4204	0.6208	0.7290	0.7345

very low absorption of all of the three chemical components. The scattering is completely dominant in the second and third spectral bands due to inefficient absorption in these ranges. In the first spectral band, absorptions due to water and sulphate become more important, and act to decrease the single scattering albedo from unity. Absorption due to NaCl is however still very low and does not contribute to the absorption. The relative importance of absorption to the total extinction increases with increasing wavelength, i.e. the single scattering albedo decreases. Constant mean values have been chosen to represent the single scattering albedo, including for the thermal range. This approach is applied although deviations from the mean values occur to a larger extent in this part of the spectrum compared to the solar range. The single scattering albedo is thus treated as mass independent in all the spectral ranges, which is a simplification. The reason for the differences in the single scattering albedo between different grid points and total wet mass densities is discussed in the following. Moving from the solar spectrum to the first thermal range (k_b=8), the relative importance of absorption to the total extinction increases. For the spectral intervals 6, 7, and 8 ($4.64<\lambda<12.5$ μm), absorption of sulphate and water takes place, whereas NaCl is non-absorbing. The absorption is stronger in the film mode than in the jet and spume modes.

This can for example be a result of higher relative contribution of sulphate to the total wet mass in the film mode. In the presence of both sulphate and water, two strong absorbing components are available.

Low mass densities are mainly the result of less water content, and the relative contributions of the other two components become more important. Such aerosols are found along coasts or over land as a result of lower relative humidity than above water. The sulphate content is of least importance for the spume mode, in turn leading to the increased significance of the NaCl in this mode. Thus, an increased single scattering albedo is found at low mass densities due to the relatively higher importance of the NaCl component that does not contribute to any absorption. This is especially seen within bands 7 and 8, and a small increase is also seen in band 6. For the latter band, the imaginary part of NaCl is however larger than in bands 7 and 8, which causes less reduction, i.e., less divergence from the mean value, of the aerosol absorption in this mode at low mass densities.

For the jet mode, some grid points are more influenced by the NaCl content and some by the sulphate content. Although the mass of NaCl naturally is much larger than that of sulphate, the contribution of sulphate to the optical properties is still seen. This is a result of the much greater absorption quality of this component, i.e. the imaginary part of the refractive index of sulphate is much greater than that of NaCl. Due to the effects of both of these components, two tails in opposite directions are found at low mass densities of the jet mode. This is especially observed within bands 6 and 7. One tail is directed towards slightly higher single scattering albedo, and another in the other direction. These are the results of NaCl and sulphate for the case of low water amounts, respectively. As the relative sulphate contribution to the total mass decreases, the effect of NaCl increases. This leads to differences in absorption and also in the single scattering albedo. For the case where water is the dominant component, the values between the two diverging tails, close to the mean value, are obtained. The fact that the absorption increases with sulphate content is a result of the peak in the imaginary part of the refractive index in this range.

Moving on to greater wavelengths, bands 4 and 5 ($12.5 < \lambda < 30$ μm), the extinction due to absorption in turn increases at low mass densities for all modes. This is most clearly seen for the larger aerosol sizes, but also the film mode single scattering albedo shows positive correlation with the mass density. This dependency is weak, however. In the 4th and 5th bands, the deviations from the mean values are lower due to the fact that the imaginary parts of the refractive indices approach each other. The absorption due to NaCl increases and the differences between the imaginary part of the refractive index of NaCl and that of the other components decrease. The mean single scattering albedo increases due to the strong absorption of sulphate and water, and due to slightly increased absorption caused by NaCl. For aerosol compositions where both water content and relative sulphate content are low, the tail towards higher single scattering albedo is no longer visible and absorption remains about the same for the whole sub domain compared to the earlier cases. The fact of increased absorption when the relative sulphate content is the highest remains at low mass densities.

The behaviour of increased absorption at low total mass densities occurs at conditions of low relative humidity, which causes low water content. By taking this behaviour into account, the absorption would be overestimated in humid environments, e.g. over the ocean, for the case of low mass densities, e.g. low wind speeds. On the other hand, by applying constant mass-independent values, the absorption in coastal areas may be underestimated. It is assumed here that the potential error of the underestimating of the absorption in coastal areas is smaller than that due to the overestimation of absorption over the ocean. For this reason, constant values will be applied in this thesis. These calculated single scattering albedos are also assumed to hold for situations where sea salt takes part in CCN formation. This assumption is based on the approximately constant behaviour for each mode and spectral band for higher mass densities.

5.2.3. The Asymmetry Parameter

The asymmetry factor describes the relative proportion of forward versus backward scattering and is an approach to describe the deviations from isotropic scattering, i.e. scattering that is equally likely to occur in both hemispheres. The asymmetry factor is defined as

$$g \equiv \frac{1}{4\pi} \int_{4\pi} p\left(\cos\Theta\right) \cos\Theta \, dw \tag{5.48}$$

where $p\left(\cos\Theta\right)$ is the phase function and Θ is the scattering angle between the scattered radiation relative to the incident direction. g is the average value of the phase function and varies between values of -1 and 1. For positive values, the photons are mainly scattered in the forward hemisphere and for negative values scattering in the backward hemisphere is indicated. For isotropic scattering, which is the case for e.g., Rayleigh scattering, g=0. For Mie scattering forward scattering becomes more important and g approaches 1 as the particle size increases. For particles, the phase function can not be described exactly by a closed-form mathematical expression and is often represented by Legendre polynomials $P_l(\cos\Theta)$

$$p\left(cos\Theta\right) \approx \sum_{l=0}^{N-1} \chi_l P_l\left(\cos\Theta\right) \tag{5.49}$$

where N is the number of terms and χ_l is the lth expansion coefficient given by

$$\chi_l = \frac{2n+1}{2} \int_{-1}^{1} p\left(cos\Theta\right) P_l\left(\cos\Theta\right) d\cos\Theta. \tag{5.50}$$

The first expansion coefficient χ_0=1 and the second coefficient is proportional to the asymmetry parameter g (Petty, 2006)

$$g = \frac{\chi_1}{3}. \tag{5.51}$$

The moments of the phase function result from the Mie calculations and the asymmetry parameter $\widetilde{g}_{k_b,i}$ is consequently obtained from the first moment of the phase function for each spectral band, aerosol mode and grid cell of the model domain. The calculated asymmetry parameter for each spectral interval and aerosol mode is shown in Figures (A.17)-(A.24).

The asymmetry parameter g_{k_b} for the whole aerosol distribution, including all three modes, is for each spectral band given by

$$g_{k_b} = \frac{1}{b_{s,k_b}} \sum_{i=1}^{3} \widetilde{g}_{k_b,i} \cdot b_{s,k_b,i} \tag{5.52}$$

where b_{s,k_b} and $b_{s,k_b,i}$ are the total scattering coefficient and the scattering coefficient for the mode i for each band k_b, respectively.

The asymmetry parameter is treated by the same approach as the single scattering albedo, using mean values. The mean values of the asymmetry parameter for each mode and interval are summarised in Table 5.3. The mean values and corresponding deviations are discussed in the following.

The positive values of the asymmetry parameters for all modes and bands indicate forward scattering. Constant values represent the asymmetry parameters well within the solar range, with only small deviations from the mean values. The asymmetry parameter varies with e.g., particle size, wavelength and single scattering albedo (Andrews et al., 2006). Andrews et al. (2006) found increased forward scattering for increased size and increased single scattering albedo, and g decreased with increasing wavelength. The median diameter of each mode is obtained from the total number and mass

Table 5.3.: Asymmetry parameters derived from Mie calculations for wet internally mixed sea salt aerosol for each mode and spectral band k_b.

	k_b (Wavelength range in μm)							
	1 (1.53-4.64)	2 (0.7-1.53)	3 (0.25-0.7)	4 (20.0-104.5)	5 (12.5-20.0)	6 (8.33-9.01, 10.31-12.5)	7 (9.01-10.31)	8 (4.64-8.33)
$\widetilde{g}_{k_b,1}$	0.6966	0.7653	0.7701	0.1040	0.1640	0.2719	0.2940	0.3887
$\widetilde{g}_{k_b,2}$	0.8017	0.7917	0.8155	0.5503	0.6737	0.7927	0.8000	0.7999
$\widetilde{g}_{k_b,3}$	0.8372	0.8357	0.8467	0.7750	0.8527	0.8896	0.8802	0.8517

densities of each mode (Equation 3.6). The deviations from the mean values are thus explained by e.g., altered particle sizes and compositions, which in turn affect the single scattering albedo. In the solar region (k_b= 1-3), larger scattering of the film mode asymmetry parameter values occurs, compared to the other modes. This implies larger variations in the mode diameter at different locations than in the other modes. The asymmetry parameter increases with larger diameters. The asymmetry parameter is, therefore, largest in the spume mode. As the particle size increases, so does the scattering in the forward direction. The average value of g for each mode decreases for longer wavelengths. From band 3 to band 1 changes from 0.77 to 0.70, from 0.82 to 0.80, and from 0.85 to 0.84 are found for the film, jet, and spume mode, respectively. Within the solar range, the asymmetry parameter ranges from 0.79 to 0.8 for the film mode. The values of the asymmetry parameters for the spectral intervals in the solar regime can be compared to those of Winter and Chýlek (1997). Values ranging between 0.75 and 0.85 were reported by Winter and Chýlek (1997) for the solar range. Thus, the calculated asymmetry parameters are in the same order of magnitude as reported in this study.

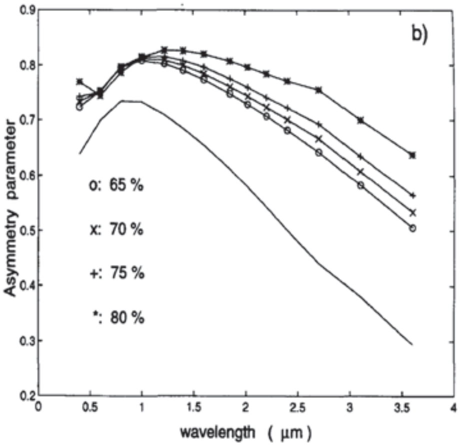

Figure 5.5.: Asymmetry parameter in the solar range from Winter and Chýlek (1997).

In moving to greater wavelengths (k_b=8), the asymmetry parameter decreases further for the two smallest modes, whereas the spume mode asymmetry parameter increases slightly. The film mode asymmetry parameter decreased from 0.70 to 0.40. Here, a close link to the decrease is seen in the corresponding single scattering albedo from 0.93 in band 1 to 0.43 in band 8. Hence, a strong decrease in the film mode asymmetry parameter is obtained at the same time that the single scattering albedo strongly decreases.

The simplifications of representing the asymmetry parameter by constant values are good approximations for the jet and spume modes for the 6th, 7th, and 8th bands. The film mode, however, slightly increases with increasing mass. This increase is very weak and is assumed to be of minor importance for the radiative effects in this range. In the 4th and 5th bands, the asymmetry parameter of each mode follows the dependency of the corresponding single scattering albedo on the total wet mass density. For the jet and spume modes, both parameters decrease at low mass densities. The film mode asymmetry and single scattering albedo slightly increase with larger mass densities. It is assumed that this weak increase is of minor importance. For the jet and spume modes, the decreased asymmetry parameters follow the strong decrease in single scattering albedo. The single scattering albedo decreases due to changes in composition at locations with a low relative contribution by water content. These results are, as already discussed in the previous section, represented by coastal locations with low relative humidities. This effect is not well represented for applications over water in situations where the mass density due to e.g., wind speeds is low. In that case, the forward scattering would be underestimated. Higher wet mass densities are, moreover, more realistic in most marine conditions and are, therefore, of the most interest for e.g., climate modelling. Based on these statements, the mean values are applied and the spread and deviations at low mass densities are neglected. It is moreover also assumed that the asymmetry parameter would remain constant in situations where sea salt takes part in CCN formation. CCN formation is however not investigated in this thesis.

Chapter 6

3-D Simulation with the Extended Model System COSMO-ART

3-Dimensional simulations are performed with the extended model system COSMO-ART for the 24th-26th July 2007. The model domain was chosen as shown in Figure 5.2.3, including large parts of the Mediterranean, South and Central Europe, and the Northeast Atlantic Ocean. The model setup and an overview of the performed simulations are presented in section 6.1.

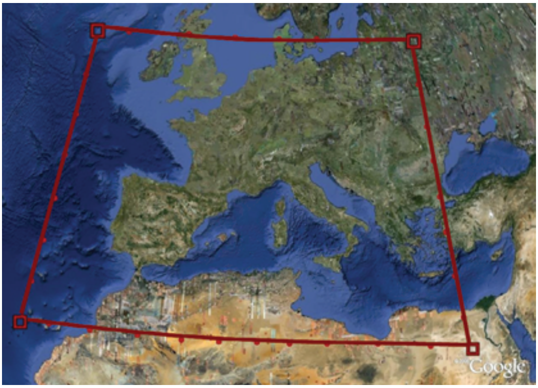

Figure 6.1.: Model domain with the lower left corner at (-19°E, 26°N) and the upper right corner at (30°E, 54°N).

The weather situation for the considered period and area is summarised in section 6.2. Thereafter, the treatment of gaseous species emissions and the emissions of gaseous precursors are described (section 6.3), followed by the 3-D simulation results in section 6.4.

6.1 Simulation Setup

The set-up of the model in terms of spatial and temporal resolutions, time integration scheme, and initial and boundary conditions is summarised in Table 6.1. The model settings in Table 6.1 are applied for all the performed simulations.

Table 6.1.: Simulation set-up.

Time step: Δt	40 s
Horizontal resolution: Δx, Δy	0.25° (≈28 km)
Vertical resolution	40 layers, max.≈20 km
Time integration scheme	Leapfrog
Initial and boundary conditions:	
Meteorological	IFS analyses (IFS, 2003)
Aerosol and gaseous	prescribed clean air conditions

An overview of the individual simulations is provided in Table 6.2. In the reference run (R), the condensation of sulphuric acid onto the aerosol and water uptake as function of ambient RH are considered. In this run, sulphuric acid is produced through the oxidation processes of precursors from anthropogenic as well as DMS emissions and no interaction with radiation takes place. To investigate the change in the aerosol size distribution due to water uptake, run D is performed where the sea salt aerosol is assumed to consist of pure NaCl. In run W_{ant} wet internally mixed aerosol is simulated, whereas the production of sulphuric acid, which goes into condensational processes, is a product of anthropogenic emissions only and the DMS emission is neglected. In run W_{dms} the production of sulphuric acid and the subsequent formation of aerosol sulphate are, on the other hand, results from DMS emissions only. In this simulation, the anthropogenic SO_2 is neglected. Finally, in simulations F, F_{ant}, and F_{all} the direct aerosol radiative effects and their feedback on the state of the atmosphere are considered. In F, the interaction between wet internally mixed sea salt aerosol and radiation is accounted for. F_{ant} represents the simulation where anthropogenic aerosol interacts with the state of the atmosphere through the DRE. In run F_{all} both sea salt and anthropogenic aerosol direct radiative effects are considered. The results and differences between these runs are presented and discussed in section 6.4.

Table 6.2.: Overview of the simulations with the extended model system COSMO-ART. Anthropogenic aerosols are treated according to Vogel et al. (2009).

Run	Composition	SSA sulphate source	DRE
R	NaCl+water+sulphate	DMS and Anthropogenic	no
D	NaCl	-	no
W_{ant}	NaCl+water+sulphate	Anthropogenic	no
W_{dms}	NaCl+water+sulphate	DMS	no
F	NaCl+water+sulphate	DMS and Anthropogenic	yes (ssa)
F_{ant}	NaCl+water+sulphate	DMS and Anthropogenic	yes (ant)
F_{all}	NaCl+water+sulphate	DMS and Anthropogenic	yes (ssa+ant)

As the contribution of sea salt to cloud droplet formation is neglected in all the simulations, the simulated aerosol burdens in these simulations represent an upper limit for cloudy areas. The focus is not put on the comparison of simulated sea salt size distributions with measurements, but rather on process studies. The relative impacts of different processes, such as the water uptake and the direct radiative effect, on the size distribution are investigated and presented within this chapter.

6.2 Synoptic Situation During 24th-26th July 2007

In the following, an overview of the weather situation during the simulation period is given. The synoptic situations for the 24th-26th July 2007 at 12 UTC are shown in Figure 6.2(a)-6.2(c). The satellite observed cloud cover at noon for the three respective days is illustrated in Figure 6.3. In Figure 6.4, the simulated wind fields at 10 m above ground are presented. On the 23rd July, an upper-level trough stretched from Great Britain southwards to Spain. A surface low level pressure system was situated near the trough and moved, together with the upper-level trough, towards the northeast. The centre of the surface low level pressure system was found above Denmark at noon on the 24th (Figure 6.2(a)). Temperatures at 2 m above ground reached a maximum of 40°C over North Africa, South Italy and Greece on the 24th. Over South Spain, large parts of the Mediterranean Sea and South Italy from 30 to 35°C. Over central Europe around 20°C, with minimum temperatures in the Alps of approx. 10-15°C. A high pressure ridge over the Northeast Atlantic became more pronounced and approached France on the evening of the 24th and made its way over France, Germany and South Scandinavia during the 25th (Figure 6.2(b)). Southwest to westerly flow was dominating, with stable and warm conditions in the simulation area. During the night of the 24th temperatures as low as 5°C were observed in Northern Spain, Southeast France, and in the Alps. Over central Europe 10-15°C occurred and mainly about 25°C over the Mediterranean and North Africa at night. At noon on the 25th the temperatures at 2 m increased up to 40-45°C above North Africa and the Greek peninsula. 35°C occurred in the south western parts of Spain and in the rest of the model domain temperatures ranged from 15-20°C over the Atlantic Ocean and central Europe, and 25-30°C over the Mediterranean Sea. During the night, the temperatures decreased locally to between 5 and 10°C in Northern Spain, parts of South France, the Alps, Romania, and Montenegro. About 15°C occurred over the British Isles and in the remaining of the domain temperatures in general range from 20-25°C.

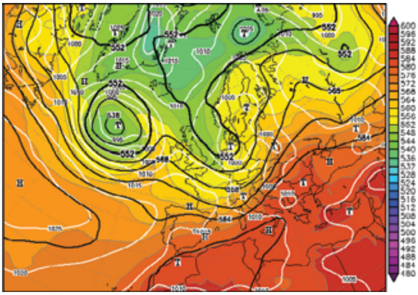

(a) 24th July 2007, 12 UTC.

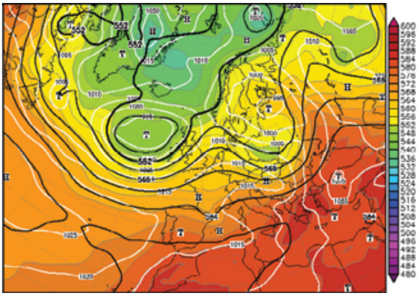

(b) 25th July 2007, 12 UTC.

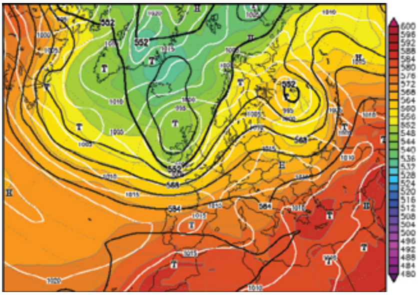

(c) 26th July 2007, 12 UTC.

Figure 6.2.: Synoptic situation represented by 500 hPa geopotential in gpdm (black contours), surface pressure in hPa (white contours), and relative topography in gpdm (colours). Copyright www.wetter3.de.

In the wake of the high pressure ridge, another trough approached from the west, leading to an increased south westerly flow over France and Germany on the 26th (Figure 6.2(c)). The temperature field at 2 m on the 26th was similar to that on the 25th. Minimum temperatures of 15°C were observed in the northeast of the model domain, i.e. over Ireland and Great Britain, and above the Atlantic Ocean. 25-30°C were observed over Central and South Europe and maximum temperatures of 40°C occurred over North Africa.

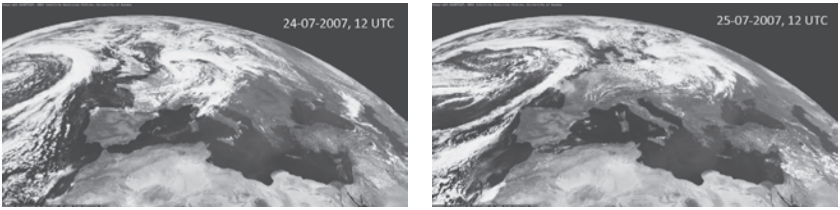

(a) 24th July 2007, 12 UTC. (b) 25th July 2007, 12 UTC.

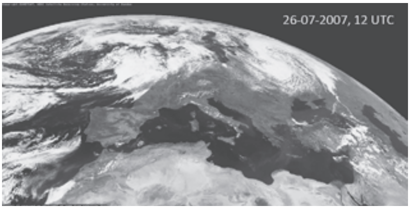

(c) 26th July 2007, 12 UTC.

Figure 6.3.: Cloud cover. Copyright EUMETSAT, NERC Satellite Receiving Station, University of Dundee.

Over the Mediterranean Sea, cloud free conditions dominated throughout the three days, 24th-26th July (Figure 6.3). On the contrary cloudy conditions dominated over the European continent for all three days, connected to the low level pressure systems passing by in the northeast direction.

On the 24th July, 12 UTC, the wind direction 10 m above ground (Figure 6.4(a)) was westerly over the Atlantic Ocean off the coast of France and over England. Southwards, the wind direction turned to the north off the Portuguese coast. The wind velocity in these regions ranged up to ≈ 7.5 m s^{-1}. Closer to the low level pressure system above the North Atlantic, the wind speed increased to approx. 15 m s^{-1}. Over central Europe and the Mediter-

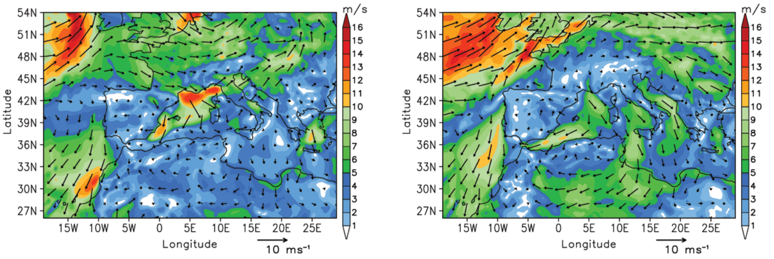

(a) 24th July 2007, 12 UTC.

(b) 25th July 2007, 12 UTC.

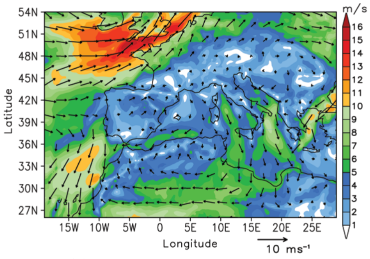

(c) 26th July 2007, 12 UTC.

Figure 6.4.: Simulated horizontal wind speed at 10 m with arrows indicating wind direction.

ranean Basin the wind speed was generally on the order of 5-7.5 m s^{-1}, 10 m above ground, with a maximum of 12 m s^{-1} west of Corsica, south of mainland France. This wind maximum decreased to approximately 7.5 m s^{-1} on the 25th, 12 UTC (Figure 6.4(b)). Over the Mediterranean Sea the wind velocity at 10 m ranged up to about 12 m s^{-1} south of Sicily. In addition, over the European continent, wind velocities up to 12 m s^{-1} occurred, for instance over Poland and the Czech Republic. Over the Atlantic Ocean and adjacent coastal regions, except for Portugal, south westerly winds were observed with wind speeds up to 15 m s^{-1}. Near the Portuguese coast, wind speeds up to 10 m s^{-1} occurred with a wind direction north to northwest, due to a surface near low level pressure with its centre above Spain. As the low level pressure above the North Atlantic moved northeast and its centre was situated north of Ireland on the 26th, 12 UTC the wind speed above the Atlantic Ocean slightly decreased compared to the previous day (Figure 6.4(c)). In the model domain, the maximum wind speed now occurred off the French west coast ($\approx$15 m s^{-1}). Off the west coast of North Africa, northerly winds with up to 10 m s^{-1} were observed due to a low level pressure above North Africa. As for the 25th, the Mediterranean wind maximum was found between Italy and the North African Coast with velocities up to approximately 7.5 m s^{-1}. Thus, the weather situation during these three days does not represent any extreme weather conditions in the area. The synoptic conditions can rather be seen as typical for the summer months of this region. No major dust event over the Mediterranean was reported during this time period. Therefore, the aerosol impacts due to marine or anthropogenic aerosol are expected to be the most dominant for these days.

6.3 Gaseous and Anthropogenic Particulate Emissions

In this section the natural and anthropogenic gaseous emissions are treated. The mixing ratios of the emitted gases and of those formed trough subsequent reactions are presented in section 6.4. Here, the emission rate of oceanic DMS is first discussed. Thereafter the treatment of anthropogenic gaseous emissions and emissions of particulate matter are described.

6.3.1. Emissions of Dimethyl Sulphide (DMS)

As decribed in chapter 4, the emission of DMS in COSMO-ART is determined as a function of the prescribed DMS sea surface concentrations, based on measurements, and the gas transfer velocity. The latter is parameterised as a function of the 10 m wind speed. The sensitivity of the emission rate to the wind speed is illustrated in Figure 6.5 for an DMS sea water concentration of 5 nmol L^{-1}, which is representative for the Mediterranean in July. In this figure, the emission rate in units of μg m^{-2} s^{-1} is given to the left and the corresponding daily averaged emission rate in μmol m^{-2} d^{-1} is given to the right. The DMS emission flux increases rather rapidly with increasing wind speed. For a wind speed of 8 m s^{-1} in the Mediterranean region, the calculated DMS emission rate is 0.015 μg m^{-2} s^{-1}, which on daily average corresponds to an emission rate of approximately 21 μmol m^{-2} d^{-1}. This fits well with the daily averaged DMS emission flux of 19 μmol m^{-2} d^{-1} for the Eastern Mediterranean in July by Kouvarakis et al. (2002). The horizontal distribution of the simulated DMS emission flux is illustrated at 8 UTC for the 25th of July in Figure 6.6. Due to the strong wind dependence of the DMS emissions, the maximum DMS fluxes coincide with the areas of large

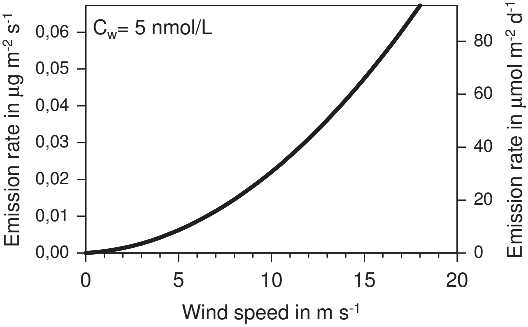

Figure 6.5.: DMS emission rate as a function of wind speed.

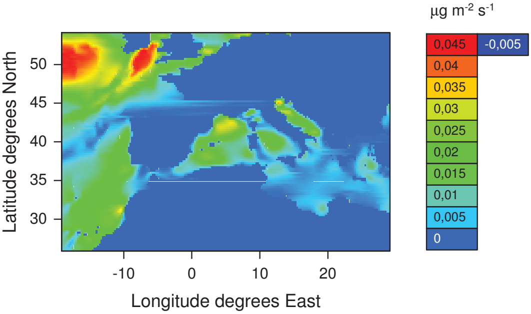

Figure 6.6.: Simulated DMS emission flux on 25th July, 8 UTC.

wind velocities. For this reason, the maximum DMS emission flux is mainly found above the Atlantic Ocean at this time. For the most windy areas, DMS emission rates up to 0.045 μg m^{-2} s^{-1} are simulated over the Atlantic Ocean. Regions with wind speeds on the order of less than 10 m s^{-1} correspond to emission rates up to 0.02 μg m^{-2} s^{-1}. This order of magnitude in DMS emission fluxes are seen for most of the domain, both over the Atlantic and the Mediterranean. Several studies provide estimates of the DMS emission rates from the sea surface to the atmosphere, whereas most are for the global scale. Some local estimates are however also available. These values are however presented as daily averaged values over longer time periods. Davison and Hewitt (1992) estimated the DMS emission rate from the sea to the atmosphere to be 0.93 μmol m^{-2} d^{-1} (approx. $6.7 \cdot 10^{-4}$ μg m^{-2} s^{-1}) for the Eastern Atlantic Ocean north of 45°N. Berresheim et al. (1991) accounted the Western North Atlantic Ocean DMS fluxes to range between 5-10 μmol m^{-2} d^{-1} (approx. 0.004-0.007 μg m^{-2} s^{-1}) in late summer and autumn. As mentioned hereinabove Kouvarakis et al. (2002) estimated the DMS flux from the Eastern Mediterranean to 19 μmol m^{-2} d^{-1} for the month of July. Thus, large variations are seen between different measurements. Compared to Kouvarakis et al. (2002) the simulated DMS emission fluxes are in reasonable order of magnitudes. The daily averaged emission rates of Berresheim et al. (1991) can be compared to the simulated emission rates in regions with wind speeds of about 5 m s^{-1} for 8 UTC on the 25th. For these regions, the emission fluxes were calculated to approx. 0.005 μg m^{-2} s^{-1}.

6.3.2. Anthropogenic Gaseous and Particulate Emissions

Anthropogenic gaseous and particulate emissions are achieved from the TNO/GEMS (Netherlands) emission data base. The pre-processing of the

TNO/GEMS data for COSMO-ART is described in Knote (2009) and here a brief overview is given. The TNO/GEMS data set contains the annual emission totals of CH_4, CO, NH_3, organic precursor gases (NMVOC), NO_x, SO_2, and particulate matter: PM_{10} and $PM_{2.5}$. An inventory of international shipping emissions containing emission totals of CO, NMVOC, NO_x, SO_x, PM_{10}, and $PM_{2.5}$ is additionally provided. The base year of the data set is 2003, whereas the shipping emissions are treated as a time invariant and no time interpolation is performed. The outputs of the pre-processor are hourly 3-D fields for each species in kg h^{-1} per grid cell, distributed at 6 height levels. For the simulations performed in this work, hourly emissions for the 25th of July are utilised for all three days of the simulation period. In this study, the gaseous emissions and emissions of $PM_{2.5}$ are considered. For the prevailing weather condition, emissions from the European continent and emissions from ships in the model domain are assumed to be of the most importance for the considered area and no emissions from Northern Africa are considered.

An example of the emissions is illustrated in Figure 6.7. The vertical totals of the emissions of ammonia (NH_3), sulphur dioxide (SO_2), nitrogen oxide (NO), nitrogen dioxide (NO_2), and $PM_{2.5}$ are depicted at 7 UTC.

Ammonia and $PM_{2.5}$ are important constituents of anthropogenic aerosol. The sea salt direct radiative effect will be compared to the effect of anthropogenic aerosol at the end of this chapter. The emissions of anthropogenic constituents are for this reason required. Furthermore, sea salt aerosol sulphate contents can be underestimated if anthropogenic SO_2 emissions are neglected, e.g. from ships. Major contributors to the gaseous and particulate matter of anthropogenic origin are cities and shipping routes. In the horizontal distribution of the emissions, except for that of NH_3, shipping routes over the Mediterranean, along the Portuguese coast, and up to the north in direction Great Britain are apparent. Large cities such as Paris,

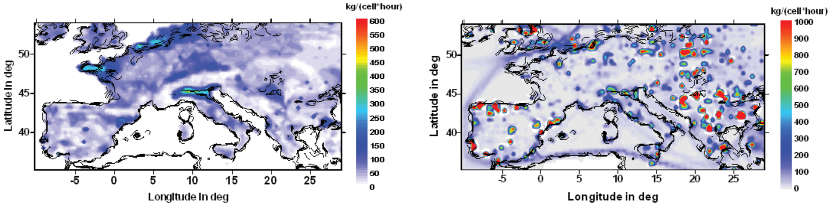

(a) NH_3. (b) SO_2.

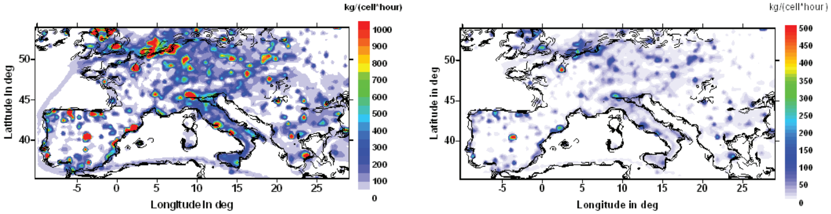

(c) NO. (d) NO_2.

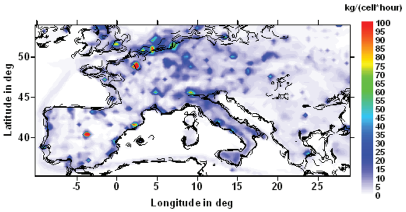

(e) $PM_{2.5}$.

Figure 6.7.: Vertical sum of the emissions at 7 UTC.

Madrid, Athens, etc. contribute the most to anthropogenic emissions for this region. The emissions of NH_3 are most significant in the Benelux, in North Western France, and in the Po Valley.

6.4 3-D Simulation Results

The following section deals with the results of the COSMO-ART simulations, which were presented in Table 6.2.

6.4.1. Distribution of Gaseous Species

DMS

The simulated DMS and DMSO surface near mixing ratios averaged over the three simulation days are illustrated in Figure 6.8 and 6.9, respectively. As described in the previous chapter, DMSO is an oxidation product of DMS. DMSO is seen to contribute to low mixing ratios in the atmosphere, in the order of some few ppt only. Average simulated DMS mixing ratios ranges between less than 1 ppt over land to up to 380 ppt for some locations over the Atlantic Ocean and Eastern Mediterranean. The distributions of DMS show large gradients. The DMS mixing ratio found by Andreae et al. (1985) from ship borne measurements was in the order of 50 ppt over the North Atlantic in continentally influenced air masses. Aircraft measurements performed over the western North Atlantic in August and September 1992 indicated DMS mixing rations ranging up to 332 ppt, with great horizontal and vertical gradients (Spicer et al., 1996). Thus, the simulated DMS mixing ratios are of reasonable order of magnitudes.

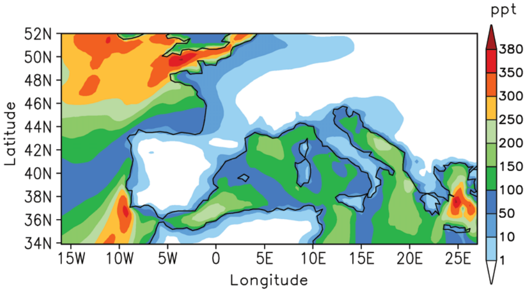

Figure 6.8.: Simulated DMS mixing ratio, averaged over three days.

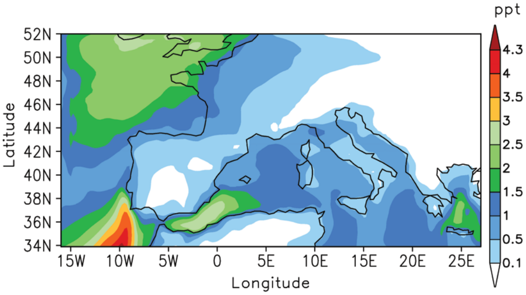

Figure 6.9.: Simulated DMSO mixing ratio, averaged over three days.

Nitrogen Oxide, Nitrogen Dioxide, and Ozone

Ozone, nitrogen oxide (NO), and nitrogen dioxide (NO_2) significantly contribute to the formations of hydroxyl (OH) and nitrate (NO_3) radicals. The simulated daily averaged horizontal distribution of NO_x ($NO+NO_2$) and ozone are illustrated in Figure 6.10. During the daytime, photolysis reactions split the ozone molecule into oxygen atoms ($O(^1D)$ and $O(^3P)$) and oxygen molecules. The $O(^1D)$ atoms in turn react with water and form OH radicals. Due to the necessary energy from the sun, the OH radical has its mixing ratio peak during the daytime. One important source for the nitrate radical is the reaction between ozone and nitrogen dioxide. This reaction is preferable at night, when no ozone destruction via photolysis reactions takes place. For this reason, nitrate mixing ratios are greater at night, in contrast to the hydroxyl radicals. The OH and NO_3 radicals play an important role for the oxidation of DMS. Furthermore, OH is crucial for the formation of sulphuric acid from sulphur dioxides. Examples of the horizontal distributions of OH and NO_3 are shown in Figure 6.11. OH is depicted on the 24th, 12 UTC, and NO_3 on the 25th, O UTC.

NO_x mixing ratios ranges up to 30 ppb. Maximum mixing ratios are found over the continent near large cities such as Madrid, Paris, and Milan. Over

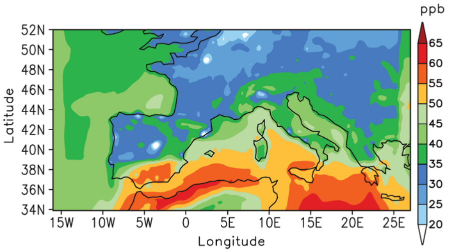

(a) O_3 distribution.

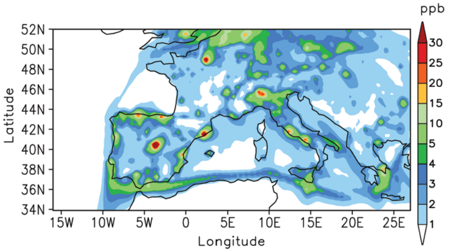

(b) NO_x ($NO+NO_2$) mixing ratios.

Figure 6.10.: Horizontal mixing ratios of O_3 and NO_x for the lowest approx. 40 m, averaged over three days.

water up to 10 ppb are found along the shipping routes. Maximum ozone mixing ratios are found over the ocean, especially over the Mediterranean Sea and the corresponding coastal areas. Up to about 65 ppb ozone is found in the South and East of the Mediterranean. Ozone mixing ratios may vary significantly. During their measurement campaign at Finokalia, Crete Island, in September 1997 Kouvarakis and Mihalopoulos (2002) measured O_3 mixing rations from 53 to 83 ppb. For this simulation period over three days averaged ozone mixing ratios around Crete Island were on the order of 50-55 ppb. Hence, the simulated ozone mixing ratios show a reasonable order of magnitude. OH mixing ratios lower than 1 ppt are simulated for the whole area, with large horizontal gradients. Simulated NO_3 mixing ratios range up to 0.8 ppb during the night. Both radicals show their lowest mixing ratios over land.

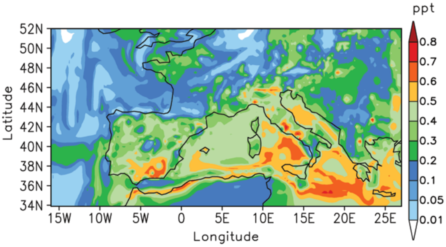

(a) OH on 24th July, 12 UTC.

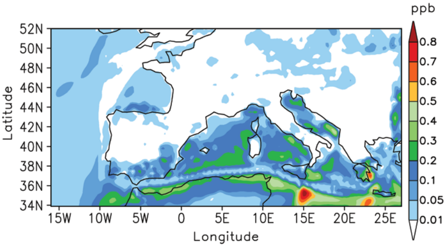

(b) NO_3 on 25th July, 0 UTC.

Figure 6.11.: Simulated mixing ratios of OH and NO_3 for the lowest approx. 40 m, averaged over three days.

Sulphur Dioxide (SO_2)

Sulphur dioxide is directly emitted from anthropogenic sources or formed from DMS and DMSO oxidation. The simulated SO_2 mixing ratios are illustrated in Figure 6.12 and 6.15. The simulated SO_2 mixing ratios of run R, where DMS and anthropogenic sources are considered (Figure 6.12), are compared with the simulation W_{ant} in which only anthropogenic emissions are taken into account (6.12) and with run W_{dms} in which only the DMS source is accounted for.

The total SO_2 mixing ratio, when both DMS and anthropogenic emissions are considered, reveals mixing ratios on the order of 0.3 ppb over the Atlantic Ocean and some 5 ppb over the Mediterranean. Continental sources locally contribute with up to 10 ppb SO_2. During their study over the Western

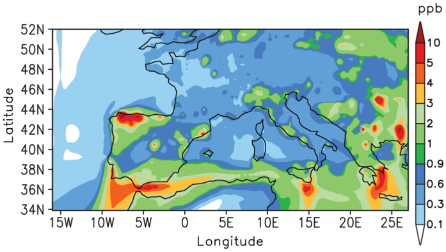

Figure 6.12.: Simulated SO_2 from DMS oxidation and anthropogenic emissions, near the surface averaged over three days.

North Atlantic Ocean Berresheim et al. (1991) found that the SO_2 levels can be as low as 10 ppt in marine air, and reach several ppb under influence of continental air. The simulated SO_2 mixing ratios can thus be concluded to be on reasonable order of magnitudes, both in clean areas and areas under continental influence. In looking at the distribution of SO_2 when only anthropogenic sources are accounted for, it is clear that the major contributor to SO_2 over the Eastern Mediterranean is anthropogenic. This is due to large anthropogenic emission rates and DMS emission rates caused by low wind speeds. In the Western Mediterranean, higher wind speeds occurred and the relative importance of DMS to SO_2 increases. In this area, DMS oxidation contributes up to 2 ppb SO_2, which locally corresponds to 50% of the total SO_2 mixing ratio. Over the Atlantic, the DMS oxidation is dominant, due to less anthropogenic emissions. Over the continent, anthropogenic emissions are the dominant source of SO_2, compared to the oceanic DMS contribution. Kloster et al. (2006) investigated the relative importance of DMS to SO_2 formation compared to when anthropogenic sources are also included. During June, July, and August, the averaged relative contribution of atmospheric DMS to the SO_2 was estimated as to 15.8% on averaged for the Northern Hemisphere. In this study, the contribution of DMS locally exceeds that of Kloster et al. (2006). Overall DMS is found to contribute significantly to the

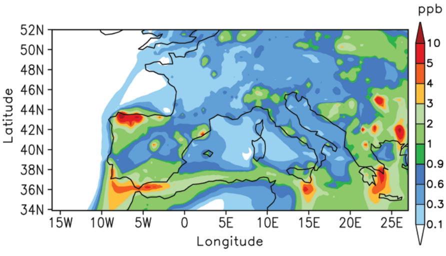

Figure 6.13.: Anthropogenic sources.

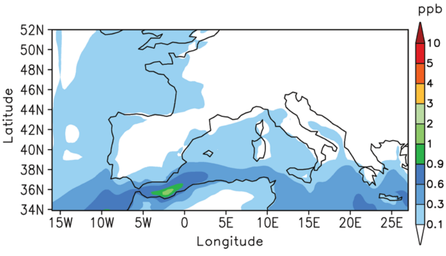

Figure 6.14.: DMS oxidation.

Figure 6.15.: Simulated SO_2 mixing ratios, respectively, averaged over three days.

simulated SO_2 mixing ratio for high wind speeds, even in polluted regions. This is most evident in the Western Mediterranean in this study.

6.4.2. Impact of Water Uptake on the Aerosol Size Distribution

To investigate the impact of the water uptake on the sea salt aerosol distribution, the simulated size distribution of dry sea salt aerosol (run D) is compared to that of internally mixed wet aerosol (run R). The difference between run D and run R gives the change of the concentrations fields when water uptake and condensation of sulphuric acid from anthropogenic emissions and DMS emissions are accounted for. When these processes are considered, the aerosol consists of additional mass and grows in size, compared to the pure dry NaCl particle. The number densities and mass densities for all three modes are averaged over the three days of the episode for both runs. The 3-day averaged dry sea salt number density and the difference in number density when water uptake is considered is illustrated in Figure 6.16 for the aerosol film mode, in Figure 6.17 for the jet mode, and in Figure 6.18 for the spume mode. The simulated dry NaCl mass density, averaged over the three days, and the corresponding difference in the NaCl mass density field when water uptake is accounted for are for the film, jet and spume modes depicted in Figure 6.19, 6.20, and 6.21, respectively. Thus, the mass density of the pure NaCl aerosol is compared with the NaCl mass density of the mixed wet sea salt aerosol.

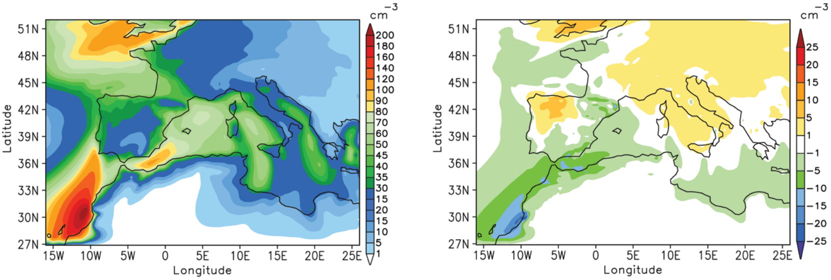

(a) Dry number density.

(b) Difference (run D-run R).

Figure 6.16.: 3-day averaged dry number density and difference of the film mode for the lowest approx. 40 m.

The film mode contributes the most to the total number density of all the dry modes, with values up to approx. 210 cm^{-3} off the west coast of North Africa. In this region, wind speeds occurred on the order of up to 10 m s^{-1} during all three days. The dry jet mode maximum number density is 1.8 cm^{-3} and the spume mode maximum number density is on the order of 0.01 cm^{-3}. Maximum NaCl mass density is simulated for the jet mode, in

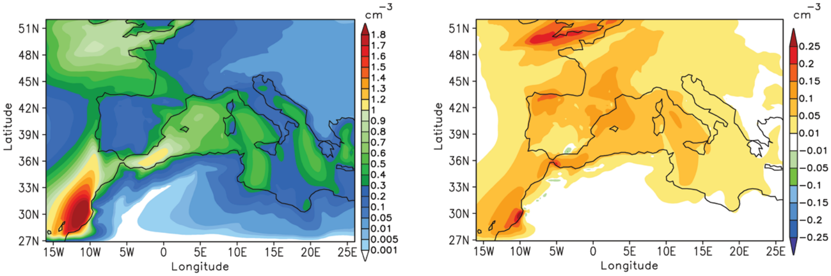

(a) Dry number density.
(b) Difference (run D-run R).

Figure 6.17.: 3-day averaged dry number density and difference of the jet mode for the lowest approx. 40 m.

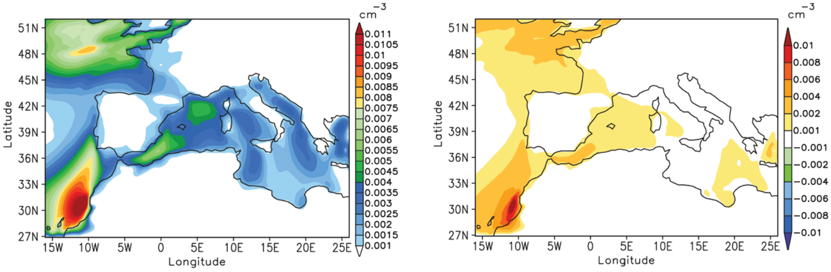

(a) Dry number density.
(b) Difference (run D-run R).

Figure 6.18.: 3-day averaged dry number density and difference of the spume mode for the lowest approx. 40 m.

the order of 75 μg m^{-3}. The maximum NaCl mass density of the film and spume modes are on average over three days 11.5 μg m^{-3} and 30 μg m^{-3}, respectively. The film and jet mode maxima are found over the Atlantic off the Nortwest African Coast. For the spume mode, three maxima are found, one of them coincides with that of the film and jet modes. In addition high mass densities in the spume mode are simulated over the Atlantic in the north of the model domain, southwest of Ireland and east of England. These are the areas where the highest wind speeds occurred, connected to the low level pressure system. The total maximum of the mass density of all modes is still found over the Atlantic off the African coast, on the order of 115 μg

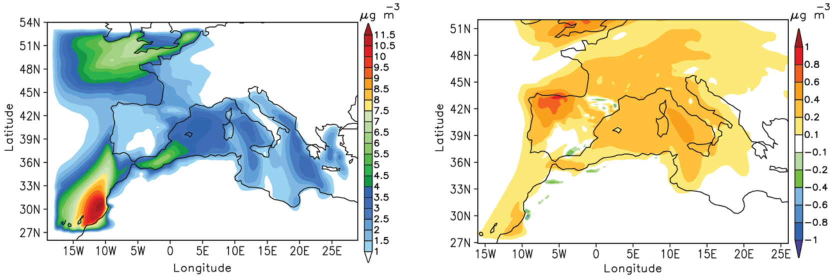

(a) Dry mass density. (b) Difference (run D-run R).

Figure 6.19.: 3-day averaged dry mass density and difference of the film mode for the lowest approx. 40 m.

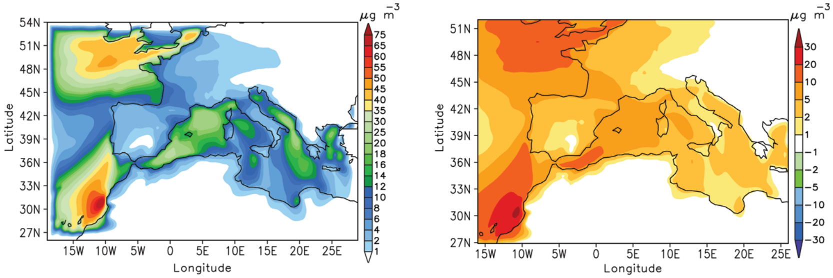

(a) Dry mass density. (b) Difference (run D-run R).

Figure 6.20.: 3-day averaged dry mass density and difference of the jet mode for the lowest approx. 40 m.

m^{-3}. Hence, when comparing the averaged simulated dry sea salt number and mass densities it is seen that the film mode contributes the most to the number density, and the least to the mass density. The spume mode contributes the least to the number density and the jet mode comprises the largest fraction of mass relative to the other two modes.

The maximum simulated total dry mass and number densities modes reached approximately 115 $\mu g\ m^{-3}$ and 210 cm^{-3}, respectively. By comparing the mass and number densities of the dry modes with the NaCl component of the wet internally mixed modes changes are found. The NaCl mass density

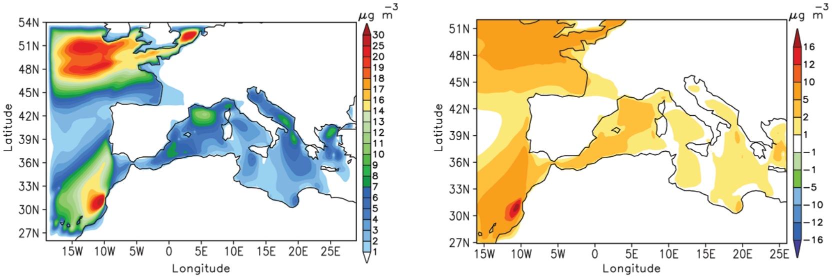

(a) Dry mass density.

(b) Difference (run D-run R).

Figure 6.21.: 3-day averaged dry mass density and difference of the spume mode for the lowest approx. 40 m.

of the wet modes is about 66 μg m^{-3} and the wet aerosol number density is on the order of 225 cm^{-3}. Thus, the number density increased in contrast to the mass density of the NaCl component, which decreased. Typical sea salt concentrations in the literature are 10-20 μg m^{-3} with respect to mass and 100-300 cm^{-3} with respect to the amount of aerosol (Song and Carmichael, 1999). Compared to these numbers, the simulated sea salt number density has a comparable order of magnitude. The mass density is however larger in the simulation than in typical observations. Observations are however generally restricted to the PM$_{10}$ aerosol fraction, i.e. particles with diameters exceeding 10 μm are excluded. The simulations, on the other hand, include sizes larger than 10 μm. By only considering the sea salt fraction within the 10 μm limit, the maximum mass density of NaCl decreases from 66 μg m^{-3} to 49 μg m^{-3}. The number density, which is dominated by the film mode, remains relatively unchanged by this restriction with a decrease of 0.6 cm^{-3}. The differences in mass between observed and simulated values are consequences of different uncertainties. The neglection of sea salt aerosol participation in cloud droplet formation, lack of adequate observations over water in windy situations, and uncertainties in measurements are the most probable causes for these differences. Aerosol measurements are still connected to problems such as aerosol losses in the particle inlet, leading to uncertainties in the measured size distribution especially for coarse mode aerosol (Heintzenberg et al., 2000; Moore et al., 2004). Cloud droplet formation is an important sink for these aerosol sizes and, if included, would lead to a decrease in the total sea salt mass density field. As the smallest size is less of importance for cloud droplet formation, the number density is expected to be less affected.

The number density difference of the film mode ranges from -20 to +7 cm^{-3}, corresponding to a difference of -8% to 3.5% of the total dry number density. The number density difference of the jet mode is maximum +0.23 cm^{-3}, corresponding to about 13% more dry aerosol than wet aerosol. For the spume mode, the corresponding difference is 0.01 cm^{-3}, which is approx. 100% of the initial dry number density of this mode. The simulated mass of dry aerosol in the film mode is 0.66 μg m^{-3} higher than the NaCl mass density of the wet internally mixed film mode, corresponding to approximately 5.7% of the total dry mass density. For the jet mode, the corresponding difference in the mass density is 28 μg m^{-3} of max. 74 μg m^{-3}, i.e. an approx. 38% decrease of NaCl. The mass density of NaCl in the dry spume mode is approx. 41% (12 of 29 μg m^{-3}) larger than that in the wet internally mixed sea salt aerosol spume mode.

The differences between the dry and internally mixed wet sea salt aerosol density fields are explained by the increase in mass, mainly due to the uptake of water. The additional mass on the aerosol leads to modifications in the aerosol mode median diameter and the simulated residence time. For the jet and spume mode, the growth mainly leads to a shorter atmospheric residence time, which results in a decrease of both the number densities (Figure 6.17 and 6.18) and mass densities (Figure 6.20 and 6.21). The shorter atmospheric residence time of the jet and spume modes can be explained by higher deposition velocities. As for the film mode, some areas of increased number density of wet jet mode aerosol are however also seen at the Spanish coast and the North African Coast. The cause of this, on first thought, rather unexpected result, is discussed in the following. The deposition velocity depends on the geometric median diameter $D_{g0,i}$ of the aerosol number distribution (e.g., Equation 3.26). For the film mode standard deviation σ_g of 1.9, the deposition rate is shown in Figure 6.22. There exists a critical diameter for which the deposition from the atmosphere is least efficient. The critical value is on the order of 2 μm for the number density and 0.5 μm for the mass density for an aerosol distribution with σ=1.9 and at an aerodynamic resistance of 50 s m^{-1}. As the median diameter of the film mode is on the same order of magnitude as this critical value, a modification in size may lead to either a decrease or increase in the deposition rate. This also happens in some areas for the jet mode. If the mode median diameter of the wet aerosol is closer or further away from the critical value compared to that of the dry aerosol mode a shorter residence time of the film mode is seen in some areas and in some regions a longer residence time. For an aerosol with a diameter smaller than the critical size a growth may lead to the removal becoming less effective and in turn the residence time increases, causing higher concentrations. To illustrate the impact of the uptake of water on the size distribution further, the film mode number and mass density distributions

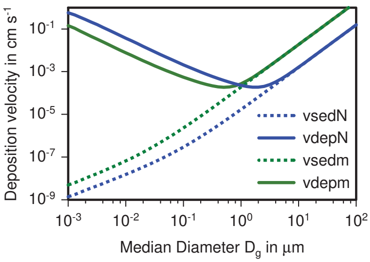

Figure 6.22.: Deposition (solid) and sedimentation (dashed) velocities for r_a=50 s m^{-1} of number (blue) and mass (green) densities for distributions with σ_g=1.9 m.

for dry and wet aerosol are compared for the grid point (29.5°N, 10.5°W) in Figure 6.23 and 6.24, respectively.

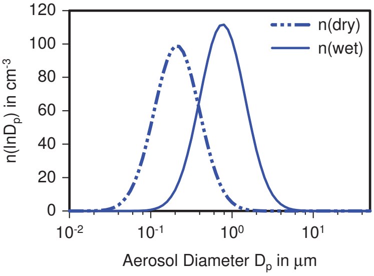

Figure 6.23.: Film mode number density distribution for dry and wet aerosol distributions, respectively.

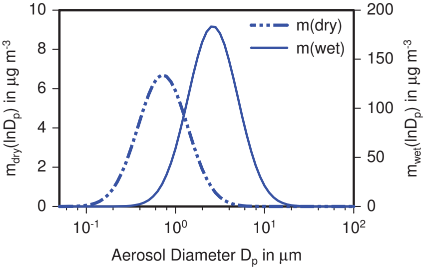

Figure 6.24.: Film mode mass density distribution for dry and wet aerosol distributions, respectively.

The daily averaged number density near the surface, for the dry and wet aerosol cases, are 159.2 cm^{-3} and 179.8 cm^{-3} at this grid point, respectively. The corresponding daily averaged mass density is 10.8 μg m^{-3} for the dry aerosol mode and 295.5 μg m^{-3} for the wet internally mixed mode. The wet internally mixed mode mass density is composed of 10.4 μg m^{-3} NaCl, 0.9 μg m^{-3} sulphate, and 284.2 μg m^{-3} water. An increase of approx. 20 cm^{-3} more wet aerosol is simulated, compared to the dry aerosol. This value corresponds to an increase of approximately 8% in the amount of aerosol. At the same time, the dry mass density decreases with about 0.4 μg m^{-3}

(4%). The fact that the number density increases at the same time as the mass density decreases is explained by the modal treatment of the deposition rates for each aerosol moment. As already noted, the deposition rates depend on the geometric median diameter. This is achieved from Equation 3.6. The density of the dry mode is determined by that of bulk NaCl ($2.2 \cdot 10^3$ kg m^{-3}) and for the wet aerosol the mass density is approximately $1.1 \cdot 10^3$ kg m^{-3}, i.e. the total density at this grid cell is dominated by that of water. The median diameter $D_{g0,1}$ is 0.21 μm for the case of dry aerosol, and increases to 0.76 μm when water uptake is considered. In looking at the critical diameters for minimum deposition rates in Figure 6.22, it is clear that such growth leads to less efficient deposition with respect to the number density. The deposition rate of the mass density, on the other hand, increases due to the aerosol growth. For this reason, the number density of the wet aerosol is deposited less efficient than the dry aerosol, and a higher number density is simulated as the aerosol takes up water and grows. For the mass density, the opposite occurs. Obviously, the water absorption process affects the sea salt aerosol size distribution. It is concluded that this process is important to consider as accurately as possible for a correct description of the sea salt aerosol size distribution in atmospheric models.

6.4.3. Simulated Sea Salt Aerosol Composition

Now, the respective contributions of each of the chemical components to the total wet internally mixed aerosol are estimated. The horizontal distribution of the total mass density and the corresponding distribution of each of the components are investigated for run R. The horizontal surface near mass distributions, averaged over three days, of each of the sea salt chemical components are shown together with the total mode mass density for the film mode (Figure 6.25), the jet mode (Figure 6.26), and the spume mode (Figure 6.27).

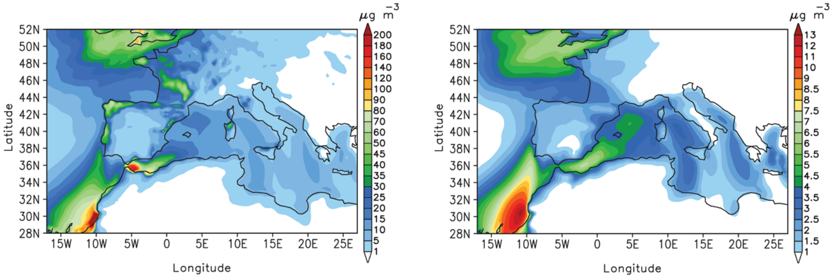

(a) Wet mass density.

(b) NaCl.

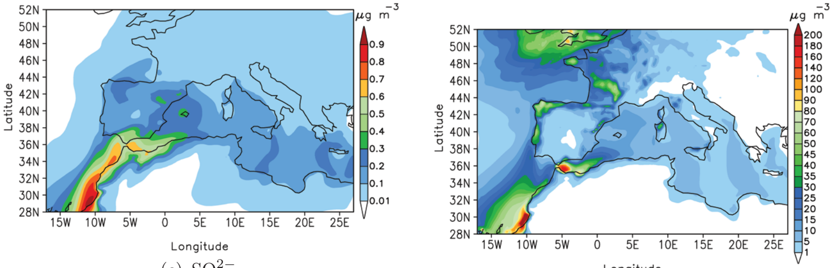

(c) SO_4^{2-}.

(d) H_2O.

Figure 6.25.: 3-day averaged film mode mass densities close to the surface for the lowest approx. 40 m.

The total wet sea salt mass density in the film mode, averaged over three days, ranges up to values of 240 μg m $^{-3}$. The mass density of NaCl shows its largest contribution to the total wet mass in regions of high wind velocities. A maximum of approx. 11 μg m $^{-3}$ is simulated near the west coast of North Africa. Over the Atlantic Ocean south of Ireland and in the western Mediterranean south of Spain, mass densities of up to 7 μg m $^{-3}$ are simulated. The water uptake on the sea salt aerosol is very efficient and the additional mass of water completely dominates the total mass density in most of the model domain. Near the west coast of North Africa the contribution of the NaCl component is on the order of 5% to the total wet aerosol mass, whereas the water content contributes with about 95%. In this region, the simulated sulphate mass density is much smaller than that of the other components, contributing less than 1% to the total mass density.

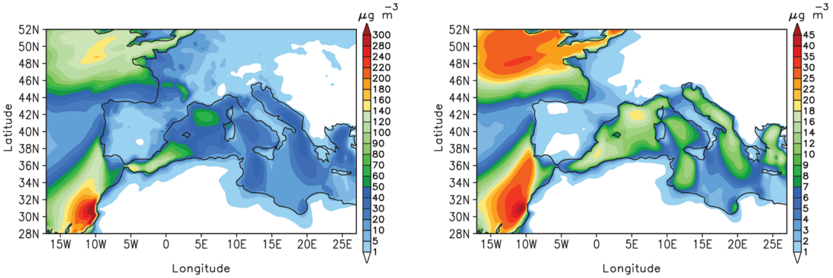

(a) Wet mass density.

(b) NaCl.

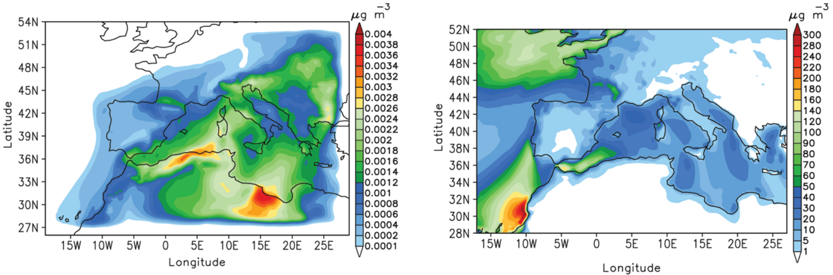

(c) SO_4^{2-}.

(d) H_2O.

Figure 6.26.: 3-day averaged jet mode mass densities close to the surface for the lowest approx. 40 m.

The largest contribution to the total mass density of the jet mode, is also given by the water content of the aerosol. The relative contribution of the different components is for instance about 13% NaCl and 87% liquid water content in the area with maximum mass density (above the Atlantic, west of the North African coast). The mean sulphate contribution to the total averaged jet mode wet mass density is in general negligible for the whole domain.

When considering the spume mode, the contribution of the sulphate components is of even less importance than for the jet mode. The contribution of

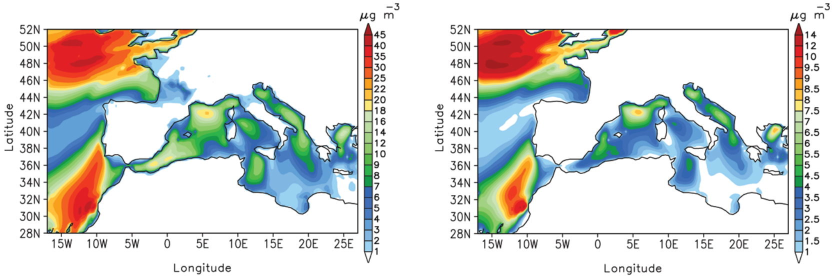

(a) Wet mass density.

(b) NaCl.

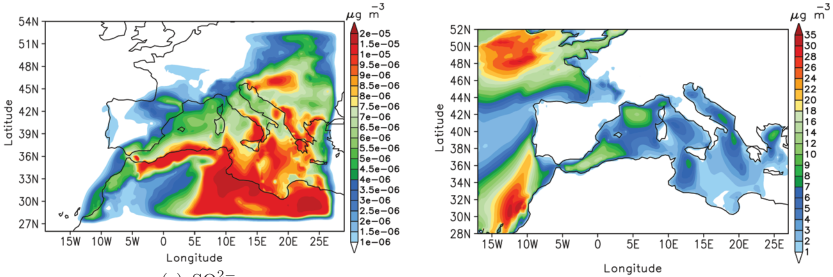

(c) SO_4^{2-}.

(d) H_2O.

Figure 6.27.: 3-day averaged mass density of the spume mode close to the surface for the lowest approx. 40 m.

the sulphate mass density to the total wet mass is dominant in the film mode. This is due to the more effective condensation onto the film mode, compared to the two larger aerosol modes. As well as for the film and jet mode, the water mass density is the dominant component of the aerosol. The respective contribution relative to the total wet mass is on the order of 77% and 23% for the water and NaCl components over the Atlantic, west of North Africa.

The contribution of each sea salt mode to the total wet mass over all modes, is for the Atlantic region near the coast of Africa approximately 36% of the film mode, 53% due to the jet mode, and 11% of the spume mode. Thus, the jet mode is the dominant mode for the mass density, and mode with the largest diameters contributes the least.

DMS and Anthropogenic Contribution to Aerosol Sulphate Content

To compare the contribution of anthropogenic emissions and DMS emissions to the simulated sea salt aerosol sulphate content, the mass density of aerosol sulphate contents in runs W_{ant} and W_{dms} are compared to that of the reference run R (cf. Table 6.2). The simulated sulphate content in run W_{ant} is a result of anthropogenic emissions exclusively, and the contribution of DMS emissions to the sea salt aerosol sulphate content is achieved from simulation W_{dms}. The relative contribution of anthropogenic and DMS emissions to the total sea salt aerosol sulphate content is determined as the fraction of the sulphate content when only one of the emissions is considered in the total sulphate content in run R, i.e. when both DMS emissions and anthropogenic emissions are taken into account. The total simulated sulphate content, for the film mode is shown in Figure 6.28. The relative contributions are presented in units of per cent in Figure 6.29(a) for the anthropogenic case and in Figure 6.29(b) for the DMS-case. The values are presented for the lowest 1 km of the troposphere.

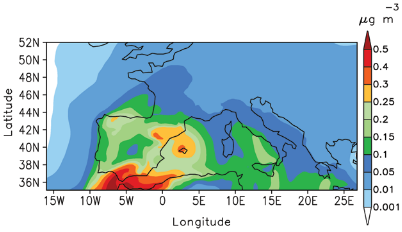

Figure 6.28.: 3-day averaged film mode SO_4^{2-} content for the lowest approx. 1 km.

The average contribution of the total sea salt aerosol sulphate content over the Mediterranean is dominated by anthropogenic sources. The relative importance of DMS oxidations to the film mode sulphate content dominates

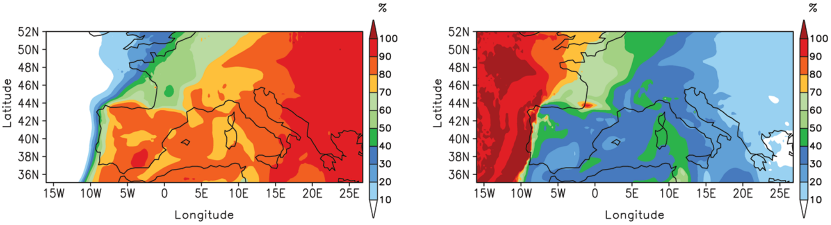

(a) Anthropogenic contribution.

(b) DMS contribution.

Figure 6.29.: Averaged relative contributions to total sea salt film mode SO_4^{2-} content, for the lowest 1 km.

over the Atlantic Ocean in this study. The relative importances of anthropogenic sources over the Mediterranean and of sulphates of natural origin over the Atlantic Ocean were on the order of up to 100% for the respective region. In an area along the Portuguese coast, both sources contribute approx. 50% to the aerosol sulphate content.

6.4.4. Horizontal and Vertical Distributions

The simulated horizontal distributions of the 3-day averaged total mass and total number densities in μg m^{-3} and cm^{-3}, respectively, are illustrated near the surface in Figure 6.30 for run R. The vertical distributions of the total mass and number densities are illustrated by showing two vertical cross sections of the 3-day averaged wet internally mixed sea salt aerosol (black lines in Figure 6.30). A longitude-altitude cross section at 37°N is depicted in Figure 6.31(a) regarding the mass density, and in Figure 6.31(b) for the number density. Latitude-altitude cross sections at -7°E between 40-53°N of the mass and number densities are shown in Figure 6.32(a) and 6.32(b), respectively. The white bars in the vertical cross sections indicate topography.

Large gradients towards lower concentrations over land are simulated both for the averaged mass and number densities. However, the number density

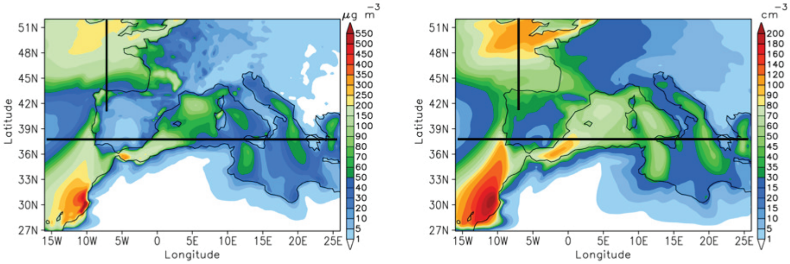

(a) Wet mass density.

(b) Number density.

Figure 6.30.: Wet mass and number density at the surface for the lowest approx. 40 m, averaged over three days.

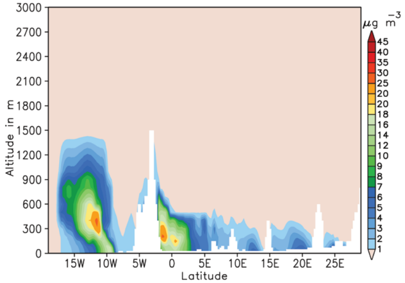

(a) Mass density.

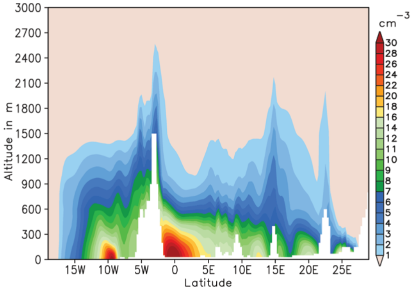

(b) Number density.

Figure 6.31.: Vertical cross sections at 37°N of 3-day averages of the mass and number density, respectively.

of sea salt aerosol is characterised by slightly smaller gradients than those for

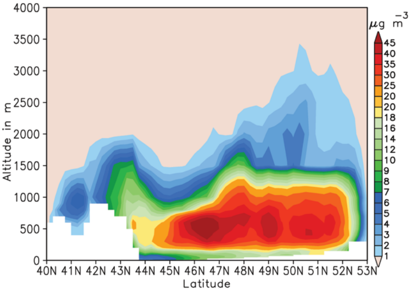

(a) Mass density.

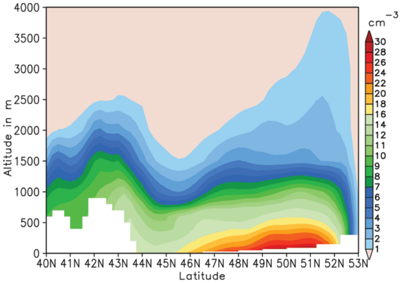

(b) Number density.

Figure 6.32.: Vertical cross sections at -7°E of 3-day averages of the mass and number density, respectively.

the mass density. As the mass density is dominated by the sea salt aerosol jet mode, and the film mode dominates the number density, this difference in mass and number transport is an indication of further transport away from source regions of the film mode compared to the jet mode. Moreover, in the vertical cross sections, the maximum altitude to which the number density of aerosol is found is seen to exceed that of the mass density. No significant mass is found above 1.4 km for the cross section along 37°N, whereas the corresponding maximum altitude for the number density is 2.5 km. For the cross section at -7°E, no significant mass is found above 3 km and the corresponding altitude for the number density is about 3.8 km. When considering the averaged mass density as a function of altitude, the maxima are found with height for both cross sections. As the number density here is lower than that at the surface, this indicates that aerosol with large sizes but less in number are responsible for these maxima. Obviously, the transport in the vertical cannot be neglected, and for this reason the burden of the whole column is of importance for e.g., radiation calculations. To only consider the surface near mass and number densities would lead to an underestimation of the sea salt aerosol loading. The elevated aerosol loadings are especially found in regions with significant upward motion, as in low level pressure areas (Figure 6.32(a)).

6.4.5. Simulated Aerosol Optical Depth (AOD)

The aerosol optical depth (AOD) is the non-dimensional vertical integral of the extinction coefficient. The AOD is wavelength dependent, and most commonly reported for a wavelength of 550 nm in the literature. The extinction of each sea salt mode at 550 nm was determined from the Mie-calculations for a pre-simulated aerosol distribution, as described in chapter 5. The mass specific extinction coefficients serve as input parameters together with the mass densities of each mode to calculate the AOD_{550} optical depth by

$$AOD_{550} = \sum_{h=1}^{N_h} (2.2845 \cdot m_{1,h} + 0.2475 \cdot m_{2,h} + 0.0829 \cdot m_{3,h}) \cdot 10^{-6} \Delta z_h. \tag{6.1}$$

$\mathrm{m}_{1,h}$-$\mathrm{m}_{3,h}$ are the total mass densities of each sea salt mode in μg m^{-3} for the respective model layers h. Δ z_h corresponds to the height of each model layer given in m and N_h is the number of layers.

The daily averaged simulated sea salt AOD_{550} for the 24th-26th of July is illustrated in Figure 6.33. The black square indicates the investigation area for the wind speed dependency of AOD, which is further described later in this section.

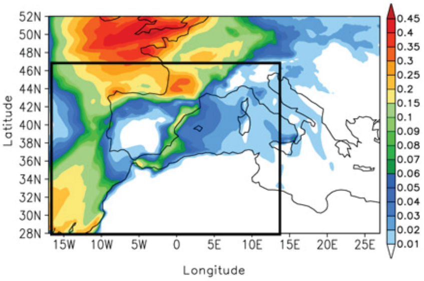

Figure 6.33.: Wet sea salt AOD at 550 nm, averaged over three days.

The corresponding daily averaged wind speed at 10 m above ground is depicted in Figure 6.34. The largest AOD values are found over the North Atlantic as a result of the relatively higher wind speeds in this part of the domain. On average, the wind speeds here reached 12 m s^{-1} over the north Atlantic during these three simulation days. Off the North African coast over the Atlantic, mean wind velocities also reached about 10-12 m s^{-1}, but for a smaller area. Over the Mediterranean, wind speeds remained below 9 m s^{-1} and were generally on the order of 5-6 m s^{-1}, on average during the three days. The simulated AOD is for this reason lower in the Mediterranean region than over the Atlantic for these days.

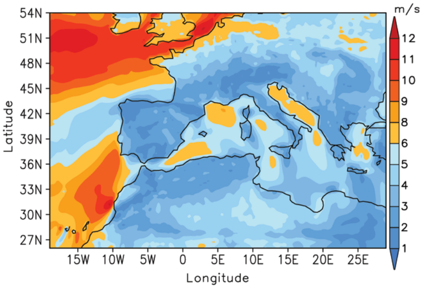

Figure 6.34.: U_{10} averaged over 24th-26th July.

AOD and Wind Speed

Currently, there is much interest in examining the relation between the AOD in maritime environments and the prevailing horizontal wind speed near the surface. It is well known that an enhancement of the AOD over oceanic regions takes place as a result of the increased contribution of sea salt aerosol with increasing wind speed near the surface (e.g., Satheesh and Krishna Moorthy, 2006; Mulcahy et al., 2008; Glantz et al., 2009; Huang et al., 2009; Mulcahy et al., 2009). At high wind speed, the natural marine AOD can rival or even exceed the AOD of anthropogenic aerosols, with values up to 0.4 compared to the typically polluted AOD in the range 0.2-0.5 (Satheesh and Krishna Moorthy, 2006; Mulcahy et al., 2008, 2009). The enhancement of maritime AOD with wind speed has been argued to be the result of several effects. Both hygroscopic growth caused by wind driven water vapour (Glantz et al., 2009) and increased sea salt aerosol mass density as a function of the wind dependent sea salt emission flux has been stressed as possible contributors (Glantz et al., 2009; Mulcahy et al., 2008). Over the North Pacific, the contribution of the hygroscopic growth was about 40% and the contribution of the sea salt aerosol mass density was 60% (Glantz et al., 2009).

Although many studies have been performed, there still exists no consensus on the relation between wind speed and AOD. The relation between AOD and surface near horizontal wind speed has been described by some findings as weak linear expressions (Smirnov et al., 2003; Jennings et al., 2003; Huang et al., 2009; Lehahn et al., 2010, e.g.,) and by others to be exponential (e.g., Satheesh and Krishna Moorthy, 2006, and references therein). Further studies describe the AOD-wind relation by power-law relations (e.g., Mulcahy et al., 2008; Glantz et al., 2009; Mulcahy et al., 2009). As all the studies are performed for different locations and time periods, the relations are difficult to compare directly. Since the sea salt emission flux is proportional to $\mathrm{U}_{10}^{3.14}$

(Monahan et al., 1986; Smith et al., 1993; Mårtensson et al., 2003) and the water absorption by sea salt is exponential with increasing ambient relative humidity (e.g., Tang et al., 1997; Tang, 1997; Lewis and Schwartz, 2004), a linear dependence of AOD and wind speed is in general rather unexpected.

To be able to describe the sea salt AOD as a function of wind speed provides the opportunity to treat the optical depth directly as a function of the accessible wind conditions in for instance climate models. In this case, the computational costs with respect to the aerosol treatment would be reduced significantly. Another field for which such relations are of interest is the evaluation of satellite retrievals. As sea salt acts as background aerosol above much of the earth's surface, a known relation between sea salt AOD and wind speed opens the possibility to filter the sea salt contribution from the composite aerosol extinction. Subsequently, the magnitude of other aerosol species contribution to the total AOD can be obtained. Such relations also provide an additional method for determining the wind speed above oceans when the marine AOD is known.

To investigate the marine AOD-wind speed relation is a complicated task. The marine aerosol optical properties can be masked by long-range transport from land based sources. The dominating aerosol background aerosol is influenced by several factors such as air mass history, variations in the state of the atmosphere, advection processes, relative humidity effects etc. Several uncertainties are connected to the AOD-wind speed investigations. AOD retrievals from satellites can be biased by the backscatter of whitecaps that are generated by enhanced wind speeds (Huang et al., 2009; Yu et al., 2009). Moreover, the marine environment has to be defined accurately. Even when defining marine regions, non marine background aerosol may be present due to long range transport. The background AOD of the Northern Atlantic is also influenced by dust transport from the Sahara, pollution from continental Europe and biomass burning from South America and Africa (Mulcahy et al., 2009). For the purpose of excluding situations affected by pollution, different methods have been utilised. Mulcahy et al. (2008) defined clean marine conditions along the Mace Head coastline based on wind direction, back trajectories, low black carbon mass concentrations ($<$50 ng m^{-3}) and number densities less than 700 cm^{-3}. For this region, the air masses of continental origin are connected to particle number densities of approximately 2000-3000 cm^{-3}, reaching a maximum of 7000 cm^{-3} in extremely polluted conditions due to nucleation events (Mulcahy et al., 2009, and references therein). In addition, the study of Mulcahy et al. (2008) was restrained to winter months to minimise the contributing fractions of biogenically produced inorganic and organic matter to the marine aerosol, which is smaller in winter compared to summer. Huang et al. (2009) utilised the standard deviation from the satellite retrieved mean AOD together with wind direction from ECMWF to exclude situations with contributions from non-marine sources. The criteria for clean marine air generally apply for the marine boundary layer. The AOD is however a columnar signal that also can be affected by entrainment from the free troposphere and the stratosphere. The background AOD is thus presumably affected by entrainment from elevated aerosol, but these contributions most probably do not contribute to the high correlation with the surface near wind speed (Kaufman et al., 2005).

It is now investigated as to how the simulated AOD$_{550}$ in this study depend on the wind speed. This study provides one of the few investigations where both AOD and wind speed data are direct functions of each other and originate from the same source. This is an advantage compared to other studies where aerosol data and wind speed are achieved from different sources with individual uncertainties. To assure that the AOD is representative of the current wind conditions, the relation is investigated for a single output and no temporal or spatial averages are applied. The data is analysed for 12 UTC at the 25th July 2007. No correlation is expected between AOD and wind speed over land, thus only grid points over the ocean are used. The obtained relation is to be compared with those from satellite observations. For this reason, pixels with cloud cover less than 1% are selected. Any effects of boundaries are overcome by choosing a smaller area within the domain, which is indicated in Figure 6.33. The reason as to why the black square is close to the southern and western boundaries in Figure 6.33 is that the figure already represents a part of the domain for which the complete boundary is not present. The northern limit of the investigation area is determined by the large amount of cloud cover above the North Atlantic. The maximum AOD is 0.3472 and the corresponding 99% percentile of the AOD data is 0.1279. To neglect data that is less well represented, the 99% percentile values are chosen (e.g., Glantz et al., 2009). This means that some of the grid cells with relatively greater values are neglected to reduce the contribution of data that is less well represented. The total and 99% percentile AOD data for cloud free marine grid cells are depicted in Figure 6.35 to the left and right, respectively. As is seen in Figure 6.35, selecting the 99% values do not interfere with the general result, i.e. the difference between all data and the reduced data is small. By considering the 99% percentile only a few less representative values at wind speeds between 8-10 m s^{-1} are neglected.

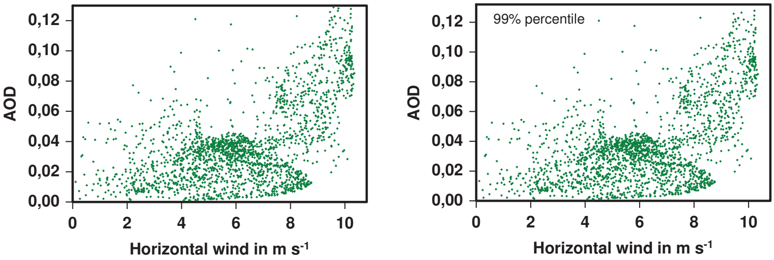

Figure 6.35.: AOD_{550} as a function of the 10 m wind speed. Left: all data points. Right: the 99% percentile values.

Following the approach of e.g., Mulcahy et al. (2008), Glantz et al. (2009), Huang et al. (2009), and Lehahn et al. (2010), the selected AOD data was classed into bins as a function of the corresponding wind speed. In this study, 2030 AOD data points were sorted into 11 bins with a bin width of 1 m s^{-1}. The average AOD within each bin and the corresponding standard deviation are depicted as a function of the average bin wind speed in Figure 6.36. The power fit according to the 11 mean values is shown in black. In addition, an exponential fit applies well to the mean AOD values (blue curve in Figure 6.36), but a higher correlation of 0.998 is achieved for the power law compared to 0.938 of the exponential fit.

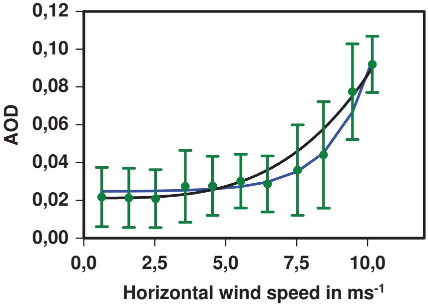

Figure 6.36.: Power law fit based on average AOD_{550} values (R=0.998) in black and exponential fit (R=0.938) in blue.

The power law of this study takes the form

$$AOD_{550} = 0.0212 + 2.5941 \cdot 10^{-5} \cdot U_{10}^{3.3992} \tag{6.2}$$

with non-dimensional AOD_{550}, and U_{10} in m s^{-1}. The power fit is illustrated together with the original 99% percentile AOD_{550} data as a function for wind speed in Figure 6.37. In resemblance to satellite based observations, an offset of the sea salt optical depth wind dependence is found at wind speeds in the order of 4 m s^{-1}. For example, Lehahn et al. (2010) found an offset of the AOD wind dependence at 3.8 m s^{-1}. For wind speeds lower than approximately 4 m s^{-1} no clear wind dependence is found and the sea salt AOD remains more or less constant.

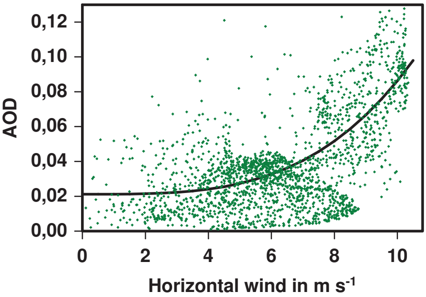

Figure 6.37.: Simulated sea salt AOD$_{550}$ in green and the observed relation in black, as a function of wind speed on 25th July, 12 UTC.

The relations by Schinozuka et al. (2004), Mulcahy et al. (2008), and Glantz et al. (2009) are compared with the relation between the simulated AOD and wind speed in this work. Schinozuka et al. (2004) examined the sea salt AOD over the Southern and tropical Pacific Oceans during the ACE-1 campaign. They approximated the sea salt contribution to the optical depth by

$$AOD(U_{10}) = 0.017 + 4.9 \cdot 10^{-5} U_{10}^3 - 3.7 \cdot 10^{-5} U_{10}^2 \tag{6.3}$$

where AOD is non-dimensional, and U$_{10}$ is given in m s^{-1}. Mulcahy et al. (2008) investigated the enhancement of marine air AOD during high wind conditions at the Mace Head atmospheric research station on the west coast of Ireland. AOD measurements were carried out between January 2002 and December 2004 by the use of a precision filter radiometer (PFR) with an accuracy of 0.01 optical depth. For wind speeds in the range of 4-18 m s^{-1} a power law curve was fitted to the AOD-data at 500 nm on the form

$$AOD_{500} = 0.06 + 5.5 \cdot 10^{-4}\, U^{2.195} \tag{6.4}$$

where U is the surface wind speed in m s^{-1}, and the AOD is non-dimensional. In this study, the AOD at 550nm was not investigated. In a recent study, Glantz et al. (2009) estimated the maritime component of AOD and its dependence on wind speed over the North Pacific for September 2001. For this purpose, retrievals of the Sea-viewing Wide Field Sensor (SeaWiFS) were combined with the wind speed obtained from the European Centre for Medium-Range Weather Forecasts (ECMWF). A power relation was found as

$$AOD_{555} = 0.0028 + 0.00032 \cdot U_{10}^2 \tag{6.5}$$

where U_{10} is the 10 m level wind speed in m s^{-1}, and the AOD is non-dimensional. A comparison with these latter relations is depicted in Figure 6.38 for the wind speed regime in which the relation of this study is valid (0.8-10.2 m s^{-1}). The AOD dependence of this study is depicted in green, that of Mulcahy et al. (2008) in red, the relation of Schinozuka et al. (2004) in orange and that of Glantz et al. (2009) in blue.

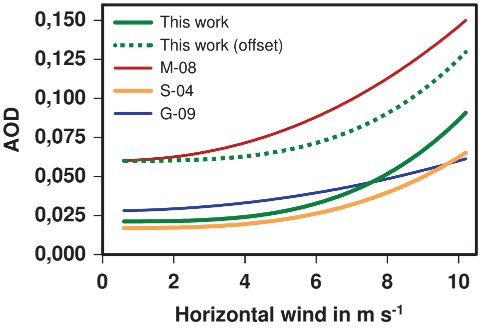

Figure 6.38.: Sea salt AOD as a function of wind speed according to Mulcahy et al. (2008) (M-08), Schinozuka et al. (2004) (S-04), and Glantz et al. (2009) (G-09). Green dotted line: Equation 6.2 with offset of 0.06.

By comparing the different relations based on satellite observations with the relation of this study it appears that there exists a wind independent AOD contribution. If this wind independent contribution did not exist, the AOD would approach zero for low wind speeds. This is the case in neither the satellite observations nor this model study. The magnitude of this contribution varies between the different studies. These values are found between 0.06 from the fit by Mulcahy et al. (2008) 0.017 of Schinozuka et al. (2004). The wind independent contribution in this work is estimated to be approximately 0.02. Wind independent contributions to the optical depth, when no other aerosols are considered, may result from for instance elevated sea salt aerosol layers in combination with relative humidity effects. Elevated aerosol layers are not expected to show any correlation with wind speeds near the surface. For high relative humidities these elevated aerosols can absorb a high amount of water and contribute significantly to the AOD, even for low aerosol concentrations. A combination of these two effects is thought to at least be one of the effects behind the wind independent AOD contribution. For wind speeds up to approximately 6 m s^{-1} the relation of this work follows that of Schinozuka et al. (2004). For wind speeds higher than 6 m s^{-1} the two relations separate and the relation from this study increases faster. For the whole wind speed interval, the power fit from Mulcahy et al. (2008) provides the highest AOD values. By the green dotted curve in Figure 6.38 the relation from this study is shown with an offset value as high as that of Mulcahy et al. (2008). This comparison between the relation from this study and that of Mulcahy et al. (2008) shows a faster increase of AOD with increasing wind speed for the latter. Overall, the relation of this study lays within the order of magnitude of those that were based on satellite retrievals. For this reason, it can be argued that for cloud free situations the calculated AOD in this work is on a reasonable order of magnitude. Since the formation of cloud droplets is neglected, the mass of sea salt is most probably overestimated in the more cloudy areas. For these regions, no comparisons with measurements can however be carried out, since the backscattering in such cases is dominated by that of clouds.

6.4.6. Influence on Atmospheric Radiative Fluxes and Temperature

The sea salt aerosol impact on the radiation fluxes is calculated as the difference in the solar (F_{SW}) and thermal (F_{LW}) radiation budgets at the surface and the top of the atmosphere (TOA), respectively, between the results of run F and run R. In simulation R no interaction between the sea salt aerosol and the atmospheric radiative fluxes is taken into consideration, and in run F sea salt interacts with radiation. The radiation budgets F_{SW} and F_{LW} are defined as the net solar and thermal radiative fluxes, respectively

$$F_{SW} = F_{SW}^{\uparrow} - F_{SW}^{\downarrow}, \tag{6.6}$$

$$F_{LW} = F_{LW}^{\uparrow} - F_{LW}^{\downarrow}. \tag{6.7}$$

The difference in the solar and thermal radiation budgets are calculated as

$$\Delta F_{SW} = F_{SW,F} - F_{SW,R}, \tag{6.8}$$

$$\Delta F_{LW} = F_{LW,F} - F_{LW,R} \tag{6.9}$$

where the indices F and R denote the values of the radiation budgets for the feedback and reference runs, respectively.

The horizontal three-day (24th-26th July) averages of the simulated ΔF_{SW} and ΔF_{LW} at the surface and the top of the atmosphere (TOA) are illustrated in Figure 6.39.

The difference in the net shortwave radiation shows similar properties at the surface and at the TOA. Over water in the approx. clear sky western Mediterranean and over the Atlantic off the African Coast a cooling is simu-

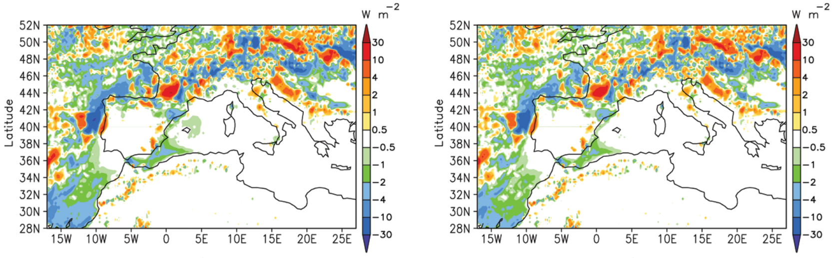

(a) Surface: ΔF_{SW}. (b) TOA: ΔF_{SW}.

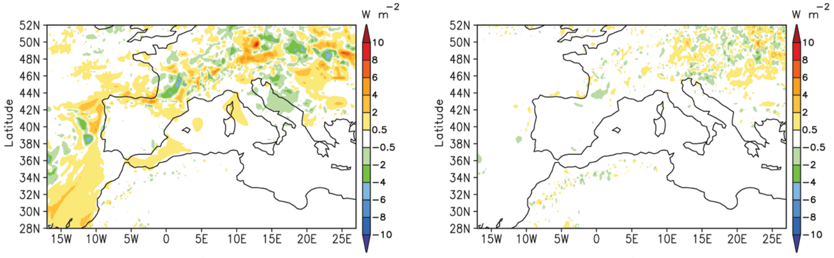

(c) Surface: ΔF_{LW}. (d) TOA: ΔF_{LW}.

Figure 6.39.: Difference (run F-run R) in solar radiation ΔF_{SW} and thermal radiation ΔF_{LW} at the surface and the top of the atmosphere, respectively, averaged over 3 days.

lated due to the sea salt aerosol. The cooling is on average down to the order of 2-4 W m^{-2} for the western Mediterranean and in the order of 4-5 W m^{-2} over the less cloudy parts of the Atlantic Ocean. Over most of the remaining parts of the model domain cloudy conditions occurred during the three days. In those areas, the sea salt DRE effect itself plays a minor role. Instead, the backscattering of clouds is clearly the dominant factor. This effect will be discussed below. The sea salt impact on the longwave radiation is the most important at the surface, whereas the effects at the TOA are even smaller. For areas of approximately cloud free conditions, the average impact on thermal radiation is in general about 0.5 W m^{-2} or lower. Near the African coast over the Atlantic Ocean, the maximum values of 2 W m^{-2} are simulated. Hence, for these conditions the longwave radiative impact is lower than the shortwave radiative impact, and with an opposite sign. These findings are supported by those of Li et al. (2008), which in their study found that the shortwave radiative forcing due to sea salt was an order of magnitude higher than that in the longwave range, and with opposite signs. From Figure 6.39 it is seen that the sea salt DRE for a typical weather situation with moderate wind speeds for this region is of minor importance. The impact of sea salt on the radiative fluxes is very small. As already mentioned, the largest radiative effects during this simulation period are caused by the clouds, which in connection to the low-level system passed over the northern parts of the domain during these three days. The spotty pattern in the differences of the radiation budgets is thus explained by the difference in cloud cover of runs F and R. In COSMO, it is distinguished between grid scale and sub-grid scale cloudiness. For cloudiness of 1 (100%) a complete grid cell is affected by cloud cover. For less than 100%, only partial cloudiness occurs. Both grid scale and sub grid scale cloudiness are determined as function of the ambient relative humidity and the treatment of clouds is accordingly highly sensitive to modifications of the atmospheric variables. For more details concerning the treatment of cloudiness cf. Doms et al. (2007). As the sea salt aerosol interacts with radiation, the thermodynamics of the atmosphere are modified. I.e., changes in atmospheric stability, temperature, and ambient relative humidity occur. These changes in turn cause a spatial shift in the cloud cover pattern. The modified cloud cover pattern again leads to a change in the incoming or outgoing radiation fluxes, i.e. the radiation budget is altered. The average difference in total cloud cover is depicted in Figure 6.40. The change in cloud cover ranges between -19% and +17%. The modifications in cloud cover lead to changes on the order of ±30 W m^{-2} in the solar range at the surface and the TOA. In the thermal range these impacts range between -4 and +10 W m^{-2} at the surface and are significantly lower at the TOA. The mean differences in the temperature at 2 m and the relative humidity for the lowest approximately 40 m are illustrated in Figure 6.41. The relative humidity is modified up to 3%. Temperature changes on the order of

-0.01 and -0.05 K are seen over the water for the less cloudy areas. As a result of the differences in the cloud cover pattern, the observed temperature differences reach up to 1 K for the more cloudy regions. These results are clear indications as to how non-linear the atmospheric response to the sea salt induced direct radiative modifications is.

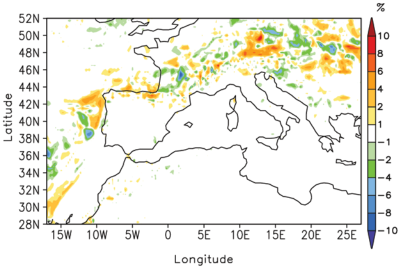

Figure 6.40.: Cloud cover difference (run F-run R), averaged over three days.

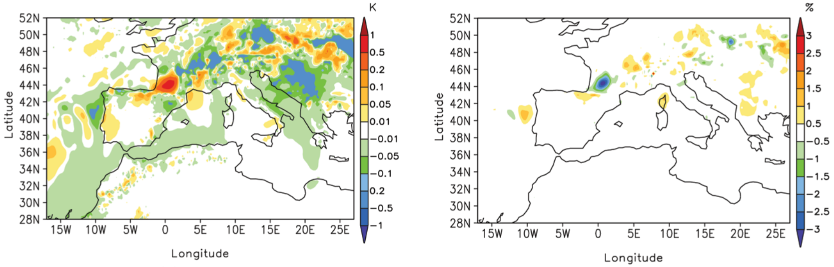

(a) ΔT_{2m}.

(b) ΔRH.

Figure 6.41.: Changes in temperature at 2 m, and relative humidity for the lowest approx. 40 m, respectively, averaged over three days.

Even though the sea salt loadings are low and only act to disturb the atmosphere slightly, it can be expected that a dependence of the changes in the radiative budgets show a dependence on the sea salt properties. An almost linear dependence of the radiative budgets on the sea salt loading was found by Li et al. (2008). In addition, Stanelle (2008) saw clear dependences between the mineral dust loading and differences in net radiation over West

Africa at the surface. For this purpose, the differences in solar and thermal radiation budgets at the surface and TOA are illustrated for every grid cell of the model domain as a function of the wet sea salt AOD at 550 nm (Figure 6.33) in Figure 6.42. Mean values and the corresponding standard deviation are given for each single case, respectively.

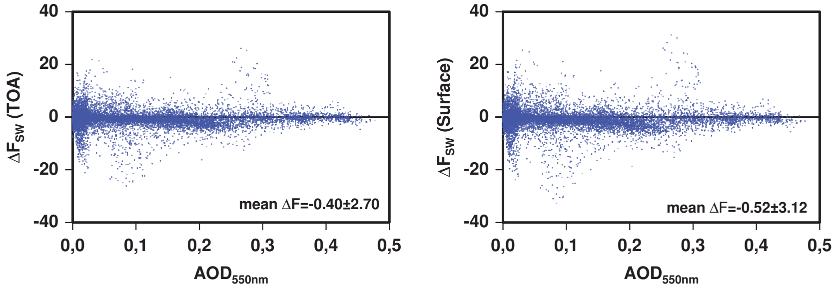

(a) TOA: ΔF_{SW}

(b) Surface: ΔF_{SW}

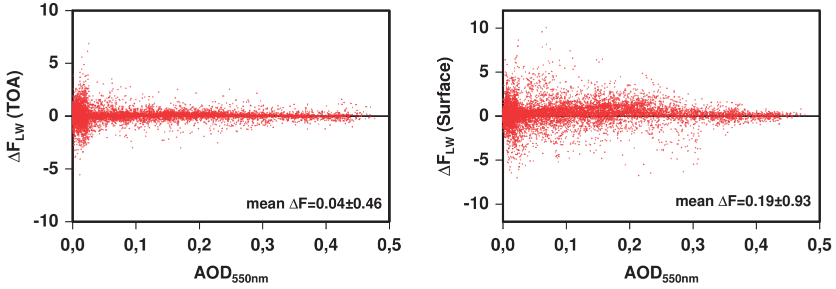

(c) TOA: ΔF_{LW}

(d) Surface: ΔF_{LW}

Figure 6.42.: Average change (run F-run R) of the solar and thermal radiation budgets Δ F_{SW} (top) and Δ F_{LW} (bottom) as a function of simulated AOD at 550 nm at the TOA (left) and at the surface (right).

On average, for all grid cells, a net cooling takes place both at the surface and at the top of the atmosphere. The shortwave net radiation is reduced by about 0.4 W m^{-2} at the TOA and 0.5 W m^{-2} at the surface when the sea salt aerosol is accounted for. The mean longwave warming is on the order of

0.04 W m^{-2} at the TOA and 0.2 W m^{-2} at the surface. The corresponding uncertainties to the respective average cooling and warming are however for both the shortwave and longwave ranges several order of magnitudes larger than the mean values. When considering all the grid points of the model domain, no dependence between the changes of the radiative budgets and the sea salt optical depth is found. The effect of the sea salt is masked out by the impact of the above-mentioned spatial shift in the cloud cover pattern.

Different effects can occur over land and ocean due to their different surface albedos. Several studies have indicated the importance of the surface albedo to the aerosol radiative effect (e.g., Li et al., 2008; Stanelle, 2008). The albedo describes in which proportion the incoming radiation is reflected by the surface. Above surfaces with low albedo, the amount of reflected radiation is thus lower than over surfaces with high albedos, such as ice or snow. The direct radiative aerosol effect has been found to diminish as the surface albedo tend to unity (Li et al., 2008). The reflected radiation from surfaces with high albedo is too large for an aerosol radiative effect to be of importance. Over surfaces with low albedo the amount of reflected radiation is small and the aerosol interaction with the reflected radiation is relatively of larger importance, than in the high albedo case. Thus, the relative importance of aerosol direct radiative effect is larger over areas with low surface albedo.

Based on these findings regarding the sea salt aerosol, it is investigated whether the sea salt aerosol in this case shows a relatively higher effect over the ocean, which is optically dark, than above land. In the following, the dependence of the modified net radiative fluxes on the sea salt optical depth is investigated for clear and cloudy skies, over land and over ocean. The mean changes of the solar and thermal radiative budgets over land and ocean are illustrated in Figure 6.43 as a function of the sea salt optical depth. The corresponding averaged changes of the radiation budgets as function of the sea salt optical depth are illustrated in Figure 6.44 for cloud free grid cells only. In Figure 6.43, where all the land and water grid cells are treated separately, large uncertainties are still found. The grid cells with clouds have to be sorted out to see the direct aerosol effect. This has been done for the respective land and water grid cells in Figure 6.44. The uncertainties now decrease, in general to the same order as the average values. A close to linear dependence of the modified radiative budgets on the AOD is also found. The solar radiative budgets decrease with increasing sea salt optical depths. Hence, a negative correlation between the solar radiative budgets decrease and the sea salt AOD is simulated. This effect is the most significant at the surface, compared to the effect at the TOA. The opposite occurs for the thermal radiative budgets, which increases with increasing optical depths. The thermal radiative budget changes are, as well as for the solar range, relatively greater at the surface. Comparing the effects over land to those over ocean, the largest difference is the higher amount of data over the oceans. This complicates any direct comparison. However, on average the cooling and warming, respectively, are relatively more significant over the ocean than over land. Even though the effects are small, this indicates the importance of the surface albedo to the sea salt DRE in this study.

The sea salt DRE was already seen to alter the surface near temperature field non-linearly (Figure 6.41(a)). The temperature at 2 m above ground is averaged over three days and illustrated as function of the averaged surface near sea salt wet mass density in Figure 6.45.

As expected from the net cooling effect due to the sea salt DRE when the whole domain is considered, the 2 m temperature change is, on average, negative. For high sea salt mass densities, almost no grid cells coincide with a surface warming. This is especially seen for cloud free grid points above the ocean in Figure 6.46. A dependence of the temperature change on the sea salt mass is seen most clearly when all the cloudy and continental grid cells are neglected. The same effect as for the radiative budgets is seen. The

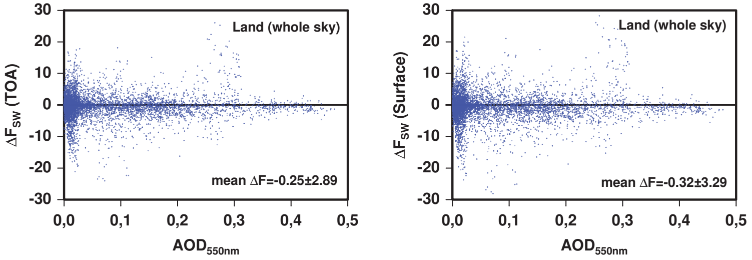

(a) TOA: ΔF_{SW}.
(b) Surface: ΔF_{SW}.

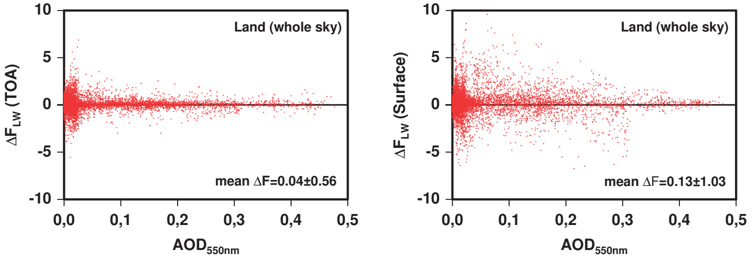

(c) TOA: ΔF_{LW}.
(d) Surface: ΔF_{LW}

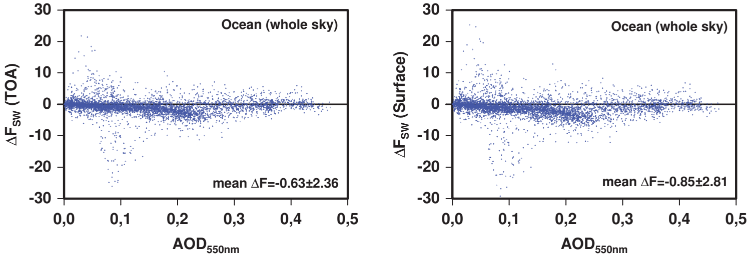

(e) TOA: ΔF_{SW}.
(f) Surface: ΔF_{SW}.

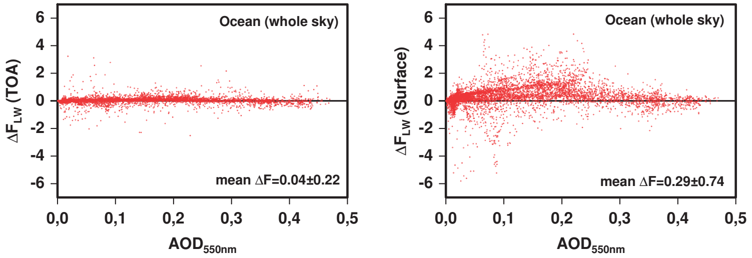

(g) TOA: ΔF_{LW}.
(h) Surface: ΔF_{LW}.

Figure 6.43.: Change (run F-run R) of the solar and thermal radiation budgets under all conditions as a function of simulated AOD, averaged over three days.

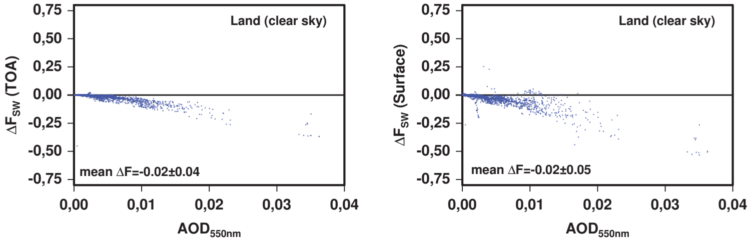

(a) TOA: ΔF_{SW}. (b) Surface: ΔF_{SW}.

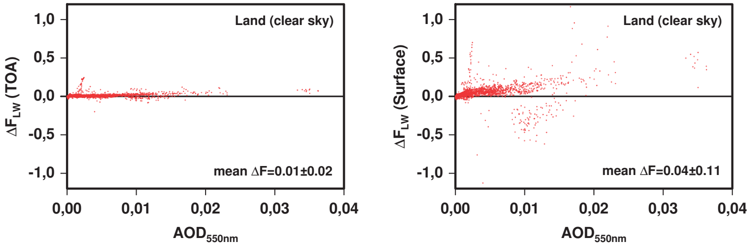

(c) TOA: ΔF_{LW}. (d) Surface: ΔF_{LW}.

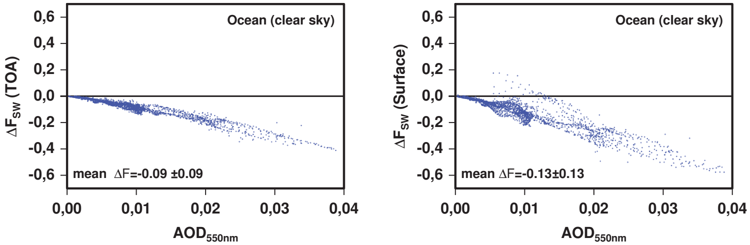

(e) TOA: ΔF_{SW}. (f) Surface: ΔF_{SW}.

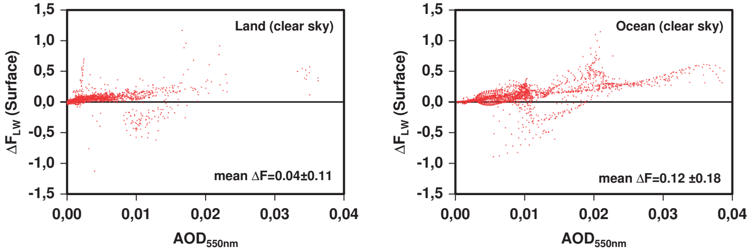

(g) TOA: ΔF_{LW}. (h) Surface: ΔF_{LW}.

Figure 6.44.: Change (run F-run R) of the solar and thermal radiation budgets at cloud free conditions as a function of simulated AOD, averaged over three days.

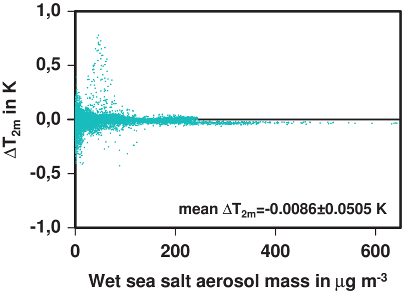

Figure 6.45.: 3-day averaged ΔT at 2 m above ground for the whole model domain as a function of average aerosol mass (run F-run R).

direct impact of the aerosol is masked out by the influence of changes in the cloud cover pattern.

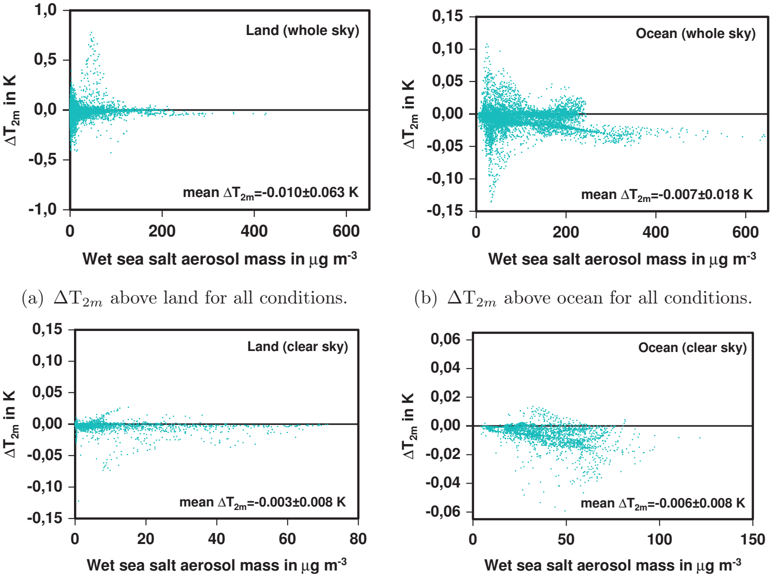

(a) ΔT_{2m} above land for all conditions. (b) ΔT_{2m} above ocean for all conditions.

(c) ΔT_{2m} above land for cloud free conditions (d) ΔT_{2m} above land for cloud free conditions

Figure 6.46.: ΔT at 2m as a function of average aerosol mass (run F-run R), averaged over three days.

The mean changes in the 2 m level temperature, solar and thermal radiative budgets are summarised in Table 6.3. Mean values and the corresponding standard deviation are presented for the complete domain and for clear and cloud free atmospheres above land and ocean, respectively. The sea salt aerosol DRE is seen to cause a reduction in the surface and TOA net solar radiation, both for clear and cloudy skies and both over land and ocean. The effect with respect to the longwave radiative budgets is a net increase. Over the clear sky ocean, the thermal and solar effects are seen to be on the same order of magnitude. The same effect is found over the clear sky land. This causes the net radiative effect for clear sky conditions to be approximately zero. Consequently, the net temperature change is small. Under consideration of the cloud free grid cells a mean cooling of 0.003 K and 0.006 K are seen over land and ocean, respectively. The mean reduction in temperature is most significant for the cloudy conditions, especially over land (-0.01 K) where the cloud cover was most significant.

Table 6.3.: Mean changes (run F-run R) in the solar and thermal net radiative fluxes in W m^{-2} and temperature difference at 2 m level in K. All the values are averaged over the simulation period 24th-26th July 2007, and presented with the corresponding standard deviation.

	Total	Land		Ocean	
		Whole Sky	Clear Sky	Whole Sky	Clear Sky
AOD_{550}	0.066±0.099	0.042±0.081	0.003±0.004	0.104±0.113	0.010±0.008
ΔF_{SW} (sfc)	-0.52±3.12	-0.32±3.29	-0.02±0.05	-0.85±2.8	-0.13±0.13
ΔF_{SW} (TOA)	-0.40±2.70	-0.25±2.89	-0.02±0.04	-0.63±2.36	-0.09±0.09
ΔF_{LW} (sfc)	+0.19±0.93	+0.13±1.03	+0.04±0.11	+0.29±0.74	+0.12±0.18
ΔF_{LW} (TOA)	+0.04±0.46	+0.04±0.56	+0.01±0.02	+0.04±0.22	+0.02±0.03
ΔT_{2m}	-0.009±0.051	-0.010±0.063	-0.003±0.008	-0.007±0.018	-0.006±0.008

6.4.7. Feedback on the Sea Salt Density Fields

As the atmospheric variables are modified due to the sea salt DRE, a feedback on the sea salt aerosol size distribution can also be expected. As already discussed in e.g., chapter 3, the advantage of online coupled models, such as COSMO-ART, is that the modified atmospheric state affects the aerosol fields, which in turn again have feedback on the atmospheric variables. This feedback loop was illustrated in Figure 3.2. The feedback mechanism, which is induced by the extinction of radiation, contains several aspects that may influence the aerosol size distribution. To distinguish between the different processes is a difficult task, since these are all coupled to each other. The altered cloud cover pattern leads to modified precipitation and thereby the washout of the aerosol is influenced. Furthermore, the modified atmospheric state in turn alters the emission flux of sea salt, as the emissions are wind speed and sea water temperature dependent. Thus, both source and sink processes are affected. The changes in the sea salt mass density and number density are the results of these atmospheric internal non-linear modifications. To investigate the average differences in the aerosol size distributions the sea salt mass density and number density for run R and F are compared. The differences in the 10 m level horizontal wind field and the surface near sea salt mass and number density distributions, averaged over three days are illustrated in Figures 6.47, 6.48 and 6.49, respectively. The difference fields are presented in their original units together with the relative importance in % compared to the reference values in each grid cell.

When the sea salt interaction with radiative fluxes is accounted for, the wind speed is on average modified by ± 0.2 m s^{-1}. Relative to the reference wind velocity (run R) the modifications range between -10 and +100%. This means that, locally, the wind speeds changed when the sea salt DRE was accounted for. The mean mass density, differences (run F-run R) range between -

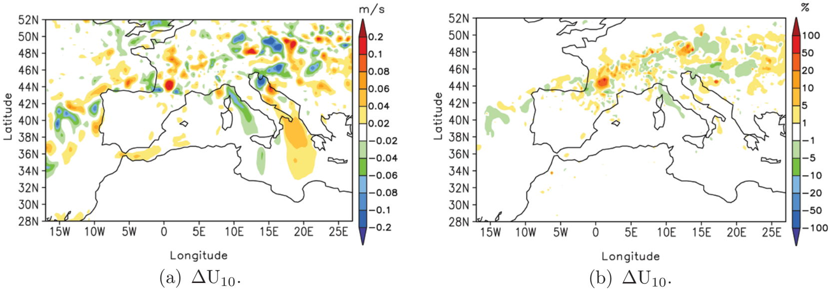

(a) ΔU_{10}. (b) ΔU_{10}.

Figure 6.47.: Simulated change (run F-run R) in the 10 m level wind velocity, averaged over 3 days.

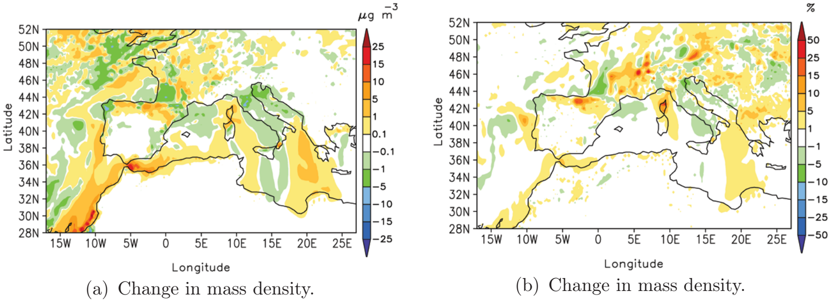

(a) Change in mass density. (b) Change in mass density.

Figure 6.48.: Simulated change (run F-run R) in sea salt mass density, averaged over 3 days.

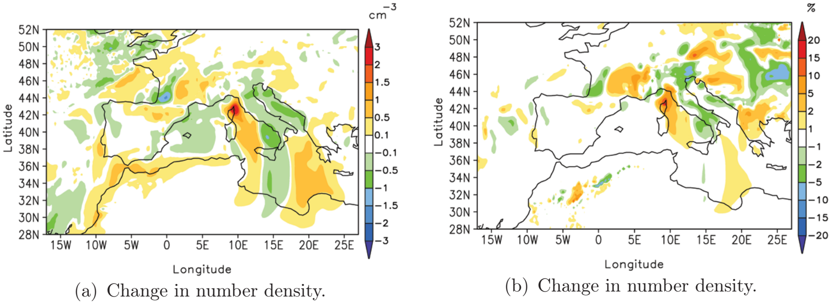

(a) Change in number density. (b) Change in number density.

Figure 6.49.: Simulated change (run F-run R) in sea salt number density, averaged over 3 days.

10 and +25 μg m^{-3}. Mass density changes can be seen to correlate with modifications in the wind velocity e.g. over the Central Mediterranean. The relative change compared to the reference mass densities in run R, where no interaction with radiation is accounted for, ranges to values of +50%. The greatest changes are seen for areas of low mass densities. Small changes contribute to large changes in per cent for these regions, such as over land. The largest modification of mass (25 μg m^{-3}) was seen south of Spain and over the Atlantic off the African coast. These differences correspond to about 1-5% of the mass density in the case of no interaction with the atmosphere. The number density of sea salt is locally modified by about -2 to +3 cm^{-3} on average over three days. North of Corsica the increase of 3 cm^{-3} corresponds to an increase of up to 20% of the reference number density. As for the mass density an area of increase aerosol densities is seen stretching from the south of Italy to the North of Africa. This area coincides with an area of slightly increased wind velocities. Along the North West African Coast, the number density increases. Relative to the reference number density these values of about 1 cm^{-3} correspond to less than 1%. The modifications in both wind and aerosol size distributions demonstrate the importance of the online coupled treatment of aerosol and atmospheric variables in atmospheric models.

6.5 Comparison with Simulated Anthropogenic DRE

The relative importance of sea salt aerosol DRE for this region is investigated by comparing the effect to that of anthropogenic aerosol. In simulations F$_{ant}$ and F$_{all}$ the feedback between anthropogenic and composite aerosols, respectively, with the atmosphere are considered. Composite aerosol is referred to as the sum of anthropogenic and sea salt aerosol. Organics and mineral dust particles are assumed to play a minor role for this region and time period, respectively. For this reason these aerosols are not considered in this comparison. The term anthropogenic is not completely correct since the nucleation of sulphuric acid from DMS sources enters the nucleation mode. The largest fractions of the aerosol modes are however still anthropogenic and the term anthropogenic is for simplicity used anyway.

In this section the simulated anthropogenic horizontal surface near concentrations and the anthropogenic optical depth are first presented. The optical depth of anthropogenic aerosol is compared to the composite optical depth when both sea salt and anthropogenic aerosols are accounted for. Thereafter, the differences in the solar and thermal radiation budgets and the 2 m level temperature fields are presented. The effect of the anthropogenic aerosol is compared to the case when both sea salt aerosol and anthropogenic aerosols are taken into consideration.

6.5.1. Simulated Fields of Anthropogenic Aerosol

The anthropogenic sub micron aerosol is described by five modes in COSMO-ART (Vogel et al., 2009). Two modes represent secondary aerosol containing internally mixtures of sulphate, ammonium, nitrate, and water. One mode represents pure soot and two more modes represent aged soot particles, containing mixtures of soot, sulphate, ammonium, nitrate, and water. All these modes are subject to condensational and coagulation processes. The mean number and mass densities of these five modes, averaged over three days are depicted in Figure 6.50 and 6.51, respectively for the lowest ca. 40 m.

Very high number densities in the soot free modes are simulated in the North of Spain. This is a result of the excessively high emissions of SO_2 in this area (Ch. Knote, 2010, personal communication). The emitted SO_2 is oxidised to sulphuric acid, which in turn nucleates and forms sulphate particles. Thus, what is seen here is a nucleation event which probably is the effect of an error in the emission data base for which a solution has until now not been

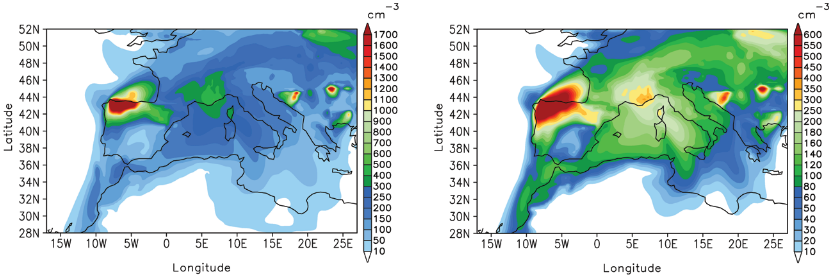

(a) Internally mixed aitken mode without soot.

(b) Internally mixed accumulation mode without soot.

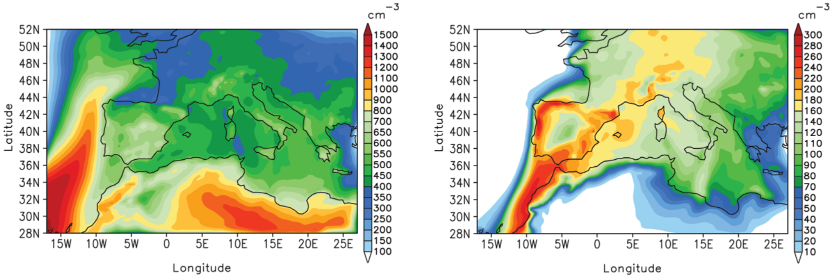

(c) Internally mixed aitken mode with soot.

(d) Internally mixed accumulation mode with soot.

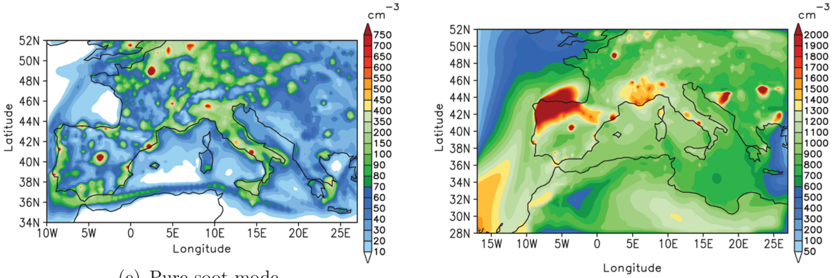

(e) Pure soot mode.

(f) Total number density.

Figure 6.50.: Simulated anthropogenic number densities near the surface for the lowest approx. 40 m.

provided. For this reason, not too much focus should be put on the number densities in this area. The pure soot mode is directly emitted and shows pattern of the shipping routes and larger cities. When the emitted soot particles age due to the condensation of sulphuric acid and coagulation with the other modes they enter the mixed soot modes. Due to advection to the south from the shipping routes, high number concentrations are seen over water in the southern part of the domain. In general, anthropogenic number densities are on the order of 1000 cm^{-3} in most of the domain. Values of more than 1600 cm^{-3} are simulated over the continent near areas of high gaseous or particulate emissions.

The mass densities are seen to show stronger horizontal gradients than the number densities. Over the Atlantic Ocean, the number densities are relatively high, but the mass is generally lower than 1 μg m^{-3} due to the small sizes of these particles. In the soot free modes, mass densities are on the order of up to 1 μg m^{-3} over the Mediterranean and 1-5 μg m^{-3} over the continent with maximum values of approximately 10 μg m^{-3}. The soot containing aitken mode mass density is in the order of 1 μg m^{-3}, with maximum values of 4 μg m^{-3}. The aged accumulation soot mode dominates the total mass density, on the order of 10 μg m^{-3} over most of the domain. The total mass density ranges from 10 μg m^{-3} over most of the domain to more than 30 μg m^{-3} locally. Over the Atlantic Ocean mass densities are less than 1 μg m^{-3}.

6.5.2. Simulated AOD and Impact on Atmospheric Variables

For radiative calculations, the optical depth is one of the crucial aerosol parameters. The optical depth of anthropogenic aerosol is now compared to the composite AOD when both anthropogenic and sea salt aerosols are considered. The aerosol optical depth at 550 nm is considered. The anthropogenic and composite optical depth of sea salt and anthropogenic aerosols are illustrated in Figure 6.52 for the 24th-26th July.

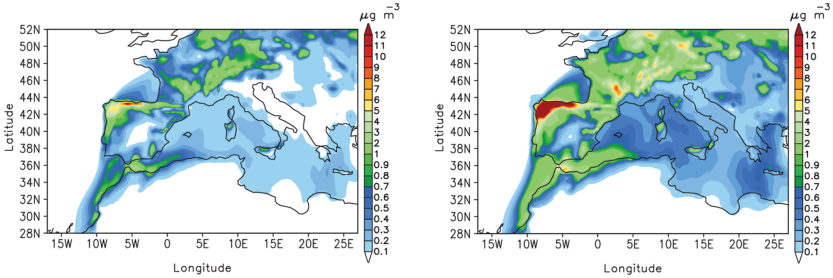

(a) Pure aitken mode. (b) Pure accumulation mode.

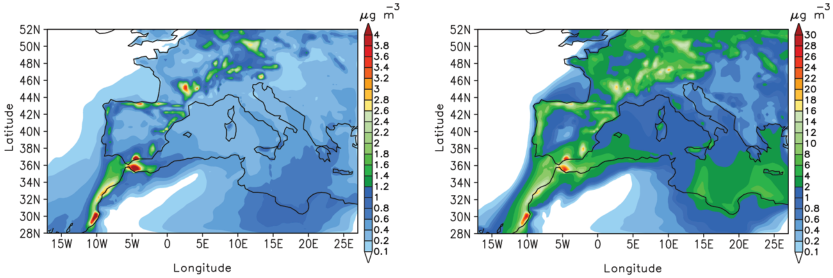

(c) Internally mixed aitken mode. (d) Internally mixed accumulation mode.

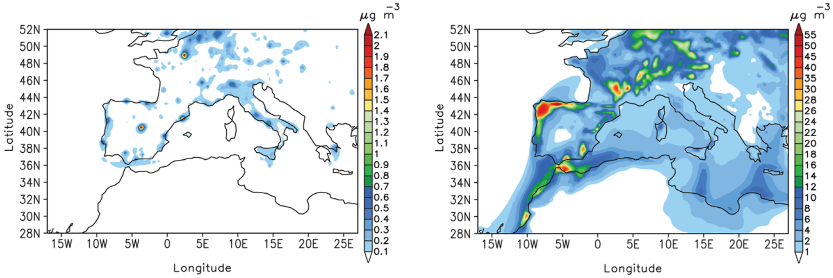

(e) Pure soot mode. (f) Total mass density.

Figure 6.51.: Simulated 3-day averaged anthropogenic mass densities near the surface for the lowest approx. 40 m.

The anthropogenic AOD is on average on the order of up to 0.25 over the European continent. This is within the typical range of anthropogenic AOD of 0.2-0.5 (Mulcahy et al., 2008, and references therein). By considering anthropogenic aerosol only, and neglecting the sea salt aerosol, the average

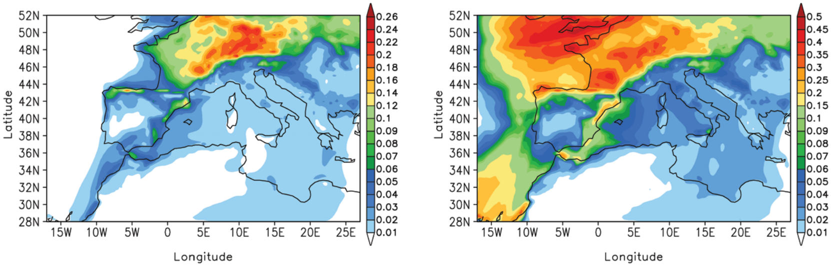

(a) Anthropogenic.

(b) Composite.

Figure 6.52.: Simulated mean anthropogenic AOD_{550} and mean sea salt and anthropogenic composite AOD_{550}. Please note the different scales.

AOD is underestimated for some parts over the continent and especially in the western Mediterranean and over the Atlantic Ocean. When the contributions of sea salt and anthropogenic aerosol to the composite AOD are accounted for, the AOD reaches values of 0.35 over the continent. Above the oceanic areas sea salt dominates the composite AOD with values exceeding 0.4 in the most windy regions (northern part of the domain), and between 0.2-0.3 over the Atlantic Ocean off the African Coast. The western Mediterranean is also dominated by the sea salt AOD, with values up to 0.2, compared to approximately 0.1 for the pure anthropogenic scenario.

The impact of the anthropogenic aerosol is now compared to the case when the effect of sea salt is also considered. The changes of the solar radiative budgets at the surface and TOA are illustrated for the anthropogenic and the composite cases in Figure 6.53. Due to the high amount of clouds over the continent, the DRE of anthropogenic aerosols is difficult to detect. The most significant difference between the anthropogenic case and the composite case is the reduction in solar radiation over the less cloudy areas over water. This is the effect of the sea salt aerosol, which is neglected only when anthropogenic aerosol is considered.

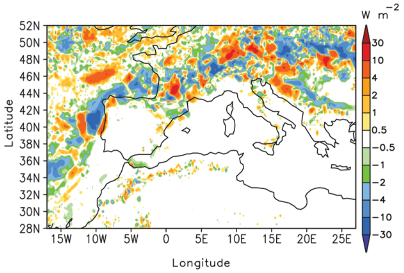

(a) TOA: ΔF_{SW} (ant).

(b) TOA: ΔF_{SW} (ant+ssa).

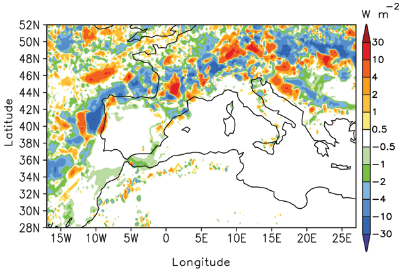

(c) Surface: ΔF_{SW} (ant).

(d) Surface: ΔF_{SW}(ant+ssa).

Figure 6.53.: Simulated changes in the solar radiative budget due to anthropogenic aerosol and both anthropogenic and sea salt aerosol, averaged over three days.

The changes in the net longwave radiation are illustrated in Figure 6.54 for the surface and TOA for the anthropogenic case and the case when both anthropogenic aerosol and sea salt aerosol are considered. At the TOA, no significant change in the longwave radiation budget can be detected as a direct result of the aerosol loading. The differences rather show spotty behaviour, indicating that spatial shifts of clouds are their origin. Comparing the pattern of the longwave radiative budget change at the surface with that of the clouds (Figure 6.55), this also follows changes in cloudiness closely for both cases. In addition, a slight warming (about 1 W m^{-2}) due to sea salt is simulated over the Atlantic Ocean for the composite case. On average, the differences in cloud cover between the anthropogenic case and the composite case are similar (Figure 6.55). Thus, the treatment of cloudiness in the model is about equally sensitive when anthropogenic aerosol is considered and when both anthropogenic and sea salt aerosols interact with radiation.

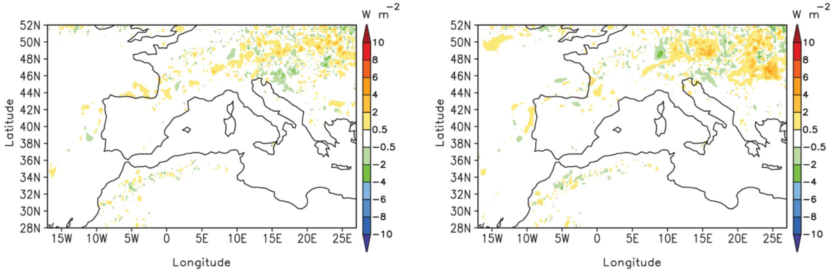

(a) TOA: ΔF_{LW} (ant).

(b) TOA: ΔF_{LW} (ant+ssa).

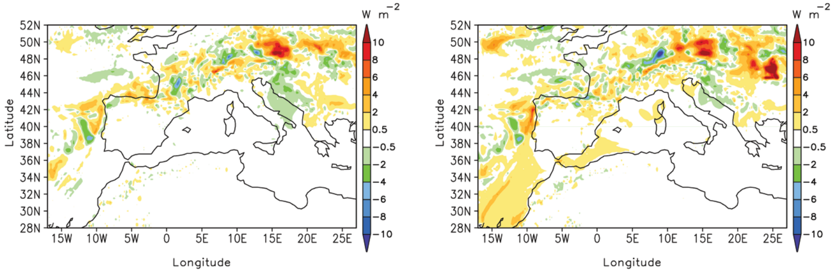

(c) Surface: ΔF_{LW} (ant).

(d) Surface: ΔF_{LW} (ant+ssa).

Figure 6.54.: Simulated changes in the thermal radiative budget due to anthropogenic aerosol and composite aerosol, respectively, averaged over three days.

The horizontal temperature changes at the 2 m level, induced by the direct radiative effects, are depicted in Figure 6.56. The temperature decreases show rather similar patterns over most of the continental parts of the domain for the two cases. In the case where the sea salt DRE is included, a temperature decrease over the Mediterranean and the South Western part of the simulation area occurs. These areas are characterized by water and mostly grid cells with less cloudiness, and here the anthropogenic loadings are negligible. For this region, the temperature difference is thus dominated by the cooling caused by the sea salt aerosol particles. This cooling is at the 2 m level on the order of -0.01 K.

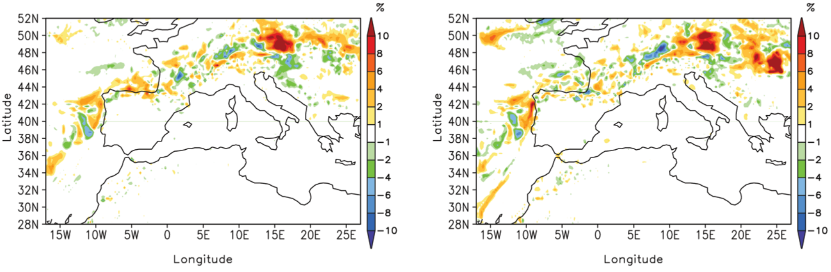

(a) Difference in cloud cover (ant).
(b) Difference in cloud cover (ant+ssa).

Figure 6.55.: Simulated change in the total cloud cover due to anthropogenic aerosol and composite aerosol, respectively, averaged over 24th-26th July.

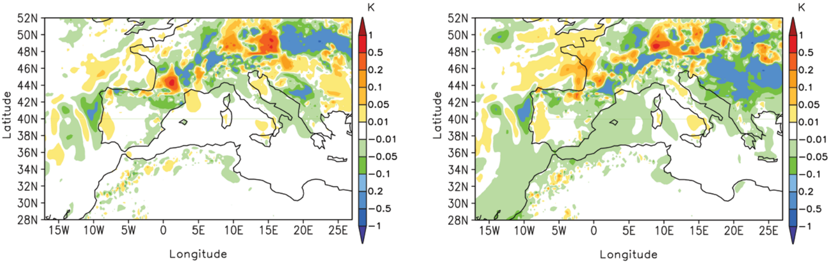

(a) T_{2m} (ant).
(b) T_{2m} (ant+ssa).

Figure 6.56.: Simulated temperature change due to anthropogenic and composite aerosol, averaged over three days.

A summary of the mean changes in the radiative budgets and temperature for the run where sea salt and anthropogenic aerosol are considered is presented in Table 6.4. The values of this table can be directly compared to Table 6.3, where the effect of sea salt exclusively was considered.

The aerosol DRE for this region during the 24th-26th July 2007 was seen to be small. The difference in the radiative budgets when both sea salt and anthropogenic aerosols are considered is larger than when only considering sea salt. This is found for the whole domain, and also when looking at land and ocean separately. The magnitude of the direct radiative effect is, however,

Table 6.4.: Summary of the DRE of anthropogenic and sea salt aerosol. Mean changes (run F_{all}-run R) in the solar and thermal net radiative fluxes in W m^{-2} and temperature difference at 2 m level in K. All values are averaged over the simulation period 24th-26th July 2007 and presented with the corresponding standard deviation.

	Total	Land		Ocean	
		Whole Sky	Clear Sky	Whole Sky	Clear Sky
AOD_{550} (tot)	0.095±0.111	0.082± 0.109	0.014± 0.009	0.114± 0.111	0.024± 0.010
AOD_{550} (ant)	0.028±0.042	0.040± 0.049	0.011± 0.006	0.010± 0.011	0.014± 0.005
AOD_{550} (ssa)	0.066±0.099	0.042± 0.081	0.003± 0.005	0.104± 0.113	0.010± 0.008
ΔF_{SW} (sfc)	-0.91±3.87	-0.79±3.94	-0.18 ±0.09	-1.10±3.75	-0.33±0.15
ΔF_{SW} (TOA)	-0.52±3.38	-0.44±3.51	+0.02 ±0.07	-0.65±3.19	-0.11±0.10
ΔF_{LW} (sfc)	+0.33±1.37	+0.34±1.59	+0.08 ±0.10	+0.33±0.94	+0.14±0.16
ΔF_{LW} (TOA)	+0.07±0.53	+0.09±0.65	+0.03 ±0.03	+0.05±0.24	+0.03±0.03
ΔT_{2m}	-0.014±0.055	-0.019±0.06	-0.007 ±0.013	-0.008±0.023	-0.006±0.007

the largest on the order of -1.1 W m^{-2} on average over the three days. This was found over the cloudy ocean. By comparing the temperature differences, the relative importance of sea salt to the composite DRE is achieved. The mean temperature differences at the 2 m level are for this purpose compared between run F_{all} and run F (cf. Table 6.3). The sea salt aerosol dominates the temperature decrease in the clear sky marine atmosphere. In the clear sky over the continent, the mean temperature decrease that is due to sea salt is about 43% of the mean decrease when anthropogenic aerosol is also considered. Hence, for the cloud free atmosphere over land the DRE of anthropogenic aerosols is the dominant. When looking at cloudy conditions, the temperature difference due to the sea salt DRE is approximately equal to that of the composite DRE. In the total domain the relative importance of sea salt is also seen. Over land in cloudy atmospheres the impacts of sea salt and the impacts of anthropogenic aerosol are about equal. This indicates a relative importance of the induced difference in cloud cover of sea salt, also over land, compared to anthropogenic aerosol. Thus, this study shows that the sea salt aerosol DRE can be found in the same or greater magnitude as that of anthropogenic aerosols, also for situations of moderate sea salt emissions.

Chapter 7

Summary and Conclusions

The direct radiative effect (DRE) of sea salt aerosol has been investigated for the regional scale. The non-hydrostatic online coupled regional scale model system COSMO-ART (Vogel et al., 2009) was for this purpose extended with respect to the treatment of the sea salt aerosol. Condensation of sulphuric acid onto the sea salt aerosol as well as the absorption of liquid water were introduced to COSMO-ART. Hence, throughout this study sea salt was treated as an internal mixture of NaCl, sulphate and water. Both natural and anthropogenic sources for the sulphuric acid were considered. For this reason, DMS emissions and the oxidation of DMS, through reactions with OH and NO_3 radicals, were taken into account. To calculate the water content the respective chemical constituents were partitioned into hypothetical electrolytes and the binary molalities were determined as a function of the ambient relative humidity (RH).

For the intention of investigating the DRE of sea salt aerosol, the aerosol optical properties are required. For this purpose, a new sea salt optical parameterisation was developed based on detailed Mie theory. This new optical parameterisation is valid for both solar and thermal ranges ($0.25<\lambda<30$ μm) and describes the optical properties of wet sea salt aerosol, containing the often measured internal mixture of NaCl and Na_2SO_4. Input variables for the Mie-calculations were wavelength dependent refractive indices and pre-simulated sea salt size distribution fields from COSMO-ART. Thus, information of the sea salt aerosol composition was specified. The effective refraction index of the aerosol was determined as a function of wavelength and composition with the partial molar refraction method (Stelson, 1990; Tang, 1997). This approach makes this parameterisation special, as the volume mixing rule usually is used. The new optical parameterisation provides the extinction coefficients, single scattering albedos, and asymmetry factors for the three sea salt aerosol modes in both sub micron and super micron sizes, and for eight spectral intervals.

The total extinction in the solar range was dominated by scattering, whereas the relative contribution of absorption became more important for longer wavelengths within the thermal range. The absorption within the thermal range was explained by the large fractions of water in all three modes. In addition to water, especially the film mode contained sulphate that also contributed to absorption in the thermal range. These absorbing components caused a decrease of the single scattering albedo from close or equal to 1 in the solar regime to less than 1 in the thermal regime. The mass specific extinction coefficient was largest for the film aerosol mode in the solar spectrum, and that of the spume mode was smallest. The extinction by the spume mode was also the least important in the thermal spectrum, whereas the relative importance of the jet mode compared to the film and spume mode increased. Thus, except for the spume mode, the extinction was seen to be the most important in the solar range. Even though the mass fraction of sea salt in the sub-micrometer range was low, compared to the large aerosol modes, this aerosol size was seen to contribute significantly to radiative extinction due to relatively larger mass extinction coefficients. The asymmetry parameter increased with increasing aerosol size and was positive, implying forward scattering. The extinction was found to depend linearly on the total wet sea salt mass density for all the spectral intervals and aerosol modes. Thus, the optical parameterisation for the extinction coefficient was based on the mass specific extinction coefficient, which was achieved from the output of the Mie-calculations, and on the simulated sea salt aerosol mass density. The asymmetry factor and single scattering albedo were seen to remain approximately constant within each respective spectral interval and regardless of the respective aerosol composition of each sea salt mode. The asymmetry parameter and single scattering albedo were represented by constants within each spectral interval and aerosol mode, respectively. This parameterisation is applicable for a wide spectrum and for variations in aerosol composition.

Simulations were performed with the extended version of COSMO-ART for a case study in July 2007. The considered area included most of the Mediterranean, parts of the North East Atlantic Ocean and South and Central Europe. During the considered days the Mediterranean was influenced by typical summer day conditions, moderate wind speeds and clear skies. The North East Atlantic was affected by a low level pressure system passing by in the northeast direction, causing high wind speeds and cloudy conditions both over the ocean and most of the continent.

In this study, sea salt radiative effects were investigated for the case of not participating in cloud droplet formation. This assumption led to overestimated mass and number densities in cloudy areas. The smallest aerosol, represented by the film mode, contributed the most to the total sea salt number density and the least to the total mass density. The spume mode contributed least to the number density and the jet mode comprised the largest fraction of mass relative to the other two modes. Simulated number and mass density fields showed large horizontal gradients towards lower concentrations over land. The film mode aerosol was the most efficiently transported, both horizontally and vertically. In the vertical, mean sea salt densities of >1 cm^{-3} were found up to altitudes of 2.5 km under cloud free atmospheric conditions over the Mediterranean. Under cloudy conditions, heights of up to 4 km were reached due to effective vertical transport in connection to the cyclone, when no formation of cloud condensation nuclei was accounted for. The effective vertical transport and elevated aerosol layers situated a few 100 m above ground indicate the importance of taking the whole sea salt column burden into consideration in for instance radiation calculations.

Due to the strong wind dependence of the DMS emissions, these emissions were strongest over the Atlantic Ocean during the simulation period. The relative importance of DMS compared to the anthropogenic emissions for SO_2 formation was found to be greatest for oceanic regions without anthropogenic emissions. Over windy areas in the Mediterranean Region DMS oxidation and anthropogenic emissions contributed with 50% each to the total SO_2. Anthropogenic emissions from shipping routes together with transport from continental sources were the dominant SO_2 sources for the Mediterranean. The anthropogenic SO_2 emissions consequently dominated the sea salt aerosol sulphate content over most of the Mediterranean. DMS oxidation was the dominant source for sea salt aerosol sulphate over the Atlantic Ocean in this study. The DMS oxidation locally contributed up to 40% of the sea salt aerosol sulphate over the Mediterranean. The condensation of sulphuric acid lead to largest amounts of sulphate in the sub micron sea salt mode, compared to the larger modes. Sulphate contributed the least to the total mass density in all the three sea salt modes. In this study, no wet-phase chemistry was considered, through which aerosol sulphate may efficiently form. This is currently introduced to COSMO-ART and the possible effect on the aerosol sulphate contents on the regional scale will be investigated in the near future. Water was the completely dominant chemical component of the sea salt aerosol for the whole size range for areas with RH exceeding 47%.

The simulations have also shown that the size distributions of the sea salt aerosol, in all size ranges, were modified by the absorption of water. Due to the additional water content, aerosol growth took place and in turn the atmospheric residence time was modified. For the sub micron mode, i.e., the film mode, the amount of aerosols was seen to increase due to the larger diameter. This was a result of less efficient deposition rates in this size range. The growth mainly resulted in shorter atmospheric residence times for the super micron modes, i.e., the jet and spume modes. For the largest sea salt mode, a decrease of up to 40% of the mass density dry component was achieved on average over three days. The number densities of the film and jet modes both decreased by up to 13%. It is a well known fact that sea salt effectively absorbs water, and here it was seen that this process impacts the size distribution of the aerosol significantly.

There currently exists much interest in examining the dependence of the sea salt aerosol optical depth and surface wind speed. There still exists no consensus on the shape of this dependence, varying from weak linear relations to strong exponential expressions (e.g., Smirnov et al., 2003; Jennings et al., 2003; Satheesh and Krishna Moorthy, 2006; Huang et al., 2009; Lehahn et al., 2010). In this study, a comparison between AOD and wind speed was performed, for which both the parameters were based on the online coupled model simulations. To the author's knowledge, this is the first time as such a comparison is made with model data. In most other studies, the information on aerosols is obtained from satellite information and the wind speed is either taken from ECMWF or QuickSCAT, which all are connected to various uncertainties. The simulated sea salt aerosol optical depth at 550 nm (AOD_{550}) showed a strong wind speed dependence, which was best represented by a power law fit. The comparison with wind dependences based on satellite observations revealed that the simulated AOD_{550} under cloud free conditions was in plausible order of magnitudes. In affinity with the satellite observations, the 10 m wind speed dependence was seen to offset at about 4 m s^{-1}.

This is the wind speed range, at which sea salt emissions set in as a result of the whitecap formation. At low wind speeds a wind independent contribution on the order of 0.02 was found from this study. As only sea salt is considered, no other aerosol could impact the AOD_{550}, this contribution was proposed to result from elevated aerosol that, due to its altitude, showed no correlation with surface wind speed. Since the simulated AOD_{550} compared well with satellite observations, a reasonable estimation of the subsequent sea salt DRE can also be expected.

By applying the new optical parameterisation within COSMO-ART, the feedback between the sea salt aerosol and the variables of the atmospheric state was studied. The radiation module GRAALS was extended to account for the optical properties of sea salt based on the currently simulated aerosol size distributions. Hence, the prescribed mean values of the optical properties were replaced with the currently simulated size distribution for the radiative calculations. The feedback loop was initialised by the extinction of atmospheric radiative fluxes by the sea salt aerosol. Due to changes in radiative fluxes, the atmospheric properties were altered in such a way that differences in both wind and aerosol size distributions occurred. The wind speed was modified with $\pm 0.2\ \mathrm{m\ s^{-1}}$, and the mass and number densities with up to 50% and 20%, respectively, with respect to the undisturbed reference fields. These modifications demonstrate the importance of the online coupled treatment of aerosol and atmospheric variables in atmospheric models.

Modifications in the thermodynamics of the atmosphere, induced by the sea salt DRE, lead to non-linearity between the AOD_{550} and the differences in the radiative budgets for cloudy conditions. By considering cloud free atmospheres the non-linear behaviour was suppressed and a more evident dependence of the radiative budget modifications on the aerosol optical depth was detected. The dependence was approximately linear, with a negative correlation for solar irradiance and positive for thermal fluxes. This dependence was seen more apparently above the ocean than over land. The mean effect over the ocean exceeded that of over land, suggesting a more meaningful effect above surfaces with lower albedo due to the relatively larger importance of the aerosol impact on the lower amount of reflected radiation over such surfaces compared to those with high albedo. Due to the interaction with thermal radiation a warming occurred at the surface, both during the night and day. For clear sky conditions, the thermal and solar effects were seen to be on the same order of magnitude. The net effect was consequently approximately zero.

The temperature difference was seen to be small for the considered days and area. The temperature decrease was on average over 3 days 0.006 K over clear sky ocean and 0.003 K over clear sky land. When including cloudy areas, the temperature decrease was at the highest on the order of 0.01 K. For high sea salt mass densities a negative correlation with the temperature difference at the 2 m level was detected. I.e., the cooling became more evident for larger sea salt aerosol loadings. The dependence was most unequivocal over the ocean, whereas any correlation above land was more diffuse. The correlation was the weakest for cloudy atmospheres due to the non-linear response of the atmosphere when spatial shifts of the cloud cover were included.

The relative importance of the sea salt DRE was compared to the DRE of composite aerosol, consisting of external mixtures of sea salt and anthropogenic aerosol. The sea salt aerosol DRE was found to dominate the temperature decrease in the clear sky marine atmosphere. The mean temperature decrease over land for clear conditions due to sea salt was approx. 43% of the mean decrease when anthropogenic aerosol also was considered. When looking at cloudy conditions, the temperature difference due to the sea salt DRE was about as large as that of the composite DRE. Over land in cloudy atmospheres, the impact of sea salt and the impact of anthropogenic aerosol were about equal. This indicated the importance of the induced difference in cloud cover of sea salt, also over land. Thus, this study shows that the sea salt aerosol DRE can be found in the same or greater order magnitude as that of anthropogenic aerosols, also for situations of moderate sea salt emissions. It is often argued that sea salt dominates the backscattering of sunlight in remote marine atmospheres. This study showed that the sea salt aerosol can also dominate the aerosol direct effect in polluted oceanic and coastal areas, and can contribute to the total DRE also over land.

Through this thesis, the COSMO-ART model system has made a major step forward, in now being able to consider the DRE of internally mixed wet sea salt aerosol. In the near future, both the direct and indirect radiative effect of sea salt will be investigated at the regional scale with COSMO-ART for various situations.

Appendix A

Results from Mie Calculations

A.1 Extinction Coefficients

In the following, the calculated extinction coefficients for the sea salt aerosol modes are presented for each of the eight spectral bands. More details are given in Section 5.2.1.

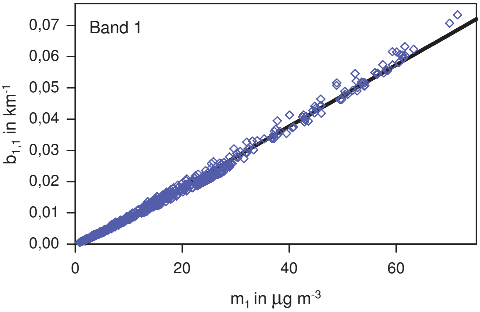

(a) The sea salt aerosol film mode, i=1

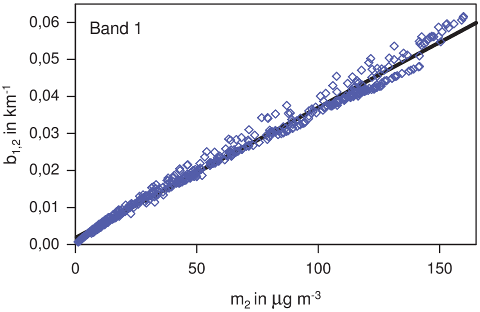

(b) The sea salt aerosol jet mode, i=2

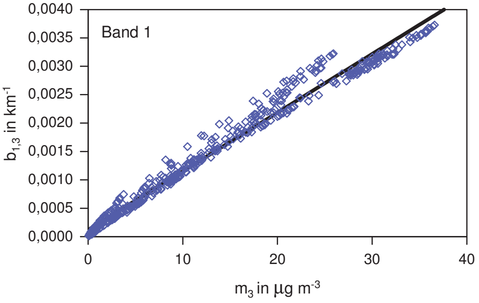

(c) The sea salt spume mode, i=3

Figure A.1.: Extinction coefficient in km^{-1} for k_b=1 as function of mass density m_i of each mode i respectively.

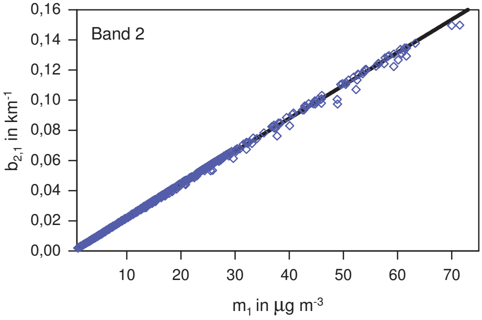

(a) The sea salt aerosol film mode, i=1

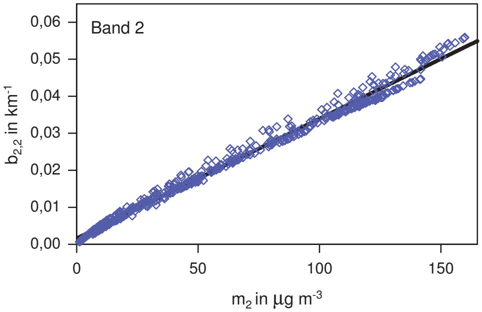

(b) The sea salt aerosol jet mode, i=2

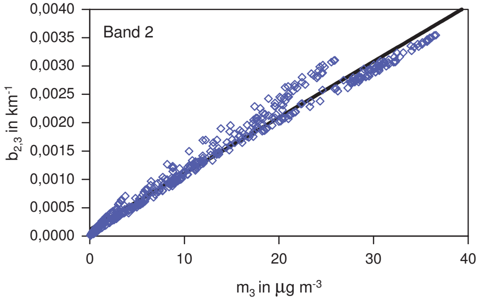

(c) The sea salt aerosol spume mode, i=3

Figure A.2.: Extinction coefficient in km^{-1} for k_b=2 as function of mass density m_i of each mode i respectively.

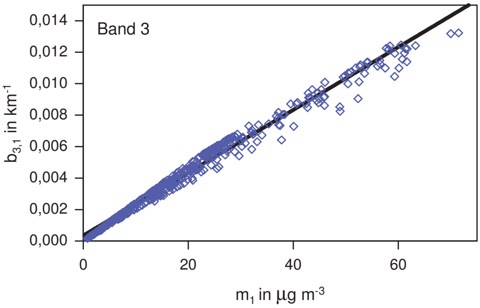

(a) The sea salt aerosol film mode, i=1

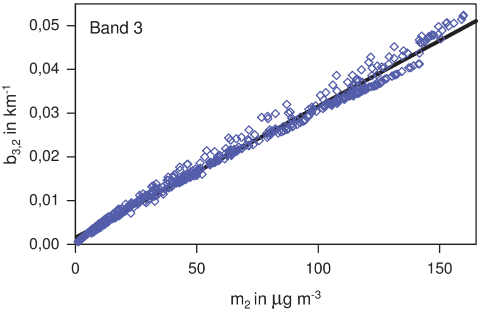

(b) The sea salt aerosol jet mode, i=2

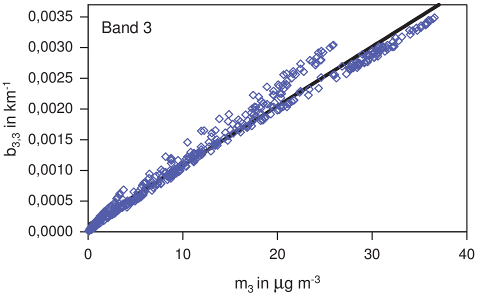

(c) The sea salt aerosol spume mode, i=3

Figure A.3.: Extinction coefficient in km^{-1} for k_b=3 as function of mass density m_i of each mode i respectively.

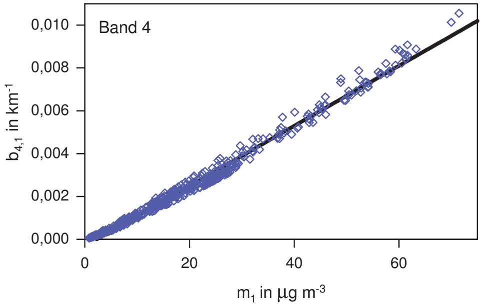

(a) The sea salt aerosol film mode, i=1

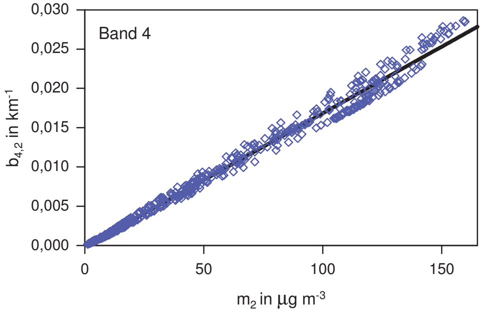

(b) The sea salt aerosol jet mode, i=2

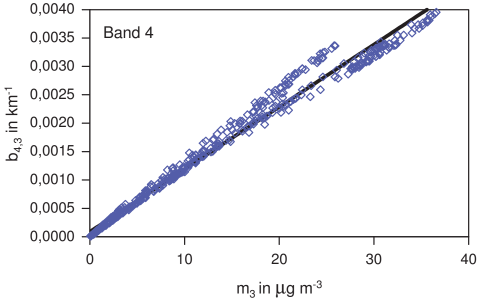

(c) The sea salt aerosol spume mode, i=3

Figure A.4.: Extinction coefficient in km^{-1} for k_b=4 as function of mass density m_i of each mode i respectively

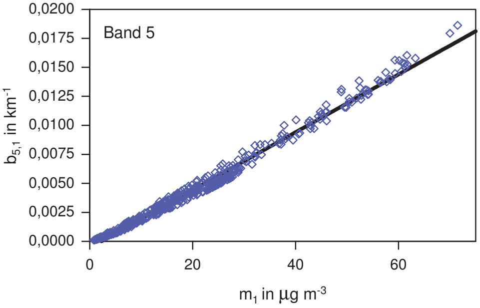

(a) The sea salt aerosol film mode, i=1

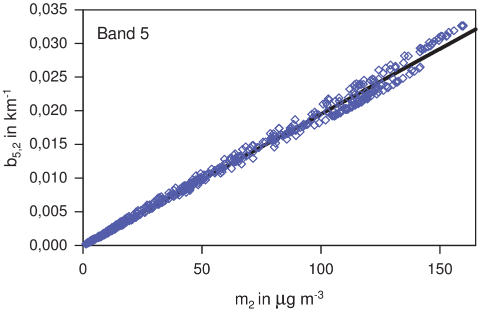

(b) The sea salt aerosol jet mode, i=2

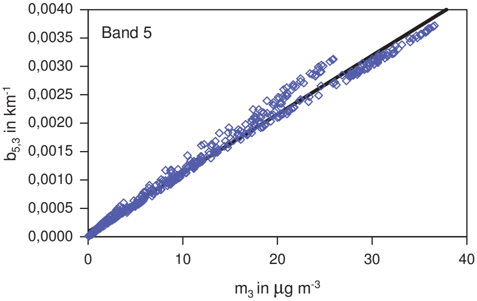

(c) The sea salt aerosol spume mode, i=3

Figure A.5.: Extinction coefficient in km^{-1} for k_b=5 as function of mass density m_i of each mode i respectively.

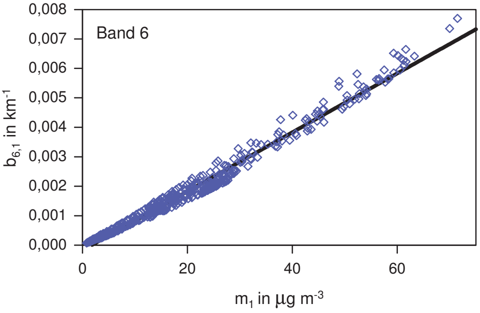

(a) The sea salt aerosol film mode, i=1

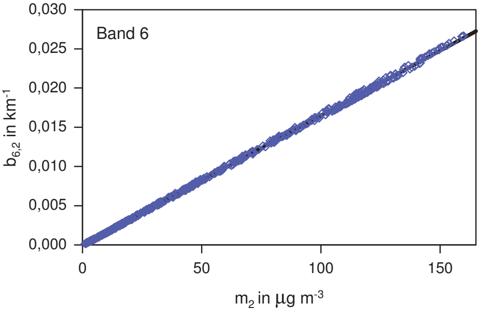

(b) The sea salt aerosol jet mode, i=2

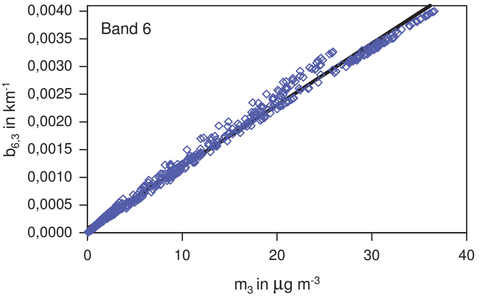

(c) The sea salt aerosol spume mode, i=3

Figure A.6.: Extinction coefficient in km^{-1} for k_b=6 as function of mass density m_i of each mode i respectively.

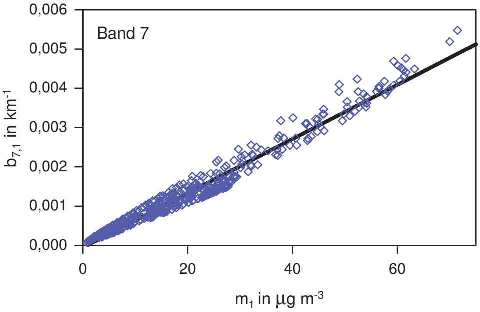

(a) The sea salt aerosol film mode, i=1

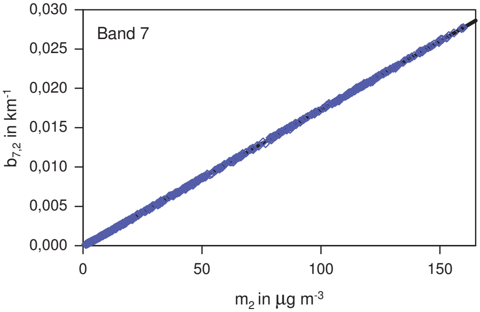

(b) The sea salt aerosol jet mode, i=2

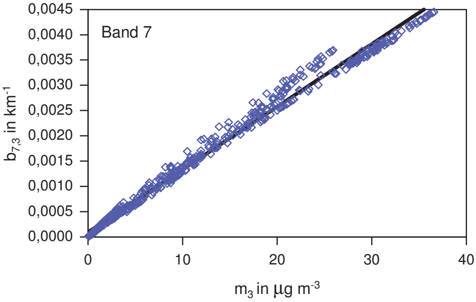

(c) The sea salt aerosol spume mode, i=3

Figure A.7.: Extinction coefficient in km^{-1} for k_b=7 as function of mass density m_i of each mode i respectively.

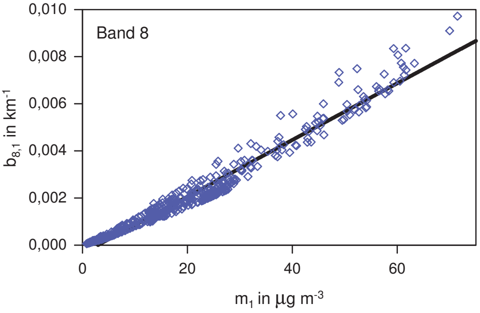

(a) The sea salt aerosol film mode, i=1

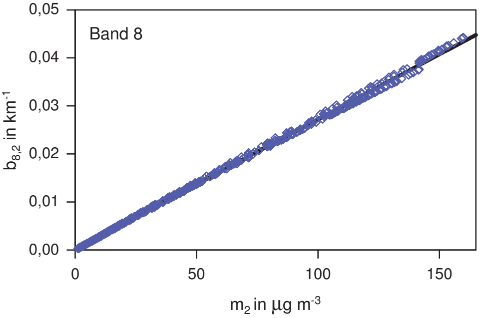

(b) The sea salt aerosol jet mode, i=2

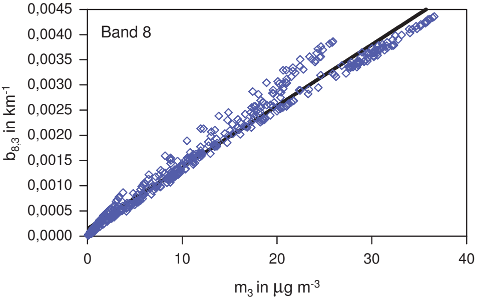

(c) The sea salt aerosol spume mode, i=3

Figure A.8.: Extinction coefficient in km^{-1} for k_b=8 as function of mass density m_i of each mode i respectively.

A.2 Single Scattering Albedo

In this Section, the calculated single scattering albedo for the sea salt aerosol modes are presented for each of the eight spectral bands. More details are given in Section 5.2.2.

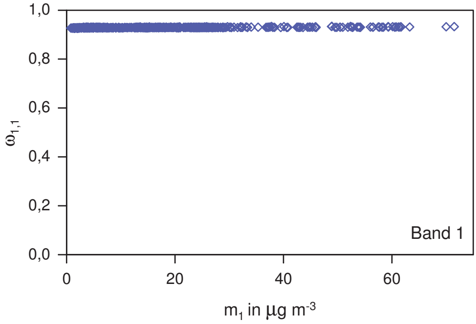

(a) The sea salt aerosol film mode, i=1

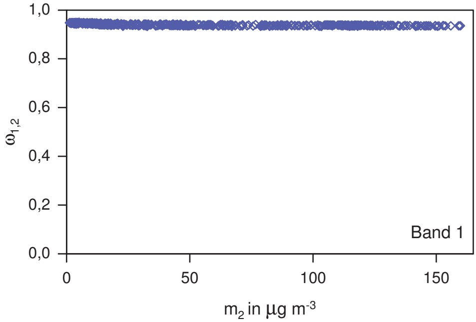

(b) The sea salt aerosol jet mode, i=2

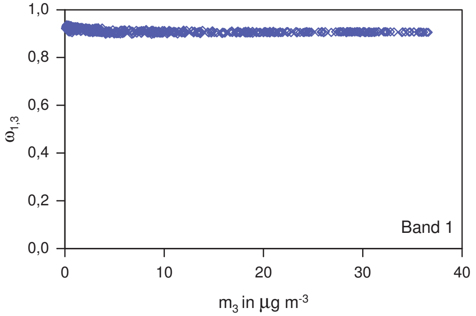

(c) The sea salt aerosol spume mode, i=3

Figure A.9.: Single scattering albedo for k_b=1 as function of mass density m_i of each mode i respectively.

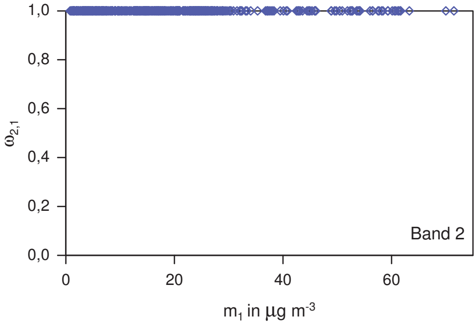

(a) The sea salt aerosol film mode, i=1

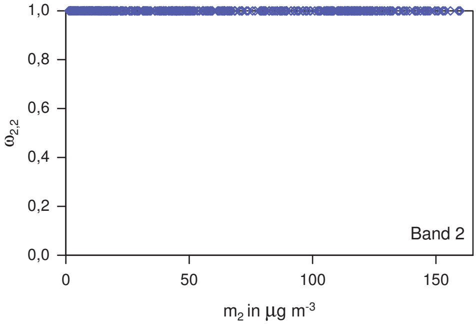

(b) The sea salt aerosol jet mode, i=2

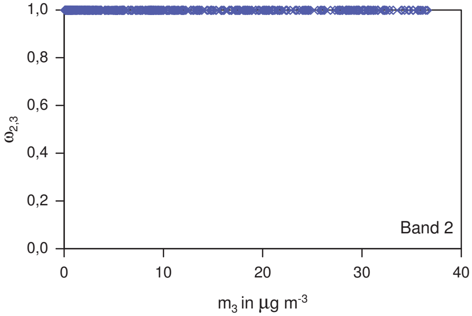

(c) The sea salt aerosol spume mode, i=3

Figure A.10.: Single scattering albedo for k_b=2 as function of mass density m_i of each mode i respectively.

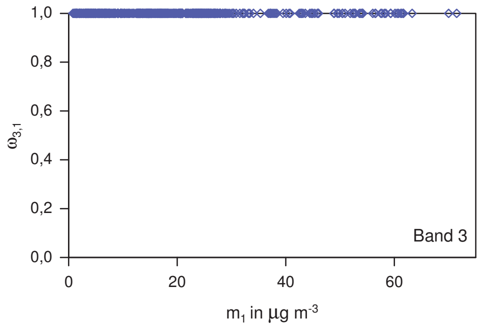

(a) The sea salt aerosol film mode, i=1

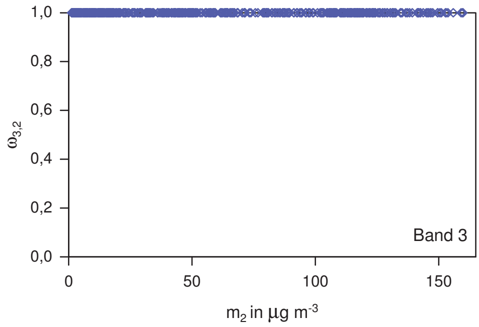

(b) The sea salt aerosol jet mode, i=2

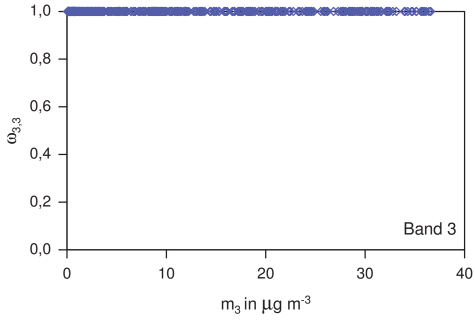

(c) The sea salt aerosol spume mode, i=3

Figure A.11.: Single scattering albedo for k_b=3 as function of mass density m_i of each mode i respectively.

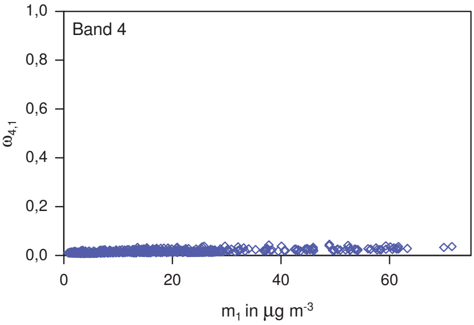

(a) The sea salt aerosol film mode, i=1

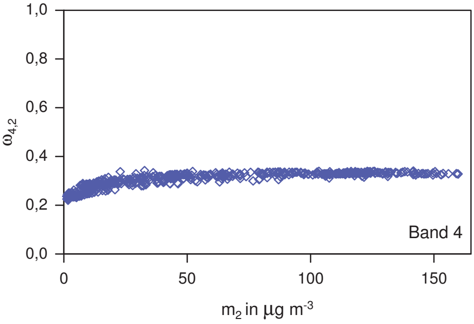

(b) The sea salt aerosol jet mode, i=2

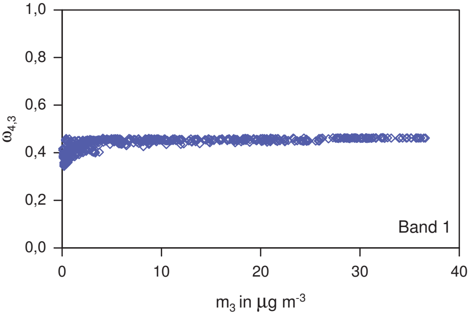

(c) The sea salt aerosol spume mode, i=3

Figure A.12.: Single scattering albedo for k_b=4 as function of mass density m_i of each mode i respectively.

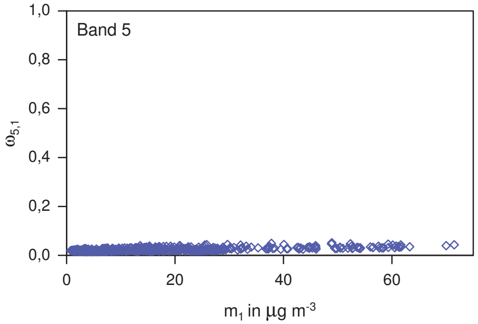

(a) The sea salt aerosol film mode, i=1

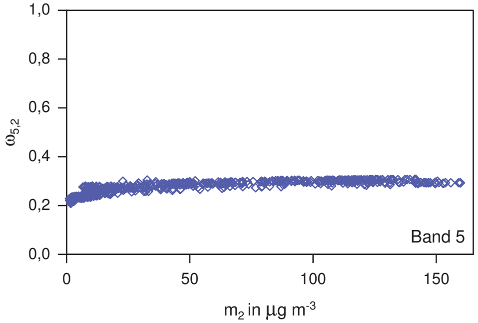

(b) The sea salt aerosol jet mode, i=2

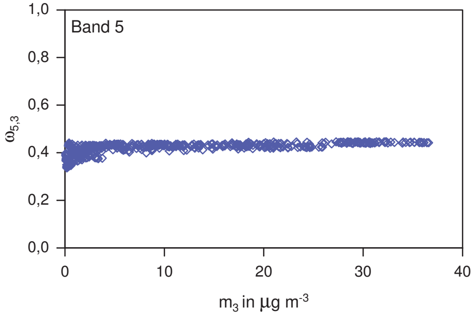

(c) The sea salt aerosol spume mode, i=3

Figure A.13.: Single scattering albedo for k_b=5 as function of mass density m_i of each mode i respectively.

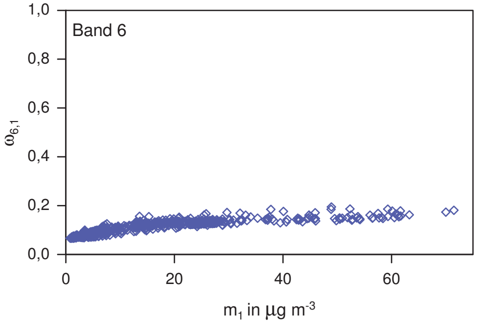

(a) The sea salt aerosol film mode, i=1

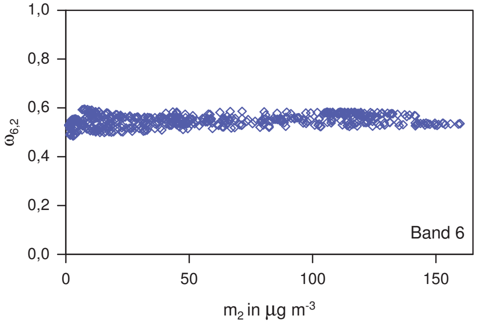

(b) The sea salt aerosol jet mode, i=2

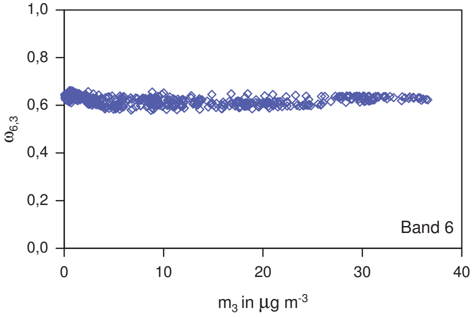

(c) The sea salt aerosol spume mode, i=3

Figure A.14.: Single scattering albedo for k_b=6 as function of mass density m_i of each mode i respectively.

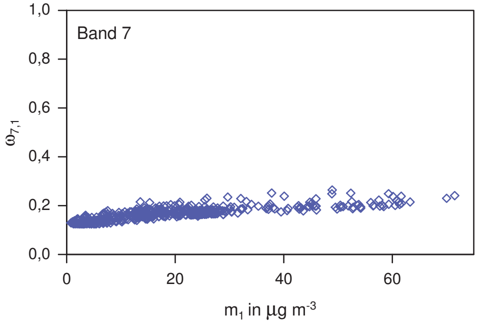

(a) The sea salt aerosol film mode, i=1

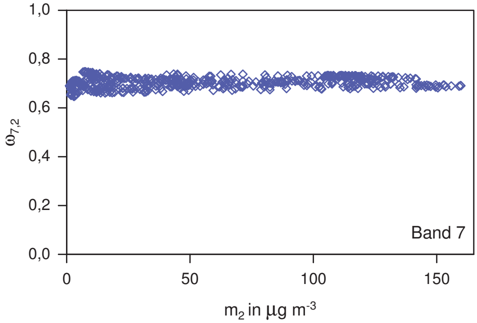

(b) The sea salt aerosol jet mode, i=2

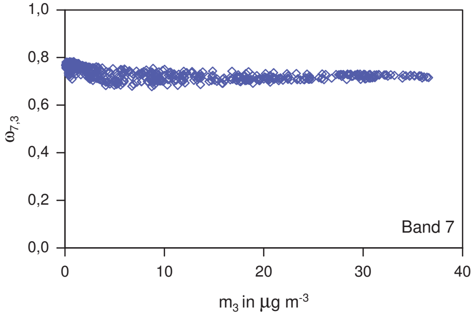

(c) The sea salt aerosol spume mode, i=3

Figure A.15.: Single scattering albedo for k_b=7 as function of mass density m_i of each mode i respectively.

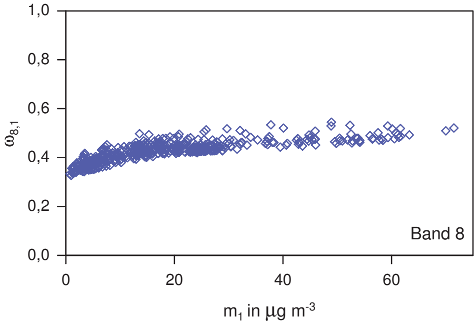

(a) The sea salt aerosol film mode, i=1

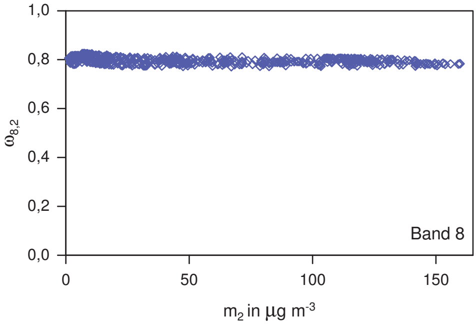

(b) The sea salt aerosol jet mode, i=2

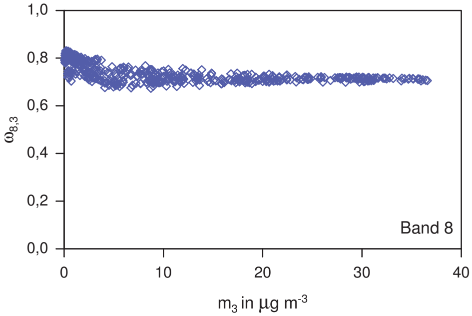

(c) The sea salt aerosol spume mode, i=3

Figure A.16.: Single scattering albedo for k_b=8 as function of mass density m_i of each mode i respectively.

A.3 Asymmetry Parameters

In the following, the calculated asymmetry parameters for the sea salt aerosol modes are presented for each of the eight spectral bands. More details are given in Section 5.2.3.

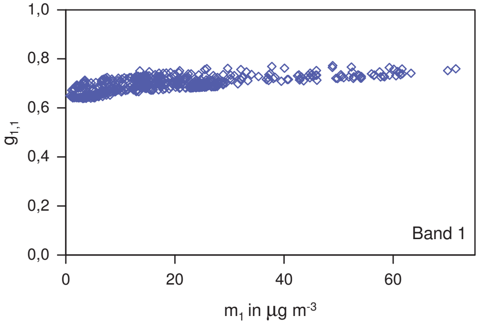

(a) The sea salt aerosol film mode, i=1

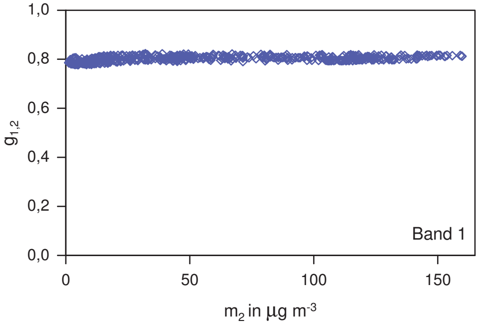

(b) The sea salt aerosol jet mode, i=2

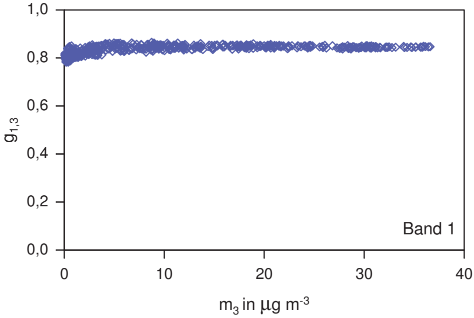

(c) The sea salt aerosol spume mode, i=3

Figure A.17.: Asymmetry parameter for k_b=1 as function of mass density m_i of each mode i respectively.

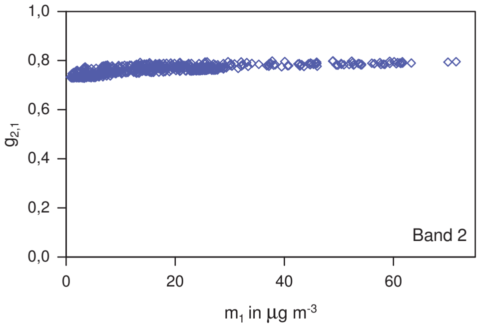

(a) The sea salt aerosol film mode, i=1

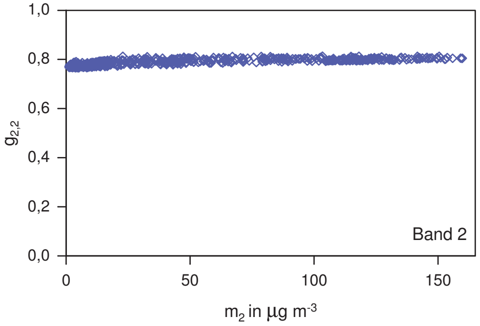

(b) The sea salt aerosol jet mode, i=2

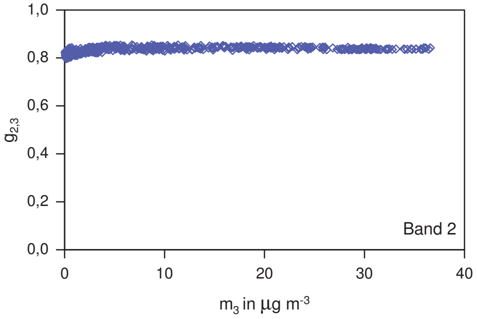

(c) The sea salt aerosol spume mode, i=3

Figure A.18.: Asymmetry parameter for k_b=2 as function of mass density m_i of each mode i respectively.

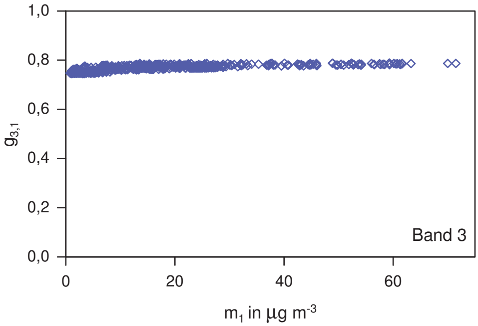

(a) The sea salt aerosol film mode, i=1

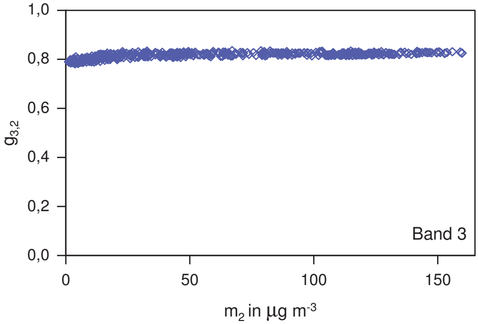

(b) The sea salt aerosol jet mode, i=2

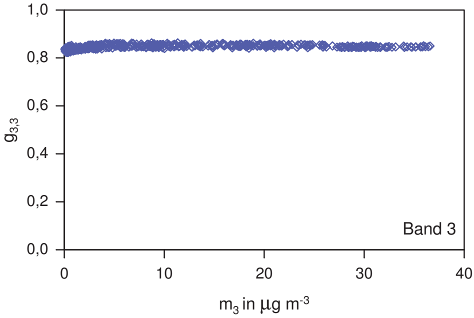

(c) The sea salt aerosol spume mode, i=3

Figure A.19.: Asymmetry parameter for k_b=3 as function of mass density m_i of each mode i respectively.

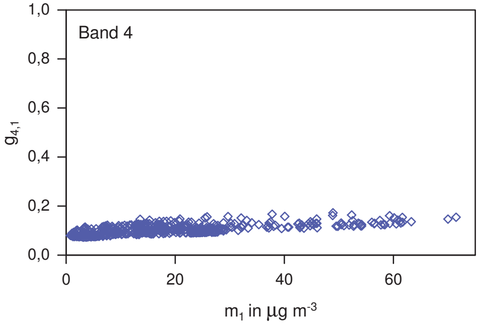

(a) The sea salt aerosol film mode, i=1

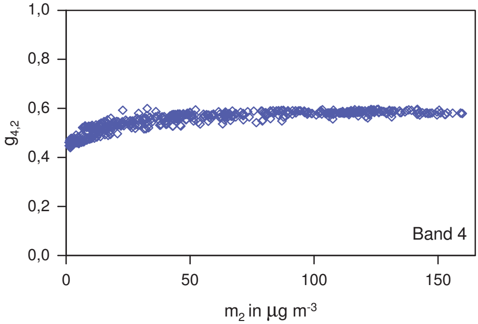

(b) The sea salt aerosol jet mode, i=2

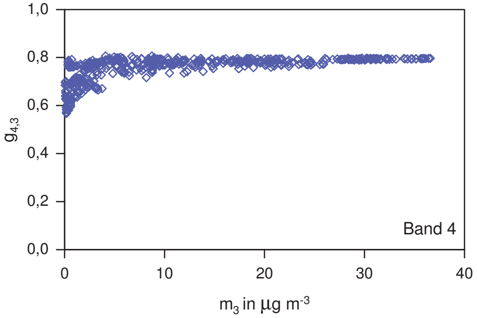

(c) The sea salt aerosol spume mode, i=3

Figure A.20.: Asymmetry parameter for k_b=4 as function of mass density m_i of each mode i respectively.

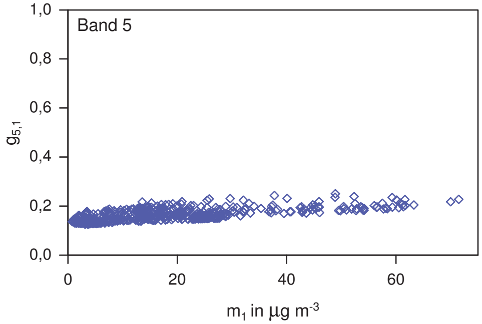

(a) The sea salt aerosol film mode, i=1

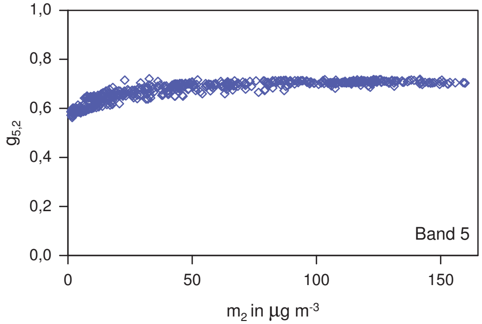

(b) The sea salt aerosol jet mode, i=2

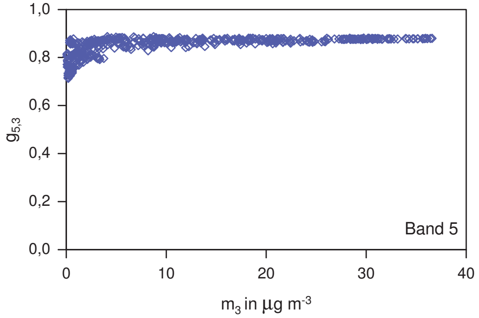

(c) The sea salt aerosol spume mode, i=3

Figure A.21.: Asymmetry parameter for k_b=5 as function of mass density m_i of each mode i respectively.

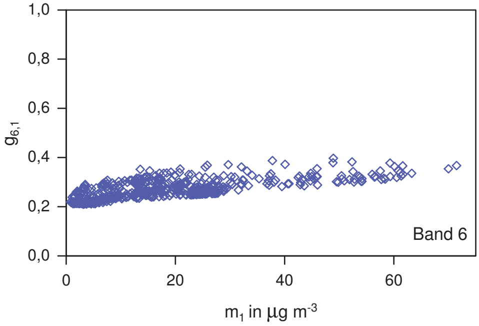

(a) The sea salt aerosol film mode, i=1

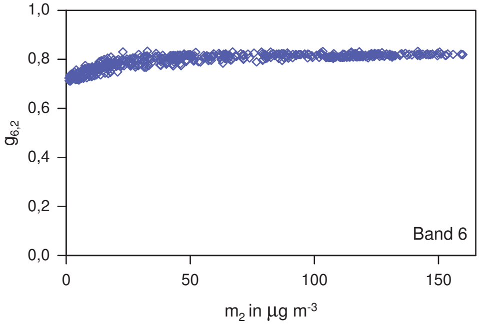

(b) The sea salt aerosol jet mode, i=2

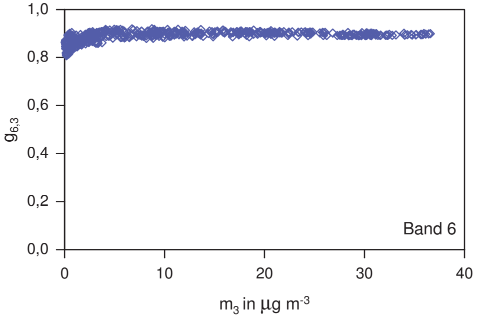

(c) The sea salt aerosol spume mode, i=3

Figure A.22.: Asymmetry parameter for k_b=6 as function of mass density m_i of each mode i respectively.

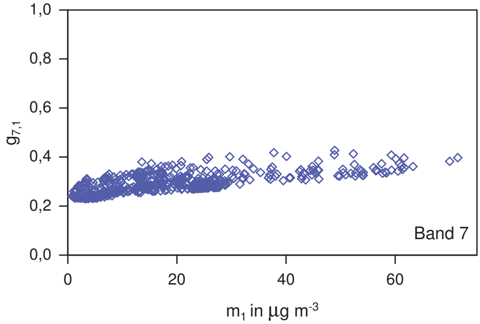

(a) The sea salt aerosol film mode, i=1

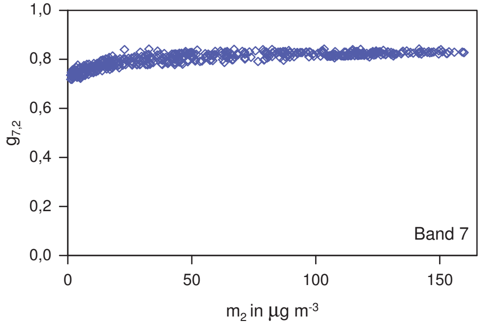

(b) The sea salt aerosol jet mode, i=2

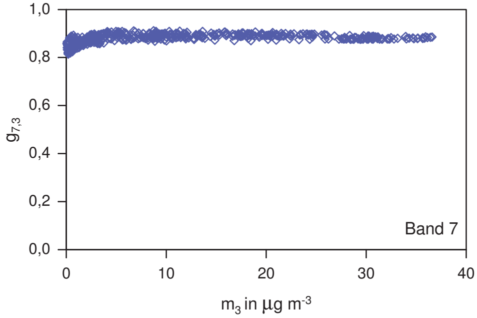

(c) The sea salt aerosol spume mode, i=3

Figure A.23.: Asymmetry parameter for k_b=7 as function of mass density m_i of each mode i respectively.

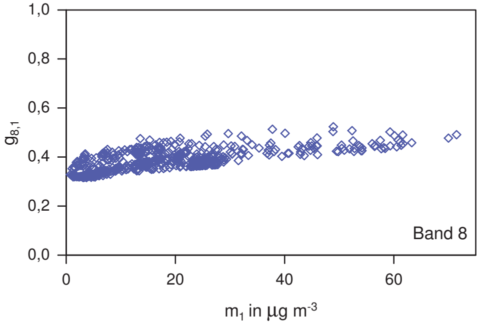

(a) The sea salt aerosol film mode, i=1

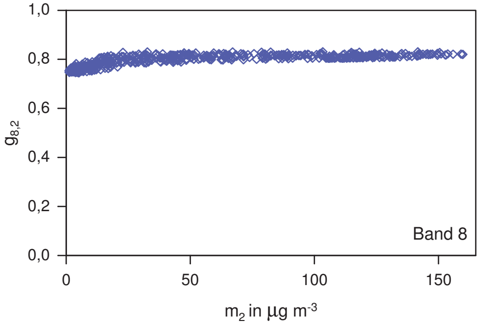

(b) The sea salt aerosol jet mode, i=2

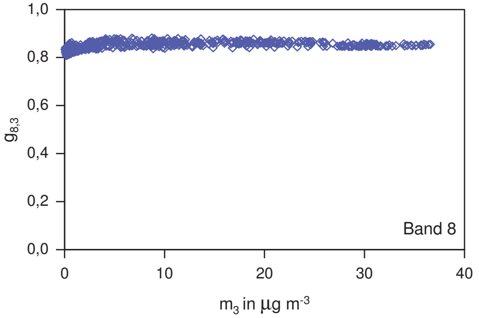

(c) The sea salt aerosol spume mode, i=3

Figure A.24.: Asymmetry parameter for k_b=8 as function of mass density m_i of each mode i respectively.

List of Symbols

Symbol	**Unit**	**Description**
Upper case letters		
A_1-A_4	-	parameters of the film mode emission parameterisation
$A_{s,\lambda}$, $A_{l,\lambda}$	m^3 mol^{-1}	molar absorption, and partial molar absorption
AOD	-	aerosol optical depth
B_1-B_4	-	parameters of the film mode emission parameterisation
B	-	parameter of the jet mode emission parameterisation
C_1, C_2	-	parameters of the spume mode emission parameterisation
C_c	-	Cunningham slip correction factor
$\dot{C}_{sulph}$	kg m^{-3} s^{-1}	total production rate of sulphuric acid
C_w	mol L^{-1}	DMS water concentration
$D_{g0,i}$, $D_{g0,i,mix}$	m	geometric median diameter with respect to the aerosol number density for mode i

$D_{g3,i}$	m	geometric median diameter with respect to the third moment of the aerosol distribution for mode i
$D_{gi,ini}$	m	geometric median diameter with respect to the aerosol number density for initialisation of mode i
$\hat{D}_k$	$m^2\ s^{-1}$	polydisperse diffusion coefficient of the k:th moment of an aerosol distribution
D_p	m	aerosol diameter
D_v	$m^2\ s^{-1}$	vapor diffusivity
F_0	$m^{-2}s^{-1}$	aerosol number flux
E_{DMS}	$kg\ m^{-3}s^{-1}$	time rate of change of the DMS mass density due to emission
$E_{m,i}$	$kg\ m^{-3}s^{-1}$	time rate of change of the mass density of mode i due to emission
$E_{N,i}$	$m^{-3}s^{-1}$	time rate of change of the number density of mode i due to emission
F_{DMS}	$kg\ m^{-2}s^{-1}$	DMS mass density flux
$F_{m,i}$	$kg\ m^{-2}s^{-1}$	mass density flux in mode i
$F_{N,i}$	$m^{-2}s^{-1}$	number density flux in mode i
F_{SW}, F_{LW}	$W\ m^{-2}$	shortwave and longwave radiation budgets
$F^{\downarrow}_{SW}$, $F^{\uparrow}_{SW}$	$W\ m^{-2}$	upward and downward directed shortwave radiation fluxes
$F^{\downarrow}_{LW}$, $F^{\uparrow}_{LW}$	$W\ m^{-2}$	upward and downward directed longwave radiation fluxes

$\Delta\mathrm{F}_{SW}$, $\Delta\mathrm{F}_{LW}$	W m^{-2}	difference in the shortwave and longwave radiation budgets initialised by the sea salt direct radiative effect
$\mathrm{F}^{\Psi_{m_i}}$, $\mathrm{F}^{\Psi_{m_{i,l}}}$	kg $\mathrm{m}^{-2}\mathrm{s}^{-1}$	turbulent flux of the mass density in mode i and substance l
$\mathrm{F}^{\Psi_{N_i}}$	$\mathrm{m}^{-2}\mathrm{s}^{-1}$	turbulent flux of the number density in mode i
$\overline{G}_3$	s^{-1}	mean total condensational growth rates for the third moment
$\overline{G}_{3,i}^{fm}$	s^{-1}	total mean condensational growth rates for the third moment of mode i for the free-molecular
$\overline{G}_{3,i}^{nc}$	s^{-1}	mean condensational growth rates for the third moment of mode i for the near-continuum regime
$\overline{G}_{3,i}$	s^{-1}	mean condensational growth rates for the third moment of mode i
$\overline{G}_{m,i}$	kg m^{-3} s^{-1}	mean condensational growth rates for the mass density of mode i
$\mathrm{I}_{3,i}^{nc}$	s^{-1}	Integral for determining the third moment condensational growth rate of mode i for the near contiuum regime
$\mathrm{I}_{3,i}^{fm}$	s^{-1}	Integral for determining the third moment condensational growth rate of mode i for the free molecular regime

$\mathrm{I}_{3,i}$	s^{-1}	Integral for determining the third moment condensational growth rate of mode i
K_w	$\mathrm{cm\ hour}^{-1}$	ocean-air interface gas transfer velocity
$\mathrm{M}_{k,i}$	$\mathrm{m}^k\ \mathrm{m}^{-3}$	k:th moment of the aerosol distribution for mode i
$\mathrm{M}_{w,DMS}$	$\mathrm{kg\ mol}^{-1}$	molecular weight of dimethyl sulphide
$\mathrm{M}_{w,j}$	$\mathrm{kg\ mol}^{-1}$	molecular weight of specie j
$\dot{M}_{3,sulph}$	$\mathrm{m}^3\ \mathrm{m}^{-3}\ \mathrm{s}^{-1}$	total rate of change of the third moment of sulphuric acid due to condensation
$\mathrm{M}_{3,i,mix}$	$\mathrm{m}^3\ \mathrm{m}^{-3}$	third moment of mode i for internally mixed aerosol distribution
N	m^{-3}	total particle number density
N_A	mol^{-1}	Avogadro's number
N_a	m^{-3}	total number density when including air molecules
N_i, $\mathrm{N}_{i,mix}$	m^{-3}	aerosol number density for pure and internally mixed mode i, respectively
$\mathrm{P}_l(\cos(\Theta))$	-	Legendre polynomials
Q_e	-	extinction efficiency
R	$\mathrm{J\ K}^{-1}\ \mathrm{mol}^{-1}$	ideal gas constant
$\mathrm{R}_{s,\lambda}$, $\mathrm{R}_{l,\lambda}$	$\mathrm{m}^3\ \mathrm{mol}^{-1}$	molar refractive index
S_i	$\mathrm{m}^2\ \mathrm{m}^{-3}$	aerosol surface area density of mode i

S_v	-	saturation ratio of condensing species
T, T_w	K	temperature, water temperature
$\Delta\mathrm{T}$, $\Delta\mathrm{T}_{2m}$	K	temperature difference
U_{10}	m s^{-1}	horizontal wind speed at 10 meters above ground
V_i	m^3 m^{-3}	aerosol volume density of mode i
V_s	m^3 m^{-3}	solution volume density
$\widetilde{V}_s$	m^3 mol^{-1}	solution molar volume density
$\overline{W}_{m,i}$	kg m^{-3} s^{-1}	mass density loss rate due to washout
$\overline{W}_{N,i}$	m^{-3} s^{-1}	number density loss rate due to washout
X_s	-	sulphate ratio
$\mathrm{Y}_{E,0}$-$\mathrm{Y}_{E,4}$	-	parameters of polynomial fits for calculations of the binary electrolyte molality
Lower case letters		
a_w	-	water activity equal to the relative humidity in fractional form
b, b_a, b_s	m^{-1}	extinction, absorption, and scattering coefficients
b_{k_b}, $\widetilde{b}_{k_b,i}$	m^{-1}	total and ith mode extinction coefficients within spectral interval k_b

$\overline{c}$	m s^{-1}	kinetic velocity of vapor molecules
c, c’	m s^{-1}	speed of light in vacuum and in medium, respectively
$\mathrm{c}_{m,s}$, $\mathrm{c}_{m,l}$	kg m^{-3}	solution mass density
$\mathrm{c}_{n,s}$, $\mathrm{c}_{n,l}$	mol m^{-3}	solution number density
f_l	-	volume fraction of specie l
g	m s^{-2}	gravitational acceleration
g	-	scattering assymetry parameter
g_{k_b}, $g_{k_b,i}$	-	total and ith mode scattering assymetry parameters within spectral interval k_b
k_B	J K^{-1}	Boltzmann constant
m_λ	-	complex index of refraction at wavelength λ
$\mathrm{m}_E^0(a_w)$	mol $\mathrm{kg}_{solvent}^{-1}$	binary electrolyte molality as function of the water activity
m_i,$\mathrm{m}_{i,mix}$	kg m^{-3}	particle mass density of mode i
$\mathrm{m}_{i,l}$	kg m^{-3}	mass density of substance l of internally mixed mode i
$\mathrm{m}_i^*(\ln D_p)$	kg m^{-3}	aerosol mass density distribution of mode i
m_j	kg m^{-3}	mass density of ion j
m_w	kg m^{-3}	aerosol liquid water content
n_E	mol m^{-3}	mole concentration of electrolyte E (NaCl, $\mathrm{Na_2SO_4}$)
$\mathrm{n}_i(D_p)$, $\mathrm{n}_i^*(\ln D_p)$	m^{-3} m^{-1}, m^{-3}	aerosol number density distribution for mode i

n_j	mol m^{-3}	mole concentration of ion j
$\mathrm{pcos}\,\Theta$	-	scattering phase function as function of scattering angle Θ
p_s	Pa	saturation vapor pressure of condensing species
r_a	s m^{-1}	aerodynamic resistance
$\overline{r}_{d,k}$	s m^{-1}	canopy resistance
r_p, r_{rh}	m	dry aerosol radius, and radius at the ambient relative humidity RH
u_*	m s^{-1}	friction velocity
$\mathbf{v}$, $\hat{\mathbf{v}}$	m s^{-1}	horizontal wind vector and the density weighted Reynolds averaged horizontal wind vector
v''		sub-gridscale value of the horizontal wind
$\overline{v}_{dep,m_i}$, $\overline{v}_{dep,m_i,mix}$	m s^{-1}	mean deposition velocity of the mass density of polydisperse aerosol
$\overline{v}_{dep,N_i}$, $\overline{v}_{dep,N_i,mix}$	m s^{-1}	mean deposition velocity of the number density of polydisperse aerosol
$\overline{v}_{sed,m_i}$, $\overline{v}_{sed,m_i,mix}$	m s^{-1}	mean sedimentation velocity of the mass density of polydisperse aerosol
$\overline{v}_{sed,m_i,l}$	m s^{-1}	mean sedimentation velocity of the mass density of component l of polydisperse aerosol
$\overline{v}_{sed,N_i}$, $\overline{v}_{sed,N_i,mix}$	m s^{-1}	mean sedimentation velocity of the number density of poly disperse aerosol

w	%	solute weight percent
w_*	m s^{-1}	convective velocity scale
x_l	-	mole fraction of substance l
y_q	-	dry solute mass fraction
Δz_s	m	height of the lowest model layer
Δz_h	m	height of the model layer h
Greek letters		
α	-	accomodation coefficient
α_p	m^{-3}	mean molecular polarisibility
γ	-	magnitude of charge of ion j
η_λ, $\eta_{s,\lambda}$, $\eta_{l,\lambda}$	-	real part of the complex refractive index
Θ	-	angle between incident and scattered radiation
κ_λ, $\kappa_{s,\lambda}$, $\kappa_{l,\lambda}$	-	imaginary part of the complex refractive index
λ	m	wavelenth of radiations
λ_{air}	m	mean free path in air
μ	kg m^{-1} s-1	dynamic viscosity coefficient of air
ν	m^2 s-1	kinematic viscosity coefficient of air
ν_a, ν_c	mol	respective number of moles of anion a and cation c in electrolyte E
ρ_q^0	kg m^{-3}	density of electrolyte condensing q in binary solution
ρ_a, $\overline{\rho}_a$	kg m$_{air}^{-3}$	total and mean density of humid air
ρ_l	kg m^{-3}	density of condensing specie l

$\rho_{i,mix}$	kg m^{-3}	aerosol density of internally mixed mode i
ρ_{NaCl}	kg m^{-3}	density of sodium chloride
ρ_p, $\rho_{p,l}$	kg m^{-3}	aerosol density and density of aerosol component l
ρ_{sulph}	kg m^{-3}	density of sulphuric acid
ρ_w	kg m^{-3}	density of water
σ_{gi}	-	geometric standard deviation of the aerosol size distribution for mode i
τ	-	aerosol optical depth
τ_a, τ_s	-	absorption and scattering optical depth
Φ	m^{-2} s^{-1}	particle flux per whitecap area
ϕ_a, ϕ_c	-	equivalent ion fractions for anions and cations respectively
χ_l	-	lth expansion coefficient of the Legendre polynomials
Ψ_T	-	size-independent portion of growth law
Ψ_{m_i}, Ψ''_{m_i}	-	normalised mass density and the sub grid-scale value
$\Psi_{m_{i,l}}$	-	normalised mass density of substance l
$\hat{\Psi}_{m_i}$, $\hat{\Psi}_{m_{i,l}}$	-	the density weighted Reynolds average of the normalised mass density

Ψ_{N_i}, $\Psi_{N_{i,mix}}$, Ψ''_{N_i}	-	normalised number density and the sub grid-scale value
$\hat{\Psi}_{N_i}$, $\hat{\Psi}_{N_{i,mix}}$	-	the density weighted Reynolds average of the normalised number density
Ω_i	-	partition coefficient for condensational growth of mode i
ω	-	single scattering albedo
ω_{k_b}, $\omega_{k_b,i}$	-	total and ith mode single scattering albedo for spectral band k$_b$

Miscellaneous characters

a	index for anions
c	index for cations
E	index for electrolytes (NaCl or Na_2SO_4)
i	subscript for each sea salt mode: film, jet and spume mode
j	index denoting ion type (H^+,Na^+,Cl^-,SO_4^{2-} or HSO_4^-)
k	order of moment of aerosol distribution
k_b	spectral band for radiative calculation
Kn_g	Knudsen number
l	subscript for substances
s	subscript for solution

Sc_k	Schmidt number
St_k	Stokes number

List of Figures

2.1. Sketch of the sea salt aerosol formation, i.e. sea spray, mechanism. 13
2.2. Averaged dry (left) and wet (right) deposition rates in g m^{-2} yr^{-1} of sea salt aerosol with dry radius of up to 5 μm for January 1999 to December 2001. Figure reproduced from Foltescu et al. (2005). 16
2.3. Global sea salt surface near mass density in μg(Na) m^{-3} for January (left) and July (right). Reproduced from Grini et al. (2002). 18
2.4. Average sea salt mass concentration in μg m^{-3} in the surface layer for January 1999-December 2001 for sea salt with a dry radius of up to 5 μm from Foltescu et al. (2005). 19
2.5. Optional caption for list of figures 23
2.6. Simplified sketch of the direct and semi-direct interaction between the aerosol and incoming solar radiation for cloud free and cloudy conditions. 26
2.7. The modal and sectional approximation to the aerosol size distribution. Reproduced from Riemer (2002). 29

3.1. The model system COSMO-ART. 34
3.2. The feedback loop accounted for in COSMO-ART. 35

3.3. Deposition of number (N) and mass density (m) for distributions with $\sigma_g = 2$ m and $r_a = 50$ s m^{-1} as a function of the geometric median diameter D$_g$. 45
3.4. Maritime aerosol optical depth in GRAALS. 49
3.5. Overview of the treatment of the aerosol radiative impact on the atmosphere and the resulting modification of the sea salt concentration and subsequent impact on the aerosol optical properties. 50

4.1. The considered DMS sea water provinces. 56

5.1. Pre-simulated mass densities of the respective chemical components of the film mode for the lowest approx. 40 m. 83
5.2. Pre-simulated mass densities of the jet mode for the lowest approx. 40 m. 83
5.3. Pre-simulated mass densities of the spume mode for the lowest approx. 40 m. 84
5.4. Real (left) and imaginary (right) parts of the refractive indices as a function of wavelength. 85
5.5. Asymmetry parameter in the solar range from Winter and Chýlek (1997). 97

6.1. Model domain with the lower left corner at (-19°E, 26°N) and the upper right corner at (30°E, 54°N). 99
6.2. Synoptic situation represented by 500 hPa geopotential in gpdm (black contours), surface pressure in hPa (white contours), and relative topography in gpdm (colours). Copyright www.wetter3.de. 103
6.3. Cloud cover. Copyright EUMETSAT, NERC Satellite Receiving Station, University of Dundee. 104
6.4. Simulated horizontal wind speed at 10 m with arrows indicating wind direction. 105

6.5. DMS emission rate as a function of wind speed. 107
6.6. Simulated DMS emission flux on 25th July, 8 UTC. 107
6.7. Vertical sum of the emissions at 7 UTC. 110
6.8. Simulated DMS mixing ratio, averaged over three days. 111
6.9. Simulated DMSO mixing ratio, averaged over three days. . . . 112
6.10. Horizontal mixing ratios of O_3 and NO_x for the lowest approx. 40 m, averaged over three days. 113
6.11. Simulated mixing ratios of OH and NO_3 for the lowest approx. 40 m, averaged over three days. 114
6.12. Simulated SO_2 from DMS oxidation and anthropogenic emissions, near the surface averaged over three days. 115
6.13. Anthropogenic sources. 116
6.14. DMS oxidation. 116
6.15. Simulated SO_2 mixing ratios, respectively, averaged over three days. 116
6.16. 3-day averaged dry number density and difference of the film mode for the lowest approx. 40 m. 117
6.17. 3-day averaged dry number density and difference of the jet mode for the lowest approx. 40 m. 118
6.18. 3-day averaged dry number density and difference of the spume mode for the lowest approx. 40 m. 118
6.19. 3-day averaged dry mass density and difference of the film mode for the lowest approx. 40 m. 119
6.20. 3-day averaged dry mass density and difference of the jet mode for the lowest approx. 40 m. 119
6.21. 3-day averaged dry mass density and difference of the spume mode for the lowest approx. 40 m. 120
6.22. Deposition (solid) and sedimentation (dashed) velocities for r_a=50 s m^{-1} of number (blue) and mass (green) densities for distributions with σ_g=1.9 m. 122

6.23. Film mode number density distribution for dry and wet aerosol distributions, respectively. 123
6.24. Film mode mass density distribution for dry and wet aerosol distributions, respectively. 123
6.25. 3-day averaged film mode mass densities close to the surface for the lowest approx. 40 m. 125
6.26. 3-day averaged jet mode mass densities close to the surface for the lowest approx. 40 m. 126
6.27. 3-day averaged mass density of the spume mode close to the surface for the lowest approx. 40 m. 127
6.28. 3-day averaged film mode SO_4^{2-} content for the lowest approx. 1 km. 128
6.29. Averaged relative contributions to total sea salt film mode SO_4^{2-} content, for the lowest 1 km. 129
6.30. Wet mass and number density at the surface for the lowest approx. 40 m, averaged over three days. 130
6.31. Vertical cross sections at 37°N of 3-day averages of the mass and number density, respectively. 130
6.32. Vertical cross sections at -7°E of 3-day averages of the mass and number density, respectively. 131
6.33. Wet sea salt AOD at 550 nm, averaged over three days. . . . 133
6.34. U_{10} averaged over 24th-26th July. 133
6.35. AOD_{550} as a function of the 10 m wind speed. Left: all data points. Right: the 99% percentile values. 137
6.36. Power law fit based on average AOD_{550} values (R=0.998) in black and exponential fit (R=0.938) in blue. 138
6.37. Simulated sea salt AOD_{550} in green and the observed relation in black, as a function of wind speed on 25th July, 12 UTC. . 139

6.38. Sea salt AOD as a function of wind speed according to Mulcahy et al. (2008) (M-08), Schinozuka et al. (2004) (S-04), and Glantz et al. (2009) (G-09). Green dotted line: Equation 6.2 with offset of 0.06. 140
6.39. Difference (run F-run R) in solar radiation ΔF_{SW} and thermal radiation ΔF_{LW} at the surface and the top of the atmosphere, respectively, averaged over 3 days. 143
6.40. Cloud cover difference (run F-run R), averaged over three days. 145
6.41. Changes in temperature at 2 m, and relative humidity for the lowest approx. 40 m, respectively, averaged over three days. . 145
6.42. Average change (run F-run R) of the solar and thermal radiation budgets Δ F_{SW} (top) and Δ F_{LW} (bottom) as a function of simulated AOD at 550 nm at the TOA (left) and at the surface (right). 146
6.43. Change (run F-run R) of the solar and thermal radiation budgets under all conditions as a function of simulated AOD, averaged over three days. 149
6.44. Change (run F-run R) of the solar and thermal radiation budgets at cloud free conditions as a function of simulated AOD, averaged over three days. 150
6.45. 3-day averaged ΔT at 2 m above ground for the whole model domain as a function of average aerosol mass (run F-run R). . 151
6.46. ΔT at 2m as a function of average aerosol mass (run F-run R), averaged over three days. 151
6.47. Simulated change (run F-run R) in the 10 m level wind velocity, averaged over 3 days. 154
6.48. Simulated change (run F-run R) in sea salt mass density, averaged over 3 days. 154
6.49. Simulated change (run F-run R) in sea salt number density, averaged over 3 days. 154

6.50. Simulated anthropogenic number densities near the surface for the lowest approx. 40 m. 157
6.51. Simulated 3-day averaged anthropogenic mass densities near the surface for the lowest approx. 40 m. 159
6.52. Simulated mean anthropogenic AOD_{550} and mean sea salt and anthropogenic composite AOD_{550}. Please note the different scales. 160
6.53. Simulated changes in the solar radiative budget due to anthropogenic aerosol and both anthropogenic and sea salt aerosol, averaged over three days. 161
6.54. Simulated changes in the thermal radiative budget due to anthropogenic aerosol and composite aerosol, respectively, averaged over three days. 162
6.55. Simulated change in the total cloud cover due to anthropogenic aerosol and composite aerosol, respectively, averaged over 24th-26th July. 163
6.56. Simulated temperature change due to anthropogenic and composite aerosol, averaged over three days. 163

A.1. Extinction coefficient in km^{-1} for k_b=1 as function of mass density m_i of each mode i respectively. 176
A.2. Extinction coefficient in km^{-1} for k_b=2 as function of mass density m_i of each mode i respectively. 177
A.3. Extinction coefficient in km^{-1} for k_b=3 as function of mass density m_i of each mode i respectively. 178
A.4. Extinction coefficient in km^{-1} for k_b=4 as function of mass density m_i of each mode i respectively 179
A.5. Extinction coefficient in km^{-1} for k_b=5 as function of mass density m_i of each mode i respectively. 180
A.6. Extinction coefficient in km^{-1} for k_b=6 as function of mass density m_i of each mode i respectively. 181

A.7. Extinction coefficient in km^{-1} for k_b=7 as function of mass density m_i of each mode i respectively. 182
A.8. Extinction coefficient in km^{-1} for k_b=8 as function of mass density m_i of each mode i respectively. 183
A.9. Single scattering albedo for k_b=1 as function of mass density m_i of each mode i respectively. 185
A.10. Single scattering albedo for k_b=2 as function of mass density m_i of each mode i respectively. 186
A.11. Single scattering albedo for k_b=3 as function of mass density m_i of each mode i respectively. 187
A.12. Single scattering albedo for k_b=4 as function of mass density m_i of each mode i respectively. 188
A.13. Single scattering albedo for k_b=5 as function of mass density m_i of each mode i respectively. 189
A.14. Single scattering albedo for k_b=6 as function of mass density m_i of each mode i respectively. 190
A.15. Single scattering albedo for k_b=7 as function of mass density m_i of each mode i respectively. 191
A.16. Single scattering albedo for k_b=8 as function of mass density m_i of each mode i respectively. 192
A.17. Asymmetry parameter for k_b=1 as function of mass density m_i of each mode i respectively. 194
A.18. Asymmetry parameter for k_b=2 as function of mass density m_i of each mode i respectively. 195
A.19. Asymmetry parameter for k_b=3 as function of mass density m_i of each mode i respectively. 196
A.20. Asymmetry parameter for k_b=4 as function of mass density m_i of each mode i respectively. 197
A.21. Asymmetry parameter for k_b=5 as function of mass density m_i of each mode i respectively. 198

A.22. Asymmetry parameter for k_b=6 as function of mass density m_i of each mode i respectively. 199
A.23. Asymmetry parameter for k_b=7 as function of mass density m_i of each mode i respectively. 200
A.24. Asymmetry parameter for k_b=8 as function of mass density m_i of each mode i respectively. 201

List of Tables

3.1. Initial median diameter $D_{gi,ini}$ and corresponding standard deviation with respect to the number density of freshly emitted aerosol in the sea salt film mode, jet mode, and spume mode. 37

3.2. List of the spectral bands considered in COSMO-ART based on the GRAALS radiation scheme (Ritter and Geleyn, 1992). 48

4.1. DMS sea water concentration in COSMO-ART. 57

4.2. Coefficients of polynomial fits of m_E^0 Eq.(4.36) obtained from Tang (1997) for NaCl and Na_2SO_4 in the sulphate-poor domain assuming a_w = RH 67

5.1. Specific extinction coefficients in $m^2 g^{-1}$ derived from Mie calculations for wet internally mixed sea salt aerosol for each mode spectral band k_b. 88

5.2. Single scattering albedo derived from Mie calculations for wet internally mixed sea salt aerosol for each mode and spectral band k_b. 91

5.3. Asymmetry parameters derived from Mie calculations for wet internally mixed sea salt aerosol for each mode and spectral band k_b. 96

6.1. Simulation set-up. 100

6.2. Overview of the simulations with the extended model system COSMO-ART. Anthropogenic aerosols are treated according to Vogel et al. (2009). 101

6.3. Mean changes (run F-run R) in the solar and thermal net radiative fluxes in W m^{-2} and temperature difference at 2 m level in K. All the values are averaged over the simulation period 24th-26th July 2007, and presented with the corresponding standard deviation. 152

6.4. Summary of the DRE of anthropogenic and sea salt aerosol. Mean changes (run F_{all}-run R) in the solar and thermal net radiative fluxes in W m^{-2} and temperature difference at 2 m level in K. All values are averaged over the simulation period 24th-26th July 2007 and presented with the corresponding standard deviation. 164

Bibliography

Andreae, M., Charlson, R., Bruynseels, F., Storms, H., van Grieken, R., and Maenhaut, W. (1986). Internal Mixture of Sea Salt, Silicates, and Excess Sulfate in Marine Aerosols. *Science*, 232:1620–1623.

Andreae, M., Ferek, R., Bermond, F., Byrd, K., Engstrom, R., Hardin, S., Houmere, P., LeMarrec, F., Raemdonck, H., and Chatfield, R. (1985). Dimethyl sulfide in the marine atmosphere. *J. Geophys. Res.*, 90(D7):12,891–12,900.

Andreas, E. (1998). A New Sea Spray Generation Function for Wind Speeds up to 32 m s^{-1}. *J. Phys. Oceanogr.*, 28:2175–2184.

Andrews, E., Sheridan, P., Fiebig, M., McComiskey, A., Ogren, J., Arnott, P., Covert, D., Elleman, R., Gasparini, R., Collins, D., Jonsson, H., Schmid, B., and Wang, J. (2006). Comparison of methods for deriving aerosol asymmetry parameter. *J. Geophys. Res.*, 111:16.

Athanasopoulou, E., Tombrou, M., Pandis, S., and Russell, A. (2008). The role of sea-salt emissions and heterogeneous chemistry in the air quality of polluted coastal areas. *Atmos. Chem. Phys.*, 8:5755–5769.

Bangert, M. (2006). *Eine Parametrisierung für die Berechnung von Photolysefrequenzen in Chemie-Transport-Modellen.* Seminararbeit (in german), Institute for meteorology and climate research, University of Karlsruhe (TH), Karlsruhe, Germany.

Barnaba, F. and Gobbi, G. (2004). Aerosol seasonal variability over the Mediterranean region and relative impact of maritime, continental and Saharan dust particles over the basin from MODIS data in the year 2001. *Atmos. Chem. Phys.*, 4:2367–2391.

Bergamo, A., Tafuro, A., Kinne, S. De Tomasi, F., and Perrone, M. (2008). Monthly-averaged anthropogenic aerosol direct radiative forcing over the Mediterranean based on AERONET aerosol properties. *Atmos. Chem. Phys.*, 8:6995–7014.

Berresheim, H., Andreae, M., Iverson, R., and Li, S. (1991). Seasonal variations of dimethylsufide emissions and atmosphreic sulfur and nitrogen species over the western north Atlantic Ocean. *Tellus B*, 43:353–372.

Blanchard, D. (1963). *The electrification of the atmosphere by particles from bubbles in the sea.* in Progr. Oceanogr.

Blanchard, D. and Woodcock, A. (1980). The production, concentration, and vertical distribution of the sea-salt aerosol. *Ann. N.Y. Acad. Sci.*, 338:330–347.

Bohren, C. and Huffman, D. (1983). *Absorption and Scattering of Light by Small Particles.* John Wiley and Sons, New York.

Bär, M. and Nester, K. (1992). Parameterization of trace gas dry deposition velocities for a regional mesoscale diffusion model. *Ann. Geophys.*, 10:912–923.

Clarke, A., Kapustin, V., Howell, S., and Moore, K. (2003). Sea-Salt Distributions from Breaking Waves: Implications for marine Aerosol Production and Optical Extinction Measurements during SEAS*. *J. Atmos. Oceanic Technol.*, 20(D12110):1362–1374.

Clarke, A. D., Owens, A. R., and Zhou, J. (2006). An ultrafine sea-salt flux from breaking waves: Implications for cloud condensation nuclei in the remote marine atmosphere. *J. Geophys. Res.*, 111(D06202):14.

Clegg, N., O'Dowd, C., Smith, M., and Lowe, J. (1998). Sulphate partitioning in marine aerosol. *J. Aerosol. Sci.*, 29:881–882.

Croft, B., Lohmann, U., Martin, R. V., Stier, P., Wurzler, S., Feichter, J., Hoose, C., Heikkilä, U., van Donkelaar, A., and Ferrachat, S. (2009). Influences of in-cloud aerosol scavenging parameterizations on aerosol concentrations and wet deposition in ECHAM5-HAM. *Atmos. Chem. Phys. Discuss.*, 9:22041–22101.

Davison, B. and Hewitt, C. (1992). Natural Sulphur Species From the North Atlantic and Their Contribution to the United Kingdom Sulphur Budget. *J. Geophys. Res.*, 97(D2):2475–2485.

Di Ioro, T., di Sarra, A., Junkermann, A. Cacciani, M., Fiocco, G., and Fuà, D. (2003). Tropospheric aerosols in the Mediterranean: 1. Microphysical and optical properties. *J. Geophys. Res.*, 108(D10).

Doms, G., Förstner, J., Heise, E., Herzog, H.-J., Raschendorfer, M., Reinhardt, T., Ritter, B., Schrodin, R., Schulz, J.-P., and Vogel, G. (2007). A description of the Nonhydrostatic Regional Model LM, Part II: Physical Parameterization. *Offenbach, Germany. Available online: http://www.cosmo-model.org.*

Eldridge, J. and Palik, E. (1985). *Sodium Chloride, in Handbook of Optical Constants of Solids.* Edited by E.D. Palik, Academic Press, Inc., Orlando.

Erickson, D. and Duce, R. (1988). On the global flux of atmospheric sea salt. *J. Geophys. Res.*, 93:14.079–14.088.

Finlayson-Pitts, B. and Hemminger, J. (2000). Physical Chemistry of Airborne Sea Salt Particles and Their Components. *J. Phys. Chem. A.*, 104:11463–11477.

Fitzgerald, J. W. (1975). Approximation formula for the equilibrium size of an aerosol particle as a function of its dry size and composition and the ambient relativity. *J. Appl. Meteor.*, 14:1044–1049.

Fitzgerald, J. W. (1991). Marine aerosols: A review. *Atmos. Environ.*, 25A:533–545.

Foltescu, V., Pryor, S., and Bennet, C. (2005). Sea salt generation, dispersion and removal on the regional scale. *Atmos. Environ.*, 39:2123–2133.

Forster, P., Ramanaswamy, V., Artaxo, P., Berntsen, T., Betts, R., Fahey, D., Haywood, J., Lean, J., Lowe, D., Myhre, G., Nganga, J., Prinn, R., Raga, G., Schulz, M., Dorland, R. C. i. A. C., and in Radiative Forcing. In: (2007). *Climate Change 2007: The Physical Basics. Contribution of Working Group I to the Fourth Assessment Report of the Intergovernmental Panel on Climate Change.* Cambridge University Press, Cambridge, United Kingdom and New York, NY, USA.

Freese, D. and Kottmeier, C. (1998). Radiation exchange between stratus clouds and pola marine surfaces. *Bound.-Lay. Meteorol.*, 87:331–356.

Gerber, H. E. (1985). *Relative-humidity parameterization of the Navy aerosol model (NAM). NRL Report 8956.* National Research Laboratory, Washington, D.C., USA.

Glantz, P., Nilsson, E., and von Hoyningen-Huene, W. (2009). Estimating a relationship between aerosol optical thickness and surface wind speed over the ocean. *Atmos. Res.*, 92:58–68.

Gong, S., Barrie, L., and Blanchet, J.-P. (1997). Modeling sea-salt aerosols in the atmosphere, 1. Model development. *J. Geophys. Res.*, 39:2123–2133.

Gong, S., Barrie, L., and Lazare, M. (2002). Canadian Aerosol Module (CAM):A size-segregated simulation of atmospheric aerosol processes for climate and air quality models 2. Global sea-salt aerosol and its budgets. *J. Geophys. Res.*, 107(D24):4779–4792.

Granqvist, C. and Hunder, O. (1977). Optical properties of ultrafine particles. *Phys. Rev. B.*, 16(8):3513–3534.

Grell, G., Peckham, S., Schmitz, R., McKeen, S., Frost, G., Skamarock, W., and Eder, B. (2005). Fully coupled "online" chemistry within the WRF model. *Atmos. Environ.*, 39:6957–6975.

Grini, A., Myhre, G., Sundet, J., and Isaksen, I. (2002). Modeling the Annual Cycle of Sea Salt in the Global 3D Model Oslo CTM2: Concentrations, Fluxes and Radiative Impact. *J. Climate.*, 15:1717–1730.

Heintzenberg, J. (1997). Measurements and modeling of aerosol single scattering albedo: progress, problems and prospects. *Beitr. Phys. Atmos.*, 70:249–263.

Heintzenberg, J., Covert, D., and van Dingenen, R. (2000). Size distribution and chemical composition of marine aerosols: a compilation and review. *Tellus*, 52B:1104–1122.

Hoose, C. (2004). *Numerische Simulationen zur Ausbreitung von Mineralstaub auf der regionalen Skala.* Diploma thesis (in german), Institute for meteorology and climate research, University of Karlsruhe (TH), Karlsruhe, Germany.

Huang, H., Thomas, G., and Grainger, R. (2009). Relationship between wind speed and aerosol optical depth over remote ocean. *Atmos. Chem. Phys. Discuss.*, 9:24511–24529.

Huneeus, N. Boucher, O. and Chevallier, F. (2009). Simplified aerosol modelling for variational data assimilation. *Geosci. Model Dev.*, 2:213–229.

IFS (2003). *IFS Documentation Cycle CY25r1, Parts I-VII.* P.W. White, European Centre for Medium-Range Weather Forecasts, Reading, England.

IPCC (2007). *Climate Change 2007: Physical Science Basis. Contribution of Working Group I to the Fourth Assessment Report of the Intergovernmental Panel on Climate Change.* Solomon, S. and Qin, D. and Chen, Z. and Marquis, M. and Averyt, K.B. and Tignor, M. and Miller, H.L. Cambridge University Press 2007.

Irshad, R., Grainger, R., Peters, D., McPheat, R., Smith, K., and Thomas, G. (2009). Laboratory measurements of the optical properties of sea salt aerosol. *Atmos. Chem. Phys.*, 9:221–230.

Jacobson, M. (1997). Development and application of a new air pollution modeling system-II. Aerosol module structure and design. *Atmos. Environ.*, 31:131–144.

Jacobson, M. (2001a). Global direct radiative forcing due to multicomponent anthropogenic and natural aerosols. *J. Geophys. Res.*, 106(D2):1551–1568.

Jacobson, M. (2001b). Strong radiative heating due to the mixing state of black carbon in atmospheric aerosols. *Nature*, 409:695–697.

Jacobson, M. (2002). Analysis of aerosol interactions with numerical techniques for solving coagulation, nucleation, condensation, dissolution, and reversible chemistry among multiple distributions. *J. Geophys. Res.*, 107(D19):4366.

Jennings, S., Kleefeld, C., O'Dowd, C., Junker, C., Spain, T., O'Brien, P., Roddy, A., and O'Connore, T. (2003). Mace Head Atmospheric Research Station- characterization of aerosol radiative parameters. *Boreal Environ. Res.*, 8:303–314.

Jensen, J. and Lee, S. (2008). Giant Sea-Salt Aerosols and Warm Rain Formation in Marine Stratocumulus. *J. Atmos. Sci.*, 65:3678–3694.

Katoshevski, D., Nenes, A., and Seinfeld, J. (1999). A study of processes that govern the maintainance of aerosols in the marine boundary layer. *J. Aerosol. Sci.*, 4:503–532.

Kaufman, Y., Koren, I., Remer, L., Tanré, A., Ginoux, P., and Fan, S. (2005). Dust transport and deposition observed from the Terra-Moderate Resolution Imaging Spectroradiometer (MODIS) spacecraft over the Atlantic Ocean. *J. Geophys. Res.*, 110(D10S12):16.

Kerkweg, A., Jöckel, P., Pozzer, A., Tost, H., Sander, R., Schulz, M., Stier, P., Vignati, E., Wilson, J., and Lelieveld, J. (2008). Consistent simulation of bromine chemistry from the marine boundary layer to the stratosphere-Part1: Model description, sea salt aerosols and pH. *Atmos. Chem. Phys.*, 8:5899–5917.

Kerminen, V.-M. and Wexler, A. (1994). Post-fog nucleation of H_2SO_4-H_2O particles in smog. *Atmos. Environ.*, 28:2399–2406.

Kettle, A. and Andreae, M. (2000). Flux of dimethylsulfide from the oceans: A comparison of updated data sets and flux models. *J. Geophys. Res.*, 105(D22):26,793–26,808.

Kloster, S., Feichter, J., Maier-Reimer, E., Six, K., Stier, P., and Wetzel, P. (2006). DMS cycle in the marine ocean-atmosphere system - a global model study. *Biogeosciences*, 3:29–51.

Knote, C. (2009). *Emissions preprocessing for COSMO-ART.* Laboratory for Air Pollution/Environmental Technology. Empa-Materials Science and Technology. Version 0.3.

Kouvarakis, G., Bardouki, H., and Mihalopoulos, N. (2002). Sulfur budget above the Eastern Mediterranean: relative contribution of anthropogenic and biogenic sources. *Tellus*, 54B:201–212.

Kouvarakis, G. and Mihalopoulos, N. (2002). Seasonal variation of dimethylsulfide in the gas phase and of methanesulfonate and non-sea-salt sulfate in the aerosols phase in the Eastern Mediterranean atmosphere. *Atmos. Environ.*, 36:929–938.

Kramm, G., Beheng, K.-D., and Müller, H. (1992). Modeling of the vertical transport of polydispersed aerosol particles in the atmospheric surface layer in *Precipitation Scavenging and Atmospheric Surface Exchange.* Vol 1, Hemisphere, Bristol, PA. pages 1125–1141.

Lee, J., McFiggans, G., Allan, J., Baker, A. R., Ball, S. M., Benton, A. K., Carpenter, L. J., Commane, R., Finley, *, B. D., Evans, M., Fuentes, E., Furneaux, Ę, K., Goddard, A., Good, N., Hamilton, J. F., Heard, D. E., Herrmann, H., Hollingsworth, A., Hopkins, J. R., Ingham, T., Irwin, M., Jones, C. E., Jones, R. L., Keene, W. C., Lawler, M. J., Lehmann, S., Lewis, A. C., Long, M. S., Mahajan, A., Methven, J., Moller, S. J., Müller, K., Müller, T., Niedermeier, N., OŠDoherty, S., Oetjen, H., Plane, J. M. C., Pszenny, A. A. P., Read, K. A., Saiz-Lopez, A., Saltzman, E. S., Sander, R., von Glasow, R., Whalley, L., Wiedensohler, A., and Young, D. (2009). Reactive Halogens in the Marine Boundary Layer (RHaMBLe): the tropical North Atlantic experiments. *Atmos. Chem. Phys. Discuss.*, 9:21,17–21,783.

Lehahn, Y., Kore, I., Boss, E., Ben-Ami, Y., and Altaratz, O. (2010). Estimating the maritime component of aerosol optical depth and its dependency on surface wind speed using MODIS and QuikSCAT data. *Atmos. Chem. Phys. Discuss.*, 10:1983–2003.

Levin, Z., Teller, A., and Ganor, E. (2005). On the interactions of mineral dust, sea-salt particles, and clouds: A measurement and modeling study from the Mediterranean Israeli Dust Experiment campaign. *J. Geophys. Res.*, 110(D20202):19.

Lewis, E. and Schwartz, S. (2004). *Sea Salt Aerosol Production: Mechanisms, Methods, Measurements and Models: A Critical Review.* American Geophysical Union, Washington DC 2004.

Lewis, E. and Schwartz, S. (2006). Comment on "size distribution of sea-salt emissions as a function of relative humidity". *Atmos. Environ.*, 40:588–590.

Li, J., Ma, X., von Salzen, K., and Dobbie, S. (2008). Parameterization of sea-salt optical properties and physics of the associated radiative forcing. *Atmos. Chem. Phys.*, 8:4787–4798.

Li-Jones, X., Savoie, D., and Prospero, J. (2001). HNO_3 losses within the cyclone inlet of a diffusion-denuder system under simulated marine environments. *Atmos. Environ.*, 35:985–993.

Liss, P. and Merlivat, L. (1986). *Air-sea gas exchange rates: Introduction and synthesis, in The role of Air-Sea Exchange in Geochemical Cycling.* D. Reidel, Norwell, Mass.

Liu, Y. and Daum, P. H. (2008). Relationship of refractive index to mass density and self-consistency of mixing rules for multicomponent mixtures like ambient aerosols. *J. Aerosol. Sci.*, 39:974–986.

Longhurst, A., Sathyendranath, S., Platt, T., and Caverhill, C. (1995). An estimate of global primary production in the ocean from satellite radiometer data. *J. Plankton. Res.*, 17:1245–1271.

Lundgren, K. (2006). Numerical Simulation of the Spatial and Temporal Distribution of Sea Salt Particles on the Regional Scale. *Thesis for M.Sc., Department of Meteorology, Stockholm University.*, page 51.

Ma, X., von Salzen, K., and Li, J. (2008). Modelling sea salt aerosol and its direct and indirect effects on climate. *Atmos. Chem. Phys.*, 7:1311–1327.

Marshall, J., Lohmann, U., Leaitch, W. R., Lehr, P., and Hayden, K. (2007). Aerosol scattering as a function of altitude in a coastal environment. *J. Geophys. Res.*, 112(D14203):13.

Middlebrook, A., Murphy, D., and Thomson, D. (1998). Observations of organic material in individual marine particles at Cape Grim during the First Aerosol Characterization Experiment (ACE 1). *J. Geophys. Res.*, 103(D13):16,475–16,483.

Miller, S., Marandino, C., de Bruyn, W., and Saltzman, E. (2009). Air-sea gas exchange of CO_2 and SMA in the North Atlantic by eddy covariance. *Geophys. Res. Lett.*, 36(L15816).

Ming, Y. and Russell, L. M. (2001). Predicted hygroscopic growth of sea salt aerosol. *J. Geophys. Res.*, 106(D22):28,259–28,274.

Modini, R., Harris, B., and Ristovski, Z. (2010). The organic fraction of bubble-generated, accumulation mode Sea Spray Aerosol (SSA). *Atmos. Chem. Phys.*, 10:2867–2877.

Mogili, P., Yang, K., Young, M., and Kleiber, P. (2007). Environmental aerosol chamber studies of extinction spectra of mineral dust aerosol components: Broadband IR-UV extinction spectra. *J. Geophys. Res.*, 112:12.

Monahan, E. (1971). Oceanic Whitecaps. *J. Phys. Oceanogr.*, 1:139–144.

Monahan, E., Spiel, E., and Davidson, K. (1986). *A model of marine aerosol generation via whitecaps and wave disruption.* D. Reidel Publishing Company.

Moore, K., Clarke, A., Kapustin, V., McNaugthton, C., Anderson, B., Winstead, E., Weber, R., Ma, Y., Lee, Y., Talbot, R., Dibb, J., Anderson, T., Doherty, S., Covert, D., and Rogers, D. (2004). A comparison of similar aerosol measurements made on the NASA P3-B, DC-8, and NSF C-130 aircraft during TRACE-P and ACE-Asia. *J. Geophys. Res.*, 109:35.

Mårtensson, M., Nilsson, E., de Leeuw, G., and Cohen, L. (2003). Laboratory simulations and parameterization of the primary marine aerosol production. *J. Geophys. Res.*, 108(D9):4297–4308.

Mulcahy, J., O'Dowd, C., and Jennings, S. (2009). Aerosol optical depth in clean marine and continental northeast Atlantic air. *J. Geophys. Res.*, 114:10.

Mulcahy, J., O'Dowd, C., Jennings, S., and Ceburnis, D. (2008). Significant enhancement of aerosol optical depth in marine air under high wind conditions. *Geophy. Res. Lett.*, 35(L16810):14.

Murphy, D., Anderson, J., Quinn, P., McInnes, L., Brechtel, F., Kreidenweis, S., Middlebrook, A., Pósfai, M., Thomson, D., and Buseck, P. (1998). Influence of sea-salt on aerosol radiative properties in the Southern Ocean marine boundary layer. *Nature*, 392:62–65.

Murphy, D., Thomson, D., and Middlebrock, A. (1997). Bromine, iodine, and chlorine in single aerosol particles at Cape Grim. *Geophy. Res. Lett.*, 24(24):3197–3200.

Myhre, G. and Grini, A. (2006). Modelling of nitrate particles: importance of sea salt. *Atmos. Chem. Phys. Discuss.*, 6:1455–1480.

Nightingale, P., Malin, G., Law, C., Watson, A., and Liss, P. (2000). In situ evaluation of air-sea gas exchange parameterizations using novel conservative and volatile tracers. *Glob. Biogeochem. Cycles.*, 14:373–387.

O'Dowd, C., Lowe, J., and Smith, M. (1999). Observations and modelling of aerosol growth in marine stratocumulus-case study. *Atmos. Environ.*, 33:3053–3062.

O'Dowd, C. and Smith, M. (1993). Physiochemical properties of aerosols over the Northeast Atlantic: Evidence for wind speed related submicron sea salt production. *J. Geophys. Res.*, 98:1137–1149.

O'Dowd, C., Smith, M., Consterdine, I., and Lowe, J. (1997). Marine aerosol, sea-salt and the marine sulphur cycle: A short review. *Atmos. Environ.*, 31:73–80.

Pace, G., di Sarra, A., Meloni, D., Piacentino, S., and Chamard, P. (2006). Aerosol optical properties at Lampedusa (Central Mediterranean). 1. Influence of transport and identification of different aerosol types. *Atmos. Chem. Phys.*, 6:697–713.

Petty, G. (2006). *A First Course in Atmospheric Radiation.* 2nd Ed. Sundog Publishing, Madison, Wisconsin.

Pham, M., Müller, J.-F., Brasseur, G., and Mégie, G. (1995). A three-dimensional study of the tropospheric sulfur cycle. *J. Geophys. Res.*, 20:26,061–26,092.

Pierce, J. and Adams, P. (2006). Global evaluation of CCN formation by direct emission of sea salt and growth of ultrafine sea salt. *J. Geophys. Res.*, 111(D06203):16.

Pregger, T., Thiruchittampalam, B., and Friedrich, R. (2007). Ermittlung von Emissionsdaten zur Untersuchung der Klimawirksamkeit von Russpartikeln in Baden-Württemberg. Final Report. *IER Universität Stuttgart.*

Quinn, P. and Bates, T. (2005). Regional aerosol properties: Comparisons of boundary layer measurements from ACE 1, ACE 2, Aerosols99, INDOEX, ACE Asia, TARFOX, and NEAQS. *J. Geophys. Res.*, 110:24.

Quinn, P., Coffman, D., Kapustin, V., and Bates, T. (1998). Aerosol optical properties in the marine boundary layer during the First Aerosol Characterization Experiment (ACE 1) and the underlying chemical and physical properties. *J. Geophys. Res.*, 103:16,547–16,563.

Randles, C., R ussell, L., and Ramaswamy, V. (2004). Hygroscopic and optical properties of organic sea salt and consequences for climate forcing. *Geophys. Res. Lett.*, 31:4.

Riemer, N. (2002). *Numerische Simulationen zur Wirkung des Aerosols auf die troposphärische Chemie und die Sichtweite.* Ph.D. thesis (in german), Institute for meteorology and climate research, University of Karlsruhe (TH), Karlsruhe, Germany.

Rinke, R. (2008). *Parametrisierung des Auswaschens von Aerosolpartikeln durch Niederschlag.* Ph.D. thesis (in german), Institute for meteorology and climate research, University of Karlsruhe (TH), Karlsruhe, Germany.

Ritter, B. and Geleyn, J.-F. (1992). A comprehensive scheme for numerical weather prediction models with potential applications in climate simulations. *Month. Wea. Rev.*, 120:303–325.

Satheesh, S. (2002). Aerosol radiative forcing over tropical Indian Ocean: modulation by sea-surface winds. *Curr. Sci. India*, 82:310–316.

Satheesh, S. and Krishna Moorthy, K. (2005). Radiative effects of natural aerosols: A review. *Atmos. Environ.*, 39:2089–2110.

Satheesh, S. and Krishna Moorthy, K. (2006). Contribution of sea-salt to aerosol optical depth over the Arabian Sea derived from MODIS observations. *Geophys. Res. Lett.*, 33:4.

Schinozuka, Y., Clarke, A., Howell, S., Kapustin, V., and Huebert, B. (2004). Sea-salt vertical profiles over the Southern and tropical Pacific oceans: Microphysics, optical properties, spatial variability, and variations with wind speed. *J. Geophys. Res.*, 109(D24201):17.

Segelstein, D. (1981). *The complex refractive index of water.* Masters Thesis, University of Missouri, Kansas City.

Seinfeld, J. H. and Pandis, S. (1998). *Atmospheric Chemistry and Physics: From Air Pollution to Climate Change.* John Wiley and Sons, Inc.

Shannon, R., Shannon, R., Medenbach, O., and Fischer, R. (2002). Refractive Index and Dispersion of Flourides and Oxides. *J. Phys. Chem. Ref. Data*, 31:931–970.

Sievering, H., Boatman, J., Gorman, E., Kim, Y., Anderson, L., Ennis, G. Luria, M., and Pandis, S. (1992). Removal of sulphur from the marine boundary layer by ozone oxidation in sea-salt aerosols. *Nature*, 360:571–573.

Slinn, S. and Slinn, W. (1980). Prediction for particle deposition on natural waters. *Atmos. Environ.*, 16:1785–1794.

Smirnov, A., Holben, B., Dubovik, O., Frouin, R., Eck, T., and Slutsker, I. (2003). Maritime component in aerosol optical models derived from Aerosol Robotic Network data. *J. Geophys. Res.*, 108:11.

Smith, M., Park, P., and Consterdine, I. (1993). Marine aerosol concentrations and estimated fluxes over the sea. *Q. J. R. Meteorol. Soc.*, 119:809–824.

Song, C. and Carmichael, G. (1999). The aging process of naturally emitted aerosol (sea-salt and mineral dust) during long range transport. *Atmos. Environ.*, 33:2203–2218.

Spicer, C., Kenny, D., Chapman, E., Busness, K., and Berkowitz, C. (1996). Observations of dimethyl sulfide over the western North Atlantic Ocean using an airborne tandem mass spectrometer. *J. Geophys. Res.*, 101(D22):29,137–29,147.

Stanelle, T. (2008). *Wechselwirkungen von Mineralstaubpartikeln mit thermodynamischen und dynamischen Prozessen in der Atmosphäre über Westafrika.* Ph.D. thesis (in german), Institute for meteorology and climate research, University of Karlsruhe (TH), Karlsruhe, Germany.

Stelson, A. (1990). Urban aerosol refractive index prediction by partial molar refraction approach. *Eniron. Sci. Technol.*, 24:1676–1679.

Steppeler, J., Doms, G., Schättler, U., Bitzer, H. W., Gassmann, A., Damrath, U., and Gregoric, G. (2003). Meso-gamma scale forecasts using the nonhydrostatic model LM. *Meteorol. Atmos. Phys.*, 82:75–96.

Stier, P., Feichter, J., Kinne, S., Kloster, S., Vignati, E., Wilson, J., Ganzeveld, L., Tegen, L., Werner, M., Balkanski, Y., Schulz, M., Boucher, O., Minikin, A., and Petzold, A. (2005). The aerosol-climate model ECHAM5-HAM. *Atmos. Chem. Phys.*, 5:1125–1156.

Stockwell, W., Middleton, P., and Chang, J. (1990). The Second Generation Regional Acid Deposition Model Chemical Mechanism for Regional Air Quality Modeling. *J. Geophys. Res.*, 95(D10):16,343–16,367.

Stokes, R. and Robinson, R. (1966). Interactions in Aqueous Nonelectrolyte Solutions. I. Solute-Solvent Equilibria. *J. Phys. Chem.*, 70:2126–2130.

Tang, I. N. (1996). Chamical and size effects of hygroscopic aerosols on light scattering coefficients. *J. Geophys. Res.*, 101(D14):19,245–19,250.

Tang, I. N. (1997). Thermodynamic and optical properties of mixed-salt aerosols of atmospheric importance. *J. Geophys. Res.*, 102(D2):1883–1893.

Tang, I. N. and Munkelwitz, H. (1994). Water activities, densities, and refractive indices of aqueous sulfates and sodium nitrate droplets of atmospheric importance. *J. Geophys. Res.*, 99(D9):18,801–18,808.

Tang, I. N., Tridico, A., and Fung, K. (1997). Thermodynamic and optical properties of sea salt aerosols. *J. Geophys. Res.*, 102(D19):23,269–23,275.

Tarrasón, L., Turner, S., and Fløisand, I. (1995). Estimation of seasonal dimethyl sulphide fluxes over the North Atlantic Ocean and their contribution to European pollution levels. *J. Geophys. Res.*, 100(D6):11,623–11,639.

Textor, C., Schulz, M., Guibert, S., Kinne, S., Balkanski, Y., Bauer, S., Berntsen, T., Berglen, T., Boucher, O., Chin, M., Dentener, F., Diehl, T., Easter, R., Feichter, H., Fillmore, D., Ghan, S., Ginoux, P., Gong, S., Grini, A., Hendricks, J., Horowitz, L., Huang, P., Isaksen, I., Iversen, T., Kloster, S., Koch, D., Kirkevåg, A., Kristjansson, J. E., Krol, M., Lauer, A., Lamarque, J. F., Liu, X., Montanaro, V., Myhre, G., Penner, J., Pitari, G., Reddy, S., Seland, O., Stier, P., Takemura, T., and Tie, X. (2006). Analysis and quantification of the diversities of aerosol life cycles within AeroCom. *Atmos. Chem. Phys.*, 6:1777–1813.

Toon, O., Pollock, J., and Khare, B. (1976). The optical constants of several atmospheric aerosol species: ammonium sulfate, aluminium oxide and sodium chloride. *J. Geophys. Res.*, 81:5733–5748.

Topping, D., McFiggans, G., and Coe, H. (2005). A curved multicomponent aerosol hygroscopicity model framework. Part 1: Inorganic compounds. *Atmos. Chem. Phys.*, 5:1205–1222.

Tzanis, C. and Varotsos, C. (2008). Tropospheric aerosol forcing of climate: a case study for the greater area of Greece. *Int. J. Remote. Sens.*, 29:2507–2517.

Vogel, B., Fiedler, F., and Vogel, H. (1995). Influence of topography and biogenic volatile organic compounds emission in the state of Baden-Württemberg on ozone concentrations during episodes of high air temperatures. *J. Geophys. Res.*, 100:22907–22928.

Vogel, B., Hoose, C., and Vogel, H. and. Kottmeier, C. (2006a). A model of dust transport applied to the Dead Sea area. *Meteorol. Z.*, 14:611–624.

Vogel, B., Vogel, H., Bäumer, D., Bangert, M., Lundgren, K., Rinke, R., and Stanelle, T. (2009). The comprehensive model system COSMO-ART - Radiative impact of aerosol on the state of the atmosphere on the regional scale. *Atmos. Chem. Phys.*, 9:8661–8680.

Vogel, H., Vogel, B., and Kottmeier, C. (2006b). Modelling of pollen dispersion with a weather forecast model system in Air Pollution Modeling and Its Application XVIII. in. *Borrego and Renner, Elsevier, ISBN 044452987X.*, pages 481–491.

von Glasgow, R. and Sander, R. (2001). Variation of sea salt aerosol pH with relative humidity. *Geophys. Res. Lett.*, 28:247–250.

Wanninkhof, R. (1992). Relationship Between Wind Speed and Gas Exchange Over the Ocean. *J. Geophys. Res.*, 97(C5):7373–7382.

Whitby, K. (1978). The physical characteristics of sulfur aerosols. *Atmos. Environ.*, 12:135–159.

Whitby, K., McMurray, P., Shankar, U., and Binkowski, F. (1991). Modal Aerosol Dynamics Modeling. *Technical Report 600/3-91/020, (NTIS PB91-161729/AS Natl. Tech. Inf. Serv. Springfeld, Va.), Atmos. Res. and Exposure Assess. Lab. U.S. Environ. Prot. Agency, Research Triangle Park, N.C.*

Wilson, J., Cuvelier, C., and Raes, F. (2001). A modeling study of global mixed aerosol fields. *J. Geophys. Res.*, 106(D24):9.

Winter, B. and Chýlek, P. (1997). Contribution of sea salt aerosol to the planetary clear-sky albedo. *Tellus*, 49B:72–79.

Wippermann, F. (1980). The applicability of several approximations in mesoscale modelling - A linear approach. *Contrib. Atmos. Phys.*, 54:298–308.

Yu, F. and Luo, G. (2009). Simulation of particle size distribution with a global aerosol model: contribution of nucleation to aerosol and CCN number concentrations. *Atmos. Chem. Phys.*, 9:7691–7710.

Yu, H., Chin, M., Remer, L., Kleidman, R., Bellouin, N., Bian, H., and Diehl, T. (2009). Variability of marine aerosol fine-mode fraction and estimates of athropogenic aerosol component over cloud-free oceans from the Moderate Resolution Imaging Spectroradiometer. *J. Geophys. Res.*, 114(D10206):11.

Zaveri, R., Easter, R. C., and Wexler, A. (2005). A new method for multicomponent activity coefficients of electrolytes in aqueous atmospheric aerosols. *J. Geophys. Res.*, 110(D02201):23.

Zhang, K., Knipping, E., Wexler, A., Bhave, P., and Tonnesen, G. (2005). Size distribution of sea-salt emissions as a function of relative humidity. *Atmos. Environ.*, 39:3373–3379.

Acknowledgements

This thesis was performed at the Institute for Meteorology and Climate Research at the Karlsruhe Institute of Technology. I want to give Prof. Christoph Kottmeier a lot of gratitude for advising and encouraging this work. Thank you for the helpful suggestions and interest in this study. Likewise, many thanks to Prof. Thomas Leisner for kindely accepting to co-supervise this thesis.

I owe Dr. Bernhard Vogel many thanks for introducing me to this interesting topic and for the constant support. I want to thank you for always having time for me, for sharing your ideas, knowledge and experience, and for spreading so much positive energy. I appreciate the way you have encouraged and motivated me throughout this thesis. I am also very grateful to Dr. Heike Vogel, especially for all the help with questions regarding the model. I value your experience and, not least, your patience. A lot of thanks to my office mate Dr. Rayk Rinke for contributing to the nice working atmosphere, your kindness, and for always being prepared to lively discuss scientific issues with me. At this place I also want to thank Max Bangert and my former colleagues Dr. Tanja Stanelle and Dr. Dominique Bäumer for a nice time together and fruitful scientific discussions. I especially want to thank Dominique for patiently sharing your experience regarding the Mie-calculations. I want to thank Gabi Klink for the help with diverse computer questions and problems. I also want to thank Friederike Schönbein for her patience and help with all kinds of bureaucratic issues. Many thanks goes to Christoph Knote for the help the emission data and to DWD for providing the external data. Also many thanks to Dr. David Topping for introducing me to the world of solvation and to Dr. Martin Schnaiter for sharing your knowledge about radiation and particles. I additionally want to thank all colleagues in the *Mittagsrunde* for the nice company during the lunch

breaks, and to the 4th floor colleagues at IMK-ASF for letting me use your microwave at any time. I want to thank all of my colleagues and friends- Romi Sasse in particular- for your support and tips, especially during these last months of my thesis.

Last but not least, I especially want to thank my parents and my sister for always being there for me, for encouraging me, and for your believe in me. You being there for me means alot!

Wissenschaftliche Berichte des Instituts für Meteorologie und Klimaforschung des Karlsruher Instituts für Technologie (0179-5619)

Bisher erschienen:

Nr. 1: *Fiedler, F. / Prenosil, T.*
Das MESOKLIP-Experiment. (Mesoskaliges Klimaprogramm im Oberrheintal).
August 1980

Nr. 2: *Tangermann-Dlugi, G.*
Numerische Simulationen atmosphärischer Grenzschichtströmungen über langgestreckten mesoskaligen Hügelketten bei neutraler thermischer Schichtung.
August 1982

Nr. 3: *Witte, N.*
Ein numerisches Modell des Wärmehaushalts fließender Gewässer unter Berücksichtigung thermischer Eingriffe.
Dezember 1982

Nr. 4: *Fiedler, F. / Höschele, K. (Hrsg.)*
Prof. Dr. Max Diem zum 70. Geburtstag.
Februar 1983 (vergriffen)

Nr. 5: *Adrian, G.*
Ein Initialisierungsverfahren für numerische mesoskalige Strömungsmodelle.
Juli 1985

Nr. 6: *Dorwarth, G.*
Numerische Berechnung des Druckwiderstandes typischer Geländeformen.
Januar 1986

Nr. 7: *Vogel, B.; Adrian, G. / Fiedler, F.*
MESOKLIP-Analysen der meteorologischen Beobachtungen von mesoskaligen Phänomenen im Oberrheingraben.
November 1987

Nr. 8: *Hugelmann, C.-P.*
Differenzenverfahren zur Behandlung der Advektion.
Februar 1988

Nr. 9: *Hafner, T.*
Experimentelle Untersuchung zum Druckwiderstand der Alpen.
April 1988

Nr. 10: *Corsmeier, U.*
Analyse turbulenter Bewegungsvorgänge in der maritimen atmosphärischen Grenzschicht.
Mai 1988

Nr. 11: *Walk, O. / Wieringa, J.(eds)*
Tsumeb Studies of the Tropical Boundary-Layer Climate.
Juli 1988

Nr. 12: *Degrazia, G. A.*
Anwendung von Ähnlichkeitsverfahren auf die turbulente Diffusion in der konvektiven und stabilen Grenzschicht.
Januar 1989

Nr. 13: *Schädler, G.*
Numerische Simulationen zur Wechselwirkung zwischen Landoberflächen und atmophärischer Grenzschicht.
November 1990

Nr. 14: *Heldt, K.*
Untersuchungen zur Überströmung eines mikroskaligen Hindernisses in der Atmosphäre.
Juli 1991

Nr. 15: *Vogel, H.*
Verteilungen reaktiver Luftbeimengungen im Lee einer Stadt – Numerische Untersuchungen der relevanten Prozesse.
Juli 1991

Nr. 16: *Höschele, K.(ed.)*
Planning Applications of Urban and Building Climatology – Proceedings of the IFHP / CIB-Symposium Berlin, October 14-15, 1991.
März 1992

Nr. 17: *Frank, H. P.*
Grenzschichtstruktur in Fronten.
März 1992

Nr. 18: *Müller, A.*
Parallelisierung numerischer Verfahren zur Beschreibung von Ausbreitungs- und chemischen Umwandlungsprozessen in der atmosphärischen Grenzschicht.
Februar 1996

Nr. 19: *Lenz, C.-J.*
Energieumsetzungen an der Erdoberfläche in gegliedertem Gelände.
Juni 1996

Nr. 20: *Schwartz, A.*
Numerische Simulationen zur Massenbilanz chemisch reaktiver Substanzen im mesoskaligen Bereich.
November 1996

Nr. 21: *Beheng, K. D.*
Professor Dr. Franz Fiedler zum 60. Geburtstag.
Januar 1998

Nr. 22: *Niemann, V.*
Numerische Simulation turbulenter Scherströmungen mit einem Kaskadenmodell.
April 1998

Nr. 23: *Koßmann, M.*
Einfluß orographisch induzierter Transportprozesse auf die Struktur der atmosphärischen Grenzschicht und die Verteilung von Spurengasen.
April 1998

Nr. 24: *Baldauf, M.*
Die effektive Rauhigkeit über komplexem Gelände – Ein Störungstheoretischer Ansatz.
Juni 1998

Nr. 25: *Noppel, H.*
Untersuchung des vertikalen Wärmetransports durch die Hangwindzirkulation auf regionaler Skala.
Dezember 1999

Nr. 26: *Kuntze, K.*
Vertikaler Austausch und chemische Umwandlung von Spurenstoffen über topographisch gegliedertem Gelände.
Oktober 2001

Nr. 27: *Wilms-Grabe, W.*
Vierdimensionale Datenassimilation als Methode zur Kopplung zweier verschiedenskaliger meteorologischer Modellsysteme.
Oktober 2001

Nr. 28: *Grabe, F.*
Simulation der Wechselwirkung zwischen Atmosphäre, Vegetation und Erdoberfläche bei Verwendung unterschiedlicher Parametrisierungsansätze.
Januar 2002

Nr. 29: *Riemer, N.*
Numerische Simulationen zur Wirkung des Aerosols auf die troposphärische Chemie und die Sichtweite.
Mai 2002

Nr. 30: *Braun, F. J.*
Mesoskalige Modellierung der Bodenhydrologie.
Dezember 2002

Nr. 31: *Kunz, M.*
Simulation von Starkniederschlägen mit langer Andauer über Mittelgebirgen.
März 2003

Nr. 32: *Bäumer, D.*
Transport und chemische Umwandlung von Luftschadstoffen im Nahbereich von Autobahnen – numerische Simulationen.
Juni 2003

Nr. 33: *Barthlott, C.*
Kohärente Wirbelstrukturen in der atmosphärischen Grenzschicht.
Juni 2003

Nr. 34: *Wieser, A.*
Messung turbulenter Spurengasflüsse vom Flugzeug aus.
Januar 2005

Nr. 35: *Blahak, U.*
Analyse des Extinktionseffektes bei Niederschlagsmessungen mit einem C-Band Radar anhand von Simulation und Messung.
Februar 2005

Nr. 36: *Bertram, I.*
Bestimmung der Wasser- und Eismasse hochreichender konvektiver Wolken anhand von Radardaten, Modellergebnissen und konzeptioneller Betrachtungen.
Mai 2005

Nr. 37: *Schmoeckel, J.*
Orographischer Einfluss auf die Strömung abgeleitet aus Sturmschäden im Schwarzwald während des Orkans „Lothar“.
Mai 2006

Nr. 38: *Schmitt, C.*
Interannual Variability in Antarctic Sea Ice Motion: Interannuelle Variabilität antarktischer Meereis-Drift.
Mai 2006

Nr. 39: *Hasel, M.*
Strukturmerkmale und Modelldarstellung der Konvektion über Mittelgebirgen.
Juli 2006

Ab Band 40 erscheinen die Wissenschaftlichen Berichte des Instituts für Meteorologie und Klimaforschung bei KIT Scientific Publishing (ISSN 0179-5619).
Die Bände sind unter www.ksp.kit.edu als PDF frei verfügbar oder als Druckausgabe bestellbar.

Nr. 40: *Lux, R.*
Modellsimulationen zur Strömungsverstärkung von orographischen Grundstrukturen bei Sturmsituationen. (2007)
ISBN 978-3-86644-140-8

Nr. 41: *Straub, W.*
Der Einfluss von Gebirgswellen auf die Initiierung und Entwicklung konvektiver Wolken. (2008)
ISBN 978-3-86644-226-9

Nr. 42: *Meißner, C.*
High-resolution sensitivity studies with the regional climate model COSMO-CLM. (2008)
ISBN 978-3-86644-228-3

Nr. 43: *Höpfner, M.*
Charakterisierung polarer stratosphärischer Wolken mittels hochauflösender Infrarotspektroskopie. (2008)
ISBN 978-3-86644-294-8

Nr. 44: *Rings, J.*
Monitoring the water content evolution of dikes. (2009)
ISBN 978-3-86644-321-1

Nr. 45: *Riemer, M.*
Außertropische Umwandlung tropischer Wirbelstürme: Einfluss auf das Strömungsmuster in den mittleren Breiten. (2012)
ISBN 978-3-86644-766-0

Nr. 46: *Anwender, D.*
Extratropical Transition in the Ensemble Prediction System of the ECMWF: Case Studies and Experiments. (2012)
ISBN 978-3-86644-767-7

Nr. 47: *Rinke, R.*
Parametrisierung des Auswaschens von Aerosolpartikeln durch Niederschlag. (2012)
ISBN 978-3-86644-768-4

Nr. 48: *Stanelle, T.*
Wechselwirkungen von Mineralstaubpartikeln mit thermodynamischen und dynamischen Prozessen in der Atmosphäre über Westafrika. (2012)
ISBN 978-3-86644-769-1

Nr. 49: *Peters, T.*
Ableitung einer Beziehung zwischen der Radarreflektivität, der Niederschlagsrate und weiteren aus Radardaten abgeleiteten Parametern unter Verwendung von Methoden der multivariaten Statistik. (2012)
ISBN 978-3-86644-323-5

Nr. 50: *Khodayar Pardo, S.*
High-resolution analysis of the initiation of deep convection forced by boundary-layer processes. (2012)
ISBN 978-3-86644-770-7

Nr. 51: *Träumner, K.*
Einmischprozesse am Oberrand der konvektiven atmosphärischen Grenzschicht. (2012)
ISBN 978-3-86644-771-4

Nr. 52: *Schwendike, J.*
Convection in an African Easterly Wave over West Africa and the Eastern Atlantic: A Model Case Study of Hurricane Helene (2006) and its Interaction with the Saharan Air Layer. (2012)
ISBN 978-3-86644-772-1

Nr. 53: *Lundgren, K.*
Direct Radiative Effects of Sea Salt on the Regional Scale. (2012)
ISBN 978-3-86644-773-8

53

KRISTINA LUNDGREN

Direct Radiative Effects of Sea Salt on the Regional Scale

This work aims to quantify the direct radiative effects of sea salt aerosol in the atmosphere. The online coupled regional scale model system COSMO-ART is extended for this objective. Furthermore, a new sea salt optical parameterisation is developed for both the shortwave and longwave spectrum. Based on numerical simulations with the extended model system, the direct radiative effects of sea salt aerosol are investigated.The simulated sea salt aerosol optical depth is found to show strong dependence on the 10 m wind speed under cloud free conditions. This relation is best described by a power law fit and compares well with satellite observations. For clear sky conditions, the simulated sea salt direct radiative effects on the shortwave and longwave radiative budgets are approximately in the same order of magnitude, but with opposite signs. This causes the net radiative effect to approach zero, which leads to a low impact on the temperature for this area.

ISBN 978-3-86644-773-8
9 783866 447738 >

ISSN 0179-5619
ISBN 978-3-86644-773-8